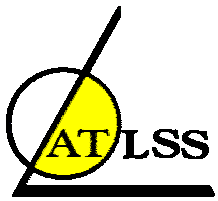

LEHIGH
University

Structural Integrity Assessment of Corrosion-Damaged Offshore Tubular Braces Subjected to Inelastic Cyclic Loading

by

Duncan Paterson
James M. Ricles

US Dept of Interior Minerals Management Service
Grant No. 1435-01-97-CT-30873-Modification #1

Pennsylvania Infrastructure Technology Alliance
Project No. IART-007

ATLSS Report No. 01-09
May, 2001

ATLSS is a National Center for Engineering Research
on Advanced Technology for Large Structural Systems

117 ATLSS Drive
Bethlehem, PA 18015-4729

Phone: (610)758-3525
Fax: (610)758-5902

www.atlss.lehigh.edu
Email: inatl@lehigh.edu

Acknowledgements

Financial support for this study was provided by the U.S. Department of the Interior Minerals Management Service (M.M.S.) (Grant #1435-01-97-CT-30873-Modification #1) and the Pennsylvania Infrastructure Technology Alliance (PITA) (Project #IART-007). Dr. Charles Smith served as the cognizant program official for the M.M.S. PITA is co-directed by Professor Richard Sause of Lehigh University and Professor Cristina Amon of Carnegie Mellon. Repair materials were provided by Hardcore Composites of New Castle, Delaware and Five Star Products, Inc. The support of all the sponsors is greatly appreciated.

The reported research was conducted at the Advanced Technology for Large Structural Systems (ATLSS) Engineering Center at Lehigh University in Bethlehem, Pennsylvania, USA and the Structural Testing Laboratories at the University of Toronto in Toronto, Ontario, Canada.

Thanks are also given to the technical staff of the ATLSS Center at Lehigh University and the technical staff of the Structural Testing Laboratories at the University of Toronto. A special thanks is given to Professor Peter Birkemoe of the Department of Civil Engineering, University of Toronto for helping to arrange the use of the laboratory facilities at the University of Toronto.

The opinions expressed herein are those of the authors, and do not necessarily reflect the views of the sponsors.

Table of Contents

List of Tables

List of Figures

Nomenclature

A	=	Area
A_g	=	Gross area of section
A_{net}	=	Net area of section
c	=	Circumferential dimension of a corrosion patch, mm
COV	=	Coefficient of variation
D	=	Outside diameter, mm
D_{ave}	=	Average measured outside diameter, mm
D_{max}	=	Maximum measured outside diameter, mm
E	=	Modulus of Elasticity (Young's Modulus), MPa
e_x	=	Eccentricity in X-axis direction, mm
e_y	=	Eccentricity in Y-axis direction, mm
F_{cr}	=	Critical buckling stress, MPa
F_y	=	Yield stress, MPa
F_u	=	Tensile (ultimate) stress, MPa
h	=	Dimension of corrosion patch along length of member, mm
h_{crit}	=	Critical dimension of h, mm
I_x	=	Moment of inertia about X-axis, mm^4
I_{xy}	=	Product of inertia, mm^4
I_y	=	Moment of inertia about Y-axis, mm^4
L	=	Length, mm
LVDT	=	Linear voltage displacement transducer
M_x	=	Moment about X-axis

M_y	=	moment about Y-axis
OOR	=	Out of roundness
OOS	=	Out of straightness
P	=	Applied load, kN
P^c_{max}	=	Maximum applied compressive load, kN
P^t_{max}	=	Maximum applied tensile load, kN
P_o	=	Axial compression design load of undamaged section
P_u	=	Ultimate load capacity, kN
P_y	=	Yield load of gross section, kN
R	=	Outside radius of tubular specimen, mm
r	=	Radius of gyration, mm
s	=	Sleeve length, mm
t	=	Original, undamaged wall thickness, mm
t_r	=	Minimum reduced wall thickness of corrosion patch, mm
x	=	distance along X-axis direction, mm
y	=	distance along Y-axis direction, mm
α	=	Slenderness parameter for local buckling equations
Δ	=	Axial displacement
Δ_y	=	Axial yield displacement
θ	=	Angle subtended by corrosion patch
ε	=	Strain, mm/mm
ν	=	Poisson's ratio

σ	=	Stress, MPa
τ_b	=	Bond stress, MPa
σ_{cr}	=	Critical buckling stress, MPa
σ_{max}	=	Maximum stress in cross section, MPa
σ_r	=	Residual stress, MPa
σ_u	=	Tensile (ultimate) stress, MPa
σ_y	=	Yield stress, MPa

Abstract

A study is presented on the residual strength and repair of patch-corroded offshore steel tubular bracing members subjected to inelastic cyclic axial loading. The objectives of this study were to investigate the effects of low cycle inelastic loading on patch-corroded steel tubular members, determine whether existing strength prediction methods for monotonic loading conditions could predict cyclic strength, and to evaluate the effectiveness of using an epoxy grouted repair sleeve to restore member resistance to low cycle inelastic loading. The objectives of the study were accomplished by conducting an experimental program involving the testing of 12 specimens. The test matrix consisted of two non-damaged specimens, eight patch-corroded specimens, and two repaired specimens with patch corrosion. Steel tubulars with diameter to thickness ratios (D/t) of 27 and 40 and a slenderness ratio (L/r) of 57 were inflicted with a single patch of non-uniform corrosion damage. Mechanical removal of portions of the wall thickness over a controlled area of the surface simulated the patch-corrosion. The severity of corrosion damage was quantified by two parameters, the reduced wall thickness-to-original wall thickness (t_r/t) and the subtending angle (θ). The repairs studied included both a steel sleeve and a carbon fiber composite sleeve.

The results of the experimental program demonstrated that corrosion damage can severely limit the ductility and strength of a tubular member. The presence of patch corrosion resulted in cyclic local buckling which lead to a through thickness crack in the cross section due to low cycle fatigue. The repaired specimen test results demonstrated that a patch-corrosion damaged tubular member can be restored to its original design strength. The SSRC Column Curve Type 1, when used in conjunction with a section

analysis of the corroded section to account for the eccentricity created by the non-uniform reduction in wall thickness, provided the best prediction for patch-corroded specimen residual axial load capacity. The average error for strength prediction was 2.6%, with a maximum error of 9.2%, and a coefficient of variation of 5.8%.

1. INTRODUCTION

1.1 PROBLEM STATEMENT

Offshore structures are subjected to highly corrosive conditions. Corrosion control has evolved as a practice for offshore platforms. Designers of early fixed offshore platforms constructed in the Gulf of Mexico were more concerned with designing for hurricanes than corrosion. The earlier platforms had protective coatings installed to prevent corrosion. As the industry continued to grow, better coatings were created and cathodic protection came into use (McClelland and Reifel 1986). Even with the improvements in corrosion protection, corrosion has been found to occur in offshore platforms having protective coatings, cathode protection, or other methods of corrosion control (Dunn 1983, Cole et al. 1987). In addition, studies have shown that corrosion has a detrimental impact to bridges (Kulicki et al. 1990), particularly in the Northern United States and Canada where salting of roadways is a common practice. For tubular members under these adverse environments, corrosion leads to a reduction in the cross section resulting in an increase in the probability of inelastic buckling and a reduction of strength.

In this study, corrosion is classified into two categories, namely uniform corrosion and patch corrosion. Figure 1.1 illustrates the difference between the two classifications of corrosion. For structural steel tubing, uniform corrosion is the condition where a consistent loss of section around the entire circumference of the tube has occurred. This type of corrosion does not create any eccentricities in loading and the centroid of the section does not change. Therefore it is simple to analyze, treating it as a member with a reduced wall thickness. Patch corrosion, however, reduces only a local area over the

circumference of a section, introducing multiple complications. First, the section is reduced increasing the stress in the member (similar to uniform corrosion but in a concentrated region). Second, the centroid shifts relative to the original location, and the section properties change. The shifting of the centroid with respect to the centrally applied axial load creates a local eccentricity, e, causing an internal moment. The combination of a reduction in the section properties and the creation of an eccentricity reduces both the global and the local buckling strength. In addition, if the corrosion is pitted, it can cause stress concentrations. All of these are undesirable effects of patch corrosion that need to be considered when evaluating the structural safety of a tubular member.

1.2 OBJECTIVES

This study was concerned with patch type corrosion and its effect on tubular members under cyclic, inelastic, axial loading. The primary objectives of the study were to:

1) compare the response of patch-corroded steel tubular brace members subjected to cyclic loading with the response of patch-corroded steel tubular brace members subjected to monotonic loading,
2) compare the hysteretic behavior of patch corroded steel tubulars to the hysteretic behavior of undamaged steel tubes,
3) investigate the effects of patch corrosion on the ductility of a tubular member under cyclic inelastic axial loading,

4) analyze the ability of a epoxy-based grout repair to restore a patch corrosion-damaged tubular member to its full capacity under cyclic loading conditions,
5) investigate the performance of two different sleeve types, steel and carbon fiber composite, for the repair of patch corroded tubulars subjected to cyclic loading.

To achieve these objectives, an experimental testing program was conducted involving the cyclic testing of ten specimens and monotonic loading of two specimens.

1.3 OUTLINE OF STUDY

Chapter 2 discusses buckling of tubular members. Chapter 3 presents previous research relevant to this study. The experimental program is discussed in Chapter 4. Chapter 5 presents the experimental behavior of the test specimens. The analysis and synthesis of the test results are presented in Chapter 6. Chapter 7 summarizes the results and presents the conclusions of the experimental study. Lastly, recommendations for future work are provided in Chapter 8.

2. BACKGROUND

This chapter presents methods used to analyze the load carrying capacity of a tubular structural member subjected to an axial load. Expressions for global and local buckling are presented.

2.1 BUCKLING EQUATIONS

The stability of tubular members is based on the ratio of the length to the radius of gyration (L/r). For large values of L/r (greater than 80), a tubular member is considered *slender* and will buckle globally. For smaller values of L/r, tubular members yield and form local buckles. Design equations are available for various ranges of L/r. The L/r used in this study is 57, indicating that the tubular is more susceptible to local buckling.

2.1.1 GLOBAL BUCKLING

Based on equilibrium conditions, the differential equations for prismatic members subjected to compressive axial forces at the ends (Galambos, 1978) are:

$$EI_x v^{iv} + Pv^{ii} - Px_o \phi^{ii} = 0 \tag{2.1}$$

$$EI_y u^{iv} + Pu^{ii} + Py_o \phi^{ii} = 0 \tag{2.2}$$

$$EI_\omega \phi^{iv} + \left(P\bar{r}_o^2 - GK_T\right)\phi^{ii} + Py_o u^{ii} - Px_o v^{ii} = 0 \tag{2.3}$$

where,

P	=	applied load
v	=	deflection in the global y-direction
u	=	deflection in the global x-direction

ϕ = angle of twist
E = Young's Modulus (modulus of elasticity)
I_x = moment of inertia about x-axis
I_y = moment of inertia about y-axis
I_ω = warping moment of inertia
x_o = x-coordinate of shear center of section
y_o = y-coordinate of shear center of section
$\bar{r}_o$ = $\sqrt{x_o^2 + y_o^2 + \frac{I_x + I_y}{A}}$
K_T = St. Venant torsion constant
G = shear modulus

For doubly symmetric, prismatic members, for which x_o and y_o are equal to zero, the solution to these equations leads to the elastic critical buckling loads where,

$$P_x = \frac{\pi^2 E I_x}{L^2} \tag{2.4}$$

$$P_y = \frac{\pi^2 E I_y}{L^2} \tag{2.5}$$

$$P_\phi = \left[\frac{\pi^2 E I_\omega}{L^2} + G K_T \right] \left[\frac{1}{\bar{r}_0^2} \right] \tag{2.6}$$

The difficulty in applying these equations to patch corroded members lies in that they require the member to have the same cross section throughout the length of the member (i.e., they are applicable only to prismatic members). The specimens tested in this study have a local section reduction, which under high stresses will yield and locally buckle. Therefore, these equations are not valid for patch-corroded members.

2.1.2 LOCAL BUCKLING EQUATIONS

Numerous closed-form expressions have been developed and appear in design codes for predicting the local buckling load of tubular sections. These expressions are used for tubular members with small L/r ratios. A typical parameter in these equations is the diameter to thickness ratio (D/t). Below are local buckling equations from two codes typically used in the offshore industry (McClelland and Reifel 1986):

1) API, (American Petroleum Institute, RP-2A 1989)

$$\frac{\sigma_{cr}}{\sigma_y} = 1.0, \qquad \text{for} \qquad \frac{D}{t} \le 60 \tag{2.7}$$

$$\frac{\sigma_{cr}}{\sigma_y} = 1.64 - 0.23 \cdot \left(\frac{D}{t}\right)^{0.25}, \quad \text{for} \qquad \frac{D}{t} > 60 \tag{2.8}$$

2) DnV, (Det Norske Veritas 1974)

$$\frac{\sigma_{cr}}{\sigma_y} = 1 - \frac{1}{3} \cdot \left[\frac{1.5 + 0.001\left(\frac{D}{t}\right)}{\alpha}\right]^2 \tag{2.9}$$

where,

$$\alpha = \frac{E/\sigma_y}{D/t}$$

For both the API and DnV equations, σ_{cr} is the critical local buckling stress and σ_y is the yield stress. E that appears in the expression for α is Young's Modulus. Both of these equations are intended for use with tubular members of constant cross section, and therefore the application to patch-corroded tubulars is invalid.

2.2 COLUMN CURVES

The Structural Stability Research Council (SSRC) provides column curves for the design of steel columns. These curves are based on an extensive database of test data. These curves take into account the many variables that can account for differences in column strength, such as cross sectional shape, material properties, residual stress patterns, initial out of straightness (OOS), and end restraints. The specimens used in this study (before corrosion damage) are stress relieved, bisymmetric shapes, where SSRC Column Curve Type 1 is applicable (Figure 2.1). The axial capacity to yield load ratio (P_u/P_y) for a column is based on the parameter λ:

$$P_u/P_y = 0.99 + 0.122\lambda - 0.367\lambda^2 \tag{2.10}$$

where,

$$\lambda = \frac{1}{\pi}\frac{L}{r}\sqrt{\frac{\sigma_y}{E}} \tag{2.11}$$

and,

σ_y	=	yield stress of the column
E	=	Young's Modulus (modulus of elasticity)
L	=	length of the column
r	=	radius of gyration of the column

For an undamaged tubular with a D/t of 40 and t = 3.2 mm, the radius of gyration is 44 mm. Thus, with L = 2464 mm, σ_y = 207 MPa and E = 200 GPa, λ = 0.576. From Equation (2.10), using Column Curve Type 1, P_u/P_y = 0.938. For an undamaged tubular with a D/t of 27 and t = 4.8 mm, the radius of gyration is 43 mm. Thus with L = 2464

mm, σ_y = 262 MPa and E = 200 GPa, λ = 0.658. Again, from Equation (2.10), P_u/P_y = 0.912.

SSRC Column Curve Type 1 is not applicable for patch corroded tubulars, since these members are non-prismatic and sensitive to local buckling. The accuracy of the expressions in this chapter for use with patch corroded tubulars will be presented in Chapter 6.

3. PREVIOUS CORRSION RESEARCH

This chapter presents previous research relevant to this study including strength predictions for patch corroded tubular bracing members, cyclic behavior of axially loaded tubular members, and repair methods for damaged tubular bracing members.

3.1 GENERAL

Numerous previous studies have been conducted to evaluate the effects of patch corrosion upon the strength of tubular structural steel (Hebor and Ricles 1994, Ostapenko et al. 1993 and 1996, Ricles et al. 1995, "Testing" 1990). The results of the previous research concluded that a tubular with patch-corrosion can suffer a loss of strength compared to a non-corroded member. Ostapenko et al. (1993, 1996) investigated the residual strength of salvaged tubes from offshore platforms with both dents and corrosion subjected to monotonic axial loading. The D/t for the tubular specimens included 33 and 28. The work of Hebor and Ricles (1994) emphasized inelastic local buckling of short tubulars with a single patch of corrosion subjected to monotonic axial loading. The research involved both experimental and non-linear finite element parametric studies. The D/t of the test specimens ranged from 34 to 64. The work performed by these researchers resulted in a recommended set of residual strength equations, which are presented in Section 3.2. These equations will be used to predict the approximate ultimate strength of the tubes to be used in the current study. In addition to the empirical equations, recommend design parameters for a steel sleeve with a cement-based or epoxy-based grout to repair the corroded area was conceptualized by Hebor and Ricles (1994).

The previous studies focused on the loss of strength from corrosion under monotonic loading and restoring the tubes to their original undamaged strength with this repair. All of the proposed repairs performed well under monotonic loading. The realization must be made that offshore platforms incur loads that are not strictly monotonic. Low cycle loading with high stress ranges and fatigue loading are also present as a result of wave loading, earthquake loading, and other time-varying loads. This creates additional complications dealing with the loss of section from corrosion. A primary objective of the current study is to investigate the effects of low cycle inelastic axial loading on the behavior of a patch corroded section and determine how the loss of ductility and energy dissipation capacity are affected by the extent of corrosion.

The results from the work of Hebor and Ricles (1994) using epoxy-based grout demonstrated the most promise for possible repair of corroded tubulars subjected to cyclic loading conditions. As was shown by Hebor and Ricles (1994), the epoxy provided an exceptional bond for force transfer from the damaged tubular to the repair sleeve. However, the critical detail of the corrosion will not be subjected to high stress concentrations during loading that can lead to cracking and or local buckling.

3.2 STRENGTH PREDICTIONS

Previous research performed on damaged offshore steel tubes produced empirical equations to predict residual strength. A review of these equations is given below.

3.2.1 STENGTH PREDICTIONS - OSTAPENKO et al. (1993, 1996)

Based on the testing of actual salvaged corroded offshore tubes (Figure 3.1),

Ostapenko et al. (1993, 1996) developed a simplified cubic equation for the residual strength, P_u, of a patch corroded tubular based on the minimum section of the corroded tube:

$$p = P_u / P_y = 0.18a_n + 0.82a_n^3, \qquad \text{for } a_n > 0.65 \tag{3.1}$$

where

P_y	=	yield load of gross section
a_n	=	A_n / A_g
A_n	=	net area of the reduced corroded section
A_g	=	gross area of the tube as defined by $\pi (2R_i + t_{max})t_{max}$
R_i	=	inside radius
t_{max}	=	maximum wall thickness in the corroded section

t_{max} of the corroded tube may no longer be the original thickness. The gross area of the corroded tubular, A_g, as defined above, may be less than original gross area, as is the case for uniform corrosion.

3.2.2 STRENGTH PREDICTIONS - HEBOR AND RICLES (1994)

Hebor and Ricles (1994) tested multiple short patch-corroded tubulars under axial load with the variation of three parameters: the diameter to thickness ratio (D/t); the ratio of reduced wall thickness to the original thickness (t_r / t); and the angle (θ) of the extent of the corrosion around the circumference. These parameters are shown in Figure 3.2. In addition, finite element analysis was used to broaden their testing matrix and define trends for tubulars with patch corrosion.

An equation was derived by Hebor and Ricles for the inelastic buckling strength of fixed end patch-corroded tubulars within a limited range of applicability as stated

below. The equation was derived by a regression analysis of the test data and finite element results using the three parameters mentioned above, where:

$$p = P_u / P_y = 1.0 - 0.001(D/t) + 0.052(t_r / t) - 0.0026\,(\theta) + 0.0028\,(t_r / t)(\theta) \le 1.0 \tag{3.2}$$

the limitations of the equation are as follows:

$$34 < D/t < 100; \qquad 0 < t_r/t < 1.0; \qquad 0^o < \theta < 360^o$$

These parameter limits are suggested as a result of the range of the parameters in the database of their study.

3.2.3 OSTAPENKO et al. (1996)

Ostapenko et al. (1996) provided another recommendation using an estimation based on an equivalent thickness of a patch-corroded tubular cross section. He recommended the use of the local buckling equations as provided by the codes (Equations (2.7) through (2.9)) with an equivalent thickness, t_a, defined as:

$$t_a = \frac{t_{a,circ} t_{a,long}}{t_{min}} \tag{3.3}$$

where,

$t_{a,circ}$ = Average thickness of 0.8R x 0.2R (or R x R/4) corrosion patch in circumferential direction, where R is the radius of the tubular

$t_{a,long}$ = Average thickness of 0.8R x 0.2R (or R x R/4) corrosion patch in longitudinal direction, where R is the radius of the tubular

t_{min} = minimum thickness of R x R/4 corrosion patch

A graphical explanation of equivalent thickness is shown in Figure 3.3. This method produced reasonable results with an average error of 8%, a minimum error of 1% and

maximum error of 16% for predicted load capacity P_u compared to experimental results. This method is preferable in that it requires little calculation outside of the using the code equations for local buckling.

3.2.4 SECTION ANALYSIS OF PATCH CORROSION - HEBOR AND RICLES (1994)

Hebor and Ricles (1994) made an additional recommendation for predicting the residual strength of a patch corroded tubular. The method showed good agreement with their experimental results, having an average error of 3% and maximum error of 15%.

Based on test observations, the method assumes that the capacity of a patch corroded tubular is based on the first yield of the section within the corrosion patch. The method involves determining the stress in the cross section considering the applied axial load, the eccentricity in the cross section caused by the corrosion patch, and elastic theory presented by Galambos (1978). The circumference of the cross section with the corrosion patch is discritized into multiple segments. Hebor and Ricles suggest using 100 equally spaced segments. Depending on the cross section, however, any discretization is satisfactory as long as it adequately captures the profile of the corroded section (Figure 3.4). Next, the geometric center of the section is found by taking the first moment of each segment about a point of reference. The difference between the geometric center of the corroded cross section and the original non-corroded cross section establishes the eccentricity of the applied axial load, P (which is applied at the non-corroded geometric center). The moments of inertia I_x and I_y about the major and minor axes, respectively,

are found by taking the sum of the second moments about the X and Y axes, respectively, with respect to the geometric center of the corroded section. Knowing these cross sectional properties, the stress at a location with coordinates x and y can then be found as follows:

$$\sigma = \frac{P}{A_d} + \left(\frac{M_x I_{xy} - M_y I_x}{I_{xy}^2 - I_x I_y} \right) x + \left(\frac{M_y I_{xy} - M_x I_y}{I_{xy}^2 - I_x I_y} \right) y \tag{3.4}$$

where,

$$I_y = \sum A_{d,i} x_i^2 \tag{3.5}$$

$$I_x = \sum A_{d,i} y_i^2 \tag{3.6}$$

$$I_{xy} = \sum A_{d_i} x_i y_i \tag{3.7}$$

$$M_x = P e_y \tag{3.8}$$

$$M_y = P e_x \tag{3.9}$$

This is the equation as presented by Galambos (1978). In this equation, the x and y coordinates are opposite of those shown in Figure 3.4 and P is positive in compression. The subscript i indicates the individual segment ranging from 1 to N total number of segments. I_y is the moment of inertia about the Y-axis, I_x is the moment of inertia about the X-axis, I_{xy} is the product of inertia, M_x is the applied moment about the X-axis, M_y is the applied moment about the Y-axis, P is the applied compression load, e_x and e_y are the eccentricities in the X-axis and Y-axis, respectively, $A_{d,i}$ is the area of one segment, and x_i and y_i are the distances of segment i to the geometric center in the X-axis and Y-axis direction, respectively. The maximum stress (σ_{max}) will be found at the center of the corrosion patch. The critical limit state value for stress is the lesser of the yield stress (σ_y) or the critical buckling stress (σ_{cr}). As noted before, it has been experimentally

found (Ostapenko et al. 1993, 1996, Hebor and Ricles 1994) that the limiting stress in tubes with patch corrosion is the yielding stress. The predicted residual strength was therefore determined by equating Equation (3.4) to the yield stress, using Equation (3.8) and (3.9) to substitute for M_x and M_y in order to determine P. The value P represents the residual axial load capacity (P_u) of the patch-corroded member.

The load predictions from this method divided by the experimental loads of Hebor and Ricles (1994) had a mean value of 0.972 with a coefficient of variation of 0.048.

3.3 PREVIOUS RESEARCH ON LOW CYCLE BUCKLING

3.3.1 LIU AND GOEL (1988)

The thrust of the work performed by Liu and Goel was to investigate local buckling and fracture in slender, cold-formed, rectangular concrete filled steel tubes (CFT) under cyclic inelastic axial loading. Unlike the current study, where the anomaly causing local buckling in the member is the corrosion patch, Liu and Goel claimed that severe local buckling in their experimental study was the result of the formation of plastic hinges. At which load step the local buckles formed depended upon the width-to-thickness ratio and slenderness ratio of the tubes.

The study of Liu and Goel evaluated the effectiveness of using various strengths of concrete over a range of slenderness ratios and width to thickness ratios to inhibit local buckling. The concrete proved to be very effective in limiting the severity of local buckling, regardless of its compressive strength. This was attributed to limiting severe localized strain concentrations from forming in the steel tube, a result of restraining the

formation of local buckling. With local buckling constrained, the tubes fractured at higher cycles, and were able to endure more cycles. Therefore, they accumulated more plastic strain than their hollow counterparts. As a result, the study was able to demonstrate that controlling and limiting the local buckling phenomenon greatly improved the ductility and energy dissipating abilities of a tubular.

3.3.2 PONS (1997)

The work of Pons examined the use of a bolted connection for structural tube bracing members, concentrating on the connection detail as a source of energy dissipation under low cycle fatigue loading. The thrust of the study was to provide an alternative to welded brace connections in high seismic regions.

One of the important conclusions from their testing is that the formation of a local buckle in the plastic hinge zone tended to dominate the energy dissipation characteristics of the specimen, regardless of the end conditions. Similar to the work performed by Liu and Goel (1988), the onset of fracture occurred in the corners of the tubes created by the high stress concentrations.

3.4 PREVIOUS RESEARCH ON THE REPAIR OF DAMAGED OFFSHORE TUBULAR MEMBERS

3.4.1 REPAIR OF DENTED TUBULARS - RICLES et al. (1992, 1997)

Gillum and Ricles (1992) and Ricles et al. (1997) devised a method for repairing dented offshore tubular bracing members. Multiple specimens were tested with varying

levels of dent damage. The effect on the load carrying capacity of the dent was evaluated. Two repair methods were investigated. One repair option was an internal grout. The other involved the use of a grouted external sleeve. The sleeve was designed based on two criteria. First, it must be able to resist the full undamaged capacity of the tube to which it was being applied. Second, the sleeve needed to be long enough to develop the necessary force transfer from the damaged tube, through the grout, to the sleeve. The sleeve length, L_s, was determined based on a simple equation, assuming a uniform bond stress between the tube and the grout:

$$L_s = \frac{2P_o}{\pi D_i \sigma_b} \geq L_{\min} \tag{3.10}$$

Where,

P_o	=	undamaged axial capacity of the damaged tube
D_i	=	diameter of the damaged tube
σ_b	=	bond stress of the grout to the tube
L_{min}	=	length necessary to extend over all of dent-damaged tubular with ovality greater than tolerance of API RP-2A

The study found that a dramatic increase in the load carrying capacity of the damaged member occurred when repaired with a grouted sleeve. The study demonstrated that for tubes with minimal dent damage, an internal grout was satisfactory. However, for any substantial damage, the internal grout failed to restore sufficient strength. The sleeve repair was found to be highly successful for all levels of damage, restoring the damaged tube to equal or greater strength than that of the undamaged tubes.

The success of the repair was attributed to the prevention of further dent growth and ovalization of the section in addition to relieving the damaged tube of axial load. A

sleeve as a repair was adapted by Hebor and Ricles (1994) for restoring the capacity of a patch-corrosion damaged tubular and is presented in Section 4.5.2.

3.4.2 REPAIR OF SINGLE PATCH CORRODED TUBULARS – HEBOR AND RICLES (1994)

Hebor and Ricles investigated the use of grouted steel sleeves to repair single patch corroded tubular members in conjunction with their work with patch-corrosion damaged short tubular members subjected to monotonic axial loading. The exact specifications of this design are described in detail in Section 4.5.2. The effectiveness of the design is shown in Figure 3.5. The figure compares the load-displacement history of the original undamaged specimen, with that of a corresponding corroded non-repaired specimen and a repaired damaged specimen. For both the damaged non-repaired and the damaged repaired specimens, the parameters of the patch corrosion were $D/t = 40$, $t_r/t = 0$, and $\Theta = 95^o$. It is clearly evident in Figure 3.5 that the repair restores the damaged specimen to its full, original undamaged capacity.

3.5 EFFECT OF THICKNESS PROFILE ON CORROSION PATCH – RICLES et al. (1995)

Various thickness profiles of patch corrosion are shown in Figure 3.6. Figure 3.7 consists of different plots examining the effect of corrosion parameters and the corrosion profile of the corrosion patch. Two models, one with a "step" profile and the other with a "cosine" profile, were compared by Ricles et al. (1995) to the profile used in experimental

tests. The discrepancy between the models increased as the width of the patch (θ) and the ratio of reduced thickness to original thickness (t_r/t) increased. The experimental data, where the maximum θ was 120º, was within 7% of the results for the two models, which provided as upper and lower bound for strength prediction. For the smaller patch widths ($q < 120º$), the profile of the corrosion patch was concluded to be an insignificant parameter. θ and t_r/t controlled the response of the damaged tubular.

Research on local and global buckling of steel plates by Dinno (1996) has also indicated that the exact shape of the patch is not critical.

4 EXPERIMENTAL PROGRAM

This chapter describes the current experimental program. The chapter begins by discussing the important parameters of patch-corrosion. Next, it identifies the test matrix and the nomenclature of the specimens. A presentation of the material properties then follows. Also presented is the design concept for the repair of patch corroded tubulars. Lastly, the overall test setup and the instrumentation layout are described.

4.1 CORROSION PARAMETERS

The critical parameters of patch corrosion are the diameter to thickness ratio (D/t), the height of the patch (h), the length along the circumference (c), and the reduced wall thickness (t_r) (Hebor and Ricles 1994, Ostapenko et al. 1996). These parameters are shown in Figure 3.2. Over the range of D/t considered in this experimental program and those used in former studies, the D/t parameter has been shown to be negligible with respect to the other parameters. Also, the height of the patch is not critical as long as it is larger than a critical height (h_{crit}) as shown by results of finite element analysis done by Hebor and Ricles (1994) and experimental and finite element work done by Ostapenko et al. (1996). For this experimental study, it was conservatively assumed that the critical height is equal to one radius, as was done by Hebor and Ricles.

The length of the patch along the circumference will be nondimensionalized by dividing it by the radius (r), providing the angle theta, $\theta = (c/r)$. The reduced thickness, t_r, will be nondimensionalized by dividing it by the original thickness (t_r/t).

4.1.1 SIMULATED CORROSION

The tubes were not salvaged nor were they left in a corrosion tank. Simulated patch corrosion was inflicted upon the test specimens by mechanical removal of material. As previous research has shown, the maximum reduced section of the corroded tube will govern behavior (Ricles et al. 1995, Ostapenko et al. 1996). For tests involving simulated corrosion, Hebor and Ricles used a "Cosine Profile" model to simulate corrosion damage (Figure 4.1). Ostapenko et al. used a similar patch layout with a slightly different profile (Figure 4.2). As mentioned in Section 3.6, finite element work performed by Ricles et al. (1995) indicated that the exact shape was not critical. The dominant parameters were the extent of the corrosion (θ)and the reduced thickness (t_r). For comparative purposes, the "Cosine Profile" model presented by Hebor and Ricles (1994) will be used in this study.

4.1.2 MEASURED CORROSION

Corrosion will not have the same dimensions and characteristics as the idealized patch being used in this study. The salvaged tubes analyzed by Ostapenko et al. (1996) have shown actual corrosion to be highly variable. This creates a discrepancy when inspecting and evaluating existing structures. Fortunately, Ostapenko et al. (1996) was able to show that the critical section will dominate the behavior and capacity of the tube. Therefore the use of a single patch to represent a tube damaged by corrosion over the entire area is acceptable. Ostapenko is currently evaluating the effects of multi-patch corrosion, but the information is not yet available to the general public.

Corrosion damage in the field can be evaluated by ultrasonic measurement techniques. Both Hebor and Ricles (1994) as well as Ostapenko et al. (1996) achieved

good results using this method. Hebor and Ricles made their recommendation based on trying various methods and concluded that ultrasonic measurement was both the easiest and most accurate. The tubes in this experiment will be measured by a different technique based on equipment availability and lab limitations. A schematic of the patch corrosion measurement setup is shown in Figure 4.3. Two 76 mm diameter round steel tubes were attached to a W12x87 column by threaded rods. The rods were post tensioned to increase the stiffness of the tubes. The corroded specimen was then fed over the lower tube and positioned on two pinpoints. From the upper tube, a dial gage read the thickness. The dial gage was calibrated with a tube of known thickness.

4.2 TEST MATRIX

The test matrix is provided in Table 4.1 where all dimensions listed are nominal dimensions. The first column lists the specimen names. The second column lists the diameter-to-thickness ratio, D/t. The third column lists the reduced thickness to original thickness ratio, t_r/t. The fourth column lists the nominal thickness, t. The fifth column lists the subtending angle, θ. Lastly, a brief description of each specimen is provided in the sixth column. The first two rows list the monotonically loaded specimen, which are designated by the letter "M" at the beginning of their name. The next eight rows list the cyclically loaded specimens, which are designated by the letter "C" at the beginning of their name. The last two rows list the cyclically loaded specimens that have been repaired. The "C" at the beginning of their name indicates that the repaired specimens were tested cyclically. The last two letters "RS" and "RC" indicate that the specimens

were repaired with a steel sleeve and a carbon fiber composite sleeve, respectively.

The names of the specimens reflect the specimens' parameters. For example, two diameter-to-thickness ratios were used, 27 and 40. The first number in the specimen name indicates the D/t of the specimen, either 27 or 40. The second number in the specimen's name corresponds to its t_r/t ratio as a percentage. If the t_r/t of a specimen is 0.33, the second number in its name is 33. Similarly, the third number in a specimen's name indicates the subtending angle, θ. 95 corresponds a to 95º subtending angle.

All specimens were ordered as ASTM A513 Type 5 Grade 1026 ERW Structural Steel Tube with an outside diameter of 127 mm. The original wall thicknesses were measured in five different locations. The 3 mm thick specimens had a measured thickness of 3.200 mm before and after annealing. The 5 mm thick specimens have a measured thickness of 4.851 mm before and after annealing. The radius of gyration (r) for all of the test specimens was approximately 43 mm. The pin-to-pin length (L) of each specimen was 2464 mm, which corresponded to an effective slenderness ratio (L/r) of 57.

The measured parameters for this study are given in Table 4.2. Corrosion profiles are shown in Figures 4.4 through 4.13. The parameter (D/t) will still be evaluated in this study even though its effects were found to be insignificant for monotonic loading. The effects of this parameter on inelastic cyclic loading remain uncertain and will be discussed in Chapter 6. Two specimens were tested monotonically to identify if the cyclic load history is bounded by the monotonic response.

The overall goal of the testing matrix was to use typical dimensions for bracing

members, providing the greatest amount of comparison utilizing a cost-effective approach to the testing. The values for the parameters used in this study (L/r, D/t, t_r/t, θ) were chosen based on multiple reasons. First, typical D/t ratios for bracing members found in fixed offshore platforms generally range from 19 to 90 (McClelland 1986). Generally, the lower end of the D/t ratio is used to avoid problems with local buckling with D/t of 48 being described as "well behaved" (Puskar 1999). Second, an accepted practice in industry is to limit the slenderness ratio from 70 to 90 (McClelland, 1986). Considering the connection fixity, the effective slenderness ratio typically found in offshore structures is thus 55 to about 65. The slenderness ratio in this study was 57. Third, the test results can be compared with previous tests (Hebor and Ricles 1994, Ostapekno et al. 1996) that had a similar range of parameters. Fourth, the inflicted damage represents a wide range of corrosion damage while at the same time limiting the cost and the required number of tests to make appropriate comparisons.

The repaired specimens were chosen based on the anticipation that the repair would work for all cases if it worked when applied to the worst case of damage, namely the specimen with through-thickness corrosion. Specimens C40-00-95-RC and C40-00-96-RS are two damaged specimens with the same patch corrosion-damage parameters as Specimen C40-00-95. Specimen C40-00-95-RC was repaired with an epoxy grouted carbon fiber composite sleeve and Specimen C40-00-95-RS with an epoxy grouted steel sleeve. A repair sleeve was placed over the damaged tubular by sliding it from the end of the test specimen. In situ repair would require that the sleeve be split into two half shells that could thereby be placed around the circumference of the corroded tubular and be

clamped together. In the current test program the repair sleeve was not split since the technology to clamp sleeves is already established and beyond the scope of this study.

Out-of-straightness (OOS) and out-of-roundness (OOR) were measured for each specimen before testing where,

$$OOS = \delta_{max,N\text{-}S} / L \tag{4.1}$$

$$OOR = (D_{max} - D_{min}) / D_{avg} \tag{4.2}$$

and,

$\delta_{max,N\text{-}S}$	=	maximum variance from centerline
L	=	length of the specimen
D_{max}	=	maximum measured diameter for a specimen
D_{min}	=	minimum measured diameter for a specimen
D_{avg}	=	average of measured diameters for a specimen

The maximum OOR and OSS values for each specimen are listed in Table 4.3. All specimens were within 0.00258 OOS and 0.00472 OOR. Both of these values are within allowed tolerances per API RP-2A (1989).

4.3 MATERIAL PROPERTIES

4.3.1 STEEL TEST SPECIMENS

All of the specimens were fabricated from the same heat number of the mill for each different thickness to insure the consistency of the material properties. Mill specifications indicated a yield strength of 613.7 MPa and a tensile strength of 689.5 MPa

for the specimens with a 4.8 mm wall thickness (D/t of 27). The yield strength was indicated as 558.5 MPa and the tensile strength was 600.0 MPa for the specimens with a 3.2 mm wall thickness (D/t of 40). Both steels had an elongation of less than 17% at fracture.

The specimen were found, through tensile coupon tests, to lack a well defined yield plateau and had low yield to tensile strength ratios. (This study was limited to these tube dimensions based on the capacity of available testing facilities. The material properties are typical of tube ordered at the required sizes.) The properties are attributed to the cold-work required to form the specification of steel used in the current study and the formation of small grain sizes produced by quickly cooling of the steel.

The properties of the steel are not representative of older existing offshore structures that were constructed with much lower yield strengths, well defined yield plateaus, and other properties typical of ASTM A36 grade material. Unfortunately, material of matching qualities is not available from steel suppliers. The specimens were therefore annealed to eliminate the strain hardening introduced by the millwork and to increase the grain size of the steel. Annealing the specimens created a better representation of existing steel tubes in offshore structures. The annealing was performed by heating the tubes to 871º C (1600º F) and then furnace cooling by 10º C (50º F) per hour down to a temperature of 704º C (1300º F) and then allowed to air cool.

To verify that the desired effect of annealing had been achieved, two sets of coupons were tested to determine the material properties before and after the heat treatment. One set of coupons was tested for each diameter to thickness ratio. Each set

consisting of one untreated and one annealed coupon. The coupons were removed from at least 64mm from the end of the tubes and 90º from the weld lines to minimize any possible edge effects and stress concentrations (Figure 4.14). Special consideration was also taken to ensure that the coupons did not have any flaws (i.e. dents or gouges) from transport.

The coupons were fabricated according to specification ASTM A370 and tested according to specification ASTM E8. ASTM A370 allows for curved coupon to be tested simply by placing the curved specimen in a testing machine and allowing the grips of the machine to flatten the coupon ends. For fear of damaging the hydraulic grips and to avoid any possible damaging of the coupon, the coupons were groove welded to steel blocks (Figure 4.15). While welding, temperature sensing devices were used to monitor the coupons and to ensure that the temperature of the coupon did not raise above 316º C (600º F) 38mm or more in from the ends of the coupons.

Results of the individual coupon tests are presented in Figures 4.16 through 4.19. Whereas the pre-annealed coupon for the D/t of 27 had a yield stress (σ_y) of 531 MPa and a tensile stress (σ_u) of 600 MPa with an elongation of 12% (Figure 4.16), the post-annealed coupon had σ_y = 253 MPa and σ_u = 403 MPa with an elongation of 44% (Figure 4.18). The pre-annealed coupon for the D/t of 40 had σ_y = 641 MPa and σ_u = 702 MPa with an elongation of 14% (Figure 4.17), the post-annealed coupon had σ_y = 206 MPa and σ_u = 338 MPa with an elongation of 47% (Figure 4.19). A summary of the mechanical properties for the annealed specimens is provided in Table 4.4. In Table 4.4, E is Young's Modulus, σ_y is the yield stress, σ_u is the peak stress, E_{sh} is the modulus at

the onset of strain hardening, ε_{sh} is the strain at the onset of strain hardening, ε_u is the strain at the peak stress, and ε_{max} is the strain at fracture.

Figures 4.20 (a) and 4.20 (b) are comparative plots between the pre-annealed and post-annealed material for D/t = 27, and 40, respectively. As expected, the post-annealed coupon is a better representation of ASTM A36 material.

4.3.2 EPOXY GROUT

The epoxy grout used in the current study, DP Epoxy Grout, was manufactured by Five Star® Products, Incorporated. This grout has many advantages. Some of the more important include: adjustable flow; chemically resistant and can be used in highly corrosive underwater environments; excellent adhesion to steel; has a relatively high modulus and strength. In addition, the grout reaches over 60% of its strength in one day and its full strength in seven days.

The grout consisted of a resin, hardener, and aggregate. The three components were mixed in a mechanical mixer withholding one bag of aggregate to increase the flow. The change was recommended since the annulus between the damaged specimen and the repair sleeve was 19 mm. According to the manufacturer, under high flow conditions, the epoxy grout has a creep of 2.2×10^{-3} mm/mm (ASTM C 1181, 1 year, 60^{o} C), a tensile strength of 13.8 MPa (ASTM C 307), and a seven-day compressive strength of 96.6 MPa (ASTM C 579 B).

The bond strength was of particular importance for the experimental program. Two bond tests were performed to determine the cohesion strength of the grout to steel.

Each bond test specimen was fabricated from a short segment of sleeve and a steel tubular (Figure 4.21), using the same materials as were used for a repaired test specimen. One of the bond test specimens had an outer steel sleeve, while the other had an outer carbon fiber composite sleeve. The tubular and sleeve were concentrically set in a jig and the annulus was filled with the epoxy grout (Figure 4.22). The epoxy grout was then allowed to cure for seven days.

The rate of loading for the two tests was 0.254 mm/min. Four linear pots were placed around the specimen to measure the differential axial displacement (i.e., slip) between the tubular and sleeve (Figure 4.23). The bond test specimens were loaded by applying an axial force on the edges of the tubular and the sleeve. A copper shim plate was placed in between the specimen ends and the load cell of the testing machine to insure an even distribution of load. Axial load was recorded by the internal load cell of the testing machine. The average stress was calculated by dividing the applied axial load, P, by the smaller contact surface area:

$$\tau_{avg} = P / (\pi D s_{bond}) \tag{4.3}$$

where,

τ_{avg}	=	average bond stress
P	=	applied axial load
D	=	outside diameter of steel tubular
s_{bond}	=	length of bond between tubular and sleeve

The average bond stress is plotted against the average of the four linear pots for both bond test specimens in Figure 4.24. The relationship between axial displacement and bond strength is initially linear. For the bond test using the composite sleeve, the

failure of the bond is abrupt but a residual bond stress of roughly 3 MPa is achieved through friction. Cohesion failure occurred between the steel tubular and the epoxy grout. The bond test using the steel sleeve did not fail in the same manner. The load reached a peak as the tubular yielded outside of the bond region. The load held as yielding developed. After continuing to load the specimen, the cohesion failed between the steel tubular and the epoxy grout. A value of τ_b = 12 MPa was used as the bond strength of the epoxy grout to steel.

4.3.3 STEEL REPAIR SLEEVE

Like the test specimens, the steel repair sleeve was ordered with designation ASTM 513 Type 5 Grade 1026 Structural Steel Tube. Mill specifications indicated a yield strength of 607 MPa and a tensile strength of 669 MPa with an elongation of 15%. Coupon testing of the material produced the same results. The steel sleeve stress-strain properties are included in Table 4.4, and a stress-strain curve from a coupon test is shown in Figure 4.25. A photograph of the steel sleeve during installation is shown in Figure 4.26.

4.3.4 COMPOSITE REPAIR SLEEVE

The composite sleeve was provided by Hardcore Composites. The sleeve is 305mm in length with an inside diameter of 178mm and a thickness of approximately 7mm. A photograph of the composite sleeve during installation is shown in Figure 4.27. Due to the small scale of the sleeve, Hardcore Composites was unable to fabricate it using

their regular equipment. For full scale repair sleeves, a much more refined and reliable method of fabrication is used. For this experiment, an innovative procedure was created to form the smaller sleeves. A PVC pipe was cut to the length necessary to form two sleeves. The individual layers of material were then placed around the PVC. The layers consisted of an internal peel ply that provided a rough surface to which the grout adhered, two sheets of carbon fiber, one sheet of TH 3400 (a glass fabric), two additional sheets of carbon fiber, an additional sheet of TH 3400, and a final outer layer of carbon fiber. Next, an epoxy resin was then infused into the material layers and allowed to cure at room temperature for 24 hours. Additionally, the sleeve was cured for four hours at 121^{o}C. Finally, the PVC pipe was removed, the sleeve cut into two 305 mm long sleeves, and the ends were sanded to remove sharp edges.

Due to high costs, no material properties were tested. The various strengths and the modulus were provided based on the material test database of Hardcore Composite. The tension strength was estimated as 160 MPa, the compressive strength as 366 MPa, and the modulus, E, as 67 GPa.

4.4 REPAIR METHODOLOGY AND DESIGN CONCEPT

The concept of the sleeve repair prototype design is to reduce the local stresses that induce local buckling at the location of the patch corrosion. A schematic of this concept is shown in Figure 4.28. The primary mechanism is the reduction of the local stresses by shear transfer through the grout to the sleeve. A secondary mechanism is the confinement of the cross section preventing the buckle to form.

Bond stress is a critical consideration for the transfer of forces from the tube to the sleeve. If the bond is inadequate, the grout will fail at the contact surface before a substantial load can be transferred to the sleeve.

In addition, confinement of the cross section can be an important factor. Experimental tests performed by Hebor and Ricles (1994) demonstrated that non-repaired, corroded specimens have a tendency to buckle outwards if the circumferential width of the patch divided by the height (c/h) is greater than one, and inward if (c/h) is approximately one. If inadequate confinement is provided, an outward buckle can form and hoop stresses on the sleeve may become very large. Furthermore, if an inward buckle were to form, both confinement and tensile capacity in the grout bond are necessary.

The desired overall result is for the repair sleeve to return the damaged specimen to its original undamaged capacity.

4.5 REPAIR DESIGN

Two important considerations must be made in the design of the repair sleeve. First, the sleeve must be able to withstand the load placed upon it through shear transfer. Second, sufficient bond surface must be provided to which the grout can adhere. Figure 4.29 shows a typical repaired specimen. It should be noted that this is a prototype design. As noted previously, actual installation in the field will require the sleeve to be split.

4.5.1 SLEEVE SECTION ANALYSIS

The design of the sleeve is based on the assumption that the sleeve will not slip.

Thereby, the strain in the sleeve (ε_{sleeve}) and the steel tube (ε_{tube}) are equal:

$$\varepsilon_{sleeve} = \varepsilon_{tube} \tag{4.4}$$

Using Equation (4.1), equilibrium, and elastic theory where,

$$\sigma = \varepsilon E \tag{4.5}$$

$$\sigma = P / A \tag{4.6}$$

an expression for the axial load developed in the sleeve, P_{sleeve}, can be derived where,

$$P_{sleeve} = P_o \bullet \left[\frac{1}{1 + \frac{(AE)_{sleeve}}{(AE)_{tube}}} \right] \tag{4.7}$$

in which,

P_{sleeve}	=	axial load developed in the sleeve,
P_o	=	original undamaged strength of the steel tube,
$(AE)_{tube}$	=	axial section stiffness of corroded tubular,
$(AE)_{sleeve}$	=	axial section stiffness of repair sleeve.

This equation compensates for changes in area between the corroded specimen and the repair sleeve and changes in the modulus of elasticity. The original undamaged design strength, P_o, and $(AE)_{tube}$ are known values. The axial load developed in the sleeve, P_{sleeve}, is therefore established for a selected sleeve section stiffness, $(AE)_{sleeve}$. The axial strength of the sleeve must exceed the load P_{sleeve} in order for the repaired tubular to have the same capacity as the undamaged tubular. Also, the sum of the strength of the sleeve and the residual strength of the corroded tubular must be equal to, or greater than, the original strength of the undamaged tubular. Equation (4.7) is represented graphically in

Figure 4.30. The required length of the repair sleeve is discussed below.

4.5.1.1 COMPOSITE SLEEVE

The effectiveness of a composite carbon fiber sleeve as a repair was evaluated since there are numerous advantages to using a composite sleeve, including:

1) Reduced weight, resulting in easier handling during installation,
2) Increased durability in marine environments (steel sleeve corrodes over time),
3) Easier to custom fit than a steel sleeve.

The area of the sleeve is dictated by the diameter of the damaged tubular and the annulus that is required by the grout placement between the sleeve and the corroded tubular. The design of the composite sleeve using Equation (4.7) is discussed below. As noted earlier, the repair was applied to the specimen with the worst case of damage, through thickness corrosion. For the test matrix, a tubular with D/t of 40, t_r/t of 0, and θ of 90º was repaired. The outside diameter of the corroded specimen is 127 mm and the annulus recommended by the grout manufacturer is 19 mm. Therefore, the minimum inside diameter of the sleeve is 165 mm. The original design capacity of the undamaged tube is $P_o = 241$ kN. This value is taken from SSRC Column Curve Type 1 for the axial capacity of a tubular column with the same dimensions as Specimen C40-100-0. The residual strength, predicted by Equation (3.2), is 183.5 kN. Thus, this value is the required strength of the sleeve. Hence, P_o, $(AE)_{tube}$, and P_{sleeve} are known. Substituting all of these values into Equation (4.7) and applying a factor of safety of 1.5 to the right hand side of

the equation, the value for $(AE)_{sleeve}$ is obtained. For the repair sleeve with an unknown thickness, the cross sectional area can be represented as:

$$A_{sleeve} = \pi \cdot (ID_{sleeve} + t_{sleeve}) \cdot t_{sleeve} \tag{4.8}$$

where,

A_{sleeve} = cross-sectional area of the repair sleeve
ID_{sleeve} = inside diameter of the repair sleeve
t_{sleeve} = thickness of the repair sleeve

Hence, $(AE)_{sleeve}$ from Equation (4.7) can be reduced to the modulus times the thickness of the repair sleeve ($E_{sleeve} \cdot t_{sleeve}$). This parameter is provided to a manufacturer of composites to produce the sleeve.

For both Specimen 40-0-95-RS (steel sleeve repair) and Specimen 40-0-95-RC (composite sleeve repair), the design required an $E \cdot t_{sleeve}$ of 400 kN/mm. Based on this value, Hardcore Composites produced a composite sleeve with a modulus of 67 GPa in the longitudinal direction of the tube and an average thickness of 7 mm, thus producing an $E \cdot t_{sleeve}$ of 469 kN/mm. (As noted before, these parameters are based on the engineering experience of the structural engineers at Hardcore Composites. An exact modulus and ultimate strength are not available due to the considerable cost to produce the materials and run the tests.)

The strength of the carbon fiber material is approximately 63.6 MPa. The stress imparted upon the repair sleeve by the patch corroded tubular is 48.5 MPa. Thus the resistance of the sleeve is greater than the load and the design is considered safe.

The confinement stresses are difficult to predict. Initially, it was decided to provide equal strength and stiffness in the longitudinal direction. The manufacturer of the

composite sleeve, Hardcore Composites, preferred to limit the design to drastically reduce the cost and the weight of the finished sleeve. Thus, the design of the composite sleeve in the circumferential direction was conservatively designed by the engineers of Hardcore Composites.

4.5.1.2 STEEL SLEEVE

The steel repair sleeve has the same modulus of elasticity as the patch corroded tubular. This reduces Equation (4.7) to an equation depending solely on area. Additionally, the manufacturer of the epoxy grout recommended an annulus of 19 mm. Thus, an inside diameter of 165 mm was used for the repair sleeve. Since the diameters of both the repair sleeve and corroded specimen are known, the calculation reduces to calculating the required sleeve thickness (t_{sleeve}). The smallest available thickness for that diameter tubular was 7mm, resulting in a sleeve D/t of 25.7. Thus, the area of the repair sleeve, $(A)_{sleeve}$, divided by the original undamaged area of the tube, $(A)_{tube}$, was 3.04. Based on Equation (4.7) the repair sleeve would develop an axial load of 0.75 P_o. Since the repair sleeve was much larger in area than the original undamaged tube, the stress in the sleeve when the specimen was loaded to P_o was approximately 0.25 σ_y, where σ_y is the yield stress. Therefore, the steel repair sleeve with an outside diameter of 179 mm and thickness of 7 mm was considered adequate.

4.5.2 SLEEVE LENGTH

The length of the repair sleeve was based on the following equation presented by

Hebor and Ricles (1994):

$$s_{req} = 2\left(\frac{P_{sleeve}}{\pi D \tau_b}\right) + h_{crit} \tag{4.9}$$

where,

s_{req}	=	required sleeve length
D	=	outside diameter of corroded tubular
τ_b	=	grout bond strength
h_{crit}	=	critical h dimension at which one half-wave local buckle may form
P_{sleeve}	=	load to be resisted by repair sleeve

The equation accounts for the required length needed to develop sufficient shear transfer. The length s_{req} being greater than h_{crit}, insures that the sleeve will still encompass the entire critical area of the patch corrosion and have adequate length for bond development.

For the current study, D = 127 mm, τ_b = 12 MPa, h_{crit} = one radius of the corroded tubulars, and P_{sleeve} = 183.5 kN. Thus, the required sleeve length, s_{req}, for the repair sleeve is 140 mm. However, when the repairs were applied to Specimens C40-00-95-RS and C40-00-95-RC, the bond strength of the grout was not known and a value of 3.8 MPa was conservatively used based on initial manufacturer recommendations. As a result, the actual length of the repair sleeves was 304 mm, an over-design by a factor of 2.2.

4.5.3 SURFACE PREPARATION

4.5.3.1 STEEL SURFACES

For the application of the repair, the surfaces of both the corroded specimen and

the steel repair sleeve required a prepared surface as specified by the epoxy grout manufacturer. The surface must comply to an SSPC–SP6 finish. Sandblasting was performed creating a constant surface roughness of 250 to 300 micro-inches.

4.5.3.2 CARBON FIBER COMPOSITE SLEEVE SURFACE

The composite sleeve was fabricated using a peel-ply surface on the interior, which upon removal from the mold produced a rough textured surface. No additional surface treatments for the inside of the composite sleeve were necessary.

4.6 TEST SETUP

The experimental tests were performed using a 2700 kN MTS Testing Machine located in the Structural Engineering Laboratories at the University of Toronto. The test specimens all were prepared by cutting a 305 mm long slot and then inserting and fillet welding in a male clevis plate on each end, as shown in Figure 4.31. The strength of the clevis plate's fillet weld was based on being able to develop 1.5 times the yield capacity of an undamaged specimen in tension. The male end plates were A572 Gr. 50 steel. In order to insure proper alignment and minimize eccentricity of the welded connection, a rigid jig was constructed. The male end plates were set in place on the jig and repeated alignment checks were performed. They were then heated as recommended by Section J2 of the LRFD manual (AISC 1994). Next, the slotted steel tubes were slid onto the male end plates and were also aligned. Tack weld were then used to keep warping to a minimum while the fillet weld was placed. After the entire assembly was allowed to cool, the specimen, with male end plates attached, was removed from the jig.

Unfortunately, while great care was taken to align the specimen in the North-South direction, less attention was given to the alignment in the East-West direction (see Figure 4.31). While cutting the slots for the male clevis end plate in the end of the tubes, great care was taken to insure that the slots were centered. While cutting with a band saw, however, the precision of the slots was lost as the band saw was not able to cut as accurately as required. The possible misalignment in the East-West direction introduced by this process may have attributed to the alignment problems that are discussed in the following chapters.

Three other plates of A572 Gr. 50 steel were cut and welded together to form the female (receiving) end of the clevis (Figure 4.32). The female end of the clevis was inserted into the universal holding grips of the MTS machine as shown in Figure 4.33. Once the receiving fixtures of the clevis were inserted, the specimen was placed into the MTS machine with the aid of a 10-ton crane. The top clevis was aligned and the top 76 mm diameter clevis pin was inserted. The specimen was then allowed to hang in place while the lower pin was placed. Next, the out-of-straightness (OOS) in the North-South direction (i.e. the direction in which global buckling was expected to occur) was measured with the specimen in place. The maximum OOS for each specimen is given in Table 4.3. Lastly, a whitewash was applied to the specimen to aid in the detection of yielding. The overall setup can be seen in Figure 4.33.

4.7 INTRUMENTATION

The instrumentation layout is shown in Figure 4.34. The desired information to

be collected during testing of each specimen included:

- The overall load-displacement history of the specimen
- The strain at points of interest indicating the effects of patch corrosion
- The effect of the corrosion patch on the moment-curvature relationship of the specimen
- Moment-axial load interaction of the cross-section with the corrosion patch
- The lateral displacements at mid-height and other points of interest
- The end rotation of the specimen

To obtain these readings a series of strain gages, Linear Variable Differential Transducers (LVDTs), string pots, and inclinometers were used. Figure 4.34 details the location of all instrumentation used for the testing procedure.

The vertical displacement history was recorded using two vertical LVDTs (LVDT1 and LVDT2) shown in Figure 4.34. Axial deformation of the specimen, Δ, was based on the average of the two vertical LVDT measurements. Linear potentiometers (referred to as "string pots") were used to measure the lateral deflection along the length of the specimen. The applied axial load was measured using the internal load cell of the MTS overhead testing machine. The inward or outward radial movement of the tube wall in the corrosion patch due to local buckling was measured using LVDT3. Inclinometers 1, 2, 3, and 4 were used to measure the rotation of the specimen. Strain gages were placed to evaluate the strain at points of interest (namely the patch region) and the overall distribution of strain throughout the specimen.

For certain tests, minor modifications were made to the instrumentation setup.

For the specimens with through thickness corrosion (C40-00-95, C40-00-95-RS and C40-00-95-RC), strain gage M1 was not placed and LVDT3 was removed. For the specimens with no patch corrosion damage (C27-100-0 and C40-100-0), LVDT 3 was moved to measure East-West lateral deflection as shown in Figure 4.35. For the repaired specimens (C40-00-95-RS and C40-00-95-RC), in addition to the changes mentioned above, six additional strain gages were added (R1 through R6) to monitor the strain in the repair sleeve as shown in Figure 4.36.

4.8 TESTING PROCEDURE

A typical cyclic axial displacement history imposed upon a specimen is shown in Figure 4.37 and it is based on Δ_y, the axial displacement at which the gross section yields. Δ_y is based on the yield stress of the annealed steel, σ_y, the total length of the specimen, L (from center to center of the clevis pins, 2464 mm as shown in Figure 4.34), and the Modulus of Elasticity, E:

$$\Delta_y = \frac{\sigma_y L}{E} \tag{4.6}$$

Load Step numbers are identified in the displacement history (1, -1, 2, -2, … 24, -24) to aid in the discussion of events during the testing of each specimen. The cyclic displacement history was chosen based on the following rational:

- It is a cyclic loading history with loading in the tension and compression range
- It simulates earthquake or wave loading for bracing

- It can be used to compare to previous tests conducted by Liu and Goel (1998) and Pons (1997)

Once the specimen was set in the MTS testing machine, all instrumentation was checked and verified for correct polarity and sensitivity. After verification of the instrumentation, the loading began at a displacement rate of 0.025mm/sec. In subsequent cycles, if the specimen reacted to the loading as predicted, the displacement rate was increased by each step until the maximum displacement rate of 0.125mm/sec was reached. At each point of interest, the specimen was held for pictures, notes, and sketches. Typical holding points were the onset of yielding in tension, formation of the local buckle, and the onset of cracking. A test was continued until the axial load capacity had deteriorated to less than 10% of the maximum axial load yield capacity of the specimen. Also, in the event that continuing a test presented the possibility of either damaging equipment or injuring bystanders, the test was terminated.

5 EXPERIMENTAL BEHAVIOR

This chapter discusses the behavior of the 12 axially loaded specimens. The maximum tensile axial load (P^t_{max}) and the maximum compressive axial load (P^c_{max}) for each specimen are summarized in Table 5.1. Column one contains the maximum axial compression load (P^c_{max}) for the monotonically loaded specimens. Columns two and three contain the maximum axial compression load (P^c_{max}) and maximum axial tension load (P^t_{max}) for the cyclically loaded specimens, respectively. For ease of comparison, the load and displacement are normalized with respect to P_y and Δ_y respectively. Δ_y is based on Equation (4.6). P_y is based on the gross section (A_g) and measured yield stress (σ_y) of the annealed steel.

All references to specimen instrumentation are made in reference to Figure 4.34 unless otherwise noted. Each specimen was oriented so that the corrosion patch faced to the South. Therefore, South is defined as the 0^o line of each specimen. This is also noted on the corrosion profile for each specimen (Figures 4.4 through 4.13).

5.1 UNDAMAGED CONTROL SPECIMENS

For each D/t ratio, an undamaged control specimen was tested to provide a reference for the damaged tubes of the respective ratio. These specimens are identified as C40-100-0 and C27-100-0.

5.1.1 SPECIMEN C40-100-0

Specimen C40-100-0 was a cyclically loaded, undamaged tube. This specimen is to be used as a control specimen for comparative purposes with the corresponding damaged tubes of D/t=40.

No corrosion patch was present for this specimen, hence instrument LVDT 3, which measures the growth of the local buckle was instead used to measure the East-West lateral displacement. The adjusted instrumentation setup is shown in Figure 4.35.

The specimen was loaded as per the loading history described in Section 4.8 with an initial loading rate of 0.025 mm/sec. The normalized axial load-axial displacement response ($P/P_y - \Delta/\Delta_y$) is shown in Figure 5.1. Figure 5.2 is a plot of the loading history with events of interest noted.

At approximately $+\Delta_y$, the entire tube formed yield lines. It was evident from visual inspection that the tube had uniformly yielded throughout the length and around the cross section. Upon reaching $+2\Delta_y$ at Load Step +1, the maximum tension load, P^t_{max}, of 249 kN was noted. The loading rate was then changed to 0.05 mm/sec.

En rout to Load Step –1, in the first compression half cycle, the load peaked at roughly Δ_y. The maximum compressive load (P^c_{max}) was -222 kN. During this cycle, the yielding became more pronounced at the midsection but no *visible* local buckle formed. Of note is that the tube displaced in the northwest direction, as can be seen by comparing Figures 5.3 and 5.4. At the peak displacement of $-5\Delta_y$, the lateral displacement to the West and North direction were 28 mm and to 83 mm, respectively. This phenomenon was attributed to the alignment of the end plates and a lack of corrosion patch to initiate a

local buckle. As previously mentioned, during fabrication of the specimens improper setting of the tube in the jig created a slight East-West eccentricity. During Load Step –1, yielding intensified in the specimen at mid-height as shown in Figure 5.5.

During Load Step +2, the tube straightened. Subsequent cycles caused lateral displacement in the northern direction only. At the end of Load Step +2, the loading rate was changed to 0.075 mm/sec.

In Load Step -2, local buckling was observed 12mm above the mid-height on the North-West Face of the tube near strain gage M5 (Figure 5.6). This event is noted on Figure 5.2. The formation of the buckle coincides with the onset of a decrease in load from the peak compressive capacity from Load Step -1 to Load Step -2 in the $P/P_y - \Delta/\Delta_y$ relationship (Figure 5.1). The lateral displacement at $-5\Delta_y$, the end of Load Step –2, was approximately 101 mm to the North. In addition, the load rate was changed to 0.10 mm/sec. In Load Step +3, the local buckle and also the tube straightened but maintained a residual northward lateral displacement of approximately 13 mm. At this point, the load rate was raised to 0.125 mm/sec; this was the final change in the loading rate.

Load Steps –3 through –7 produced no appreciable change in the behavior of the tube. The noticeable trends were that the local buckle tended to ovalize the cross section in each subsequent cycle, there was a slight increase in the northward lateral displacement, and the maximum compressive load in each subsequent cycle decreased. When subjecting the specimen to tension load the local buckle would tend to straighten. While in compression the depth of the local buckle increased, causing cyclic plastic strain. At the end of Load Step –7 ($-10\Delta y$), the local buckle was 70mm deep and

approximately 140mm around the circumference. The next significant event occurred during Load Step +8.

Load Step +8 produced cracking in both edges of the local buckle (Figure 5.7). The occurrence is noted in Figures 5.1 and 5.2 and is due to low cycle fatigue caused by the cyclic local buckling. In Load Step +10, a significant portion of the section had cracked on the surface throughout most of the width of the local buckle (Figure 5.8). No through-thickness cracking was visible.

At no time did Specimen C40-100-0 reach a point that could be considered complete failure of the section. The section had significantly ovalized but the cracking did not grow significantly though the wall of the section. However, since the compressive load carrying capacity of the specimen had degraded to 12% of the peak compressive load capacity (P^c_{max}) at Load Step –9 it was decided to modify the load history by subjecting the specimen to an axial shortening of $-15\Delta y$ during Load Step –10. This change is noted by the dashed line in Figure 5.2. During this step, the local buckle significantly ovalized the tube and the load carrying capacity leveled off to approximately 9.5% of its original capacity. Also of note was that the strain on the southern face, opposite the face where the local buckle formed, had significantly risen into tension with each increase in axial displacement. The lateral displacement for the tube was 224 mm in the northern direction and the width that the local buckle had subtended was 170 mm. A photograph of the specimen at the end of Load Step –10 is shown in Figure 5.9. After Load Step –10, the test was stopped and the specimen was unloaded.

Figure 5.10 is a plot of the mid-height strains form gages M1 through M6. These gages are positioned as indicated on Figure 4.35. In Figure 5.10 ε_y and θ are the yield strain and the position around the circumference in degrees, respectively. The strains are plotted for four different times: at one half the peak tension load (0.5 P^t_{max}) during Load Step +1; at the peak tension load (P^t_{max}) during Load Step +1; at the peak tension displacement of $2\Delta_y$ during load step +1; and at the peak compression load (P^c_{max}) during Load Step -1. The strains remain roughly uniform at 0.5 P^t_{max} and at P^t_{max}. The section yielded evenly in tension at P^t_{max}. At $2\Delta_y$, Strain gages M5 and M6 indicate that the beam has deformed inelastically. For the mid-height strain at peak compressive load (P^c_{max}) during Load Step –1, strain gage M5 is much higher than the yield strain (about three times) while the remaining strains around the circumference of the cross section are below the yield strain. This distribution of strain is due to the local buckling at strain gage M5, showing that a local buckle formed even though it was not visible.

Figures 5.11 and 5.12 are a plots of the strains at 1/4 of the height (strain gages B1 through B4), and 3/4 of the height (strain gages T1 through T4). The strains remain roughly uniform as the section yielded in tension at P^t_{max}. The effects of inelastic loading are indicated by strain gage T3 at $2\Delta_y$. The strains in Figures 5.12 and 5.13 remain elastic at the peak compression load (P^c_{max}) during Load Step –1 in contrast to the strain at mid-height at strain gages M5 (Figure 5.11), which goes well beyond yield strain due to the onset of local buckling during Load Step -1.

The compressive load carrying capacity of the specimen did not immediately drop when the local buckle formed during Load Step -1, as seen in Figure 5.1. Local buckling

occurred in the North-West face of the specimen, while global buckling is expected in the North-South direction. The compression load did not drop until the yielding and local buckle sufficiently encompassed a greater portion of the section causing the specimen to buckle globally in the North-South direction. Global buckling to the North lead to a significant drop in capacity.

5.1.2 SPECIMEN C27-100-0

Specimen C27-100-0 was a cyclically loaded, undamaged tube. This specimen is to be used as a control specimen for comparative purposes with the corresponding damaged tubes of D/t=27.

No corrosion patch was present for this specimen, hence instrument LVDT 3, which measures the growth of the local buckle was used instead to measure the East-West lateral displacement. The adjusted instrumentation setup is shown in Figure 4.35.

The specimen was loaded as per the loading history described in Section 4.8 with an initial loading rate of 0.025 mm/sec. The normalized axial load-axial displacement response ($P/P_y - \Delta/\Delta_y$) is shown in Figure 5.13. Figure 5.14 is a plot of the loading history with events of interest noted.

At approximately $+\Delta_y$, the entire tube formed yield lines. It was evident from visual inspection that the tube had uniformly yielded throughout the length and around the cross section. Upon reaching $+2\Delta y$ at Load Step +1, the maximum tension load, P^t_{max}, of 480 kN was noted. The loading rate was then changed to 0.05 mm/sec.

En rout to Load Step –1, in the first compression half cycle, the load peaked at

roughly $-\Delta_y$. The maximum compressive load (P^c_{max}) was -462 kN. During this cycle, the yielding became more pronounced at the midsection but no local buckle formed. Of note is that the tube displaced in the western direction, as can be seen by comparing Figures 5.15 and 5.16. This phenomenon was attributed to the alignment of the end plates and a lack of corrosion patch to initiate a local buckle. As mentioned previously, during fabrication of the specimens improper setting of the tube in the jig created a slight East-West eccentricity. During Load Step -1, yielding intensified in the specimen at mid-height as shown in Figure 5.17. Due to possible damage to the testing machine, the loading was held at $-3.25\Delta_y$ as indicated in Figure 5.14. The lateral displacement to the West and to the North were 42 mm and 6 mm respectively. The specimen was then straightened in Load Step +2, which had the displacement changed to $+2.5\Delta_y$ to accomplish this. During Load Step –2, the specimen continued to displace and buckle to the West and loading was again halted at $-3.25\Delta_y$. The process of straightening was repeated during Load Step +3. During Load Step –3, a local buckle formed on the southern face at approximately mid-height (Figure 5.18). This event is noted on Figure 5.14. The deflection of the specimen, however, was still primarily to the West. Load Step +4 was used to straighten the specimen to $+2\Delta_y$. During Load Step –4, the specimen buckled solely to the North. At the end of Load Step –4 the loading rate was changed to 0.075 mm/sec and the remaining normal loading history was recommenced. All of the changes to the load history are shown on Figure 5.14.

The onset of global buckling in the northern direction coincided with the onset of a decrease in compressive load capacity from Load Step -3 to Load Step -4 in the P/P_y –

Δ/Δ_y relationship (Figure 5.13). The lateral displacement at $-5\Delta_y$ the end of Load Step –4, was approximately 120 mm to the North. In addition, the load rate was changed to 0.10 mm/sec. In Load Step +4, the tube straightened but maintained a residual northward lateral displacement of approximately 17 mm. At this point, the load rate was raised to 0.125 mm/sec; this was the final change in the loading rate.

Load Steps –6 through –7 produced no appreciable change in the behavior of the tube. The only noticeable trends were that the local buckle tended to ovalize the cross section in each subsequent cycle and there was a slight increase in the northward lateral displacement. At the end of Load Step –7 (-10Δy), the local buckle was 13 mm deep and approximately 107 mm around the circumference. The lateral displacement in the northern direction was 197 mm.

At no time did Specimen C27-100-0 reach a point that could be considered complete failure of the section. Although cyclic local buckling occurred, no cracking was recorded, only significant ovalization. However, since the compressive load carrying capacity of the specimen had degraded to 13% of the peak compressive load capacity (P^c_{max}) at Load Step –9 it was decided to modify the load history by subjecting the specimen to an axial shortening of $-15\Delta_y$ during Load Step –10. This change is noted by the dashed line in Figure 5.14 and is the same change that was performed for Specimen C40-100-0. During this step, the local buckle significantly ovalized the tube and the load carrying capacity leveled off to approximately 11% of its original capacity. Also of note was that the strain on the northern face, opposite the face where the local buckle formed, had significantly risen into tension with each increase in displacement. At $-15\Delta_y$, the

lateral displacement for the tube was 250 mm in the northern direction. A photograph of the specimen at the end of Load Step –10 is shown in Figure 5.19. After Load Step –10, the test was stopped and the specimen was unloaded.

Figure 5.20 is a plot of the mid-height strains form gages M1 through M6. These gages are positioned as indicated on Figure 4.35. In Figure 5.20 ε_y and θ are the yield strain and the position around the circumference in degrees, respectively. The strains are plotted for four different times: at one half the peak tension load (0.5 P^t_{max}) during Load Step +1; at the peak tension load (P^t_{max}) during Load Step +1; at the peak tension displacement of $2\Delta_y$ during load step +1; and at the peak compression load (P^c_{max}) during Load Step -1. The strains remain roughly uniform at 0.5 P^t_{max} and at P^t_{max}. The section yielded evenly in tension at P^t_{max} and remained so at $2\Delta_y$. At P^c_{max}, the strains are uniform and equal to the yield strain, indicating that the whole section has yielded without a local buckle. It is not until the Load Step –3 that the local buckle formed at the mid-height. Unfortunately, at Load Step –3, the strain gages were damaged by the high cyclic strains.

Figures 5.21 and 5.22 are a plots of the strains at 1/4 of the height (strain gages B1 through B4), and 3/4 of the height (strain gages T1 through T4). The strains remain roughly uniform as the section yielded in tension at P^t_{max}. The effects of inelastic loading are indicated by strain gage T4 at $2\Delta_y$. The strains in Figure 5.21 remain elastic at the peak compression load (P^c_{max}) during Load Step -1. In Figure 5.22, however, the strain in strain gage T4 on the West face of the specimen is well beyond the yield strain. The high strain at T4 during Load Step –1 is the result of the gage malfunctioning.

Global displacement first occurred in the western direction while it is expected in the North-South direction. The compression load did not significantly drop until the specimen buckled globally to the North. Yielding initiated in the midsection, forming a local buckle on the southern face in Load Step -3. The formation of the local buckle initiated the northward global buckle and subsequently the loss of axial load carrying capacity.

5.2 DAMAGED SPECIMENS

5.2.1 MONOTONIC LOADING

5.2.1.1 SPECIMEN M40-33-95

Specimen M40-33-95 was a monotonically loaded, non-repaired tube. This specimen was inflicted with corrosion that reduced the wall thickness to 34% of its original thickness with a subtending angle of 95.1^{o}. The corrosion profile can be seen in Figure 4.4. Instrumentation is shown in Figure 4.34.

The specimen was loaded axially in compression with an initial loading rate of 0.125 mm/sec. The normalized axial load-axial displacement response ($P/P_y - \Delta/\Delta_y$) is shown in Figure 5.23. A local buckle quickly formed on the southern face at the mid-height of the specimen in the corrosion patch while the specimen buckled globally to the North (Figure 5.24). The growth of the local buckle is shown in Figure 5.25 and the lateral displacement at the mid-height of the specimen is shown in Figure 5.26. Both of these figures indicate that the sharp drop in the load carrying capacity of the specimen coincides with the initiation of the local buckle and global buckling. Just after reaching

the peak load of -220 kN, the load was held and the loading rate was changed to 0.025 mm/sec. (The loading rate was decreased since the data acquisition unit could not record data fast enough at the higher rate.) As the axial displacement increased, the section ovalized, the lateral displacement increased, and the local buckle grew inward and circumferentially. At the final displacement of $-15\Delta_y$, the lateral displacement to the North was 203 mm. The load carrying capacity deteriorated to approximately 8.9% of its original capacity.

Figure 5.27 is a plot of the strains at mid-height from strain gages M1 through M6. These gages are positioned as indicated in Figure 4.31. Strain gage M5 was damaged during shipping. So assuming that the section can be treated as symmetric, the dashed line indicates the strain at M5 using the reading from strain gage M3. The strains are plotted at the peak axial compressive load (P^c_{max}). The strains within the patch are well beyond the yield strain while the maximum strain outside of the corrosion patch region (at strain gage M3) is roughly twice the yield strain. This indicates the formation of inelastic local buckling in the corrosion patch.

Figures 5.28 and 5.29 are a plots of the strains at 1/4 of the height (strain gages B1 through B4), and 3/4 of the height (strain gages T1 through T4). The strains in Figures 5.28 and 5.29 are near the yield strain at the peak compression load (P^c_{max}) during Load Step -1. Comparing the strains at the quarter-points to those of the mid-height, the strain concentration and the formation of a local buckle in the corrosion patch is evident.

5.2.1.2 SPECIMEN M27-33-95

Specimen M27-33-95 was a monotonically loaded, non-repaired tube. This specimen was inflicted with corrosion that reduced the wall thickness to 33% of its original thickness with a subtending angle of 94.7°. The corrosion profile can be seen in Figure 4.5. Instrumentation is shown in Figure 4.34.

The specimen was loaded axially in compression with an initial loading rate of 0.025 mm/sec. The normalized axial load-axial displacement response ($P/P_y - \Delta/\Delta_y$) is shown in Figure 5.30. A local buckle quickly formed on the southern face at mid-height of the specimen in the corrosion patch while the specimen buckled globally to the North (Figure 5.31). The growth of the local buckle is shown in Figure 5.32 and the lateral displacement at mid-height of the specimen is shown in Figure 5.33. Both of these figures indicate that the sharp drop in the load carrying capacity of the specimen coincides with the initiation of the local buckle and global buckling. The peak load was approximately 410 kN. As the axial displacement increased, the section ovalized, the lateral displacement increased, and the local buckle grew inward and circumferentially. At the final displacement of $-15\Delta_y$, the lateral displacement to the North was 246 mm. The load carrying capacity leveled off to approximately 11% of its original capacity.

Figure 5.34 is a plot of the strains at mid-height from strain gages M1 through M6. These gages are positioned as indicated in Figure 4.34. The strains are plotted for peak axial compressive load. The strains within the patch are well beyond the yield strain while the strains outside of the corrosion patch region remain near the yield strain. This indicates the formation of inelastic local buckling in the corrosion patch

Figures 5.35 and 5.36 are a plots of the strains at 1/4 of the height (strain gages B1

through B4), and 3/4 of the height (strain gages T1 through T4). The strains in Figures 5.35 and 5.36 are near the yield strain at the peak compression load (P^c_{max}) during Load Step -1. Comparing the strains at the quarter-points to those of the mid-height, the strain concentration and the formation of a local buckle in the corrosion patch is evident.

5.2.2 CYCLIC LOADING

5.2.2.1 SPECIMEN C40-67-95

Specimen C40-67-95 was a cyclically loaded, non-repaired tube. This specimen was inflicted with corrosion that reduced the wall thickness to 67% of its original thickness with a subtending angle of 94.3^o. The corrosion profile can be seen in Figure 4.6. Instrumentation is shown in Figure 4.34.

The specimen was loaded in accordance with the loading history described in Section 4.8 using an initial loading rate of 0.025 mm/sec. The normalized axial load-axial displacement response ($P/P_y - \Delta/\Delta_y$) is shown in Figure 5.37. Figure 5.38 is a plot of the loading history with events of interest noted.

At approximately $+\Delta y$, the entire tube formed yield lines that initiated from the outermost edges of the corrosion patch. It was evident from visual inspection that the tube had yielded throughout the whitewash region, with the initial yield lines stemming from the corrosion patch (Figure 5.39). Upon reaching $+2\Delta_y$ during Load Step +1, the maximum tension load of 237 kN was reached. The loading rate was then changed to 0.05 mm/sec.

En rout to Load Step –1, in the first compression cycle, the load peaked at roughly

$-\Delta_y$. The maximum compressive load (P^c_{max}) was about 226 kN. During this cycle, the yielding became more pronounced at the midsection and a local buckle formed in the corrosion patch (Figure 5.40). This event is noted on Figure 5.38. The growth of the local buckle is shown in Figure 5.41 and the lateral displacement at the mid-height of the specimen is shown in Figure 5.42. The buckle initiated in the patch just to the west of strain gage M1, while the LVDT monitored the corrosion patch just to the east of strain gage M1. Figures 5.41 and 5.42 indicate that the sharp drop in the load carrying capacity of the specimen coincides with the initiation of global buckling which was initiated by the local buckle.

Of note is that the tube displaced in the North-West direction. This phenomenon was attributed to the alignment of the end plates. As mentioned previously, during fabrication of the specimens, improper setting of the tube in the jig created a slight East-West eccentricity. At peak displacement of $-5\Delta y$ of Load Step -1, the lateral displacement at mid-height was 67 mm to the North and 16 mm to the West. Yielding, stemming form the corrosion patch, intensified and covered a distance of 381 mm both above and below the centerline of the corrosion patch. For Load Step +2, the loading rate was changed to 0.075 mm/sec. The peak load for this step was 213 kN in tension and the mid-height lateral displacement was negligible. Before commencing the next cycle, the loading rate was changed to 0.01 mm/sec.

In Load Step -2, the local buckle continued to become more pronounced. The northern lateral displacement at $-5\Delta y$, the end of Load Step –2, was 103 mm. At this point, the load rate was increased to 0.125 mm/sec; this was the final change in the

loading rate.

Load Steps +3 through -7 produced no appreciable change in the reaction of the specimen. The noticeable trends were that the local buckle tended to ovalize the cross section in each subsequent cycle and there was a slight increase in the northward lateral displacement. Also, with load reversal from compression to tension, cyclic local buckling occurred in the corrosion patch. During Load Step –7, the first load step of $-10\Delta_y$ had a mid-height lateral displacement of 176 mm.

During Load Step +8, the specimen formed a through thickness crack (Figure 5.43). The crack formed as a result of low cycle fatigue in the corrosion patch. In subsequent load steps, the crack continued to grow. At Load Step +9, the through thickness crack had grown to encompass a length of 170 mm around the circumference of the specimen. The extent of the fracture was very large and the compressive load carrying capacity of the specimen had degraded to 11% of the peak compressive load capacity (P^c_{max}) at Load Step –9. Hence, it was decided to modify the load history by subjecting the specimen to an axial shortening of $-15\Delta_y$ during Load Step –10. This change is noted by the dashed line in Figure 5.38. During this step, the local buckle significantly ovalized the tube and the load carrying capacity deteriorated to approximately 7.5% of its original capacity. Also of note was that the strain on the northern face, opposite the face where the local buckle formed, had developed significant tension. At $-15\Delta_y$, the lateral displacement for the tube was 217 mm in the northern direction. A photograph of the specimen at the end of Load Step –10 is shown in Figure 5.44. After Load Step –10, the test was stopped and the specimen was unloaded.

Figure 5.45 is a plot of the mid-height strains form gages M1 through M6. These gages are positioned as indicated on Figure 4.34. In Figure 5.45 ε_y and θ are the yield strain and the position around the circumference in degrees, respectively. The strains are plotted for four different times: at one half the peak tension load ($0.5\ P^t_{max}$) during Load Step +1; at the peak tension load (P^t_{max}) during Load Step +1; at the peak tension displacement of $2\Delta_y$ during load step +1; and at the peak compression load (P^c_{max}) during Load Step -1. At $0.5\ P^t_{max}$, the strain in the center of the patch is 0.9 times the yield strain. This indicated a strain concentration in the corrosion patch. The entire patch has gone well beyond yielding at P^t_{max}. At peak compressive load (P^c_{max}) during Load Step –1, the tensile plastic strain induced during Load Step +1 has not been recovered in the patch, even though a local buckle has formed. Strain gage M1, for example, shows however that the relative change in strain from Load Step +1 to Load Step –1 is much higher than the yield strain (about seven times the yield strain). Thus, the corrosion patch has yielded in compression and formed the local buckle seen in Figure 5.40.

Figures 5.46 and 5.47 are a plots of the strains at 1/4 of the height (strain gages B1 through B4), and 3/4 of the height (strain gages T1 through T4). The strains remain roughly uniform as the section yielded evenly in tension at P^t_{max}. The strains in Figures 5.46 and 5.47 are near the yield strain at the peak compression load (P^c_{max}) during Load Step –1 in contrast to the strains at mid-height which goes well beyond yield strain. The high strain at the mid-height during Load Step –1 is the result of a strain concentration and local buckling.

Initially, the mid-height displacement was in the North-West direction while it

was expected to the North. The compression load did not drop until the local buckle sufficiently developed in the corrosion patch. As the local buckle grew, the specimen began to displace in the North-South direction. The decrease in load during Load Step –1 corresponds to the specimen buckling globally to the North caused by the local buckle.

5.2.2.2 SPECIMEN C40-33-95

Specimen C40-33-95 was a cyclically loaded, non-repaired tube. This specimen was inflicted with corrosion that reduced the wall thickness to 34% of its original thickness with a subtending angle of 95^o. The corrosion profile can be seen in Figure 4.7. Instrumentation is shown in Figure 4.34.

The specimen was loaded as per the loading history described in Section 4.8 with an initial loading rate of 0.025 mm/sec. The normalized axial load-axial displacement response ($P/P_y - \Delta/\Delta_y$) is shown in Figure 5.48. Figure 5.49 is a plot of the loading history with events of interest noted.

At approximately $+\Delta y$, the entire tube formed yield lines that initiated from the outermost edges of the corrosion patch. It was evident from visual inspection that the tube had yielded throughout the whitewash region with the majority of the yield lines stemming from the corrosion patch (Figure 5.50). Upon reaching $+2\Delta y$ at Load Step +1, the specimen maximum tension load, P^t_{max}, of about 236 kN was achieved. The loading rate was then changed to 0.05 mm/sec.

En rout to Load Step –1, in the first compression cycle, the load peaked at roughly $1\Delta y$. The maximum compressive load (P^c_{max}) was about 200 kN. During this cycle, the

yielding became more pronounced at the midsection and a local buckle formed in the corrosion patch (Figure 5.51). This event is noted on Figure 5.49. The growth of the local buckle is shown in Figure 5.52 and the lateral displacement at the mid-height of the specimen is shown in Figure 5.53. Both of these figures indicate that the sharp drop in the load carrying capacity of the specimen coincides with the initiation of the local buckle and global buckling.

Of note is that the tube displaced solely to the North. Unlike the specimens with no or little patch corrosion damage, the eccentricity of the corrosion patch dominated the eccentricity caused by the end plates. At peak displacement of $-5\Delta y$ of Load Step -1, the lateral displacement at mid-height was 112 mm to the North. Yielding, stemming form the corrosion patch, intensified and covered a distance of 229 mm both above and below the centerline of the patch. One note of interest is that the local buckle formed inward on the eastern edge of the corrosion patch and outward on the western edge (Figure 5.51). The loading rate for Load Step +2 was changed to 0.075 mm/sec. The peak load for this step was 154 kN in tension with a mid-height lateral displacement of 25mm. Before commencing the next cycle, the loading rate was changed to 0.01 mm/sec.

In Load Step -2, the local buckle continued to grow inwards on the eastern edge of the corrosion patch and outwards on the western edge. The northern lateral displacement at $-5\Delta_y$ at the end of Load Step –2 was 116 mm. At this point, the load rate was raised to 0.125 mm/sec; this was the final change in the loading.

Shortly after passing through zero load en rout to Load Step +3, through thickness cracking was noticed on the western edge of the local buckle and surface cracking on the

eastern edge. The crack formed as a result of low cycle fatigue caused by cyclic local buckling in the corrosion patch. The photograph in Figure 5.54 was taken after reaching the end of the Load Step. The event is noted in Figure 5.49. At the end of Load Step +3, the specimen maintained a residual mid-height lateral displacement of approximately 24 mm.

Load Steps –3 through –4 produced no significant changes in the behavior of the specimen. In Load Step +4, the crack grew from both edges of the patch and at the completion of the load step, the two individual cracks met and formed one single through thickness crack that encompassed the entire length of the patch (Figure 5.55).

During subsequent load steps, the crack continued to grow. At Load Step +10, the through thickness crack had grown to encompass a length of 178 mm around the circumference of the cross-section with the corrosion patch. The compressive load carrying capacity of the specimen had degraded to 10% of the peak compressive load capacity (P^c_{max}) at Load Step –9. Hence, it was decided to modify the load history by subjecting the specimen to an axial shortening of $-15\Delta_y$ during Load Step –10. The dashed line in Figure 5.49 notes this change. During this load step, the cross section at mid-height significantly ovalized and the load carrying capacity had deteriorated to approximately 8% of its original capacity. Also of note was that the strain on the northern face, opposite the face where the local buckle formed, had developed a significant amount of tension with each increase in axial displacement. At $-15\Delta_y$, the lateral displacement for the tube was 217 mm in the northern direction. A photograph of the specimen at the end of Load Step –10 is shown in Figure 5.56. After Load Step –10,

the test was stopped and the specimen was unloaded.

Figure 5.57 is a plot of the mid-height strains form gages M1 through M6. These gages are positioned as indicated on Figure 4.34. In Figure 5.57 ε_y and θ are the yield strain and the position around the circumference in degrees, respectively. The strains are plotted for four different times: at one half the peak tension load (0.5 P^t_{max}) during Load Step +1; at the peak tension load (P^t_{max}) during Load Step +1; at the peak tension displacement of $2\Delta_y$ during load step +1; and at the peak compression load (P^c_{max}) during Load Step -1. At 0.5 P^t_{max}, the strain in the center of the patch is 3.5 times the yield strain. This indicated a strain concentration in the corrosion patch. The entire patch has gone well beyond yielding at P^t_{max}. At peak compressive load (P^c_{max}) during Load Step –1, the tensile plastic strain induced during Load Step +1 has not been recovered in the patch, even though a local buckle has formed. Strain gage M1, for example, shows however that the relative change in strain from $2\Delta_y$ during Load Step +1 to P^c_{max} during Load Step –1 is higher than the yield strain (about nine times the yield strain). Thus, the corrosion patch has yielded in compression and formed the local buckle seen in Figure 5.51. Also shown in Figure 5.57 is the effect of the outward buckle that formed under strain gage M3. At the peak compression load, the strain at M3 has increased in tensile strain by approximately 10 ε_y.

Figures 5.58 and 5.59 are a plots of the strains at 1/4 of the height (strain gages B1 through B4), and 3/4 of the height (strain gages T1 through T4). The strains remain roughly uniform as the section yielded evenly in tension at P^t_{max}. The strains in Figures 5.58 and 5.59 are near the yield strain at the peak compression load (P^c_{max}) during Load

Step –1 in contrast to the strains at mid-height which goes well beyond yield strain. The high strains at the mid-height during Load Step –1 are the result of the strain concentration and local buckling.

5.2.2.3 SPECIMEN C40-00-95

Specimen C40-00-95 was a cyclically loaded, non-repaired tube. This specimen was inflicted with corrosion that reduced the wall thickness to 0% (through thickness) of its original thickness with a subtending angle of 94.9º. The corrosion profile can be seen in Figure 4.8. Instrumentation is shown in Figure 4.34. As mentioned previously, since the corrosion patch is through the thickness, LVDT 3, which measures the local displacement of the corrosion patch, was removed. Likewise, Strain gage M1 could not be placed due to the hole in the corrosion patch.

The specimen was loaded as per the loading history described in Section 4.8 with an initial loading rate of 0.025 mm/sec. The normalized axial load-axial displacement response ($P/P_y - \Delta/\Delta_y$) is shown in Figure 5.60. Figure 5.61 is a plot of the loading history with events of interest noted.

At approximately Δ_y during Load Step +1, the specimen formed yield lines initiating from the outermost edges of the corrosion patch. In addition, the eastern and western edges of the hole created by the corrosion began to crack (Figure 5.62). This event is noted on Figure 5.61. Upon reaching $+2\Delta y$ at Load Step +1, the maximum tension load, (P^t_{max}), of about 221 kN was noted. The loading rate was then changed to 0.05 mm/sec.

En rout to Load Step –1, in the first compression cycle, the load peaked at roughly -1Δy. The maximum compressive load (P^c_{max}) was 208 kN. During this cycle, the yielding became more pronounced at the midsection and a two local buckles formed at the eastern and western edges of the hole in the corrosion patch (Figure 5.63). The event is noted on Figure 5.61. The lateral displacement at the mid-height of the specimen is shown in Figure 5.64. The figure indicates that the sharp drop in the load carrying capacity of the specimen coincided with the initiation of global buckling after developing local buckling at the corrosion patch.

Of note is that the tube displaced solely to the North. Unlike the specimens with no or little damage, the eccentricity of the corrosion patch dominated the eccentricity caused by the end plates. At peak displacement of –5Δy of Load Step -1, the lateral displacement at mid-height was 110 mm to the North. Another note of interest is that the local buckle tended to overlap itself on the eastern edge of the corrosion patch and buckled outward on the western edge (Figure 5.63). In addition, the buckle formed at an angle to the horizontal cross section, as is also shown in 5.63. For Load Step +2, the loading rate was changed to 0.075 mm/sec. The peak load for this step was 158 kN in tension and a residual mid-height lateral displacement of 19 mm was present. The cracking at the edges of the patch grew slightly. Before commencing the next cycle, the loading rate was changed to 0.01 mm/sec.

Load Steps –2 through –8 produced no significant changes in the behavior of the specimen. In Load Step +8, the crack had grew significantly. The through thickness crack had grown to 38 mm to the East and 39 mm to the West from the edge of the hole.

Each crack continued for an additional length of approximately 30 mm on the surface for a total crack length of 162 mm.

During Load Step +10, the through thickness crack formed by low cycle fatigue (caused by cyclic local buckling) had grown to encompass a length of 180 mm around the circumference. At Load Step –9 The extent of the fracture was very large and the compressive load carrying capacity of the specimen had degraded to 8.7% of the peak compressive load capacity (P^c_{max}). Hence, it was decided to modify the load history by subjecting the specimen to an axial shortening of $-15\Delta_y$ during Load Step –10. This change is noted by the dashed line in Figure 5.61. During this step, the cross section at mid-height significantly ovalized and the load carrying capacity deteriorated to approximately 6.5% of its original capacity. Also of note was that the strain on the northern face, opposite the face where the local buckle formed, had developed a significant amount of tensile strain with each increase in axial displacement. At $-15\Delta_y$, the lateral displacement for the tube was 211 mm to the North. A photograph of the specimen at the end of Load Step –10 is shown in Figure 5.65. After Load Step –10, the test was stopped and the specimen was unloaded.

Figure 5.66 is a plot of the strains at mid-height from strain gages M2 through M6. These gages are positioned as indicated on Figure 4.34. The strains are plotted for four different times: at one half the peak tension load ($0.5\ P^t_{max}$) during Load Step +1; at the peak tension load (P^t_{max}) during Load Step +1; at the peak tension displacement of $2\Delta_y$ during load step +1; and at the peak compression load (P^c_{max}) during Load Step -1. At $0.5\ P^t_{max}$, the strains at the edges of the patch are the highest but have not passed the yield

strain. The entire cross section has gone well beyond yielding at P^t_{max}, with the largest strain in the patch. At $2\Delta_y$, the entire cross section at mid-height has yielded. The high strains opposite the patch are the result of the tubular straightening. At peak compressive load, P^c_{max}, during Load Step –1, the plastic strain induced during Load Step +1 has not been recovered in the patch, even though a local buckle has formed. Strain gages M2 and M6 demonstrate however the relative change in strain from $2\Delta_y$ during Load Step +1 to P^c_{max} during Load Step –1 is higher than the yield strain, ε_y (more than twice the yield strain). Thus, the corrosion patch has yielded in compression as it formed the local buckle seen in Figure 5.63. As before, the global and local buckling lead to a significant drop in the axial load carrying capacity of the specimen.

Figures 5.67 and 5.68 are a plots of the strains at 1/4 of the height (strain gages B1 through B4), and 3/4 of the height (strain gages T1 through T4). The strains remain roughly uniform as the section yielded evenly in tension at P^t_{max}. The strains in Figures 5.67 and 5.68 are near the yield strain at the peak compression load (P^c_{max}) during Load Step –1 in contrast to the strains in the section at mid-height which go beyond yield strain. The high strain at the mid-height during Load Step –1 is the result of the hole in the wall of the tubular and the occurrence of local buckling.

5.2.2.4 SPECIMEN C27-33-58

Specimen C27-33-58 was a cyclically loaded, non-repaired tube. This specimen was inflicted with corrosion that reduced the wall thickness to 35% of its original thickness with a subtending angle of 57.9^o. The corrosion profile can be seen in Figure

4.9. Instrumentation is shown in Figure 4.34.

The specimen was loaded as per the loading history described in Section 4.8 with an initial loading rate of 0.025 mm/sec. The normalized axial load-axial displacement response ($P/P_y - \Delta/\Delta_y$) is shown in Figure 5.69. Figure 5.70 is a plot of the loading history with events of interest noted.

At approximately Δ_y, the entire tube formed yield lines that initiated from the corrosion patch. Upon reaching $+2\Delta y$ at Load Step +1, the maximum tension load (P^t_{max}) of about 490 kN was noted. The loading rate was then changed to 0.05 mm/sec.

En rout to Load Step –1, in the first compression half cycle, the load peaked at roughly Δ_y. The maximum compressive load (P^c_{max}) was about -440 kN. During this cycle, the yielding became more pronounced at the midsection but no local buckle formed. Of note is that the tube displaced to the West. This phenomenon was attributed to the alignment of the end plates. During fabrication of the specimens, improper setting of the tube in the jig created a slight East-West eccentricity. During Load Step -1, yielding intensified in the specimen at mid-height as shown in Figure 5.71. Due to possible damage to the testing machine, the axial displacement was held at $-3.25\Delta_y$. The lateral displacement to the West and to the North were approximately 51 mm and 2 mm, respectively. The specimen was then straightened in Load Step +2, which had a revised displacement amplitude of $+2.5\Delta_y$. During Load Step –2, the specimen buckled to the North-West and loading was again halted at $-3.25\Delta_y$. A local buckle formed on the eastern edge of the corrosion patch (Figure 5.72) but the lateral displacement to the West was still too great to continue. This event is indicated in Figure 5.64. The process of

straightening was repeated during Load Step +3. During Load Step –3, the local buckle encompassed a greater portion of the corrosion patch. As a result, the specimen laterally displaced primarily to the North. The growth of the local buckle is shown in Figure 5.73 and the lateral displacement at the mid-height of the specimen is shown in Figure 5.74. Both of these figures indicate that the drop in the load carrying capacity of the specimen from Load Step –2 to Load Step –3 coincides with when the local buckle formed and the specimen buckled globally to the North. At the end of Load Step –3 the loading rate was changed to 0.075 mm/sec and the normal load history was resumed. All of the changes to the load history are shown on Figure 5.70.

The onset of global buckling in the northern direction coincided with the onset of a decrease in load from the peak compressive capacity in Load Step -3 in the $P/P_y - \Delta/\Delta_y$ relationship (Figure 5.69). At the end of Load Step –3, where the axial displacement was $-5\Delta_y$, the lateral displacement was approximately 130 mm to the North. In addition, the load rate was changed to 0.10 mm/sec. In Load Step +3, the tube straightened but maintained a residual northward lateral displacement of approximately 14 mm. At this point, the load rate was raised to 0.125 mm/sec; this was the final change in the loading rate.

Shortly after passing through zero load en rout to Load Step +5, through thickness cracking was noticed in the corrosion patch. The crack formed as a result of low cycle fatigue cracking caused by cyclic local buckling of the corrosion patch. The photograph in Figure 5.75 was taken after reaching the end of the load step. The event was noted on Figure 5.70. At the end of Load Step +5, the specimen maintained a residual mid-height

lateral displacement of approximately 46 mm.

Due to the cyclic local buckling during Load Steps –4 through +7, significant increases in the length of the crack occurred. In Load Step +7, approximately half of the section had a through thickness crack. (Figure 5.76). At Load Step +10, the through thickness crack had grown to encompass a length of 200 mm around the circumference. The extent of the fracture was very large and the compressive load carrying capacity of the specimen had degraded to 10% of the peak compressive load capacity (P^c_{max}) at Load Step –9, corresponding to an axial shortening of $-10\Delta_y$. Hence, it was decided to modify the load history by subjecting the specimen to an axial shortening of $-15\Delta_y$ during Load Step –10. This change is noted by the dashed line in Figure 5.70. During this step, the cross section at mid-height significantly ovalized and the load carrying capacity deteriorated to approximately 9% of its original capacity P^c_{max}. Also of note was that the strain on the northern face, opposite the face where the local buckle formed, had developed a significant amount of tensile strain with each increase in displacement. At $-15\Delta_y$, the lateral displacement for the tube was 270 mm in the northern direction. A photograph of the specimen at the end of Load Step –10 is shown in Figure 5.77. After Load Step –10, the test was stopped and the specimen was unloaded.

Figures 5.78 is a plot of the strains at mid-height from strain gages M1 through M6. These gages are positioned as indicated on Figure 4.34. The strains are plotted for four different times: at one half the peak tension load ($0.5\ P^t_{max}$) during Load Step +1; at the peak tension load (P^t_{max}) during Load Step +1; at the peak tension displacement of $2\Delta_y$ during load step +1; and at the peak compression load (P^c_{max}) during Load Step -1. At 0.5

P^t_{max}, the strain in the center of the patch is 1.7 times the yield strain (ε_y). The corrosion patch created a stress concentration that caused a high strain in the corrosion patch, leading to yielding in the patch below the yield load (P_y). The entire patch has gone well beyond yielding at P^t_{max}. The largest negative change in strain between $2\Delta_y$ and P^c_{max} is shown by strain gage M5. Although the largest negative change in strain is expected in the corrosion patch, the large western lateral displacement caused by the end plate eccentricity increased the strains away from the corrosion patch.

Figures 5.79 and 5.80 are a plots of the strains at 1/4 of the height (strain gages B1 through B4), and 3/4 of the height (strain gages T1 through T4). The strains remain roughly uniform as the section yielded evenly in tension at P^t_{max}. The strains in Figures 5.79 and 5.80 are at roughly ε_y at P^t_{max} and are near the yield strain at P^c_{max} in contrast to the strains at mid-height which go well beyond yield strain. The high strains at the mid-height during Load Steps +1 and –1 are the result of the strain concentration caused by the corrosion patch.

5.2.2.5 SPECIMEN C27-33-95

Specimen C27-33-95 was a cyclically loaded, non-repaired tube. This specimen was inflicted with corrosion that reduced the wall thickness to 33% of its original thickness with a subtending angle of 95.0^o. The corrosion profile can be seen in Figure 4.10. Instrumentation is shown in Figure 4.34.

The specimen was loaded as per the loading history described in Section 4.8 with an initial loading rate of 0.025 mm/sec. The normalized axial load-axial displacement

response ($P/P_y - \Delta/\Delta_y$) is shown in Figure 5.81. Figure 5.82 is a plot of the loading history with events of interest noted.

At approximately $+\Delta_y$, the entire tube formed yield lines that initiated from the corrosion patch. Upon reaching $+2\Delta y$ at Load Step +1, the maximum tension load of about 465 kN was achieved. The loading rate was then changed to 0.05 mm/sec.

En rout to Load Step –1, in the first compression half cycle, the compressive load peaked at roughly $-\Delta_y$. The maximum compressive load (P^c_{max}) was about -403 kN. During this load step, the yielding became more pronounced at the midsection and a local buckle formed just before reaching the peak compression load (Figure 5.83). This event is noted on Figure 5.82. The growth of the local buckle is shown in Figure 5.84 and the lateral displacement at the mid-height of the specimen is shown in Figure 5.85. Both of these figures indicate that the sharp drop in the load carrying capacity of the specimen coincides with the initiation of the local buckle and global buckling.

Of note is that the tube displaced solely to the North. Unlike the specimens with no or little damage, the eccentricity of the corrosion patch dominated the eccentricity caused by the end plates. At peak displacement of $-5\Delta y$ of Load Step -1, the lateral displacement at mid-height was 142 mm to the North. Yielding, stemming form the corrosion patch, intensified and covered a distance of 229 mm both above and below the centerline of the patch. For Load Step +2, the loading rate was changed to 0.075 mm/sec. The peak load for this step was 303 kN in tension and a residual mid-height lateral displacement of 24 mm occurred. Before commencing the next cycle, the loading rate was changed to 0.01 mm/sec.

In Load Step -2, the local buckle continued to grown. The northern lateral displacement at the end of Load Step –2 (where the axial displacement was $-5\Delta_y$) was 144 mm. At this point, the load rate was raised to 0.125 mm/sec; this was the final change in the loading.

Shortly after passing through zero load en rout to Load Step +3, through-thickness cracking was noticed on both edges of the local buckle. The crack formed as a result of low cycle fatigue due to cyclic local buckling occurring in the corrosion patch. The photograph in Figure 5.86 was taken after reaching the end of the Load Step. The event was noted on Figure 5.81. At the end of Load Step +3, the specimen had a residual mid-height lateral displacement of approximately 24 mm.

Load Steps –3 and +4 produced a significant increase in the crack growth. In Load Step +4, the crack subtended 250 mm of the cross section. (Figure 5.87). The extent of the fracture was very large and the compressive load carrying capacity of the specimen had degraded to 13% of the peak compressive load capacity (P^c_{max}) at Load Step –4. Hence, it was decided to modify the load history by subjecting the specimen to an axial shortening of $-15\Delta_y$ during Load Step –5. This change is noted by the dashed line in Figure 5.82. During this load step, the cross section at mid-height significantly ovalized and the load carrying capacity deteriorated to approximately 13% of its original capacity. At $-10\Delta_y$, the tension strain on the side opposite the fracture was greater than 23000 micro-strains. The test was immediately stopped in fear of fracturing the entire section and damaging the testing equipment. A photograph of the specimen at the end of Load Step –5 is shown in Figure 5.88.

Figures 5.89 is a plot of the strains at mid-height from strain gages M1 through M6. These gages are positioned as indicated on Figure 4.34. The strains are plotted for four different times: at one half the peak tension load (0.5 P^t_{max}) during Load Step +1; at the peak tension load (P^t_{max}) during Load Step +1; at the peak tension displacement of $2\Delta_y$ during load step +1; and at the peak compression load (P^c_{max}) during Load Step -1. At 0.5 P^t_{max}, the strain in the center of the patch is three times the yield strain, ε_y. The corrosion patch creates a stress concentration that causes initial yielding in the patch below the yield load. The entire patch has gone well beyond yielding at P^t_{max}. At peak compressive load (P^c_{max}) during Load Step –1, the plastic strain induced during Load Step +1 has not been recovered in the patch, even though a local buckle has formed. Strain gage M1 demonstrates however the relative change in strain from $2\Delta_y$ during Load Step +1 to P^c_{max} during Load Step –1 is much higher than the yield strain (about two to five times ε_y). Thus, the corrosion patch has yielded in compression and formed the local buckle seen in Figure 5.83.

Figures 5.90 and 5.91 are a plots of the strains at 1/4 of the height (strain gages B1 through B4), and 3/4 of the height (strain gages T1 through T4). The strains remain roughly uniform as the section yielded evenly in tension at P^t_{max}. The strains in Figures 5.90 and 5.91 are at roughly ε_y at P^t_{max} and are near the yield strain at P^c_{max} in contrast to the strains at mid-height in the corrosion patch which go well beyond yield strain. The high strains at the mid-height during Load Steps +1 and –1 are the result of the strain concentration caused by the corrosion patch and local buckling.

5.2.2.6 SPECIMEN C27-33-311

Specimen C27-33-311 was a cyclically loaded, non-repaired tube. This specimen was inflicted with corrosion that reduced the wall thickness to 35% of its original thickness with a subtending angle of 310.4°. The corrosion profile can be seen in Figure 4.11. Instrumentation is shown in Figure 4.34.

The specimen was loaded as per the loading history described in Section 4.8 with an initial loading rate of 0.025 mm/sec. The load-displacements history is shown in Figure 5.92. Figure 5.93 is a plot of the loading history with events of interest noted.

During Load Step +1, the specimen visibly deflected to the South due to the eccentricity of the section. At an axial displacement of approximately $1.3\Delta_y$, the entire corroded area fractured in tension (Figure 5.94). This is because the ratio of the gross area to the reduced area is less than the ratio of the tensile stress to the yield stress of the material. The axial displacement of the specimen was immediately held and the maximum tension load, P^t_{max}, of about 391 kN was recorded. In order to salvage some data from the test, the decision was made to attempt Load Step –1. In this Load Step, the fracture surfaces came together and closed, which enabled compressive load to develop before losing capacity due to global buckling in the northern direction. The section began quickly forming yield lines around the patch at approximately $-0.5\Delta_y$. Shortly after this point the bottom "lip" of the fracture began to overlap the top "lip" and the load sharply dropped. The maximum compression load, P^c_{max}, of about 239 kN was recorded. The peak displacement of $-5\Delta y$ was reached and it was noticed that P/Py was less than 5%. At this point the load was removed and the test was stopped. The final state of the

specimen is shown in Figure 5.95.

Figure 5.96 is a plot of the strains at mid-height from strain gages M1 through M6. These gages are positions as indicated on Figure 4.34. The strains are plotted for two different times; at one half the peak tension load (0.5 P^t_{max}); and at the peak tension load (P^t_{max}). The strains indicate that at 0.5 P^t_{max}, yielding has already occurred in the patch and the only strain gage outside the patch has not been affected. At P^t_{max}, the section fractured through the section. The section fracture disabled the strain gages at mid-height and no further measurements from these gages could be made.

Figures 5.97 and 5.98 are a plots of the strains at 1/4 of the height (strain gages B1 through B4), and 3/4 of the height (strain gages T1 through T4). The strains remain roughly uniform as the section yielded evenly in tension P^t_{max}. The strains in Figures 5.97 and 5.98 are at roughly equal to the yield strain at P^t_{max} and are near the yield strain at P^c_{max} in contrast to the strains at mid-height which go well beyond yield strain before the fracture. The high strains at the mid-height during Load Step +1 are the result of the strain concentration caused by the corrosion patch.

5.3 REPAIRED SPECIMENS

5.3.1 STEEL SLEEVE – SPECIMEN C40-00-95-RS

Specimen C40-00-95-RS was a cyclically loaded, repaired tube. This specimen was inflicted with corrosion that reduced the wall thickness to 0% of its original thickness with a subtending angle of 94.6º. The corrosion profile can be seen in Figure 4.12. The repair is a grouted steel sleeve as described in section 4.5.1.2.

The specimen was loaded as per the loading history described in Section 4.8 with an initial loading rate of 0.025 mm/sec. The normalized axial load-axial displacement response ($P/P_y - \Delta/\Delta_y$) is shown in Figure 5.99. Figure 5.100 is a plot of the loading history with events of interest noted.

Also, as previously mentioned, since the local buckle could not effectively be measured, LVDT 3, which measures the local displacement of the corrosion patch, was removed. Likewise, Strain gage M1 could not be placed due to the hole in the corrosion patch. The additional instrumentation consists of strain gages R1-R6. They are placed at mid-height of the specimen on the exterior of the repair sleeve. The changes in instrumentation are shown in Figure 4.36.

During Load Step +1, at approximately Δ_y, the specimen yielded at the ends of the tube near the end plates. Upon reaching $+5\Delta_y$ at the end of Load Step +1, the maximum axial tension load (P^t_{max}) of 254 kN was reached. The loading rate was then changed to 0.05 mm/sec.

En rout to Load Step –1, the compressive axial load peaked at roughly $-\Delta_y$. The maximum compression load (P^c_{max}) was about –242 kN. During this cycle, the yielding became slightly more pronounced throughout the length of the specimen. Of note is that the specimen displaced laterally to the West. At the peak displacement of $-5\Delta_y$, the lateral displacement was negligible to the North and approximately 40 mm to the West. This phenomenon was attributed to the alignment of the end plates and the repair which prevented a local buckle and stiffened the tubular. The lateral deformations were caused by curvature in the corroded tubular outside of the repair region. As mentioned

previously, during fabrication of the specimens, improper setting of the tube in the jig created a slight East-West eccentricity. Load Step +2 sufficiently straightened the specimen. Load Step –2 produced a local buckle on the East face of the specimen at roughly one third of the height from the bottom (Figure 5.101). The specimen incurred large lateral displacements to the West causing the lower end plate to bend severely (Figure 5.102). Returning to $+\Delta_y$ in Load Step +2, the specimen straightened but now maintained a residual westward lateral displacement of about 10 mm.

During Load Step –3, the specimen continued to displace to the West while the local buckle on the eastern side grew. The lateral displacement to the North at no time became larger that 2 mm (Figure 5.103). This again caused bending in the lower end plate. The westward displacement became more severe and the test was terminated for fear of damaging the testing equipment.

Although local buckling occurred on the tubular outside of the repair region, the specimen maintained its compressive axial capacity. This phenomenon is shown in Figure 5.99. The maintenance in capacity in compression can be attributed to the direction of buckling. Since the specimen buckled to the West, the clevises began to bend and resist load. As the buckling became more severe, the end plates provided more resistance and carried more load, maintaining the maximum compression load, P^c_{max}, for the specimen.

Figure 5.104 compares the strains of strain gages M2 through M6 on the corroded tubular and strain gages R1 through R6 on the steel repair sleeve for one half the peak tensile load ($0.5\ P^t_{max}$) in Load Step +1. These gages are positioned as indicated on

Figure 4.36. The strains are far below the yield strain and are identical. Similarly, Figure 5.105 compares the strains of strain gages M2 through M6 on the corroded tubular and strain gages R1 through R6 on the steel repair sleeve for the peak tensile load (P^t_{max}) in Load Step +1. Again, the strains are far below the yield strain and are identical. Lastly, Figure 5.106 compares the strains of strain gages M2 through M6 on the corroded tubular and strain gages R1 through R6 on the steel repair sleeve for the peak compression load, P^c_{max}, in Load Step -1. As before, the strains are far below the yield strain and are identical. These plots demonstrate that the strains are equal for the repair and the damaged tubular and that the assumption for Equation (4.4) is valid.

Figures 5.107 and 5.108 are a plots of the strains at 1/4 of the height (strain gages B1 through B4), and 3/4 of the height (strain gages T1 through T4). The strains remain roughly uniform as the section yielded evenly in tension at P^t_{max}. The strains in Figures 5.107 and 5.108 are at roughly equal to the yield strain at P^t_{max} and are near the yield strain at P^c_{max}. Unlike the other test specimens, for the peak compression load, P^c_{max}, the strains at the quarter-points are well above the yield strain. Comparing this with the strain in the repair sleeve and at the mid-height on the tubular, it is clear that the repair has removed the strain concentration effects of the corrosion patch and forced the failure mode of the specimen outside of the repair region.

After testing, the grout was examined at the ends of the repair sleeve. On the top end of the sleeve, for approximately 170 mm around the circumference of the inner damaged tube, contact was lost between the grout and the specimen (Figure 5.109). On the bottom of the sleeve, the grout was still in full contact.

Overall, the repair was effective in restoring the patch corrosion-damaged tubular (C40-00-95) to its original undamaged strength (P^c_{max} of Specimen C40-100-0). For Specimen C40-00-95, the maximum compression load and maximum tension load were 208 kN and 221 kN, respectively. Specimen C40-100-0 had a maximum compression load and maximum tension load of 221 kN and 249 kN, respectively. For Specimen C40-00-95-RS, the maximum compression load and the maximum tension load were 242 kN and 254 kN, respectively. The maximum load carrying capacities of the repaired specimen being greater than those of Specimen C40-100-0 can be attributed to the additional resistance provided by the repair sleeve.

5.3.2 COMPOSITE SLEEVE – SPECIMEN C40-00-95-RC

Specimen C40-00-95-RC was a cyclically loaded, repaired tube. This specimen was inflicted with corrosion that reduced the wall thickness to 0% of its original thickness with a subtending angle of 94.6º. The corrosion profile can be seen in Figure 4.13. The repair is a grouted carbon fiber composite sleeve, as described in Section 4.5.1.1.

The specimen was loaded as per the loading history described in Section 4.8 with an initial loading rate of 0.025 mm/sec. The normalized axial load-axial displacement response ($P/P_y - \Delta/\Delta_y$) is shown in Figure 5.110. Figure 5.111 is a plot of the loading history with events of interest noted.

Also, as mentioned previously, since the local buckle could not effectively be measured, LVDT 3, which measures the local displacement of the corrosion patch, was removed. Likewise, Strain gage M1 could not be placed due to the hole in the corrosion

patch. The additional instrumentation consists of strain gages R1-R6. They are placed at mid-height of the specimen on the exterior of the repair sleeve. The changes in instrumentation are shown in Figure 4.36.

During Load Step +1, at approximately $+\Delta_y$, the specimen yielded at the ends of the tube near the end plates. Upon reaching $+5\Delta_y$ at the end of Load Step +1, the maximum axial tension load (P^t_{max}) of about 252 kN was noted. The loading rate was then changed to 0.05 mm/sec.

En rout to Load Step –1, the load peaked at roughly $-\Delta_y$. The maximum compression load (P^c_{max}) was about –241 kN. During this cycle, the yielding became slightly more pronounced throughout the length of the specimen. Of note is that the specimen displaced laterally to the East as a local buckle formed on the West face of the specimen at roughly one quarter of the height from the bottom (Figure 5.112). At the peak displacement of $-5\Delta_y$, the lateral displacement was negligible to the North and approximately 26 mm to the East. This phenomenon was attributed to the alignment of the end plates and the repair which prevented a local buckle in the corrosion patch and stiffened the tubular. The lateral deformations were caused by curvature in the corroded tubular outside of the repair region. During fabrication of the specimens, improper setting of the tube in the jig created a slight East-West eccentricity. Load Step +2 sufficiently straightened the specimen. In Load Step –2 the local buckle on the West face of the specimen continued to grow. The specimen incurred large lateral displacements to the East causing the lower end plate to significantly bend (Figure 5.113). Returning to $+\Delta_y$ in Load Step +2, the specimen straightened but now maintained a residual westward

lateral displacement of 3 mm.

During Load Step –3, the specimen continued to displace to the East while the local buckle on the western side grew. The lateral displacement to the North at no time became larger than about 2 mm (Figure 5.114). This again caused bending in the lower end plate. The eastward displacement became more severe and the test was terminated for fear of damaging the testing equipment.

Although local buckling occurred on the tubular outside of the repair region, the specimen maintained its compressive axial capacity. This phenomenon is shown in Figure 5.110. The maintenance in capacity in compression can be attributed to the direction of buckling. Since the specimen buckled to the West, the clevises began to bend and resist load. As the buckling became more severe, the end plates provided more resistance and carried more load, maintaining the maximum compression load, P^{c}_{max}, for the specimen.

Figure 5.115 compares the strains of strain gages M2 through M6 on the corroded tubular and strain gages R1 through R6 on the steel repair sleeve for one half the peak tensile load, 0.5 P^{t}_{max}, in Load Step +1. These gages are positioned as indicated on Figure 4.36. The strains are less than the yield strain and are identical. Similarly, Figure 5.116 compares the strains of strain gages M2 through M6 on the corroded tubular and strain gages R1 through R6 on the steel repair sleeve for the peak tensile load (P^{t}_{max}) in Load Step +1. Again, the strains are less than the yield strain and are identical. Lastly, Figure 5.117 compares the strains of strain gages M2 through M6 on the corroded tubular and strain gages R1 through R6 on the steel repair sleeve for the peak compression load

(P^c_{max}) in Load Step -1. As before, the strains are far below the yield strain and are identical. These plots demonstrate that the strains are equal for the repair and the damaged tubular and that the assumption for Equation (4.4) is valid.

Figures 5.118 and 5.119 are a plots of the strains at 1/4 of the height (strain gages B1 through B4), and 3/4 of the height (strain gages T1 through T4). The strains remain roughly uniform as the section yielded evenly in tension at P^t_{max}. The strains in Figures 5.118 and 5.119 are at roughly equal to the yield strain at P^t_{max}. Unlike the non-repaired test specimens, for the peak compression load (P^c_{max}) the strains at the quarter-points are well above the yield strain. Comparing this with the strain in the repair sleeve and at the mid-height on the tubular, it is clear that the repair has removed the strain concentration effects of the corrosion patch and forced the failure mode of the specimen outside of the repair region.

After testing, the grout was examined at the ends of the repair sleeve. On the top end of the sleeve, for approximately 146 mm around the circumference of the inner damaged tube, contact was lost between the grout and the specimen exactly in the same manner as the steel sleeve repair (Figure 5.109). On the bottom of the sleeve, the grout was still in full contact.

Overall the repair was effective in restoring the patch corrosion-damaged tubular (C40-00-95) to its original undamaged strength (P^c_{max} of Specimen C40-100-0). For Specimen C40-00-95, the maximum compression load and maximum tension load were 208 kN and 221 kN, respectively. Specimen C40-100-0 had a maximum compression load and maximum tension load of 221 kN and 249 kN, respectively. For Specimen C40-

00-95-RC, the maximum compression load and the maximum tension load were 241 kN and 252 kN, respectively. The maximum load carrying capacities of the repaired specimen being greater than those of Specimen C40-100-0, can be attributed to the additional resistance provided by the repair sleeve.

5.4 SUMMARY

Overall, the responses of the specimens were as anticipated. The figures showing strain at mid-height at one half the peak load and at the peak load demonstrated that patch corrosion lead to early local yielding and local buckling at loads below the yield loads (P_y) of the specimens causing a loss in capacity. Examining the load-displacement history for each specimen, patch corrosion appeared to reduce a tubular's maximum compression strength (P^c_{max}) and tension strength (P^t_{max}). Also shown in the load-displacement histories, patch corrosion appeared to cause load carrying capacity to drop more quickly and thus reduced the ductility, μ. Conversely, the repair was very successful in restoring a patch corroded tubular to its original undamaged capacity as shown in Table 5.1.

The peak axial tension load was 254 kN and 252 kN for Specimens C40-00-95-RS and C40-00-95-RS, respectively. The peak axial compression load was 242 kN and 241 kN for Specimens C40-00-95-RS and C40-00-95-RS, respectively. This indicates that the steel repair sleeve and the carbon fiber composite sleeve repairs are equally effective in repairing a patch-corrosion damaged steel tubular.

6 ANALYSIS OF RESULTS

An evaluation of the experimental results is presented in Chapter 6. The effects of the corrosion parameters upon specimen axial load capacity and energy dissipation capacity are evaluated by comparing specimen responses to each other. The effect that patch corrosion has on the moment-curvature and moment-axial load relationships is analyzed. The cyclic loading history is compared to the monotonic load history. The ability to predict the strength of a patch corroded tubular using the formulations presented in Chapters 2 and 3 is addressed. Lastly, the effectiveness of the repair sleeve design is evaluated.

6.1 EFFECT OF CORROSION ON AXIAL CAPACITY

6.1.1 EFFECT OF t_r / t

The normalized axial tension capacity (P^t_{max}/P_y) is plotted against the extent of the reduced thickness (t_r/t) in Figure 6.1 where P_y is the gross area multiplied by the yield stress of the specimen ($A_g \sigma_y$). The normalized compression capacity (P^c_{max}/P_o) is plotted against the extent of the reduced thickness (t_r/t) in Figure 6.2 where P_o is the compression axial load capacity of the undamaged specimen taken from SSRC Column Curve Type 1.

As shown in Figure 6.1, Specimen C40-100-0 had a P^t_{max}/P_y ratio of 0.945, Specimen C40-67-95 had a P^t_{max}/P_y ratio of 0.902, Specimen C40-33-95 had a P^t_{max}/P_y ratio of 0.897, and Specimen C40-00-95 had a P^t_{max}/P_y ratio of 0.840. The trend indicates a decrease in tensile axial capacity as the thickness is reduced.

As shown in Figure 6.2, Specimen C40-100-0 had a P^c_{max}/P_o ratio of 0.916,

Specimen C40-67-95 had a P^c_{max}/P_o ratio of 0.933, Specimen C40-33-95 had a P^c_{max}/P_o ratio of 0.826, Specimen M40-33-95 had a P^c_{max}/P_o ratio of 0.911, and Specimen C40-00-95 had a P^c_{max}/P_o ratio of 0.860. The trend indicates a decrease in axial capacity as the thickness is reduced. Specimen C40-67-95 has a higher capacity than the undamaged tubular (Specimen C40-100-0). This discrepancy arises from the condition of the welded end plate. The eccentricity of the endplate for this specimen caused North-West displacement as previously mentioned in Section 5.2.2.1, increasing the effect length of the specimen since buckling to the west creates a partial fixity end condition.

The reduced thickness has more of an effect when the damaged tubular is loaded in compression. Overall, a tubular with patch corrosion will decrease in axial capacity as the thickness in the corrosion patch decreases.

6.1.2 EFFECT OF θ

The normalized axial tension capacity (P^t_{max}/P_y) is plotted against the extent of the corrosion around the circumference (θ) in Figure 6.3. The normalized compression capacity (P^c_{max}/P_o) is plotted against the extent of the corrosion around the circumference (θ) in Figure 6.4.

As shown in Figure 6.3, Specimen C27-100-0 had a P^t_{max}/P_y ratio of 0.969, Specimen C27-33-58 had a P^t_{max}/P_y ratio of 0.989, Specimen C27-33-95 had a P^t_{max}/P_y ratio of 0.938, and Specimen C27-33-311 had a P^t_{max}/P_y ratio of 0.789. A decrease in axial capacity is seen as θ increases.

As shown in Figure 6.4, Specimen C27-100-0 had a P^c_{max}/P_o ratio of 1.027,

Specimen C27-33-58 had a P^c_{max}/P_o ratio of 0.977, Specimen C27-33-95 had a P^c_{max}/P_o ratio of 0.895, Specimen M27-33-95 had a P^c_{max}/P_o ratio of 0.911, and Specimen C27-33-311 had a P^c_{max}/P_o ratio of 0.530. It is apparent in Figure 6.4 that the compressive axial load capacity also decreases as θ increases.

The effect of θ is much greater when the damaged tubulars are loaded in compression. Overall, θ has an appreciable effect on the axial capacity of a patch corroded tubular.

The test results indicate that the effect of the subtending angle (θ) appears to be more significant than the effect of the reduced thickness (t_r/t). Hebor and Ricles (1994) found similar results. Figure 6.5 is a plot of the normalized compressive axial load capacity verses t_r/t for a tubular with a D/t of 34 and two different subtending angles (θ). The plot shows that the reduced thickness (t_r) becomes more important when the subtending angle (θ) is larger.

6.1.3 EFFECT OF D/t

Figure 6.6 shows the normalized tension load capacity (P^t_{max}/P_y) plotted against the D/t ratio. The tension axial load capacity does not appear to be effected by the D/t ratio.

Figure 6.7 shows the normalized axial compression load capacity (P^c_{max}/P_o) plotted against the D/t ratio. For the monotonically loaded specimens (Specimens M27-33-95 and M40-33-95), there is no change in capacity. For the cyclically loaded

specimens (Specimens C27-100-0, C40-100-0, C27-33-95, and C40-33-95) there is a small reduction in capacity when the D/t increased from 27 to 40. Specimen C27-100-0 has a P^c_{max}/P_o of 1.027 while Specimen C40-100-0 has a P^c_{max}/P_o of 0.916. Similarly, Specimen C27-33-95 has a P^c_{max}/P_o of 0.895 while Specimen C40-33-95 has a P^c_{max}/P_o of 0.826. The decrease in strength of the cyclically loaded specimens is due to the Baushinger effect, which causes a reduction in the material modulus and hence earlier local buckling to which the larger D/t of 40 is more sensitive. Overall, D/t appears to have a minimal influence on the peak axial capacity of a patch corroded tubular.

6.2 EFFECT OF CORROSION ON ENERGY DISSIPATION

The specimen total energy dissipation (E_D) and the energy dissipation per load cycle (E_{Di}) were evaluated. The energy dissipated in a load cycle is that which occurs over a full cycle of loading, beginning with zero load. This is illustrated in Figure 6.8, where shaded areas in the axial load-axial displacement response (P-Δ) represent the energy dissipated over the course of a load cycle. The energy dissipated per load cycle (E_{Di}) was determined from the measured specimen axial load-axial displacement response using Equation (6.1):

$$E_{Di} = \sum_{k=1}^{N-1} \left(\frac{P_{k+1} + P_k}{2} \right) \left(\Delta_{k+1} - \Delta_k \right) \tag{6.1}$$

When P_k, Δ_k, N are equal to the axial load at load point k during the loading cycle, corresponding axial displacement at load point k, and total number of load points during the load cycle, respectively. For each specimen the energy dissipated per load cycle was

summed to obtain the specimen total energy dissipated (E_D) where for a specimen

$$E_D = \sum_{i=1}^{M} E_{Di} \tag{6.2}$$

In Equation (6.2) M is the total number of load cycles during the testing of the specimen.

The dissipated energy (E_{Di}) was normalized by the energy dissipated by an elastic-perfectly plastic system (E_{EPi}) going through the same deformation as that imposed during the load cycle. This system was assumed to have the capacity P_i of the maximum tension and compression load, respectively, achieved in the two half cycles of the load cycle. E_{EPi} is illustrated in Figure 6.9 where

$$E_{EPi} = P_{mi}^{t}\left(-\Delta_{o,i} + \Delta_i^t - \frac{P_{mi}^t}{K}\right) + P_{mi}^{c}\left(\Delta_i^c - \Delta_i^t + \frac{P_{mi}^t}{K} - \frac{P_{mi}^c}{K}\right) \tag{6.3}$$

In Equation (6.3) P^t_{mi} and P^c_{mi} are the maximum tension and compression load, respectively, achieved during the load cycle. $\Delta_{o,i}$ is the initial deformation of the specimen. Δ^t_i and Δ^c_i are the maximum deformations imposed to the specimen under axial tension and compression load, respectively. K in Equation (6.3) is the initial stiffness in the axial load-axial deformation response relationship for the initial load step. The purpose of normalizing E_{Di} by E_{EPi} for each load cycle was to evaluate and compare the deterioration in energy dissipation capacity over the course of a loading cycle.

Figure 6.10 shows the total energy dissipated (E_D) by each specimen. All specimens were loaded for 10 load cycles, except for the monotonically loaded specimen (Specimens M27-33-95 and M40-33-95), the repaired specimens (C40-00-95-RS, C40-00-95-RC) which were loaded for 2 ½ cycles, Specimen C27-33-95 which was loaded for

5 cycles, and Specimen C27-33-311 which fractured during the first half cycle.

The amount of energy that was dissipated by each specimen depended on its ability to sustain axial load capacity (i.e., ductility). Patch corrosion had a noticeable effect on the ductility of each specimen. For the undamaged specimens, Specimen C27-100-0 never formed any cracks and Specimen C40-100-0 only formed surface cracks after Load Step +8. All other specimens formed through thickness cracks on or before Load Step +8. This cracking limited the tension load carrying capacity of the specimens in tension, where as local buckling reduced the load carrying capacity in compression. For a given D/t ratio the specimens having the larger total energy dissipation (E_D) in Figure 6.10 are those with a smaller amount of corrosion. For a given D/t ratio, E_D is seen to be smaller for specimens with a larger angle θ (specimens of a D/t ratio of 27) or a larger reduction in wall thickness in the corrosion patch (specimens with a D/t ratio of 40).

6.2.1 EFFECT OF t_r/t

The energy dissipated per cycle (E_{Di}) and the normalized energy dissipated (E_{Di}/E_{EPi}) per load cycle are plotted in Figures 6.11 (a) and (b), respectively, for the cyclically loaded non-repaired specimens with a D/t ratio of 40. The effect of reducing the thickness of the corrosion patch on the energy dissipation capacity of a tubular is apparent in Figure 6.11 (D/t and θ are held constant for specimens with a D/t ratio of 40). Undamaged Specimen C40-100-0 is included in Figure 6.11 as a basis of comparison.

As shown in Figure 6.11 (a), with the exception of Specimen C40-67-95 (as explained below), the energy dissipated per cycle decreases at the thickness is reduced.

This is a result of the corrosion patch forming a local buckle leading to a strength deterioration of the specimen. The large increase in E_{Di} in Cycle 5 is caused by a greater amount of axial displacement during the load step (see Figure 4.37). Similarly, the large drop in E_D in Cycle 9 is due to the small displacement range (see Figure 4.37). The discrepancy in the data from Specimen C40-67-95 arises from the condition of the welded end plate. The eccentricity of the endplate for this specimen caused North-West displacement, as previously mentioned, decreasing the effective length of the specimen as buckling to the west creates a partial fixity end condition. Thus, a higher load could be sustained per cycle increasing the energy that was dissipated.

Figure 6.11 (b) shows that for the initial cycles, the normalized dissipated energy capacity (E_{Di}/E_{EPi}) decreases more in specimens where the remaining tube wall thickness is smaller. The same exception noted above applies to Specimen C40-67-95. The decrease in normalized dissipated energy is a result of the corrosion patch forming a local buckle leading to strength deterioration of the specimen. As the loading continues, the effect of the reduced thickness lessens as the effects of cyclic buckling (section ovalization, loss of section from cracking, etc.) begin to dominate. The deterioration in energy dissipation capacity stabilizes at about 0.1 E_{EPi} to 0.2 E_{EPi} .

6.2.2 EFFECT OF θ

The energy dissipated per cycle (E_{Di}) and the normalized energy dissipated (E_{Di}/E_{EPi}) per load cycle are plotted in Figures 6.12 (a) and (b), respectively, for the cyclically loaded non-repaired specimens with a D/t ratio of 27. The effect of increasing the subtending angle (θ) of the corrosion patch for a given t_r on the energy dissipation

capacity of a tubular is apparent in Figure 6.12 (D/t and t_r are held constant for specimens with a D/t ratio of 27). Undamaged Specimen C27-100-0 is included in Figure 6.12 as a basis of comparison.

As shown in Figure 6.12 (a), the energy dissipated per cycle (E_{Di}) decreases as the subtending angle (θ) is increased. This is a result of the corrosion patch forming a local buckle leading to a deterioration in strength of the specimen. Testing of Specimen C27-33-311 was terminated at the end of Cycle 1 due to a fracture of the net section in the corrosion patch during the first load step. Testing of Specimen C27-33-95 was terminated at the end of Cycle 5 due to massive loss of section from fracture.

Figure 6.12 (b) shows that for the initial cycles, specimens with a larger θ have a greater reduction in energy dissipation capacity. This is a result of the corrosion patch forming a local buckle inducing global buckling of the specimen. The larger the subtending angle, the quicker the energy dissipating capacity of the specimen decreases in subsequent cycles. Eventually the effect of θ lessens as the effects of cyclic buckling (section ovalization, loss of section from cracking, etc.) begin to dominate, and the deterioration in energy dissipation capacity (E_{Di}) stabilizes at about 0.1 E_{EPi} to 0.2 E_{EPi}.

6.2.3 EFFECT OF D/t

The energy dissipated per cycle (E_{Di}) and the normalized energy dissipated (E_{Di}/E_{EPi}) per load cycle are plotted in Figures 6.13 (a) and (b), respectively, comparing the effect of D/t for undamaged specimens (Specimens C27-100-0, and C40-100-0), and two damaged specimens (Specimens C27-33-95 and C40-33-95).

Figure 6.13 (a) shows that the specimens with a smaller D/t ratio dissipate more

energy per cycle (E_{Di}). This is expected since the specimens with smaller D/t are able to carry more load over a given displacement. Examining both Figures 6.13 (a) and (b), for the undamaged tubulars, the specimen with a smaller D/t ratio better sustained its energy dissipation capacity. For the damaged tubulars, however, the loss in energy dissipation capacity per load cycle is similar up through cycle 3, after which Specimen C27-33-95 began to develop a large crack in the corrosion patch from low cycle fatigue. This led to greater deterioration in the strength of Specimen C27-33-95.

6.3 MOMENT-CURVATURE RESPONSE AND MOMENT-AXIAL LOAD INTERACTION

The moment-curvature (M-ϕ) response of the section at mid-height, were the corrosion damage was present, were determined for the specimens. The moment M was determined at the geometric centroid of the corroded cross-section,

$$M = P\,(e + \delta_o + \delta) \tag{6.4}$$

where P, e, δ_o, and δ are equal to the applied axial load eccentricity in the cross section (see Figure 1.1), lateral displacement associated with the initial out-of-straightness at mid height, and lateral displacement at mid-height under the applied axial load, respectively. A positive moment imposes compressive stress on the corrosion patch, as shown in Figure 6.14. The curvature (ϕ) is calculated as the difference between the measured rotations by inclinometers 2 and 3 ($\theta_2 - \theta_3$) divided by the distance between them (ℓ = 254 mm) where,

$$\phi = \frac{\theta_2 - \theta_3}{\ell} \tag{6.5}$$

Positive curvature is defined as a counter-clockwise relative rotation $\Delta\theta = \theta_2 - \theta_3$ (see Figure 6.14). Figures 6.15 through 6.26 show the moment-curvature response for the specimens.

Figures 6.19 through 6.21 indicate that as the remaining wall thickness in the corrosion patch decreases the moment carrying capacity is reduced. This is expected since the axial load carrying capacity decreases as well. Figures 6.22 through 6.24 show the effects of varying θ on the moment-curvature response. The effect of the subtending angle (θ) of patch corrosion is similar to the effect of the reduced wall thickness. The moment carrying capacity of the tubular reduces as θ increases. Figures 6.25 and 6.26 show the effect of the repair. The lack of any significant moment or curvature is due to the additional stiffness provided by the repair sleeves. For all non-repaired specimens the maximum moment achieved by the specimens with corrosion damage was less than that achieved by their corresponding non-damaged specimens (Specimens C10-100-0 and C27-100-0). For all non-repaired specimens the maximum positive moment was approximately 0.9 times the maximum negative moment. Positive moment coincided with axial compressive load. The reason for this latter phenomenon is due to non-proportional loading with respect to moment and axial force when reversing the axial load from tension to compression, and the effects of moment-axial load interaction. Moment-axial load interaction will be discussed below. Under tension axial load the amount of lateral displacement δ is smaller compared to when a compressive axial load is applied.

Consequently for the same magnitude of axial force, a smaller moment develops when the applied axial load is tension due to the "P-delta" effect.

The moment-axial load (M-P) interaction surface was determined by assuming that the entire cross section has yielded, and applying the following equations:

$$P = \int \sigma_y dA \tag{6.6}$$

$$M = \int \sigma_y z dA \tag{6.7}$$

where P is axial load, M is moment, σ_y is the measured yield stress of the material, dA is an infinitesimal unit of the corroded cross sectional area, and z is the distance of dA from the centroid of the damaged section in the North-South direction. Moving the location of the neutral axis across the depth of the section and evaluating Equations (6.6) and (6.7) at each location enables the M-P interaction surface to be determined. For the calculation of the M-P interaction surface the positive sign convention had the axial load in tension and the moment as shown in Figure 6.14.

Figures 6.27 through 6.38 are plots of the axial load (P) divided by the yield load of the corroded cross section ($P_{y,sect} = \sigma_y A_{reduced}$) against the moment (M) divided by the flexural plastic capacity of the corroded cross section ($M_{p,sect}$). In these figures the experimental force path for the first half cycle in tension and compression are noted. In almost every figure, initially the experimental loading path reaches the M-P surface and appears to stay on, or near, the surface when yielding. As local buckling develops in the corrosion patch of the specimen in successive cycles, the M-P surface is not reached while P is in compression. When P is in tension, the M-P surface is reached by the

experimental loading patch until the section fractures. Since the experimental load path reaches the M-P surface, it is concluded that the initial capacity of the specimens is controlled by the plastic strength of the corroded section, and that stability (local and global buckling) and fracture control the deterioration in strength, ductility and energy dissipation capacity.

6.4 CYCLIC vs. MONOTONIC LOAD HISTORY

Specimens C40-33-95 and C27-33-95 were loaded using the cyclic load history described in Section 4.8 while their counterparts M40-33-95 and M27-33-95 were loaded monotonically in compression. Figures 6.39 and 6.40 compare the normalized axial load-displacement response for Specimens M27-33-95 and C27-33-95, and Specimens M40-33-95 and C40-33-95, respectively. The moment-curvature (M-ϕ) response for the corroded section at mid height is compared in Figures 6.21 and 6.23. The comparisons shown in Figures 6.39 and 6.40, as well as in Figures 6.21 and 6.23, indicate that the response of the specimens with monotonic load histories provides an envelope for the response to compression of the cyclically loaded specimens. The maximum compressive axial load (P^c_{max}) was slightly less in the cyclically loaded specimens compared to the monotonically loaded specimens. The slight drop for the cyclic response can be attributed to the Baushinger effect.

6.5 STRENGTH PREDICTION

Table 6.1 presents the predicted compressive loads for non-repaired specimens

using several different methods that were presented in Chapters 2 and 3. Columns three through eight in Table 6.1 contain the ratio of predicted axial compression load capacity ($P^c_{u,pred}$) to specimen measured experimental compressive load capacity(P^c_{max}) for each specimen listed in column 1. Column three contains the values as predicted by the section analysis presented by Hebor and Ricles (1994). The forth column contains the predicted strength ($P^c_{u,pred}$) based on the adaptation of the SSRC Column Curve Type 1 combined with a corroded section analysis where:

$$P^c_{u,pred} = \left(\frac{P_{u,2.10}}{P_y} \right) \cdot P_{u,3.4} \tag{6.8}$$

In Equation (6.8) $P_{u,2.10}$, $P_{u,3.4}$, and P_y are equal to P_u as calculated by Equation (2.10), P_u as calculated by Equation (3.4), and the yield load, respectively. Equation (6.8) is based on modifying the short column strength (i.e., the yield load, P_y) to that of a corroded short column, with the result being multiplied by the right hand side of Equation (2.10) to account for long column effects. In Table 6.1 the fifth column is the API Code prediction (Equation (2.7) or (2.8)) with the recommendation made by Ostapenko of using an equivalent reduced wall thickness (t_a) (Equation 3.3). Column six in Table 6.1 contains the predictions from the DnV code (Equation (2.9)), using the equivalent reduced thickness (t_a) (Equation (3.3)). The seventh column in Table 6.1 is the load capacity predicted by the regression equation presented by Hebor and Ricles (1994) (Equation (3.2)). The eighth column in Table 6.1 contains the predicted values by Equation (3.1) developed by Ostapenko et al. (1996).

The comparison of $P^c_{u,pred}$ with P^c_{max} for the specimens is also shown in the scatter

diagram presented in Figure 6.41. As shown in Table 6.1 and Figure 6.41, the most reliable and conservative prediction method is the adaptation of SSRC column curve and the section analysis model by Hebor and Ricles (1994). The average $P^c_{u,pred} / P^c_{max}$ ratio was 0.974, with a maximum error of 9.2% and coefficient variation (COV) of 5.8%. The prediction methods using Ostapenko et al.'s Equation (3.1) also provides a conservative average prediction ($P^c_{u,pred} / P^c_{max}$ has an average value of 0.899), however the maximum error is 24.7% and COV is 15.0%. The section analysis without considering second order effects resulted in an average of 1.056 for $P^c_{u,pred} / P^c_{max}$, with a maximum error of 16.3% and a COV of 4.9%. The prediction using the regression equation by Hebor and Ricles (1994) provided the closest average result to the experimental results, but is slightly conservative with an average ratio of 1.014 for $P^c_{u,pred} / P^c_{max}$, and has a maximum error of 16.3%, and COV of 7.2%. The remaining two predictions (API and DnV codes using t_a) had average values for $P^c_{u,pred} / P^c_{max}$ of 1.098 and 1.097 using the API and DnV codes, respectively, with maximum errors of 23.5% and 23.2% and COVs of 5.6%.

Since the method of using SSRC Column Curve 1 combined with a section analysis appears to give the most accurate results for predicting compressive axial load capacity, this method is recommended for use in strength prediction.

The predicted tensile axial loads for non-repaired specimens are presented in Table 6.2. The specimens are listed in column one of Table 6.2. Column two in Table 6.2 contains the measured peak experimental tension load (P^t_{max}). Columns three and four in Table 6.2 contain the ratio of predicted axial tension load capacity to specimen measured experimental tension load ($P^t_{u,pred}/P^t_{max}$) for each specimen listed in column 1.

Column three contains the results where Equation (6.6) was used to determine $P^t_{u,pred}$, where the area of integration is the corroded cross section and the effects of the eccentricity are not considered. Column four contains the results using the section analysis presented by Hebor and Ricles (1994) for tension axial load to determine $P^t_{u,pred}$, thereby considering the effects of eccentricity caused by the corroded section. A scatter diagram comparing $P^t_{u,pred}$ to P^t_{max} is presented in Figure 6.42. Table 6.2 and Figure 6.42 show that using Equation (6.6) provides slightly better results, with an average of 0.997, a maximum error of 6.8% and a COV of 4.3% for the ratio of $P^t_{u,pred}/P^t_{max}$. Specimen C27-33-311 has been excluded from the statistics. This specimen was subjected to a severe stress concentration that resulted in fracture of the net section. Both the prediction method presented by Hebor and Ricles (1994) and Equation (6.6) are based on yielding of the section, and are therefore deem inappropriate to apply to Specimen C27-33-311.

6.6 EVALUATION OF REPAIR

Both the steel and composite sleeves produced the same results. Both sleeve designs managed to nullify the effects of the patch-corrosion, eliminating any local stress concentrations caused by the patch corrosion and restoring the axial load capacity of the tubular. Table 6.3 presents the maximum experimental axial compression loads (P^c_{max}) for undamaged tubular Specimen C40-100-0, corroded tubular Specimen C40-00-95, and both repaired tubulars, (Specimens C40-00-95-RS and C40-00-95-RC). P^c_{max} for Specimens C40-100-0 and C40-00-95 are 221.6 kN and 208.1 kN, respectively. P^c_{max} for Specimens C40-00-95-RS and C40-00-95-RC are 241.9 kN and 241.2 kN, respectively.

The repaired specimens thereby have an increase in compressive axial load capacity compared to the undamaged specimen. This is due to the presence of the sleeve, creating a non-prismatic member that has a larger global buckling load. The value predicted by SSCR Column Curve Type 1 for Specimen C40-100-0 is 245 kN (where $\sigma_y = 206$ MPa). Thus, the damaged specimen has essentially been restored to its original design strength.

Figure 6.43 is a plot of the cyclic energy dissipated (E_{Di}) and normalized energy dissipated (E_{Di}/E_{Pi}) per load cycle for the undamaged Specimen C40-100-0, the through-thickness patch corroded Specimen C40-00-95 and the two repaired specimens, C40-00-95-RS and C40-00-95-RC. The displacement history for Specimens C40-00-95-RS and C40-00-95-RC consisted of two and a half load cycles. Because Figure 6.43 is on a cycle by cycle basis (instead of half cycle), only the results through the second load cycle for the repaired specimens are compared with the other specimens. Figure 6.43 indicates that the energy dissipating capacity of the damaged tubular with the repair sleeve applied is much greater than that of the undamaged specimen.

Consequently, both designs show potential for use in the repair of corroded tubular members.

7 SUMMARY AND CONCLUSIONS

7.1 SUMMARY

This study was concerned with patch type corrosion and its effect on tubular members under inelastic cyclic axial loading. The testing consisted of two monotonically loaded corroded specimens, two cyclically loaded non-corroded control specimens, six cyclically loaded corroded, non-repaired specimens, and two cyclically loaded corroded, repaired specimens. The corroded tubulars had a single patch of corrosion. The test matrix included two diameter-to-thickness ratios (27 and 40). The thickness of the corrosion patch varied from 100% to 0% of the original wall thickness of the tubular. The subtending angle of the corrosion patch varied from 0º to 331º.

Results from the tests provided a direct comparison between a non-corroded bracing member, a corroded non-repaired bracing member, and a repaired corroded bracing member. They also provided insight into the use of composite materials as a solution to repairing steel in a highly corrosive environment.

7.2 CONCLUSIONS

Based on the results presented in this study, the following conclusions are presented:

1) High stress concentrations develop in the corrosion patch leading to a reduction in strength.
2) The reduced wall thickness and subtending angle of a corrosion patch are the dominating factors for strength reduction. Smaller diameter-to-thickness ratios

provide more ductility for no corrosion damage. This phenomenon is not as noticeable for patch corroded tubulars.

3) The ability of a tubular bracing member to dissipate energy is greatly reduced by patch corrosion.
4) Monotonic loading histories of patch corroded tubular bracing members provide an envelope for the compressive load carrying capacity of a cyclically loaded tubular with similar damage.
5) The moment-axial load interaction capacity surface provides a strength envelope for the experimental load path of the specimens.
6) Previous work with patch corroded tubular members provided methods for the prediction of their residual strength for monotonic load histories. Of these methods, using the SSRC Column Curve Type 1 in conjunction with the section analysis presented by Hebor and Ricles (1994) provided the best conservative strength prediction for the single patch corroded tubulars subjected to cyclic axial load.
7) Epoxy grout is effective in transferring forces to the repair sleeve and eliminating the high stress concentrations around the patch corrosion.
8) A sleeve repair is an effective tool in restoring a corroded tube to its full, undamaged axial capacity.
9) Massive corrosion damage (Specimen C27-33-311) will lead to fracture of the section in tension without much ductility, and should be a priority to repair.

8 FUTURE WORK

Items recommended for future work include:

(1) Broadening the test database to refine the appropriate strength prediction equations and investigate the effects of multiple corrosion patches.

(2) Analyze the effects of hydrostatic loads to better represent in situ conditions for fixed offshore platform tubular bracing members.

(3) Examine appropriate methods for field installation of a repair sleeve.

(4) Refine the sleeve design equations involving required length, strength and stiffness.

9. REFERENCES

1. American Petroleum Institute, (1989) "Recommended Practice for Planning, Design, and Constructing Fixed Offshore Platforms, API, RP-2A", Washington, D.C.,

2. American Institute of Steel Construction, (1994) "Manual of Steel Construction: Load and Resistance Factor Design," 2nd Ed.

3. ASTM, (1998) "Test Methods and Definitions for Mechanical Testing of Steel Products" A370-97a

4. ASTM, (1998) "Test Method for Tensile Strength of Chemical-Resistant Mortar, Grouts, and Monolithic Surfacings" C307-94

5. ASTM, (1998) "Test Method for Compressive Strength of Chemical-Resistant Mortar, Grouts, Monolithic Surfacings, and Polymer Concretes" C579 B-96

6. ASTM, (1998) "Test Method for Compressive Creep of Chemical-Resistant Polymer Machinery Grouts" C1181-96

7. ASTM, (1998) "Test Methods for Tension Testing of Metallic Material" E8-98

8. Chen, W.F., and Lui, E.M., (1987) *Structural Stability: Theory and Implementation,* Elsevier Science Publishing Co., Inc., New York.

9. Cole, M.W., Marucci, T.F., and Taft, D.G., (1987) "MODU Marine Safety: Structural Inspection and Readiness Surveys," *Journal of Petroleum Technology,* Society of Petroleum Engineers, Vol. 39, p. 1437

10. Det Norske Veritas (DnV), (1974) "Rules for the Design, Construction, and Inspection of Fixed Offshore Structures", Oslo.

11. Dinno, D.K., (1996) "The Effect of Corrosion on the Stability of Plate Girders Using Finite Elements," Thesis, University of Toronto, Toronto, Ontario.

12. Dunn, F.P., (1983) "Offshore Platform Inspection," Proceedings of the International Symposium on the Role of Design, Inspection, and redundancy in Marine Structural Reliability, Marine Board, National Research Council, National Academic Press.

13. Galambos, T.V., (1998) *Guide to stability Design Criteria for metal Structures, 5th Ed.,* John Wiley, New York.

14. Galambos, T.V., (1978) *Structural Members and Frames,* Prentice Hall, New Jersey.

15. Hebor, M.F., and Ricles, J.M., (1994) "Residual Strength and Repair of Corroded Marine Tubulars," ATLSS Report No. 94-10, Lehigh University, Bethlehem, PA.

16. Krahl, N.W., and Karsan, D.I., (1985) "Axial Strength of Grouted Pile-to-Sleeve Connections." *Journal of the Structural Division,* American Society of Civil Engineers, Vol. III, No. 4, p. 889.

17. Kulicki, J.M., Prucz, J.M., Sorgenfrei, D.F., Mertz, D.R., Young, W.T., (1990) "Guidelines for Evaluating Corrosion Effects in Existing Steel Bridges," National Cooperative Highway Research Program Report #333, National Research Council, Washington, D.C.

18. Liu, Z., and Goel, S.C., (1988) "Cyclic Load behavior of Concrete-Filled Tubular Braces." *Journal of Structural Engineering,* American Society of Civil Engineers, Vol. 114, No. 7, pp. 1488-1506.

19. McClelland, B., and Reifel, M.D., (1986) *Planning and Design of Fixed Offshore Platforms,* VNR, New York.

20. McCormac, J.C., (1992) *Structural Steel Design (ASD Method) 4th Ed.,* Harper Collins.

21. Ostapenko, A., Berger, T.W., Chambers, S.L., and Hebor, M.F., (1996) "Corrosion Damage- Effect on Strength Tubular Columns with Patch Corrosion," ATLSS Report No. 96-01, Lehigh University, Bethlehem, PA.

22. Ostapenko, A., Wood, B.A., Chowdhury, A., Hebor, M.F., (1993) "Residual Strength of Damaged and Deteriorated Tubular Members in Offshore Structures", ATLSS Report No. 93-03, Lehigh University, Bethlehem, PA.

23. Puskar, F., (1999) Private Correspondence, November.

24. Pons, H.F., (1997) "Dynamic Behavior of Tubular Bracing Members with Single Plate Concentric Connections." Thesis: University of Toronto, Toronto, Ontario.

25. Ricles, J.M., Bruin, W.M., and Sooi, T.K., (1997) "Repair of Dented Tubular Columns- Whole Column Approach," ATLSS Report No. 97-13, Lehigh University, Bethlehem, PA.

26. Ricles, J.M., Bruin, W.M., Sooi, T.K., Hebor, M.F., and Scheonwetter, P.C., (1995) "Residual Strength Assessment and Repair of Damaged Offshore Tubulars," Presented at the 27th Annual OTC in Houston, Texas, OTC 7807.

27. Ricles, J.M. and M. Hebor, (1994) "Residual Strength and Epoxy-Based Grout Repair of Corroded Offshore Tubulars," Paper S-19, *Proceedings - BOSS '94*, Cambridge, MA.

28. Ricles, J.M., Hebor, M.F., and D. Paterson, (1999) "Structural Testing of Corroded Offshore Tubular Members," *Proceedings – International Workshop on Corrosion Control for Marine Structures and Pipelines*, U.S. Minerals Management Service Sponsored Workshop, Galveston, TX.

29. Salmon, C.G., and Johnson, J.E., (1996) *Steel Structures: Design and Behavior, 4th Ed.,* Harper Collins College Publishers, New York.

30. "SSPC – SP6," SSPC: The Society for Protective Coatings, *www.sspc.org*

31. "Testing and Evaluation of Damaged Jacket Braces," (1990) PMB Engineering, Inc., Texas A&M University, *Final Report*, PMB Engineering, Inc., Houston.

Specimen	D/t	tr / t	t (mm)	Θ (degrees)	Description of Specimen
C40-100-0	40	1.00	3	0	Undamaged, cyclic loading
C27-100-0	27	1.00	5	0	Undamaged, cyclic loading
M40-33-95	40	0.33	3	95	Damaged, unrepaired, monotonic loading
M27-33-95	27	0.33	3	95	Damaged, unrepaired, monotonic loading
C40-67-95	40	0.67	3	95	Damaged, unrepaired, cyclic loading
C40-33-95	40	0.33	3	95	Damaged, unrepaired, cyclic loading
C40-00-95	40	0.00	3	95	Damaged, unrepaired, cyclic loading
C27-33-58	27	0.33	5	58	Damaged, unrepaired, cyclic loading
C27-33-95	27	0.33	5	95	Damaged, unrepaired, cyclic loading
C27-33-311	27	0.33	5	311	Damaged, unrepaired, cyclic loading
C40-00-95RS	40	0.00	3	95	Damaged, repaired w/ steel, cyclic loading
C40-00-95RC	40	0.00	3	95	Damaged, repaired w/ composite, cyclic loading

Table 4.1 Test Matrix

Specimen	Specimen Dimensions (Measured)									Corrosion Dimensions (Measured)				
	D (mm)	t (mm)	L (pin to pin) (mm)	D/t	r (mm)	L/r	L/D	P_y (kN)	Δ_y (mm)	t_r (mm)	t_r / t	c (mm)	Θ radians	Θ degrees
C40-100-0	126.9	3.2	2464	39.6	43.2	57.1	19.4	262.8	2.5	3.2	1.00	0	0.00	0.0
C27-100-0	127.2	4.9	2464	25.9	43.7	56.4	19.4	495.4	3.3	4.9	1.00	0	0.00	0.0
M40-33-95	127.1	3.2	2464	39.7	43.2	57.1	19.4	263.2	2.5	1.1	0.34	103	1.66	95.1
M27-33-95	127.0	4.9	2464	25.9	43.7	56.4	19.4	494.6	3.3	1.6	0.33	101	1.65	94.7
C40-67-95	127.1	3.2	2464	39.7	43.2	57.1	19.4	263.2	2.5	2.1	0.67	102	1.65	94.3
C40-33-95	127.1	3.2	2464	39.7	43.2	57.1	19.4	263.2	2.5	1.1	0.34	103	1.66	95.0
C40-00-95	127.1	3.2	2464	39.7	43.2	57.1	19.4	263.2	2.5	0.0	0.00	103	1.66	94.9
C27-33-58	127.1	4.9	2464	26.0	43.7	56.4	19.4	495.0	3.3	1.7	0.35	62	1.01	57.9
C27-33-95	127.1	4.9	2464	26.0	43.7	56.4	19.4	495.0	3.3	1.6	0.33	101	1.66	95.0
C27-33-311	127.1	4.9	2464	26.1	43.7	56.4	19.4	495.0	3.3	1.7	0.35	331	5.42	310.4
C40-00-95RS	127.0	3.2	2464	40.0	43.2	57.1	19.4	263.0	2.5	0.0	0.00	102	1.65	94.6
C40-00-95RC	127.1	3.2	2464	39.8	43.2	57.1	19.4	263.2	2.5	0.0	0.00	102	1.65	94.6

Note: $\Delta_y = \sigma_y L / E$
$P_y = \sigma_y A$

Table 4.2 Measured Dimensions of Test Specimens

Specimen	OOS δ_{max} / L	OOR $(D_{max} - D_{ave}) / D_{ave}$
C40-100-0	0.0004	0.0047
C27-100-0	0.0012	0.0026
M40-33-95	0.0004	0.0008
M27-33-95	0.0008	0.0014
C40-67-95	0.0010	0.0013
C40-33-95	0.0008	0.0026
C40-0-95	0.0004	0.0008
C27-33-58	0.0016	0.0010
C27-33-95	0.0016	0.0011
C27-33-311	0.0026	0.0024
C40-00-95-RS	0.0012	0.0006
C40-00-95-RC	0.0014	0.0015

Table 4.3 Maximum Measured Out-of-Straightness and Out-of-Roundness

D/t	E (GPa)	σ_y (MPa)	σ_u (MPa)	E_{sh} (GPa)	ε_{sh} (mm/mm)	ε_u (mm/mm)	ε_{max} (mm/mm)
27	195	253	403	3.24	0.033	0.250	0.417
40	192	206	338	2.44	0.034	0.342	0.512
Steel Sleeve	197	607	669	3.33	0.009	0.073	0.159

Table 4.4 Summary of Steel Properties from Tension Coupon Tests

Specimen	P^{c}_{max} (Compresion) Monotonic (kN)	P^{c}_{max} (Compresion) Cyclic (kN)	P^{t}_{max} (Tension) Cyclic (kN)
C40-100-0	-	221.6	248.5
C27-100-0	-	462.1	480.0
M40-33-95	220.3	-	-
M27-33-95	409.6	-	-
C40-67-95	-	225.7	237.0
C40-33-95	-	199.9	235.9
C40-00-95	-	208.1	220.6
C27-33-58	-	439.6	489.9
C27-33-95	-	402.7	464.8
C27-33-311	-	238.5	390.7
C40-00-95RS	-	241.9	254.0
C40-00-95RC	-	241.2	251.7

Table 5.1 Maximum Experimental Values for Axial Load

Specimen	P^c_{max} (kN)	$P^c_{u,pred} / P^c_{max}$ Section Analysis (kN)	$P^c_{u,pred} / P^c_{max}$ SSRC Curve Type 1 (kN)	$P^c_{u,pred} / P^c_{max}$ API (kN)	$P^c_{u,pred} / P^c_{max}$ DnV (kN)	$P^c_{u,pred} / P^c_{max}$ Hebor (kN)	$P^c_{u,pred} / P^c_{max}$ Ostapenko (kN)
C40-100-0	221.6	1.163	1.092	1.163	1.163	1.163	1.163
C27-100-0	462.1	1.068	0.973	1.068	1.068	1.068	1.068
M40-33-95	220.3	0.989	0.928	1.027	1.025	0.954	0.764
M27-33-95	409.6	1.016	0.927	1.056	1.055	0.998	0.783
C40-67-95	225.7	1.072	1.006	1.079	1.077	1.054	0.948
C40-33-95	199.9	1.127	1.057	1.156	1.154	1.052	0.901
C40-00-95	208.1	1.005	0.913	1.065	1.063	0.882	0.753
C27-33-58	439.6	1.046	0.953	1.054	1.053	1.000	0.914
C27-33-95	402.7	1.038	0.947	1.076	1.075	1.015	0.801
C27-33-311	238.5	1.034	0.943	1.235	1.232	0.957	0.352
Average:		1.056	0.974	1.098	1.097	1.014	0.899
Maximum error:		16.3%	9.2%	23.5%	23.2%	16.3%	24.7%
COV:		4.9%	5.8%	5.6%	5.6%	7.2%	15.0%

* Specimen C27-33-311 is out of range for Ostapenko Equation and therefore has been excluded from the statistical analysis

Table 6.1 Comparison of Specimen Predicted Compressive Load Capacity ($P^c_{u,pred}$) with Experimental Axial Compression Load Capacity (P^c_{max})

Specimen	P^t_{max} (kN)	$P^t_{u,pred}$ / P^t_{max} Section Analysis without eccentricity (kN)	$P^t_{u,pred}$ / P^t_{max} Section Analysis with eccentricity (kN)
C40-100-0	248.5	1.058	1.058
C27-100-0	480.0	1.032	1.032
M40-33-95	-	-	-
M27-33-95	-	-	-
C40-67-95	237.0	1.027	1.021
C40-33-95	235.9	0.980	0.955
C40-00-95	220.6	1.004	0.948
C27-33-58	489.9	0.946	0.938
C27-33-95	464.8	0.932	0.900
C27-33-311	390.7	0.754	0.631
	Average:	0.997	0.979
	Maximum error:	6.8%	10.0%
	COV:	4.3%	5.5%

Note: Average, Error and COV Excludes Specimen C27-33-311

Table 6.2 Comparison of Specimen Predicted Tensile Load Capacity ($P^t_{u,pred}$) with Experimental Axial Tensile Load Capacity (P^t_{max})

Specimen	P^c_{max} (kN)	P^t_{max} (kN)
C40-100-0	221.6	248.5
C40-00-95	208.1	220.6
C40-00-95RS	241.9	254.0
C40-00-95RC	241.2	251.7

Table 6.3 Peak Axial Loads for Non-damaged (C40-100-0), Patch Corroded Non-repaired (C40-00-95), and Patch Corroded Repaired (C40-00-95-RS, C40-00-95-RC) Specimens

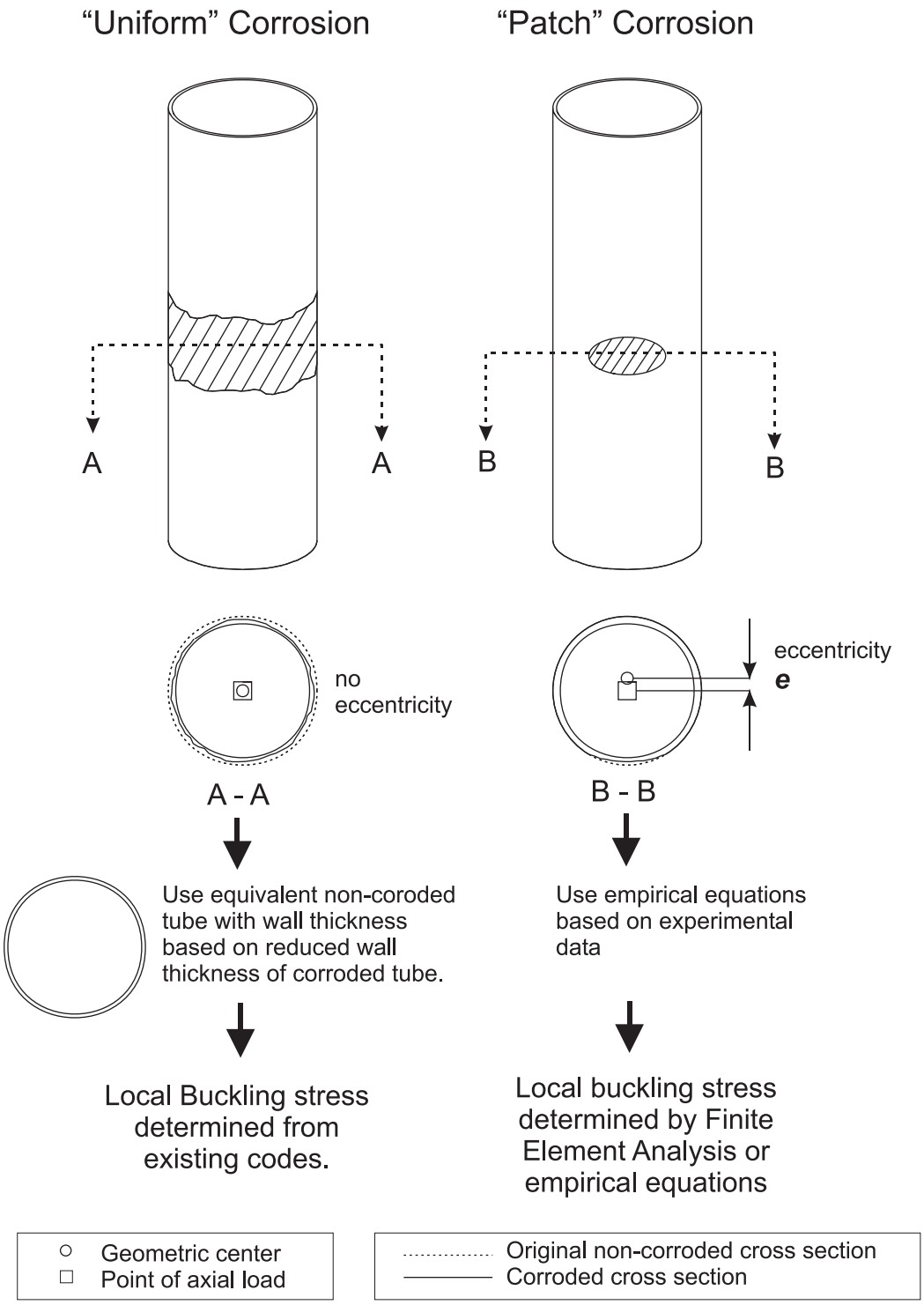

Figure 1.1 Comparison of Uniform Corrosion and Patch Corrosion (Hebor and Ricles 1994)

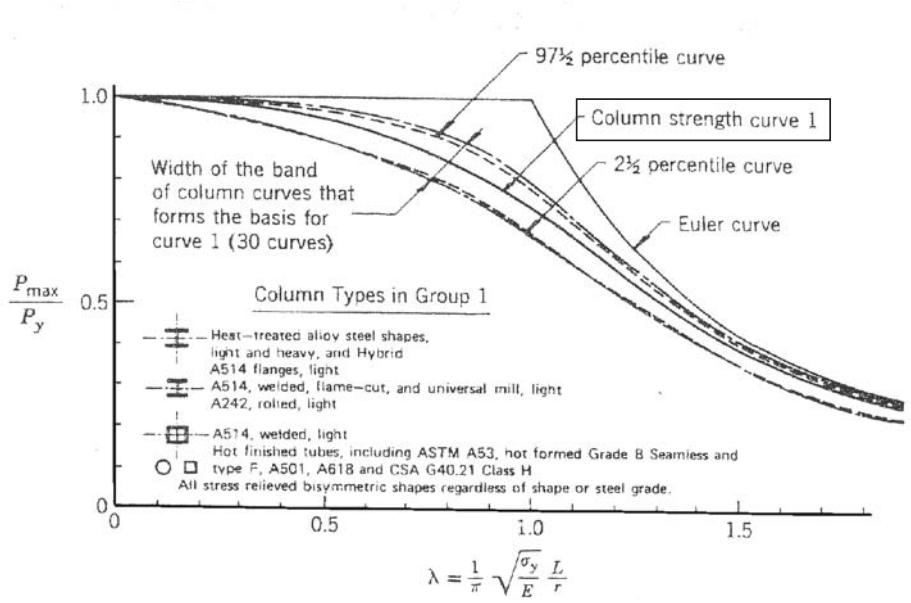

Figure 2.1 SSRC Column Curve Type 1 (Galambos 1998)

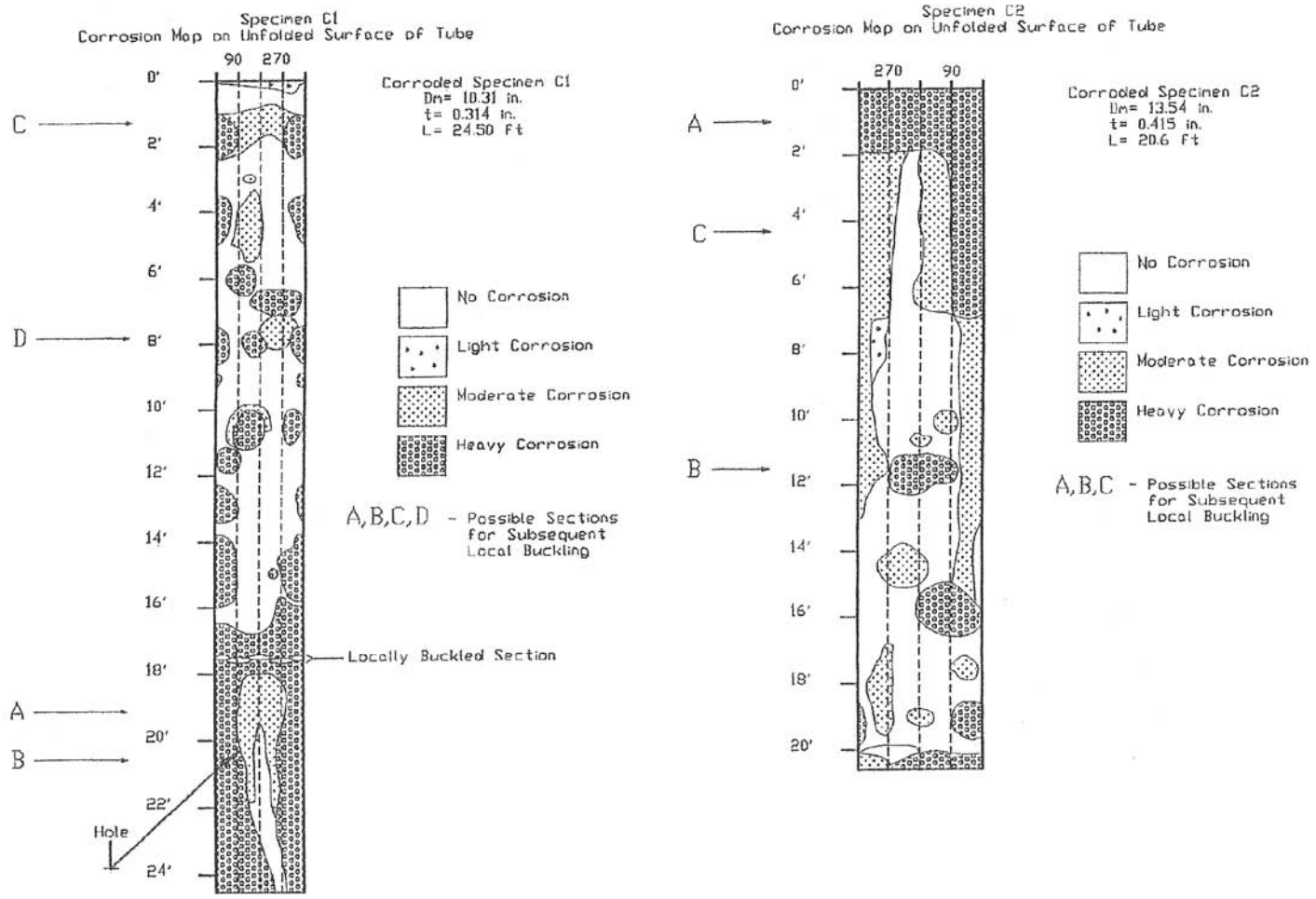

Figure 3.1 Corrosion of Two Tubular Braces from Gulf of Mexico Offshore Platforms (Ostapenko et. al. 1993)

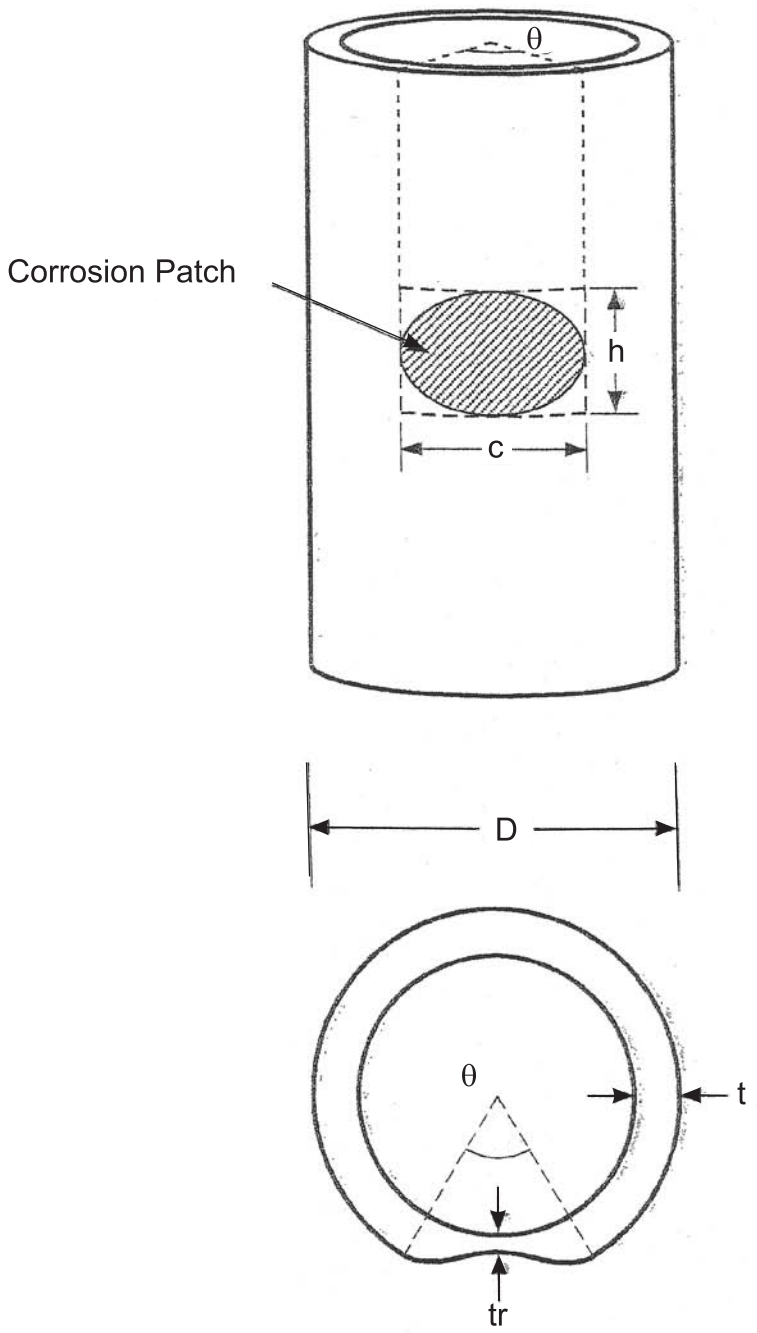

Figure 3.2 Patch Corrosion Parameters (Hebor and Ricles 1994)

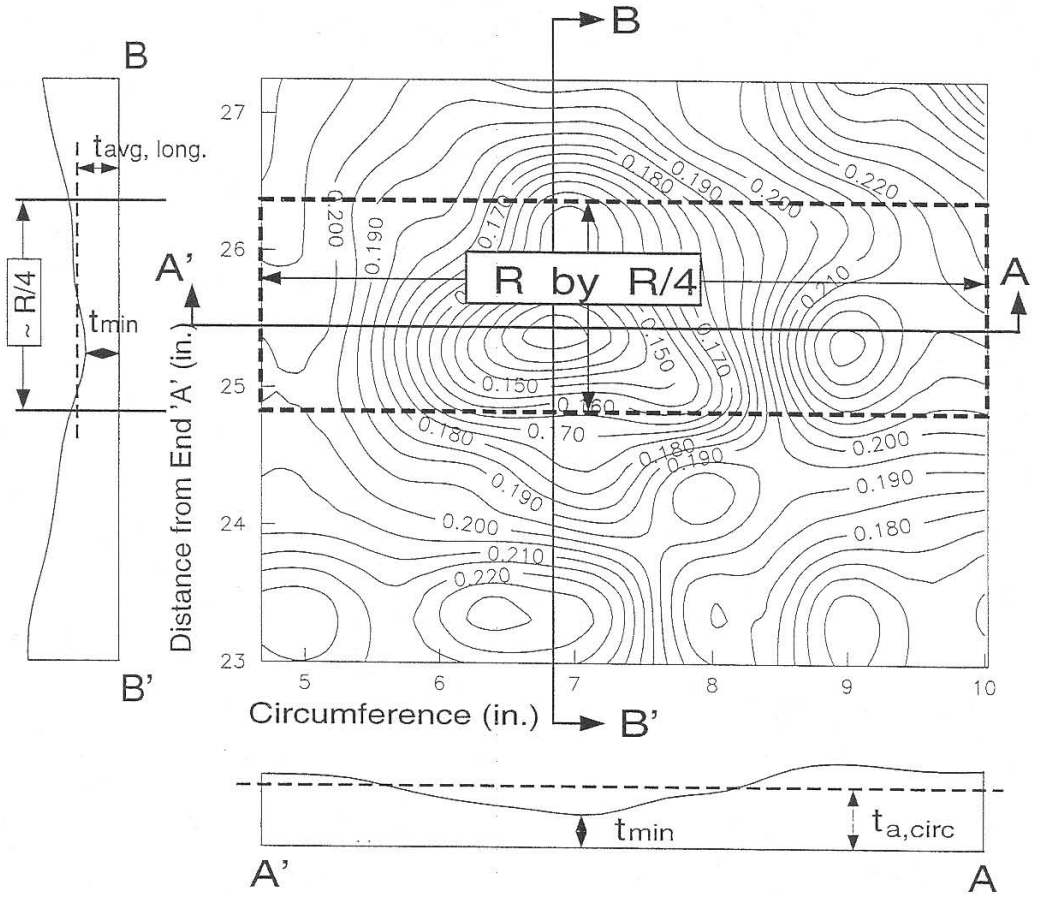

$$t_a = \left(\frac{t_{a,long}}{t_{min}} \right) t_{a,circ}$$

Figure 3.3 Definition of Average Thickness (Ostapenko et. al. 1996)

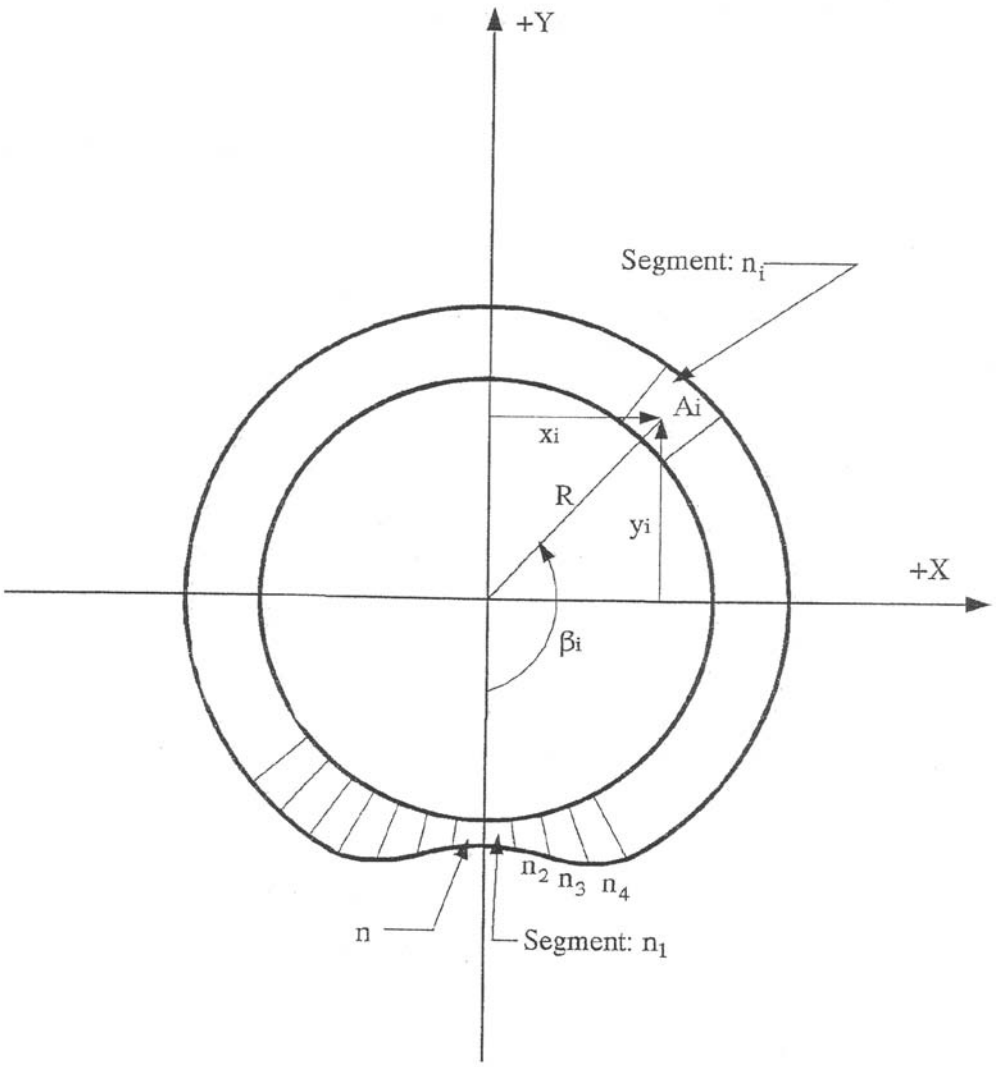

Figure 3.4 Cross Section Discritization (Hebor and Ricles 1994)

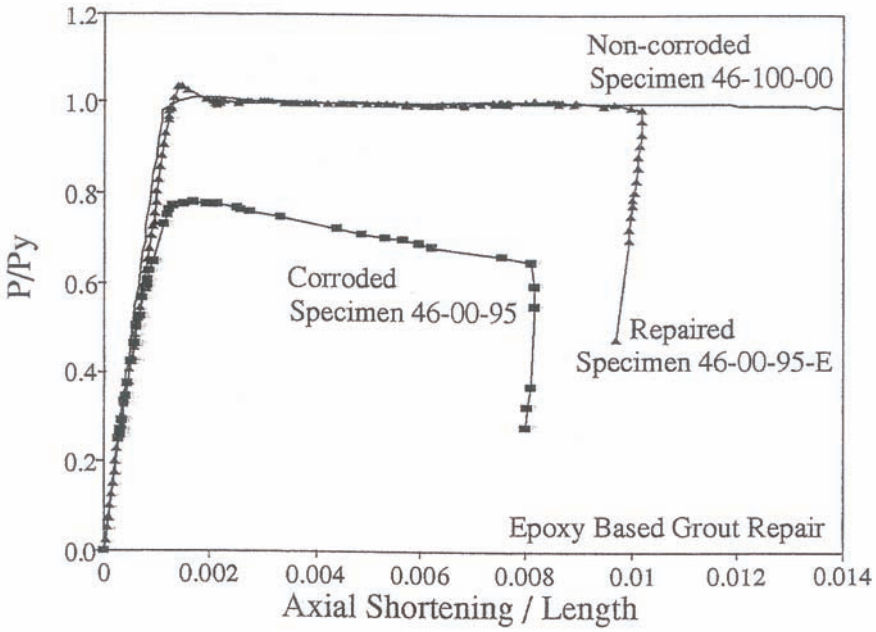

Figure 3.5 Effect of Sleeve Repair (Hebor and Ricles 1994)

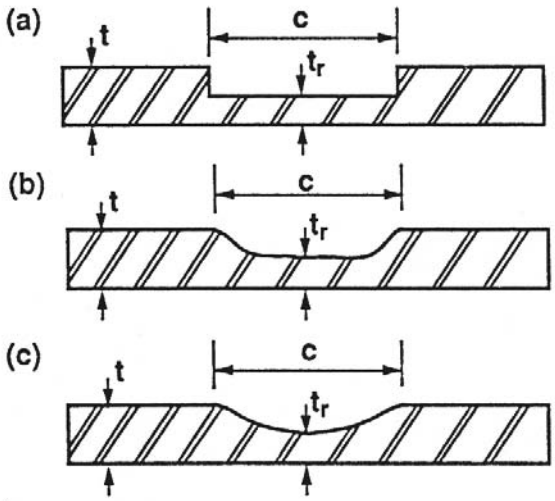

Figure 3.6 (a) "Step," (b) Experimental, and (c) "Cosine" Thickness Profiles for Patch Corrosion (Ricles et. al. 1995)

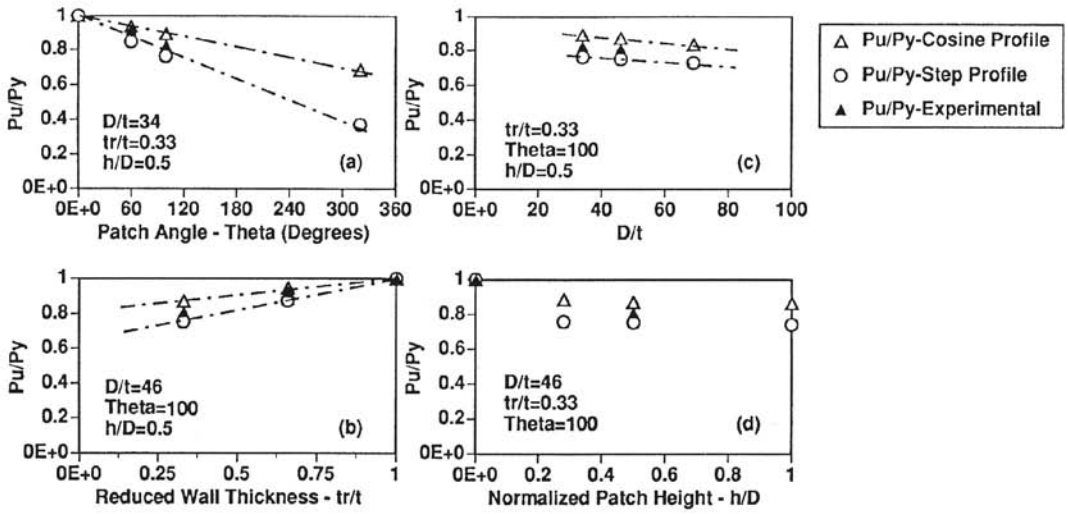

Figure 3.7 Variation of Axial Capacity as a Function of Corrosion Parameters and Profile (Ricles et. al. 1995)

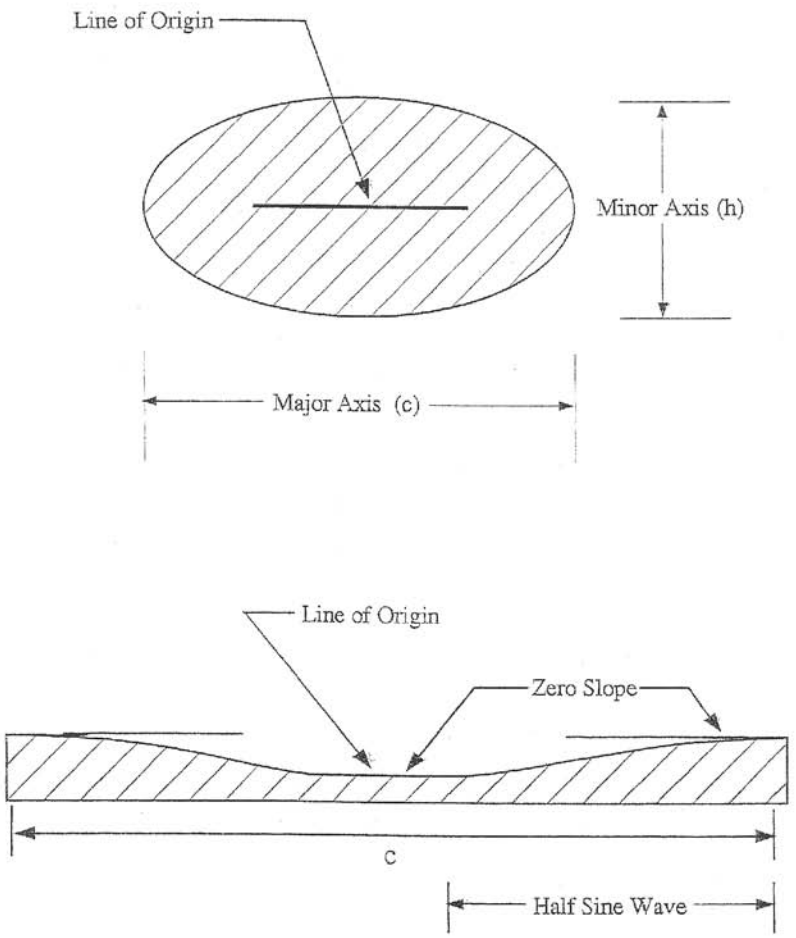

Figure 4.1 Cosine Profile Model (Hebor and Ricles 1994)

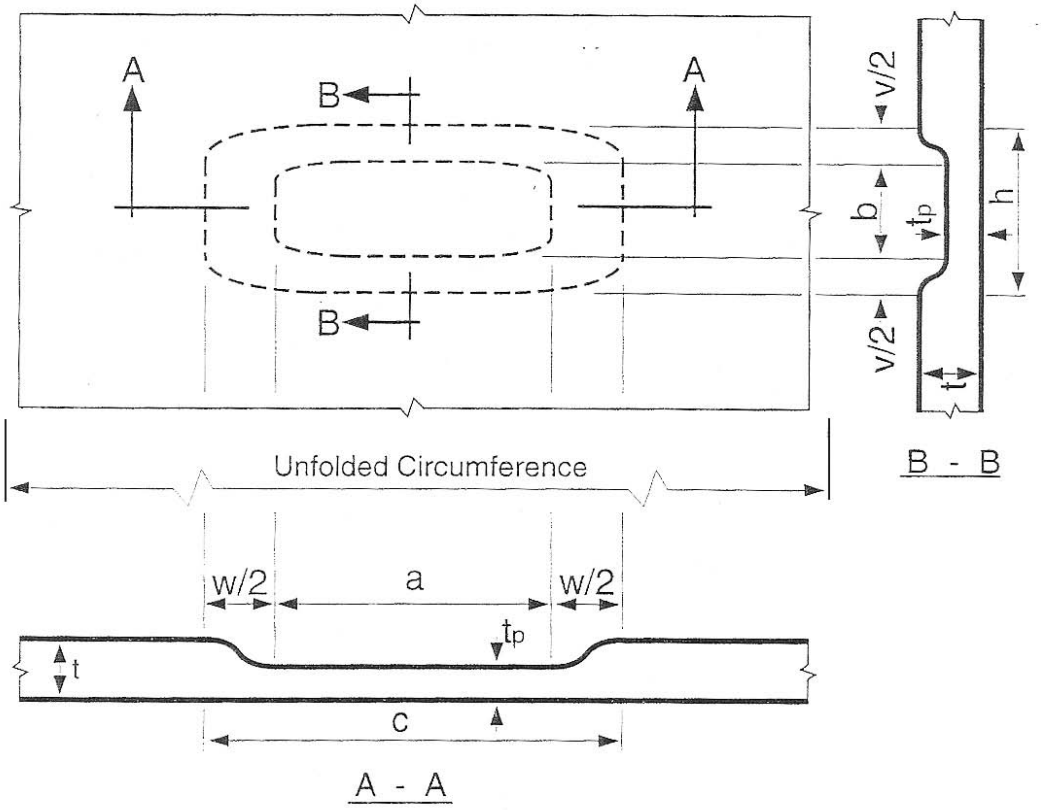

w/2 = circumferential width of cosine variation of wall thickness
v/2 = longitudinal width of cosine variation of wall thickness
c = circumferential width of the main corrosion patch
h = Longitudinal length of corrosion patch
t_p = wall thickness in constant thickness region of corrosion patch

Figure 4.2 Layout of Corrosion Patch (Ostapenko et. al. 1996)

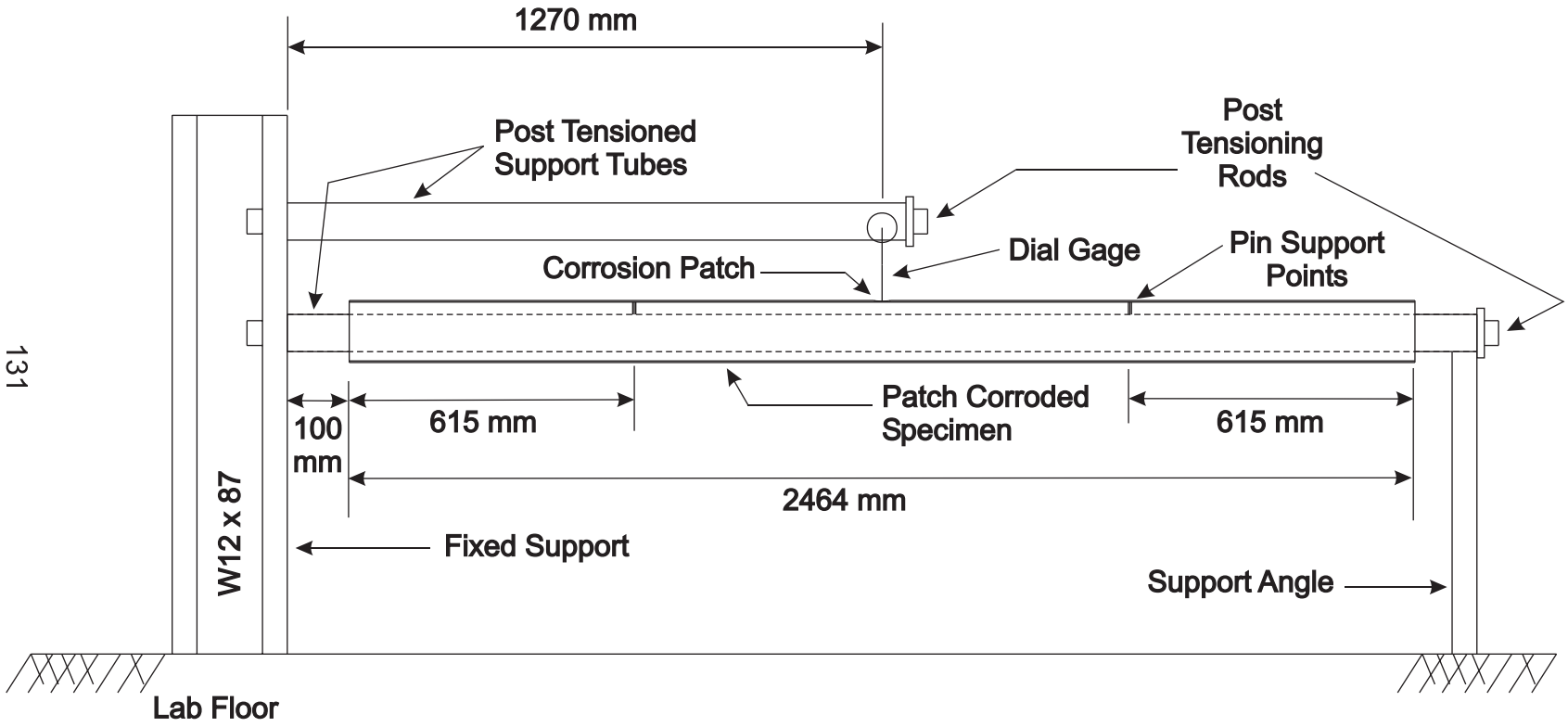

Figure 4.3 Setup for Measuring Corrosion Patch

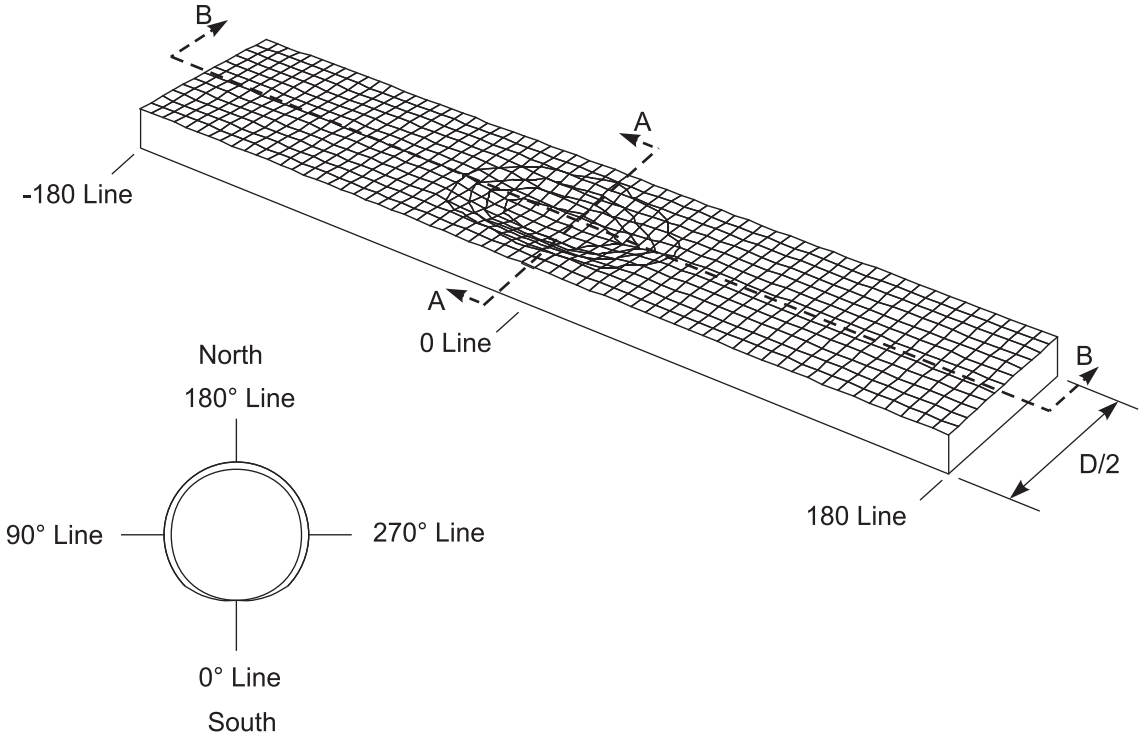

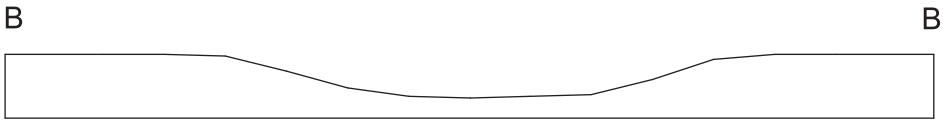

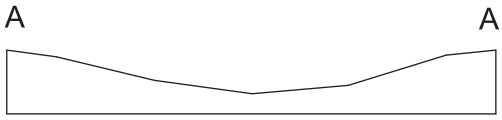

D/t = 40
t_i/t = 0.34
θ = 95.1°

Figure 4.4 Surface Plots and Cross sectional Thickness Profiles from Measured Corrosion Dimensions, Specimen M40-33-95

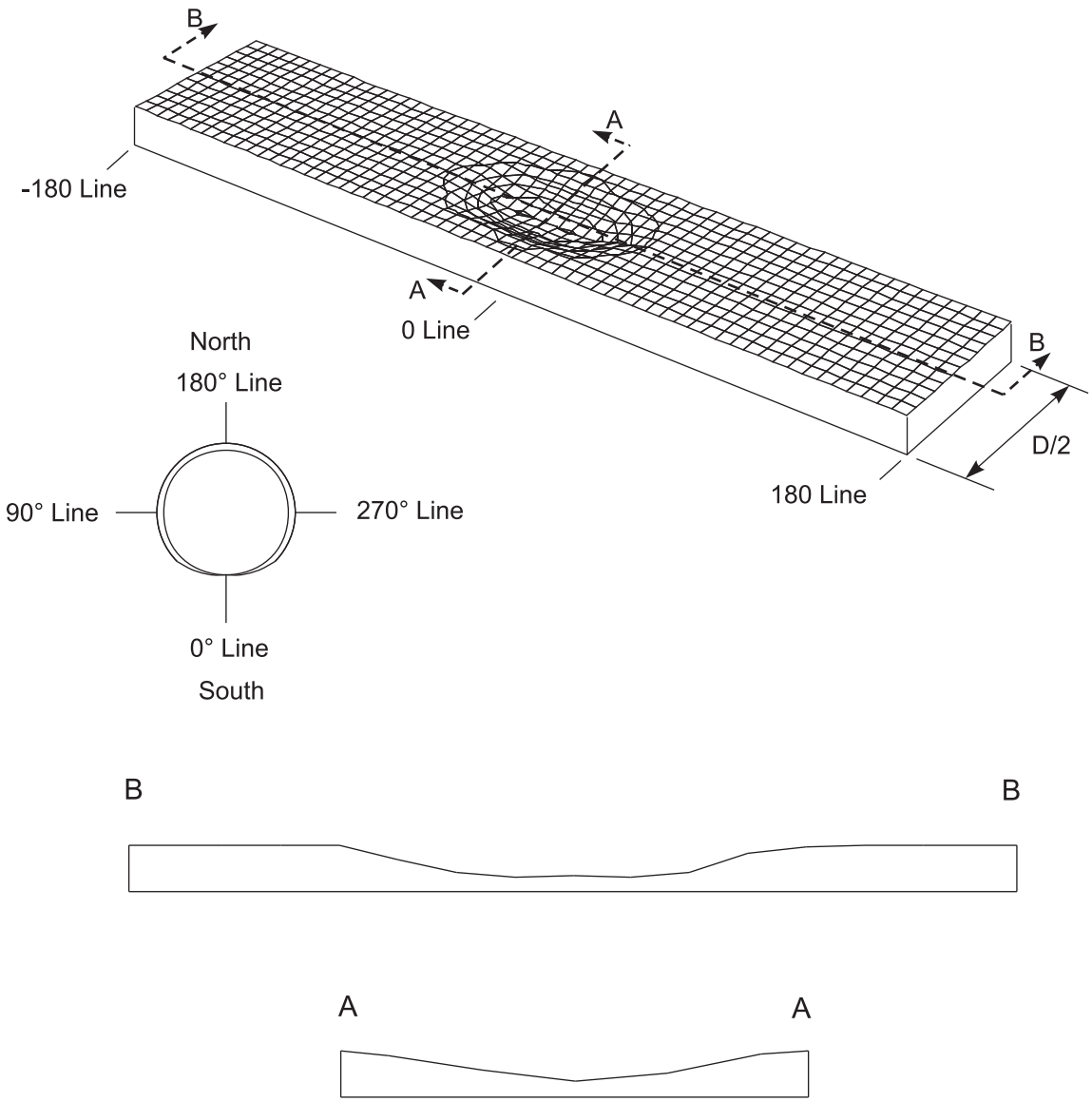

D/t = 27
t_i/t = 0.33
θ = 94.7°

Figure 4.5 Surface Plots and Cross sectional Thickness Profiles from Measured Corrosion Dimensions, Specimen M27-33-95

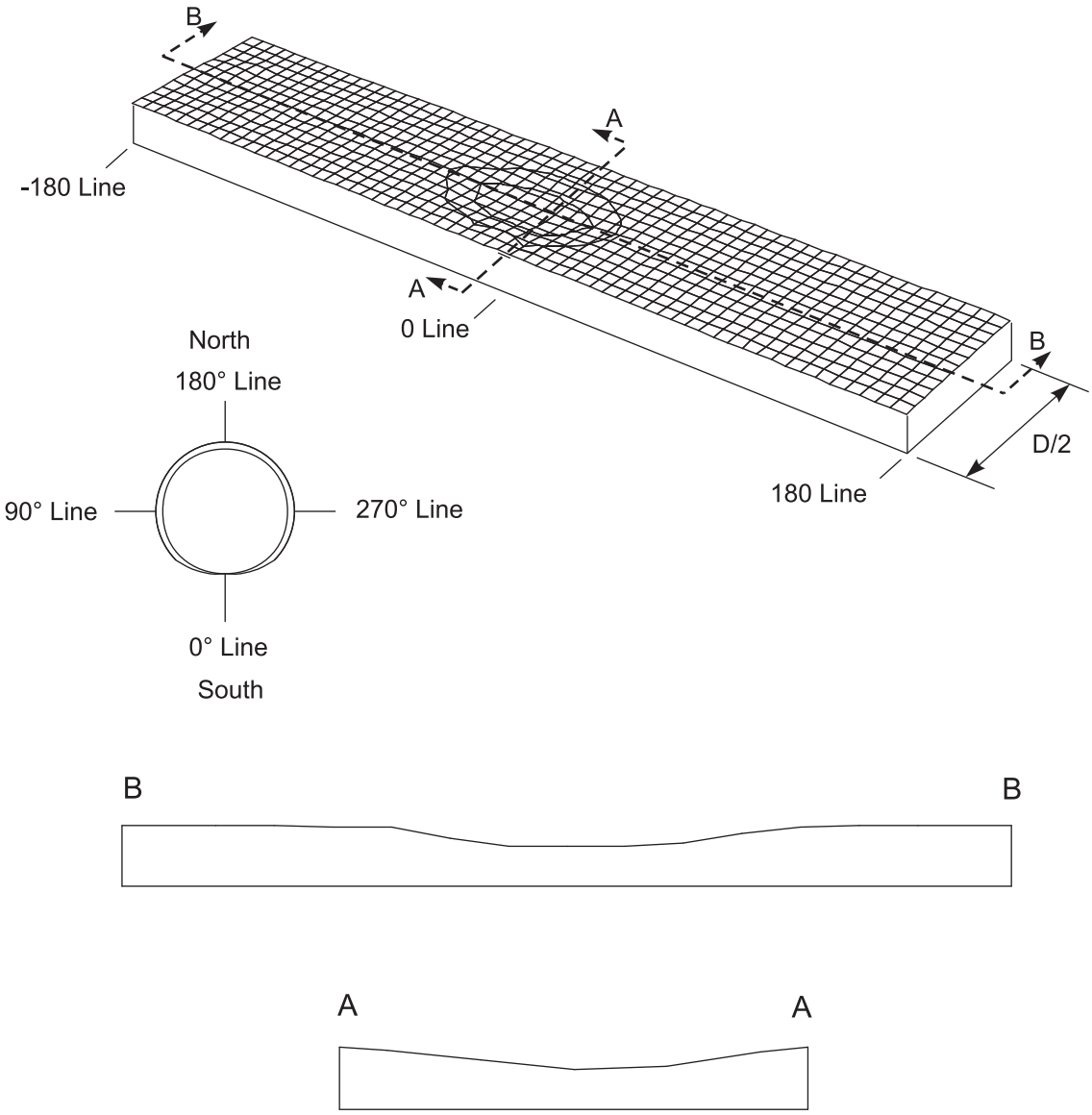

D/t = 40
t_i/t = 0.67
θ = 94.3°

Figure 4.6 Surface Plots and Cross sectional Thickness Profiles from Measured Corrosion Dimensions, Specimen C40-67-95

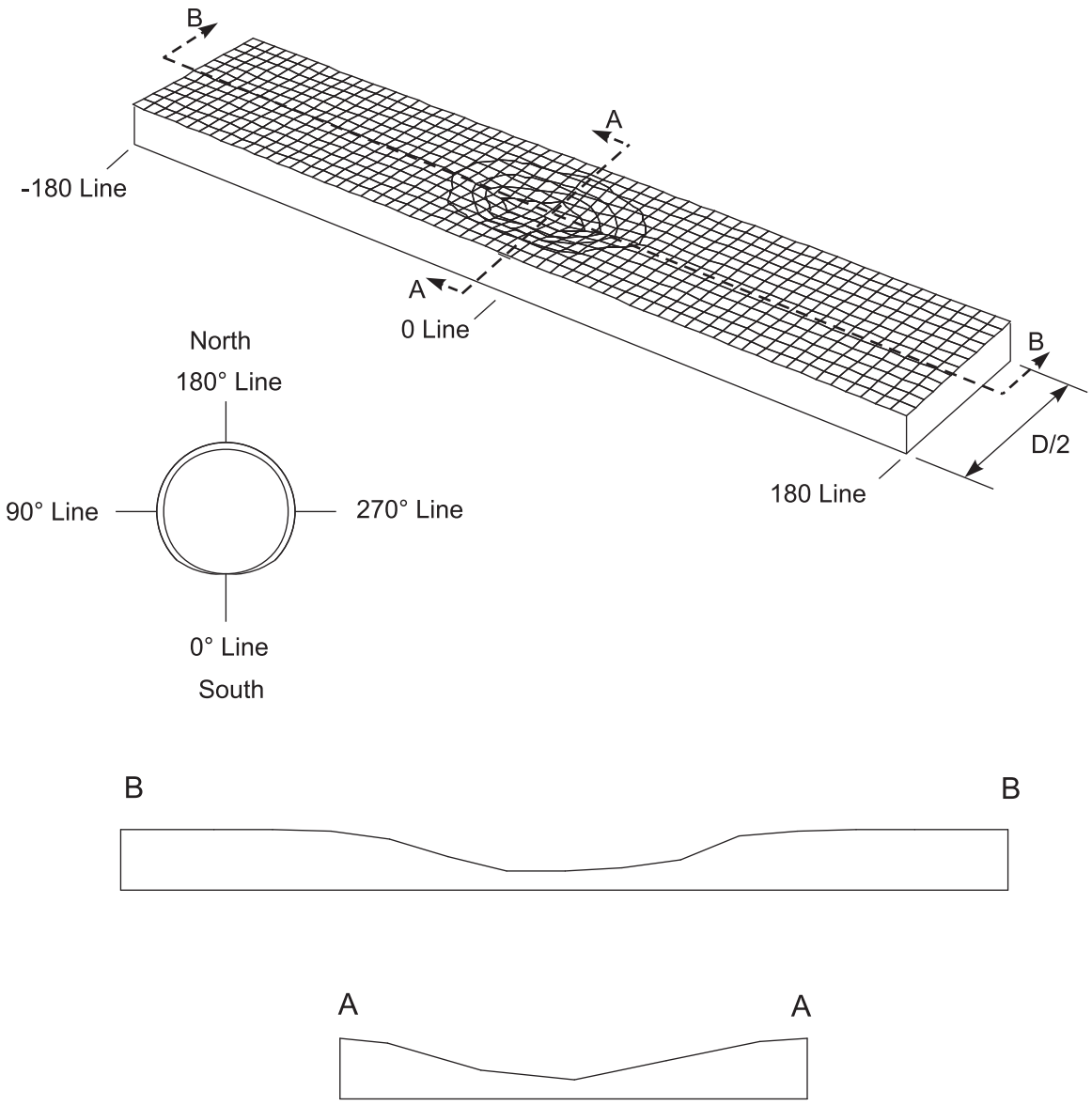

D/t = 40
t_i/t = 0.34
θ = 95.0°

Figure 4.7 Surface Plots and Cross sectional Thickness Profiles from Measured Corrosion Dimensions, Specimen C40-33-95

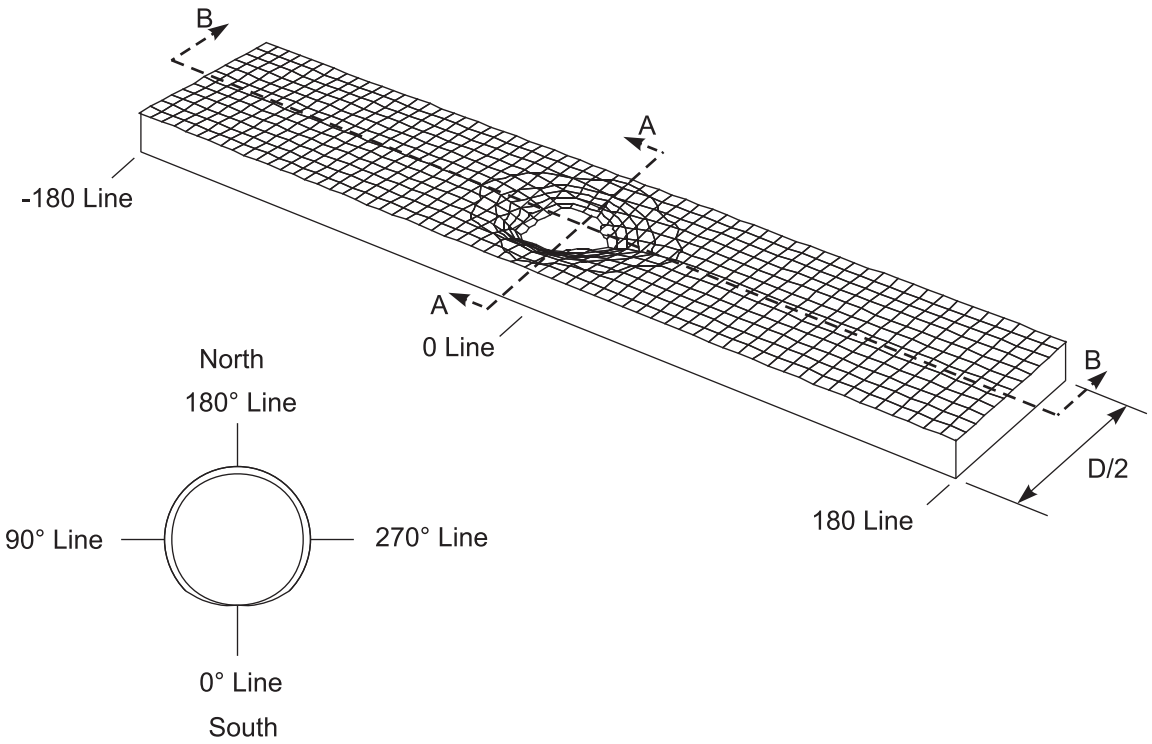

D/t = 40
t_r/t = 0.00
θ = 94.9°

Figure 4.8 Surface Plots and Cross sectional Thickness Profiles from Measured Corrosion Dimensions, Specimen C40-00-95

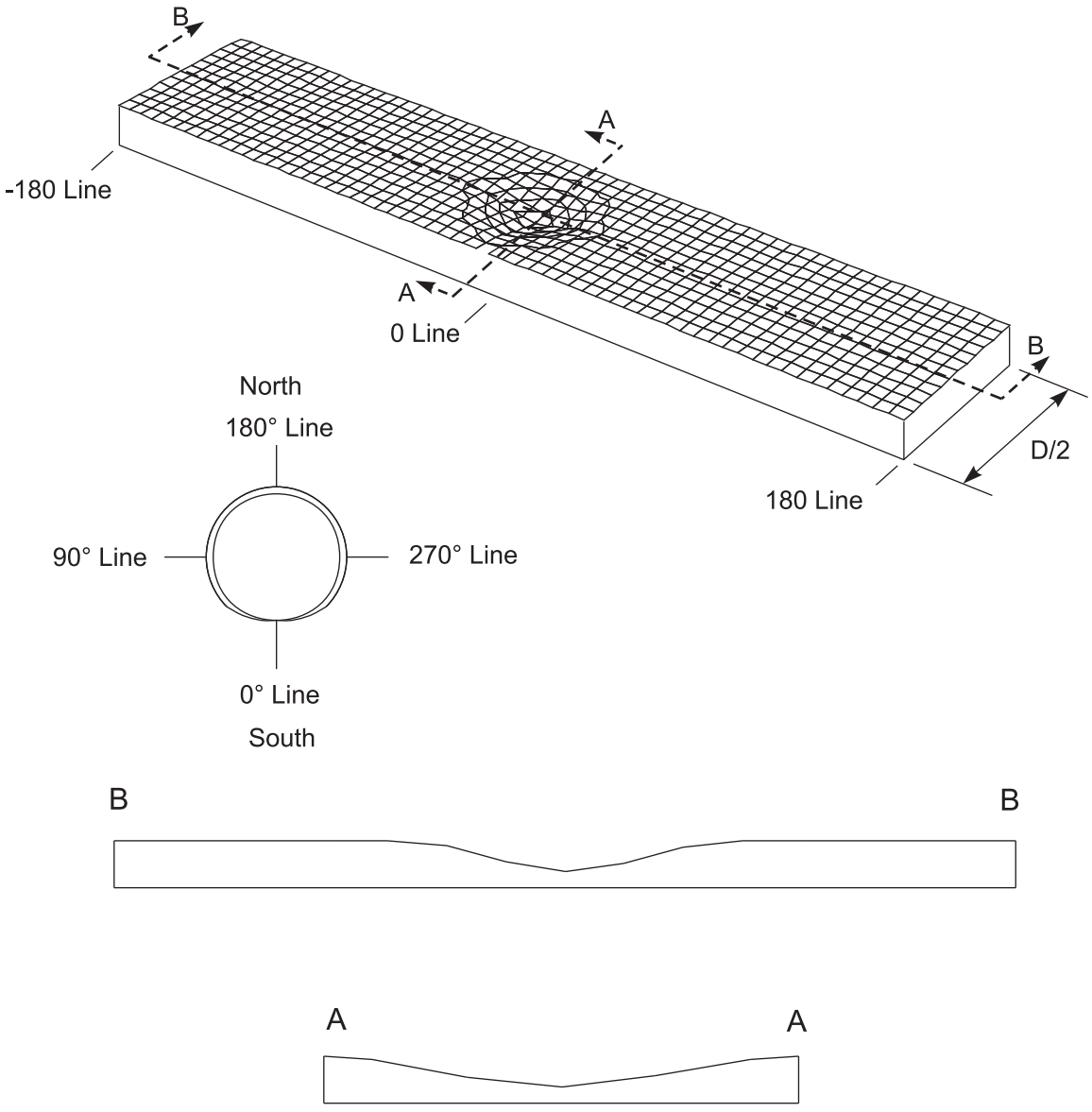

D/t = 27
t_r/t = 0.35
θ = 57.9°

Figure 4.9 Surface Plots and Cross sectional Thickness Profiles from Measured Corrosion Dimensions, Specimen C27-33-58

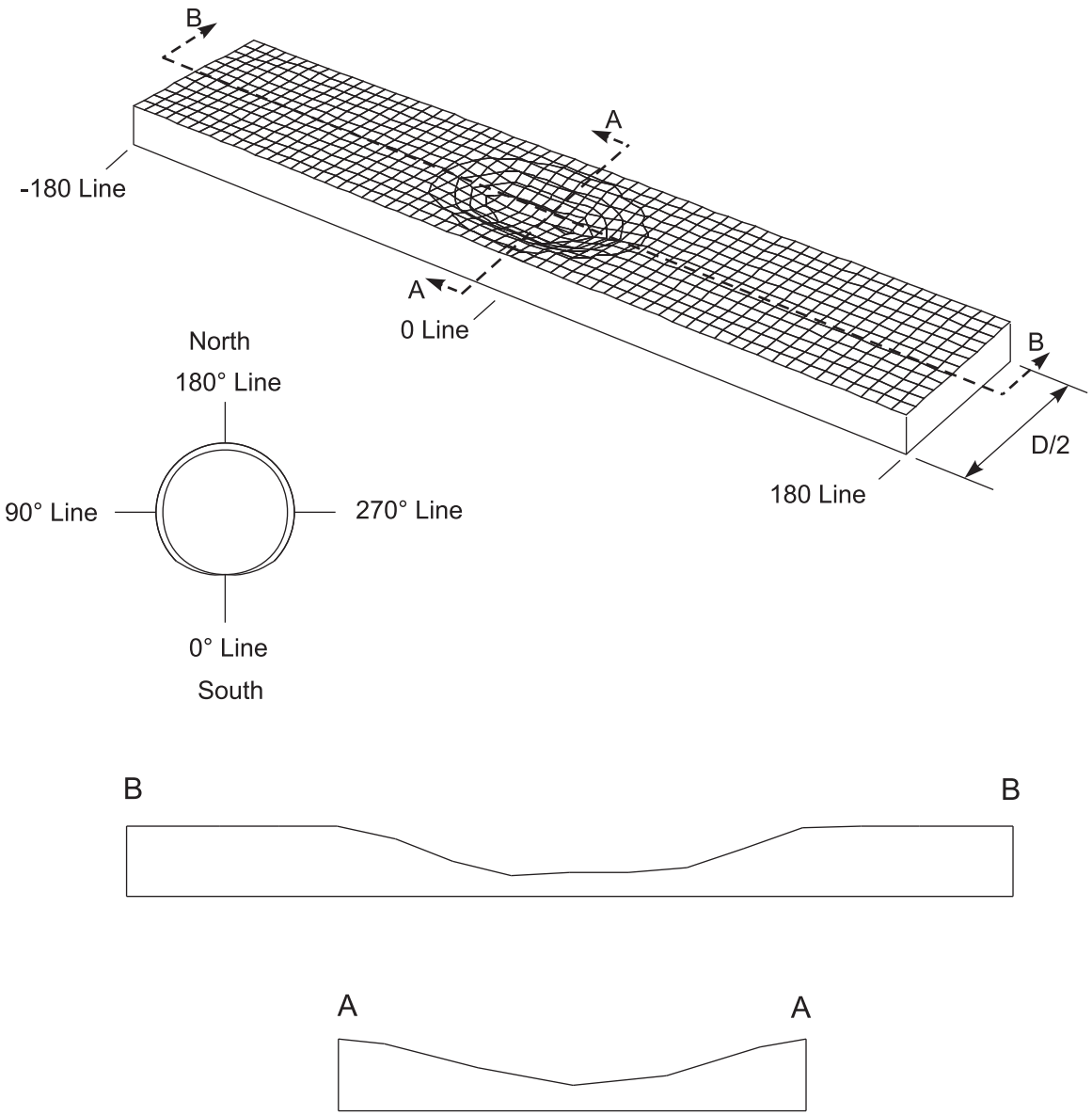

D/t = 27
t_i/t = 0.33
θ = 95.0°

Figure 4.10 Surface Plots and Cross sectional Thickness Profiles from Measured Corrosion Dimensions, Specimen C27-33-95

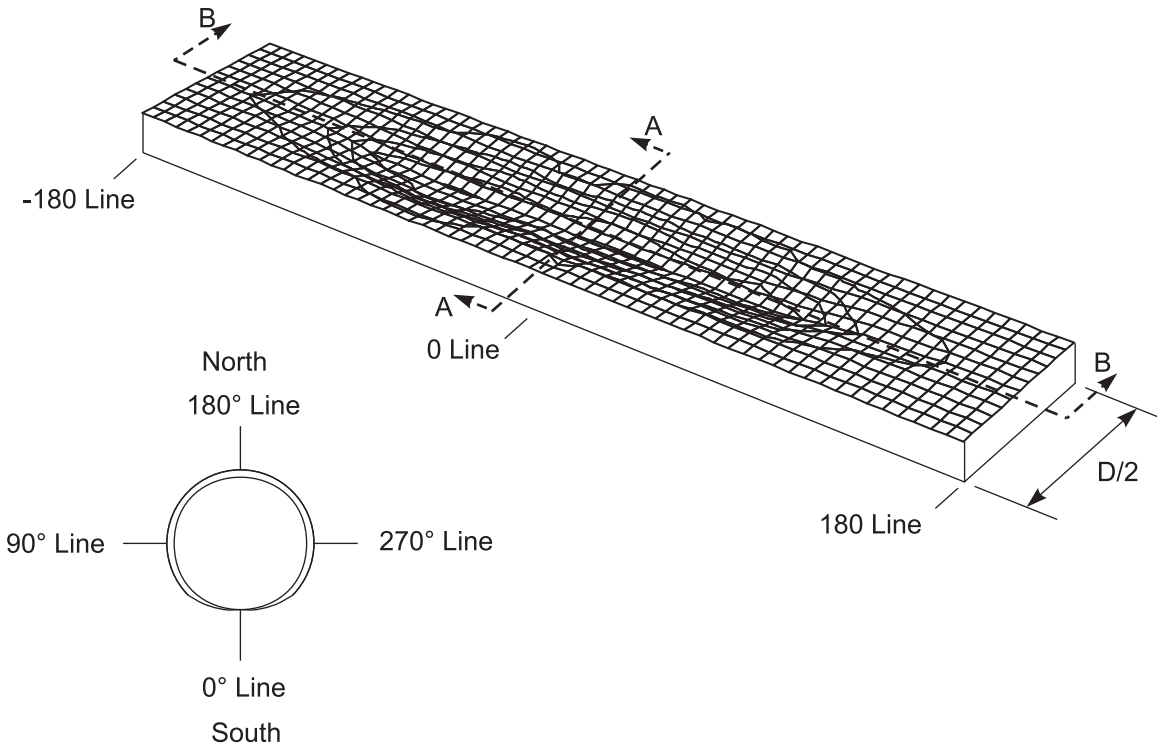

$D/t = 27$
$t_r/t = 0.35$
$\theta = 310.4°$

Figure 4.11 Surface Plots and Cross sectional Thickness Profiles from Measured Corrosion Dimensions, Specimen C27-33-311

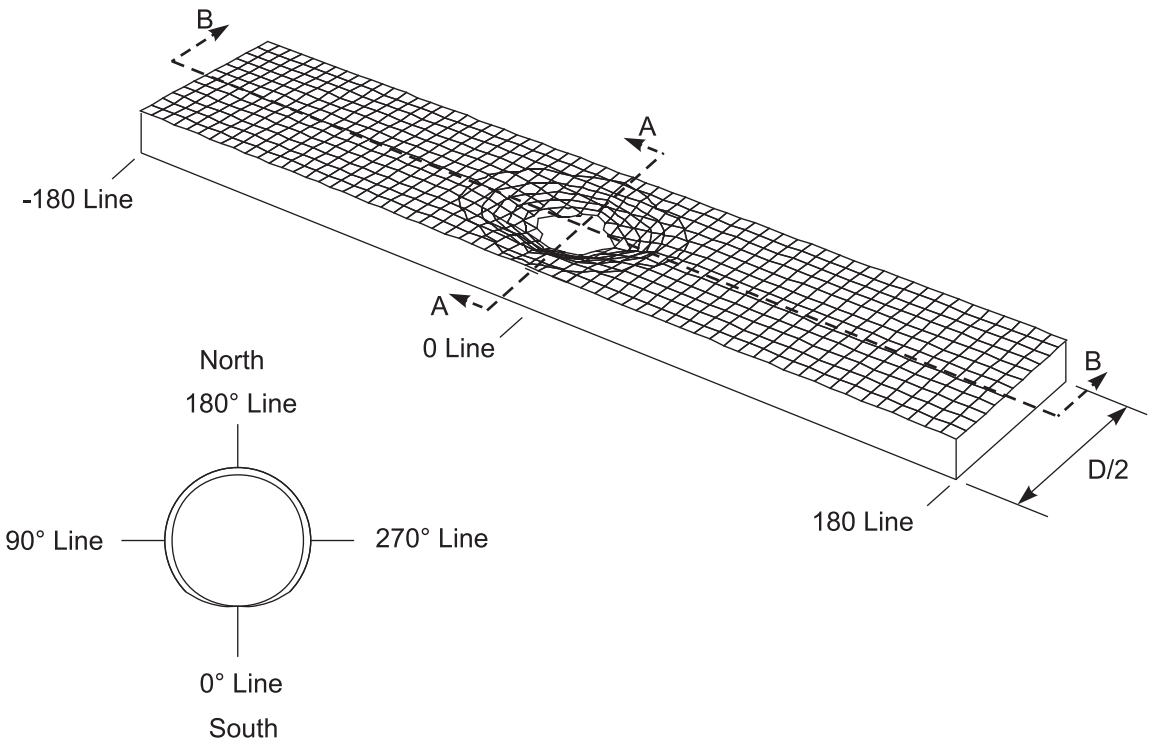

D/t = 40
t_i/t = 0.00
θ = 94.6°

Figure 4.12 Surface Plots and Cross sectional Thickness Profiles from Measured Corrosion Dimensions, Specimen C40-00-95-RS

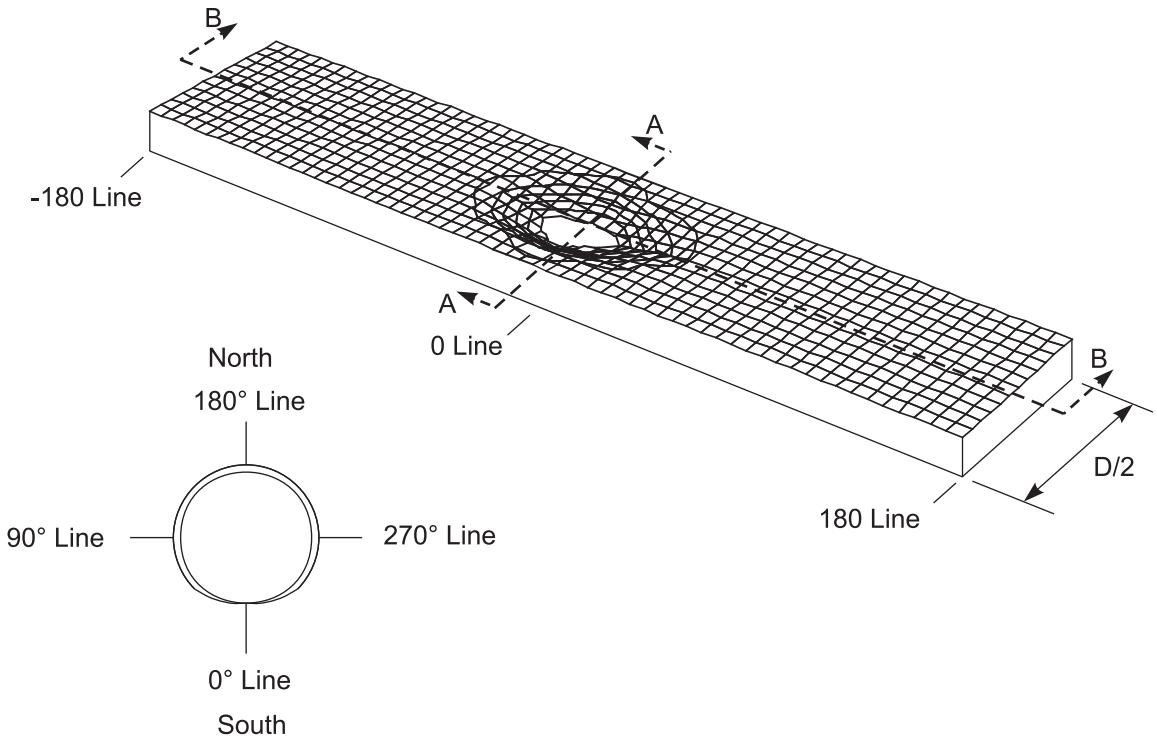

D/t = 40
t_i/t = 0.00
θ = 94.9°

Figure 4.13 Surface Plots and Cross sectional Thickness Profiles from Measured Corrosion Dimensions, Specimen C40-00-95-RC

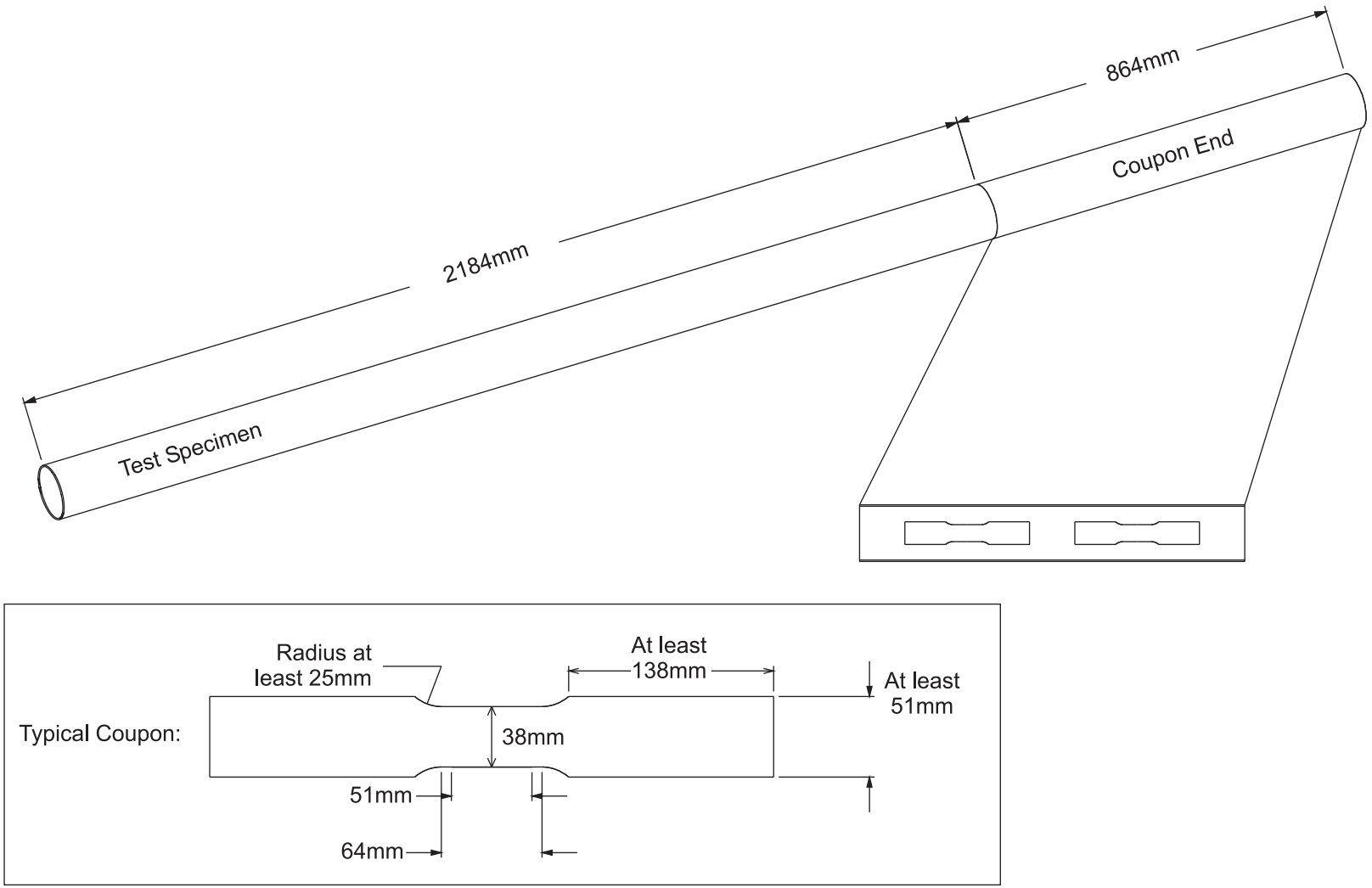

Figure 4.14 Typical Coupon Location and Dimensions

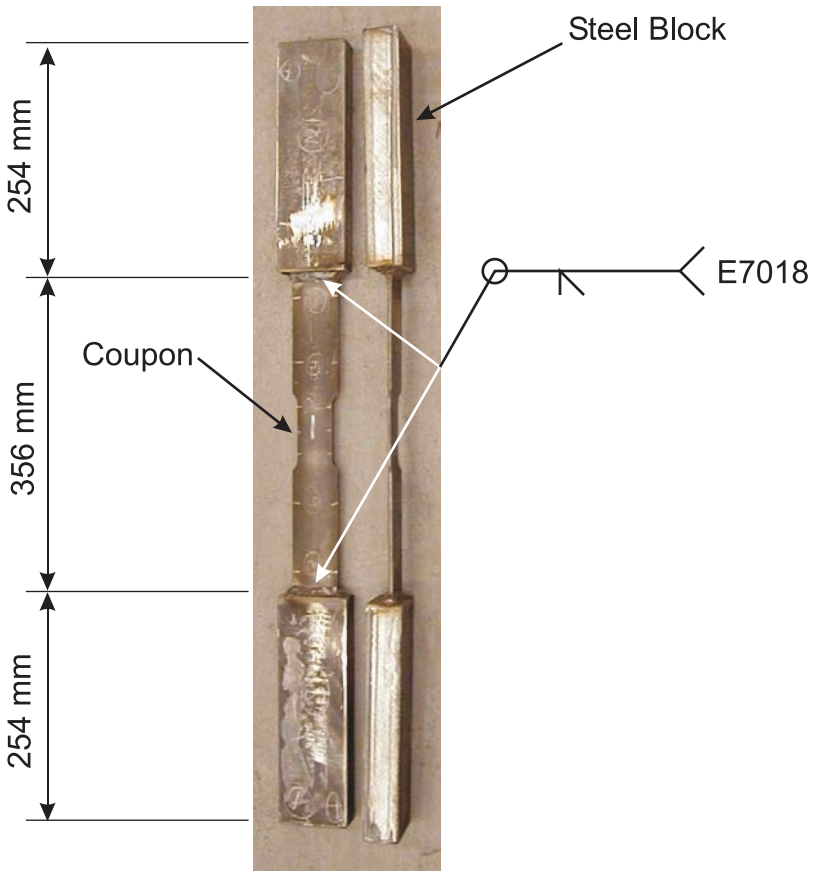

Figure 4.15 Coupon Welded to Steel Blocks

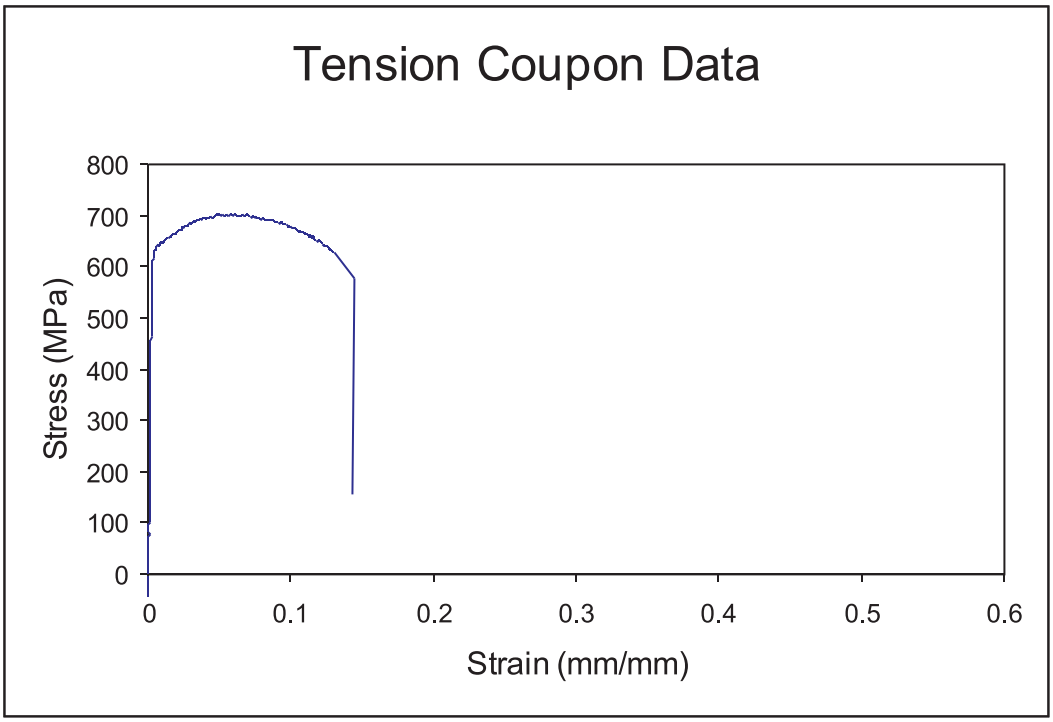

Figure 4.16 Stress-Strain Plot for D/t = 27, Pre-annealed

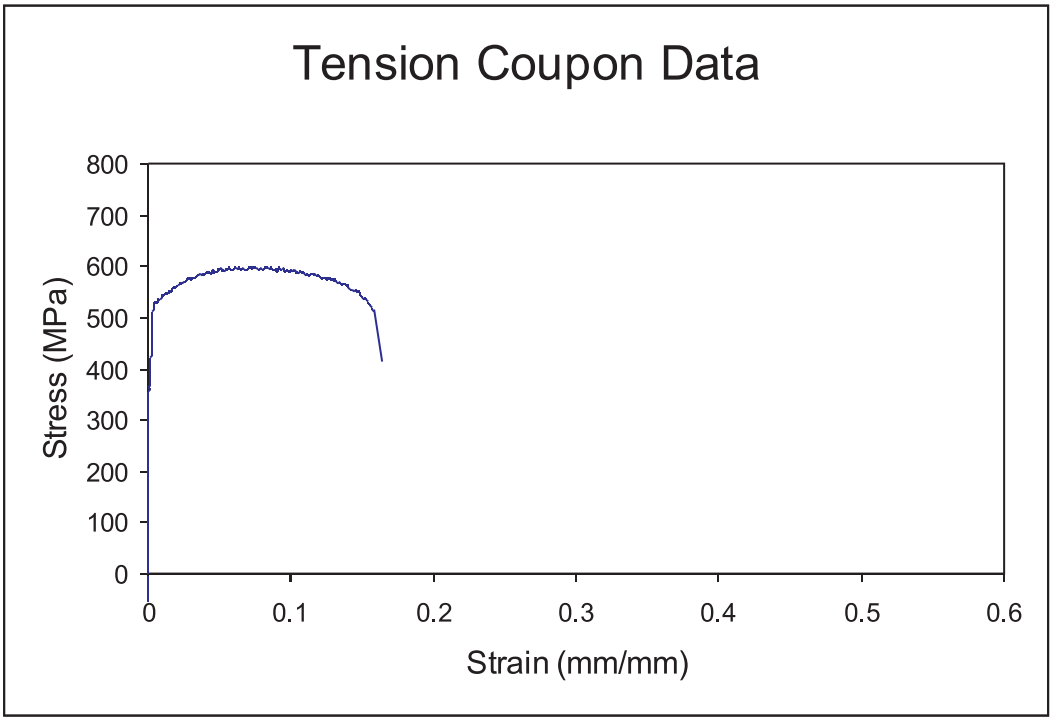

Figure 4.17 Stress-Strain Plot for D/t = 40, Pre-annealed

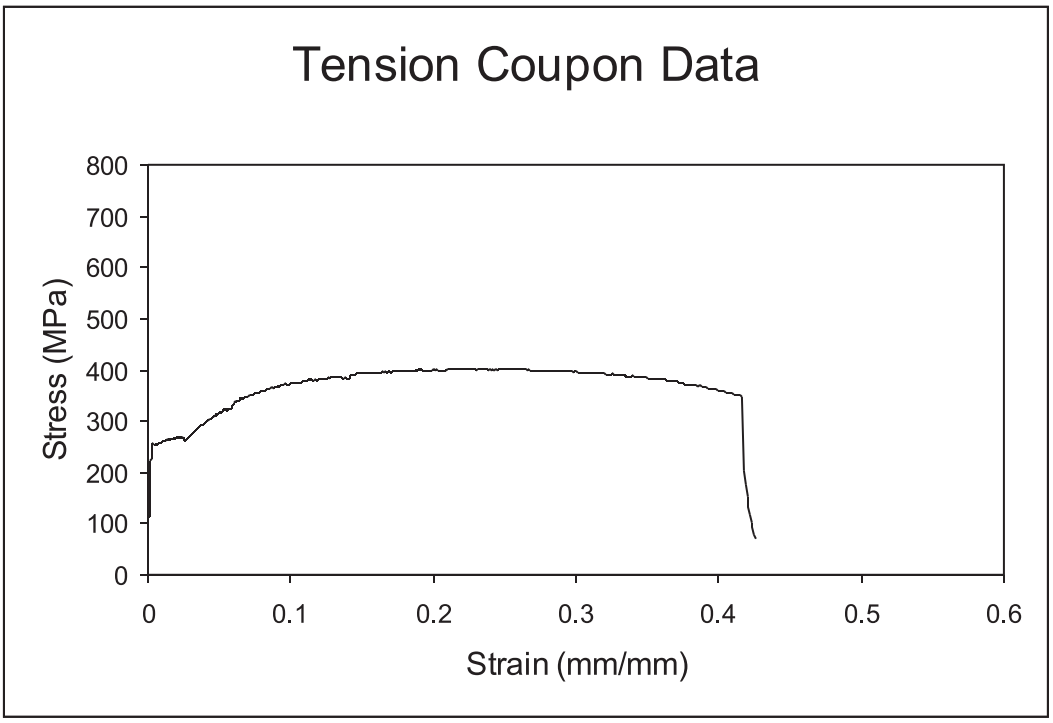

Figure 4.18 Stress-Strain Plot for D/t = 27, Annealed

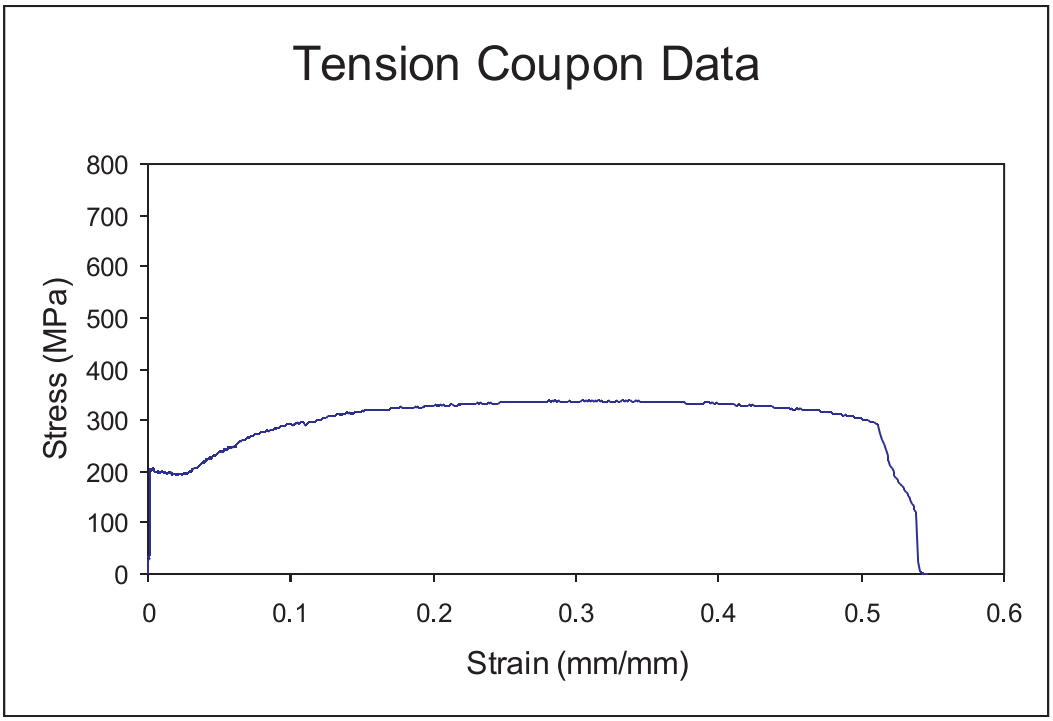

Figure 4.19 Stress-Strain Plot for D/t = 40, Annelaed

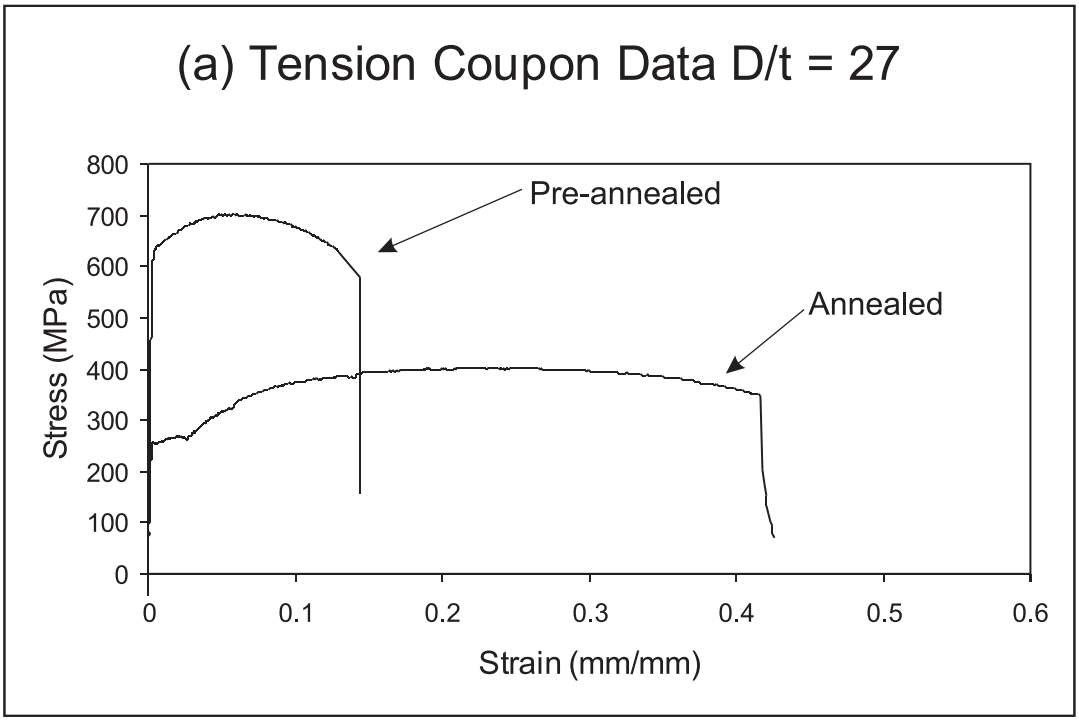

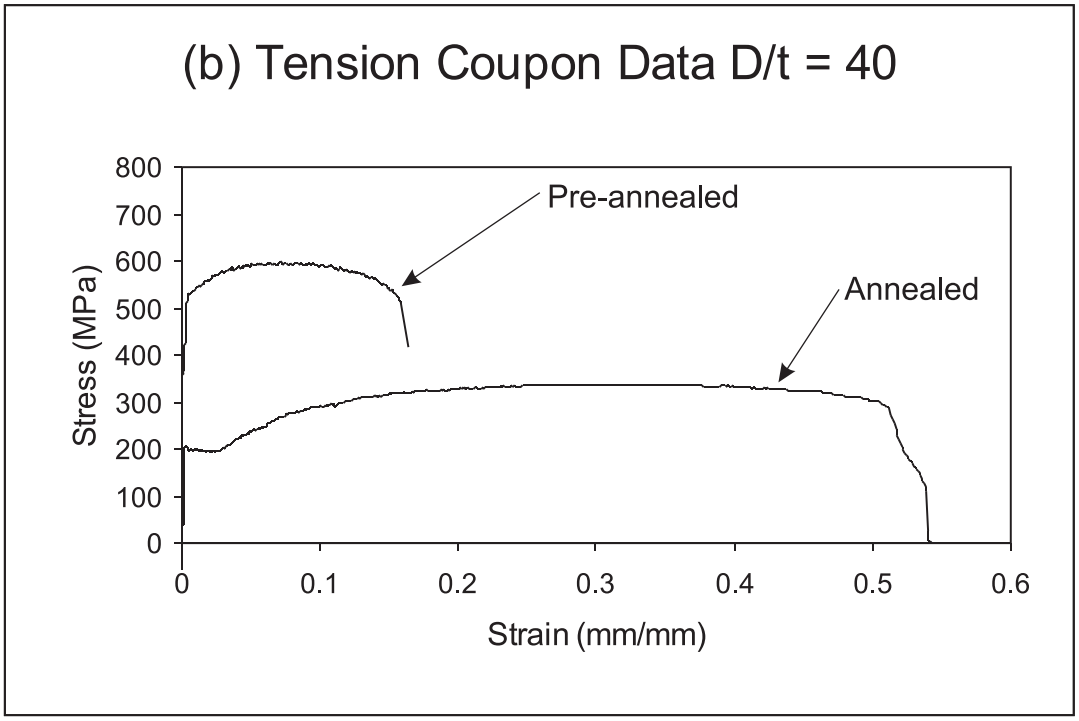

Figure 4.20 Comparison Plot of Pre-anneled and Post-annealed Steel

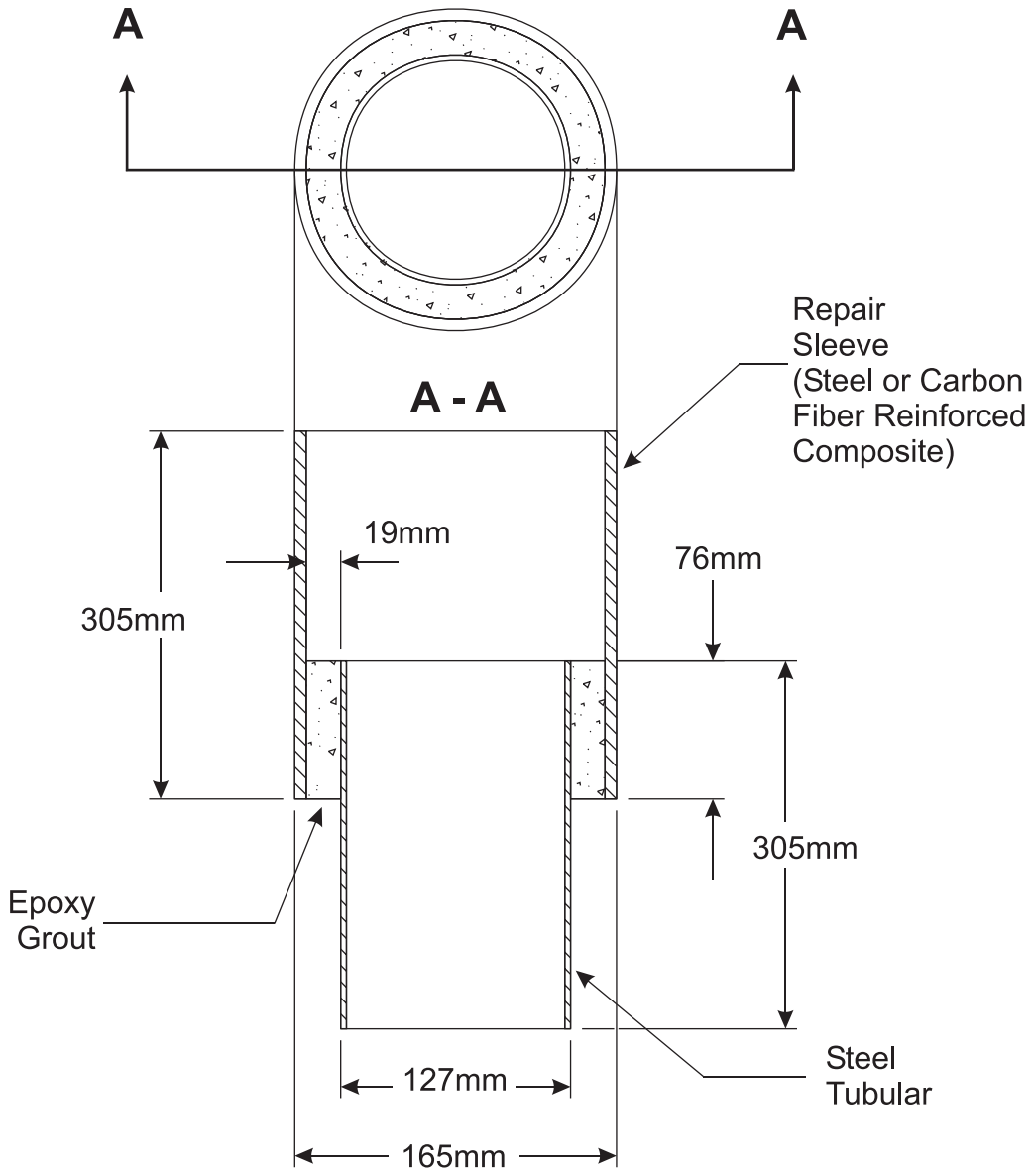

Figure 4.21 Details of a Bond Test Specimen

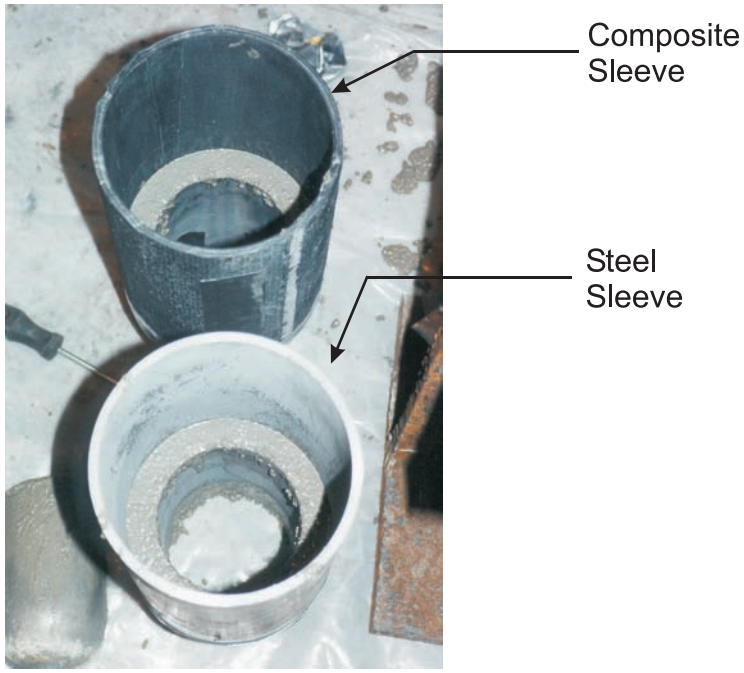

Figure 4.22 Photograph of Constructed Bond Test Specimens

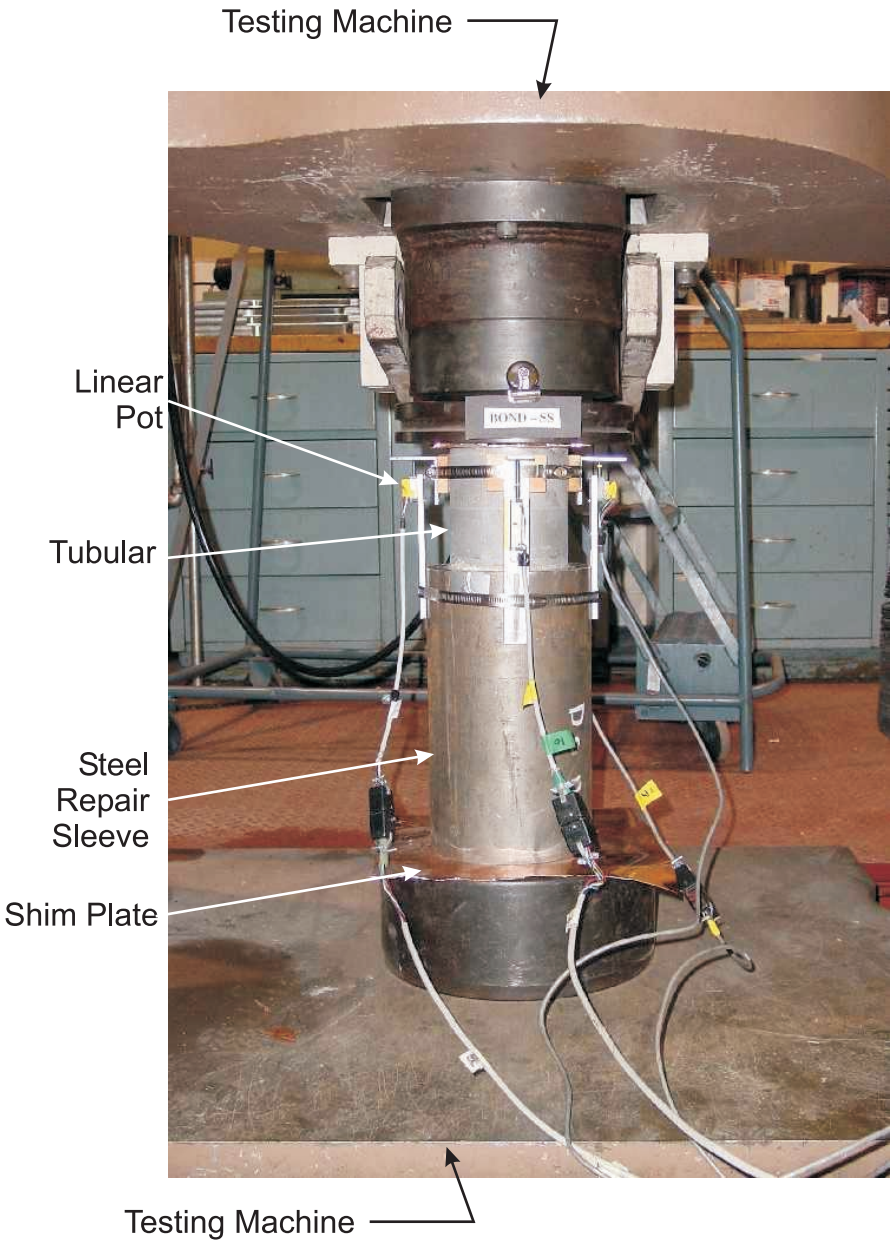

Figure 4.23 Photo of Bond Test Specimen in Testing Machine (Three of Four Linear Pots Shown)

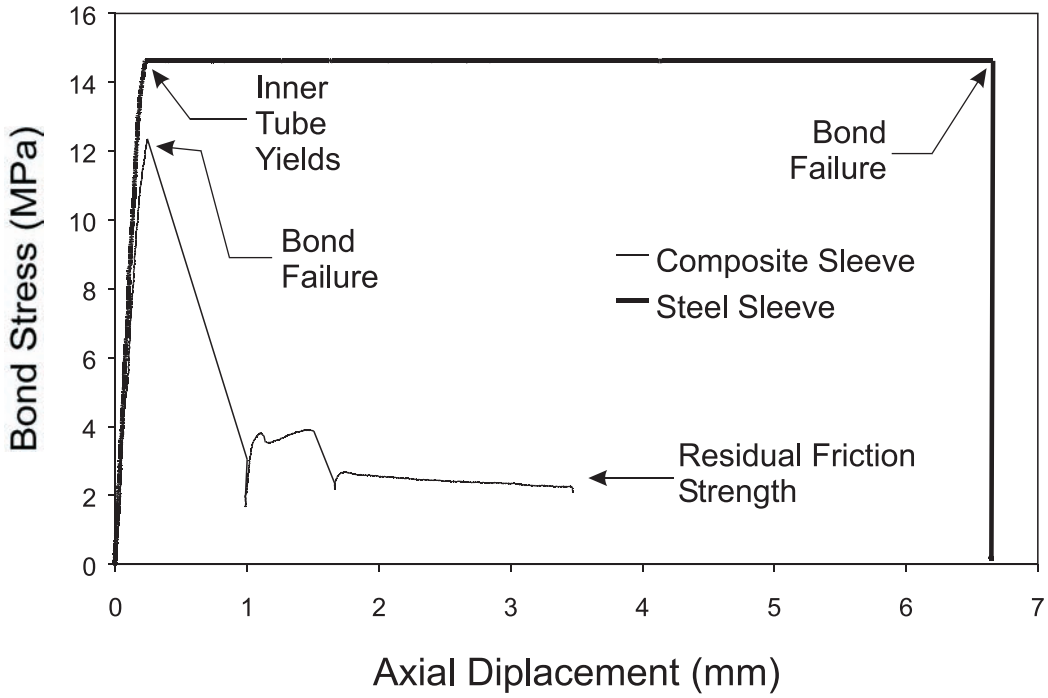

Figure 4.24 Bond Strength of Steel and Composite Sleeves to Inner Tubular of D/t = 40

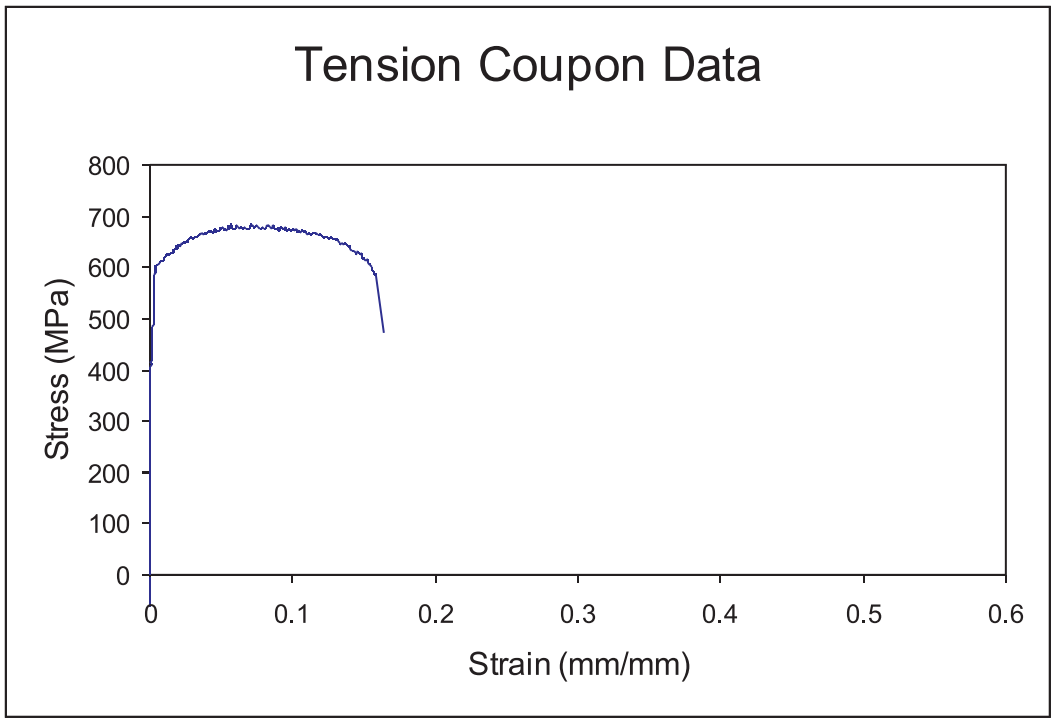

Figure 4.25 Stress-Strain Plot for Steel Repair Sleeve

Figure 4.26 Local View of Specimen C40-00-95-RS with Steel Repair Sleeve Installed

Figure 4.27 Local View of Specimen C40-00-95-RC with Composite Repair Sleeve Installed

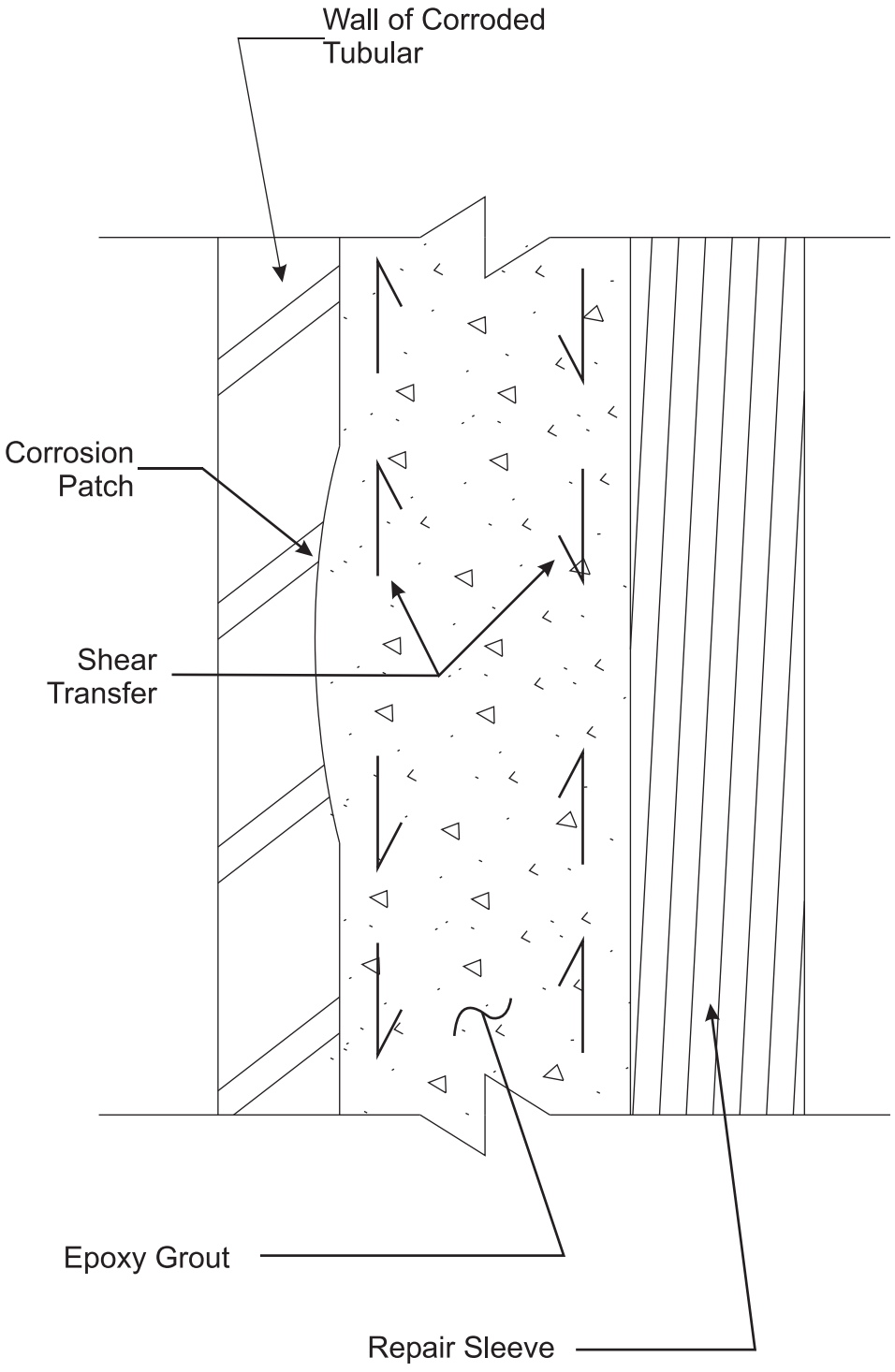

Figure 4.28 Local Section of Grouted Sleeve Repair at Corrosion Patch

Figure 4.29 Typical Repaired Specimen

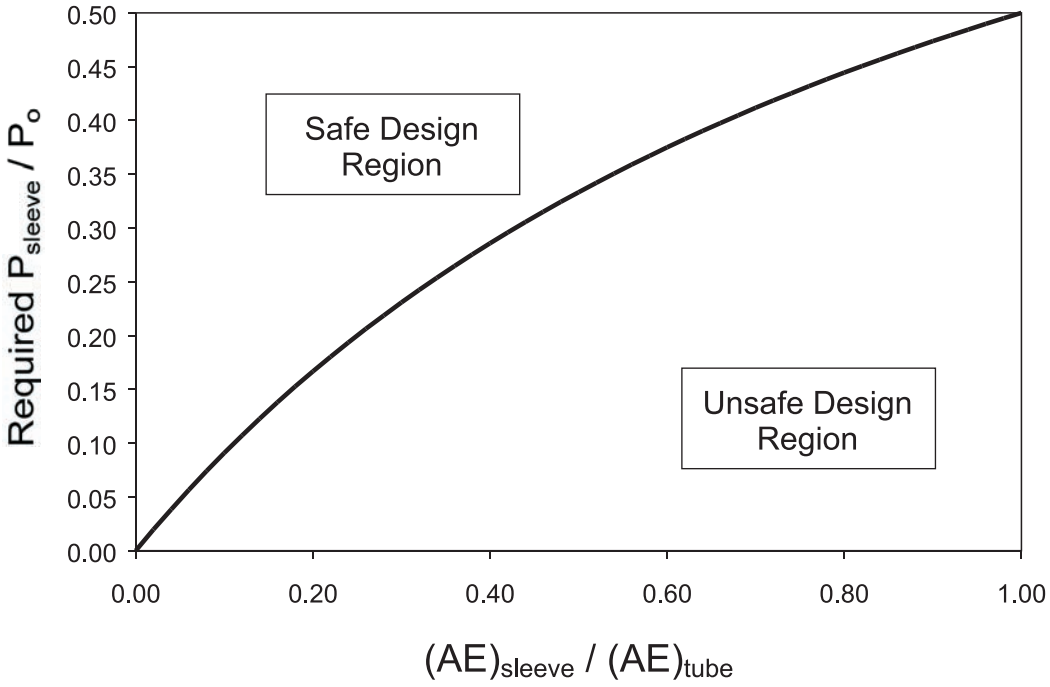

Figure 4.30 Graphical Representation of Sleeve Design Equation

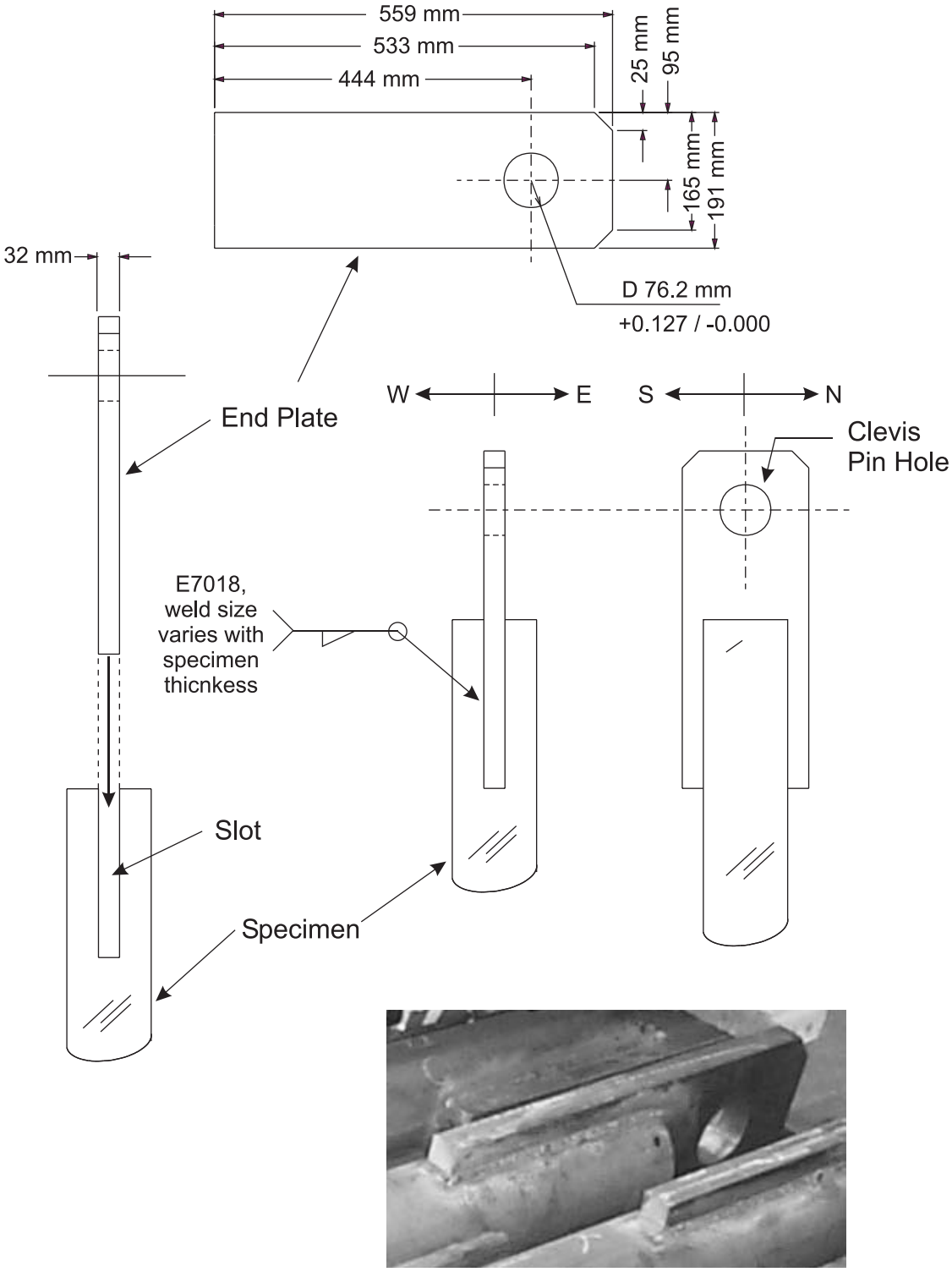

Figure 4.31 Male Clevis End Plate Attachment to Specimens

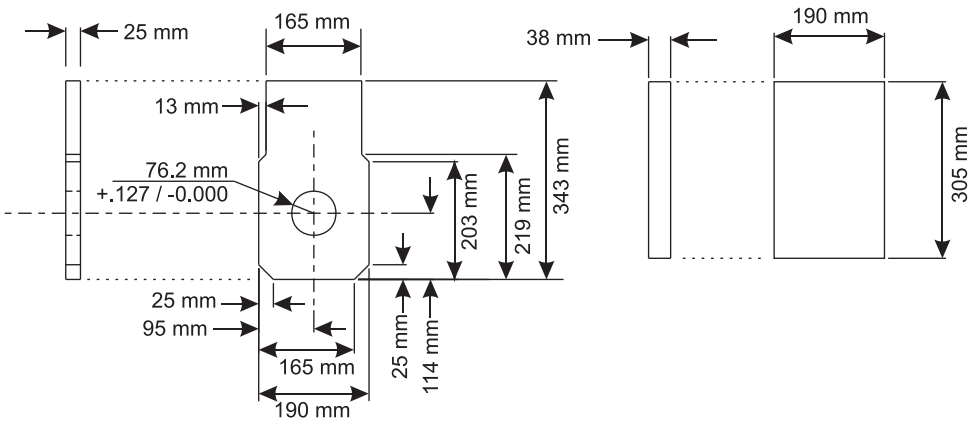

(a) Dimensions of Female Clevis Components

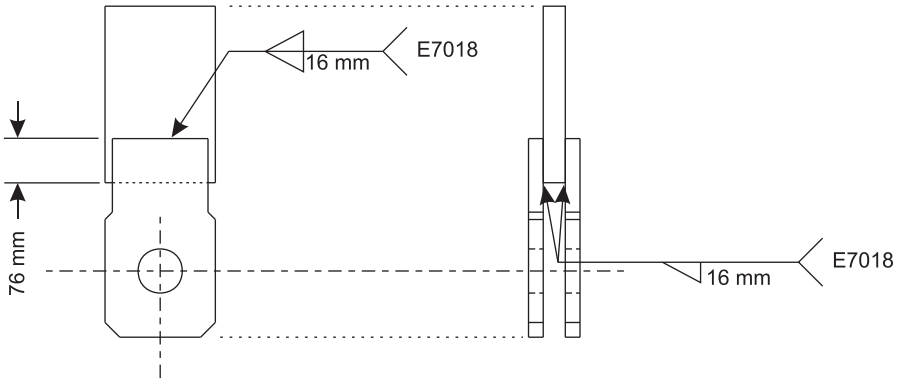

(b) Assembled Female Clevis

Figure 4.32 Female Clevis

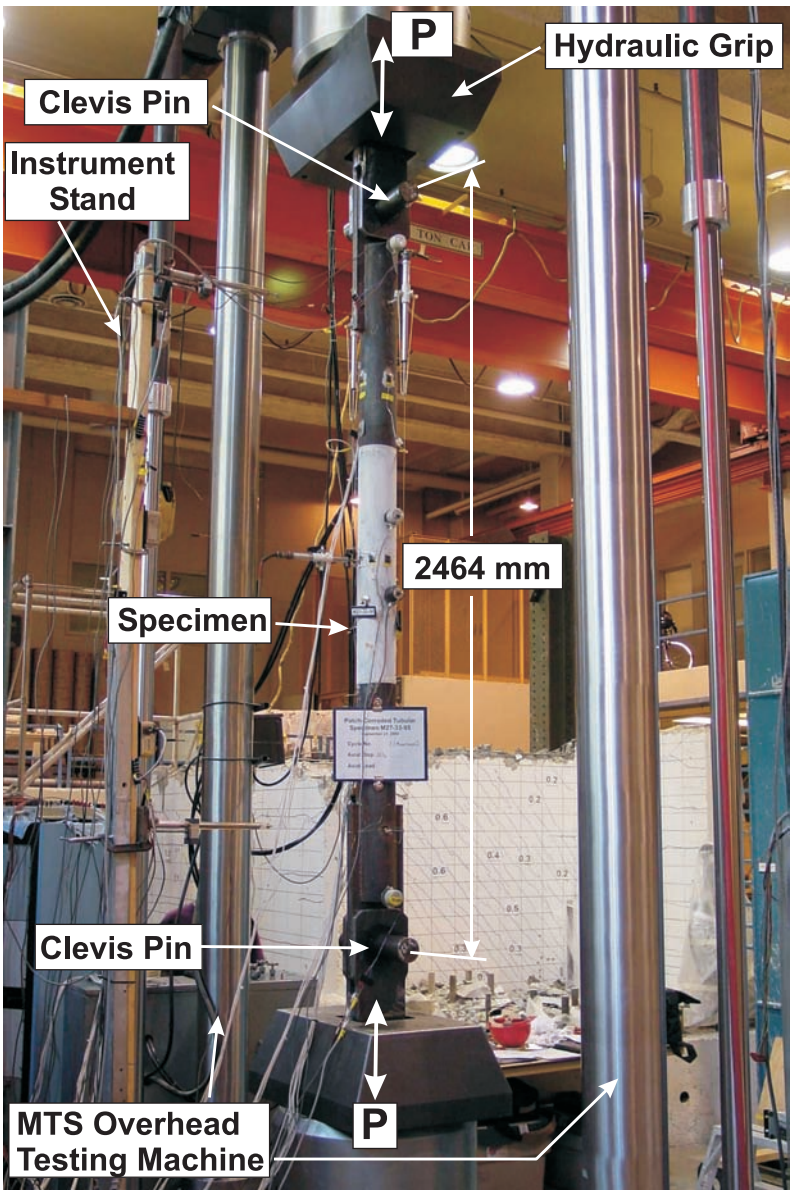

Figure 4.33 Overall Setup of Specimen in MTS Testing Machine

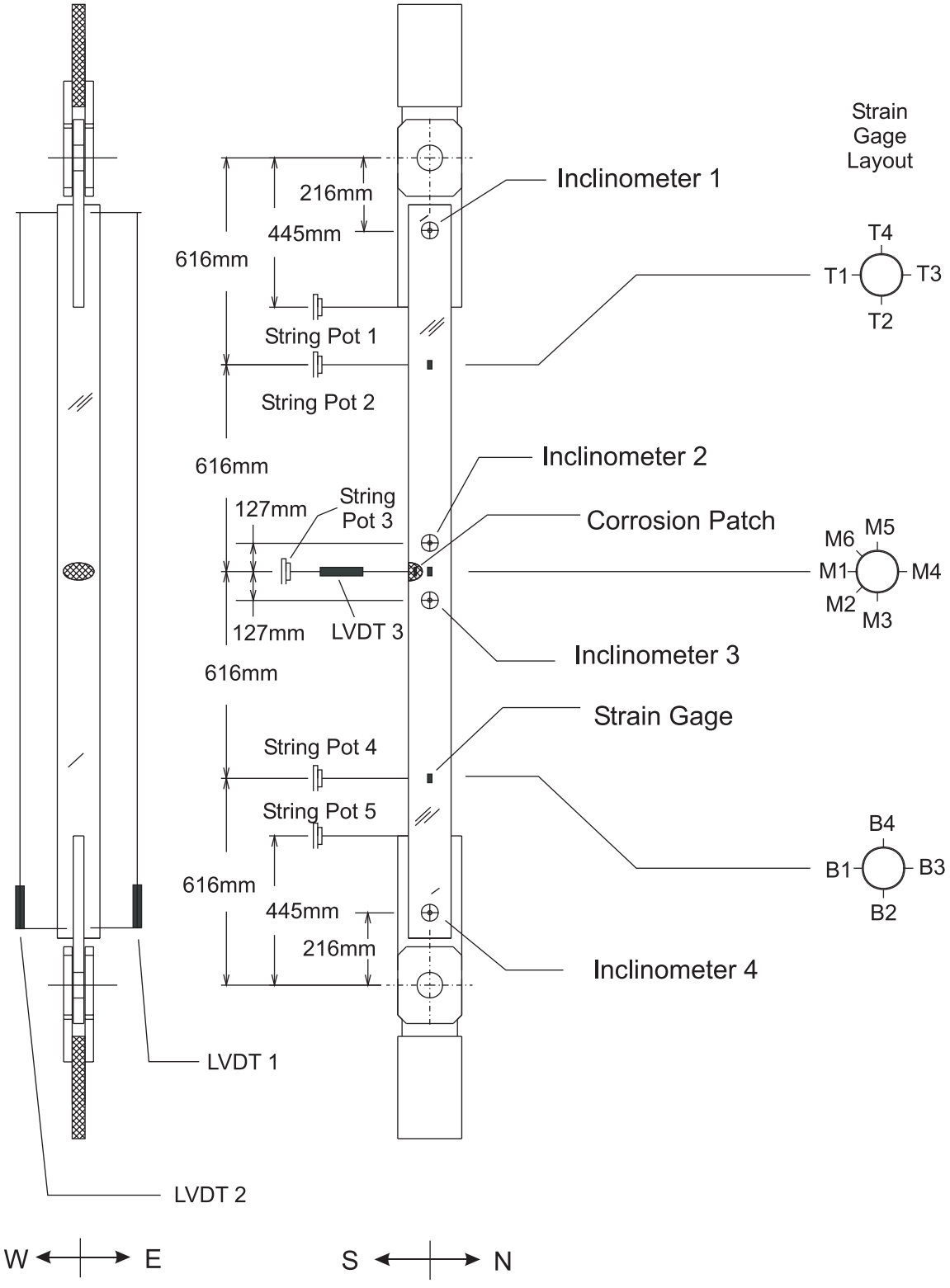

Figure 4.34 Instrumentation Layout for Specimens

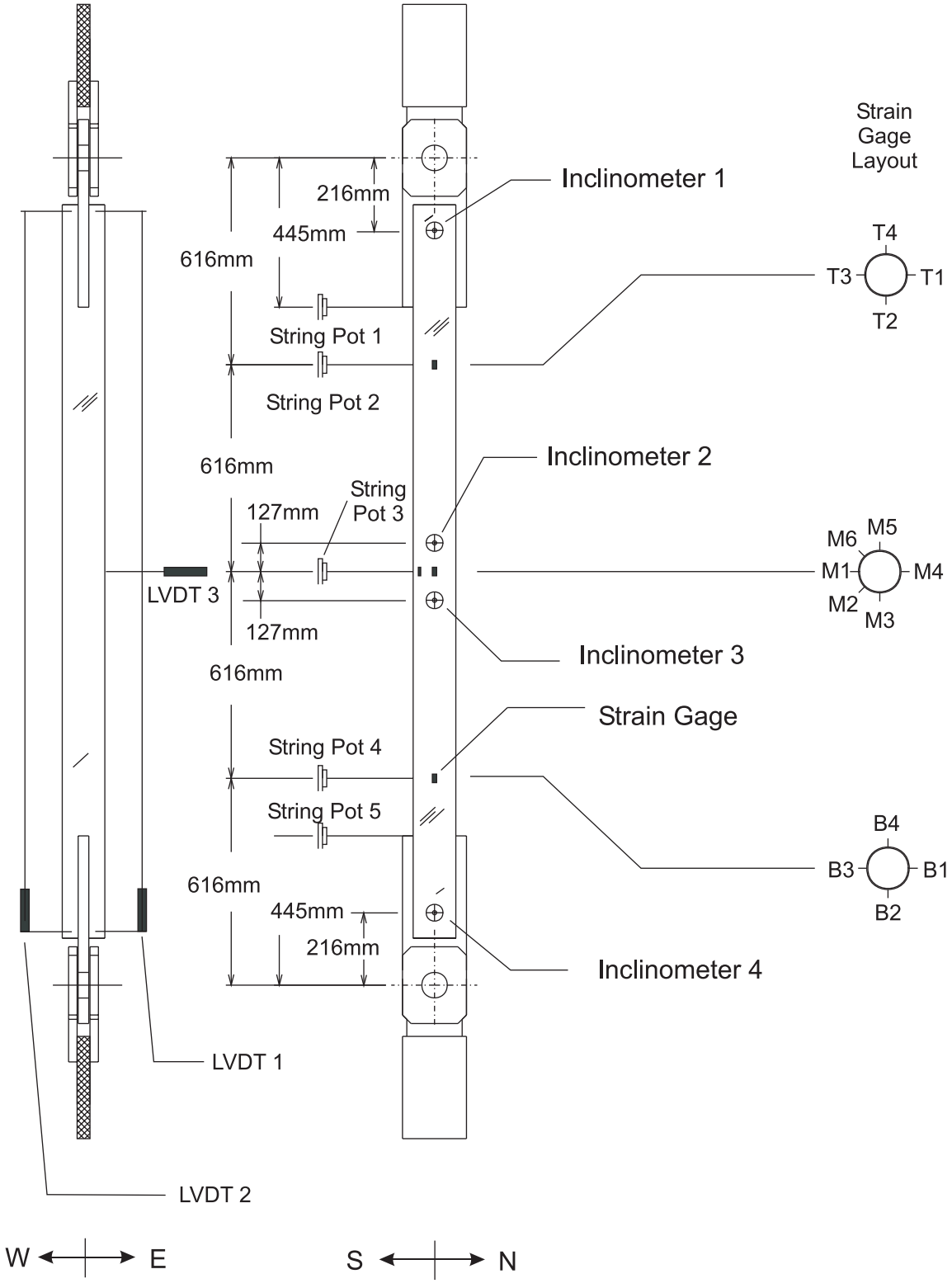

Figure 4.35 Adjusted Instrumentation for Non-corroded Specimens

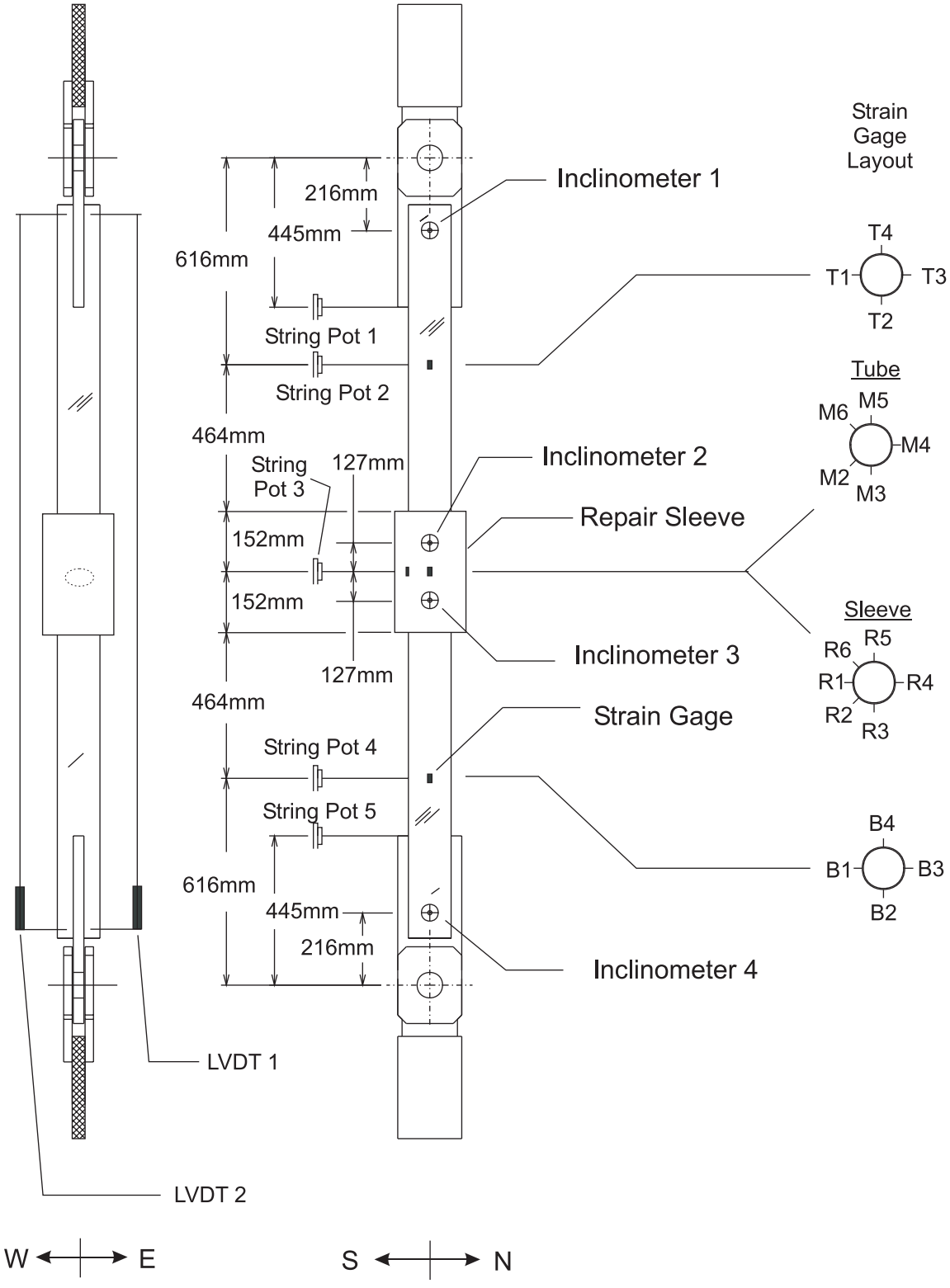

Figure 4.36 Adjusted Instrumentation for Repaired Specimens

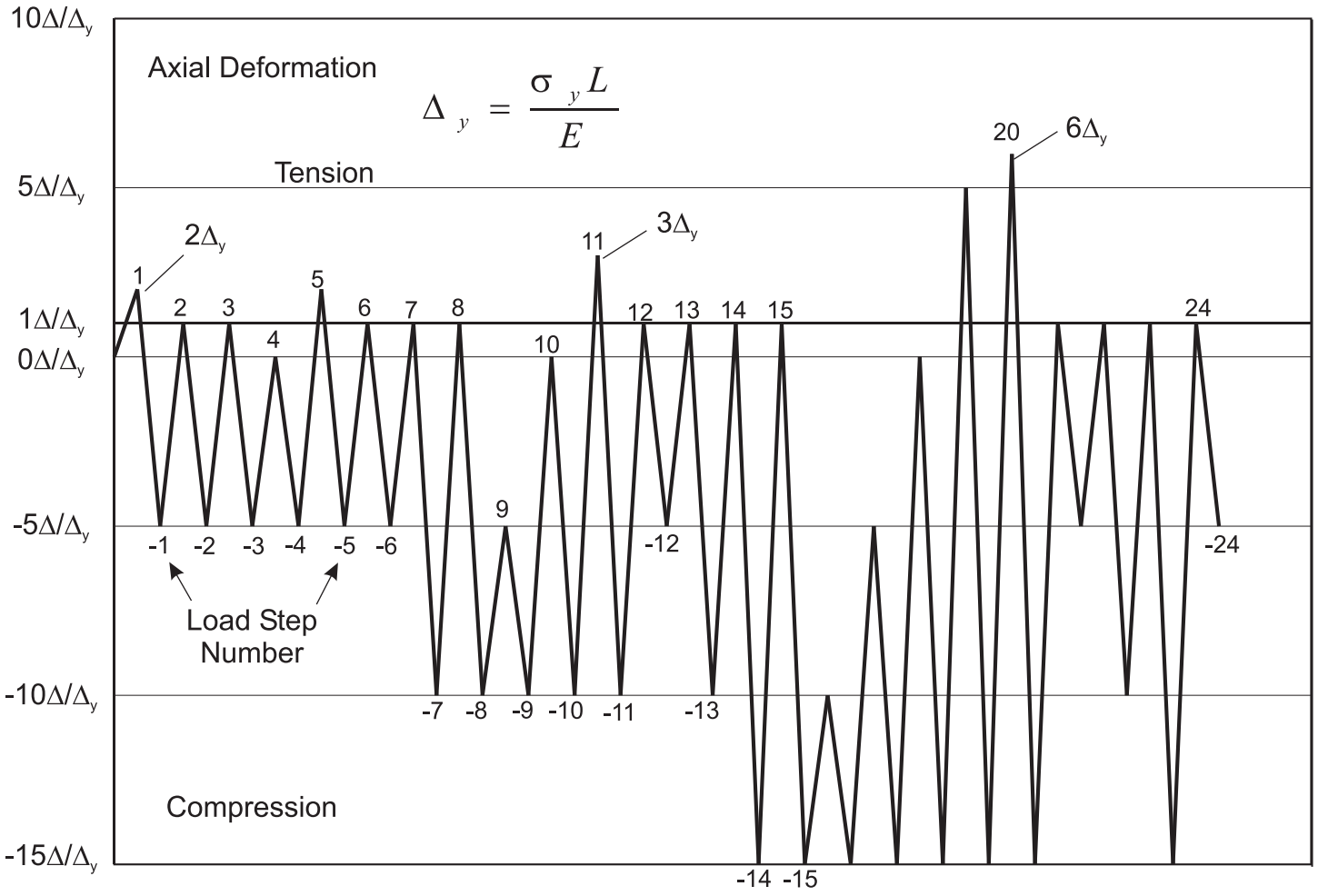

Figure 4.37 Load History

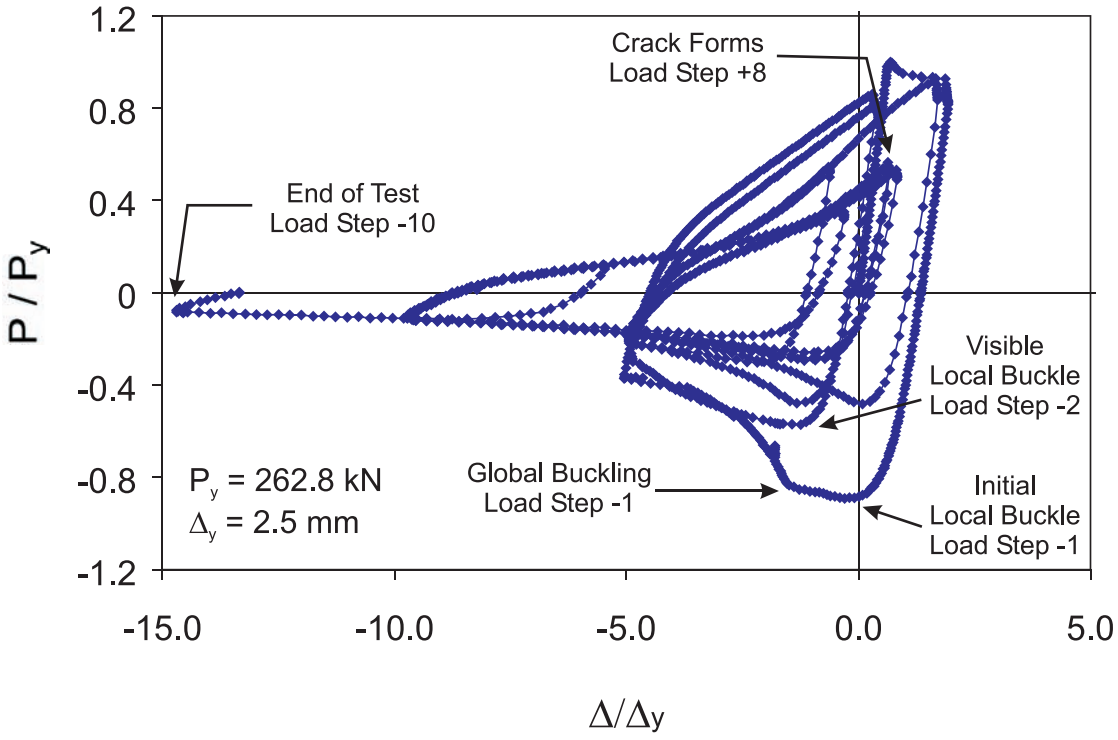

Figure 5.1 Normalized Axial Load - Axial Displacement, Specimen C40-100-0

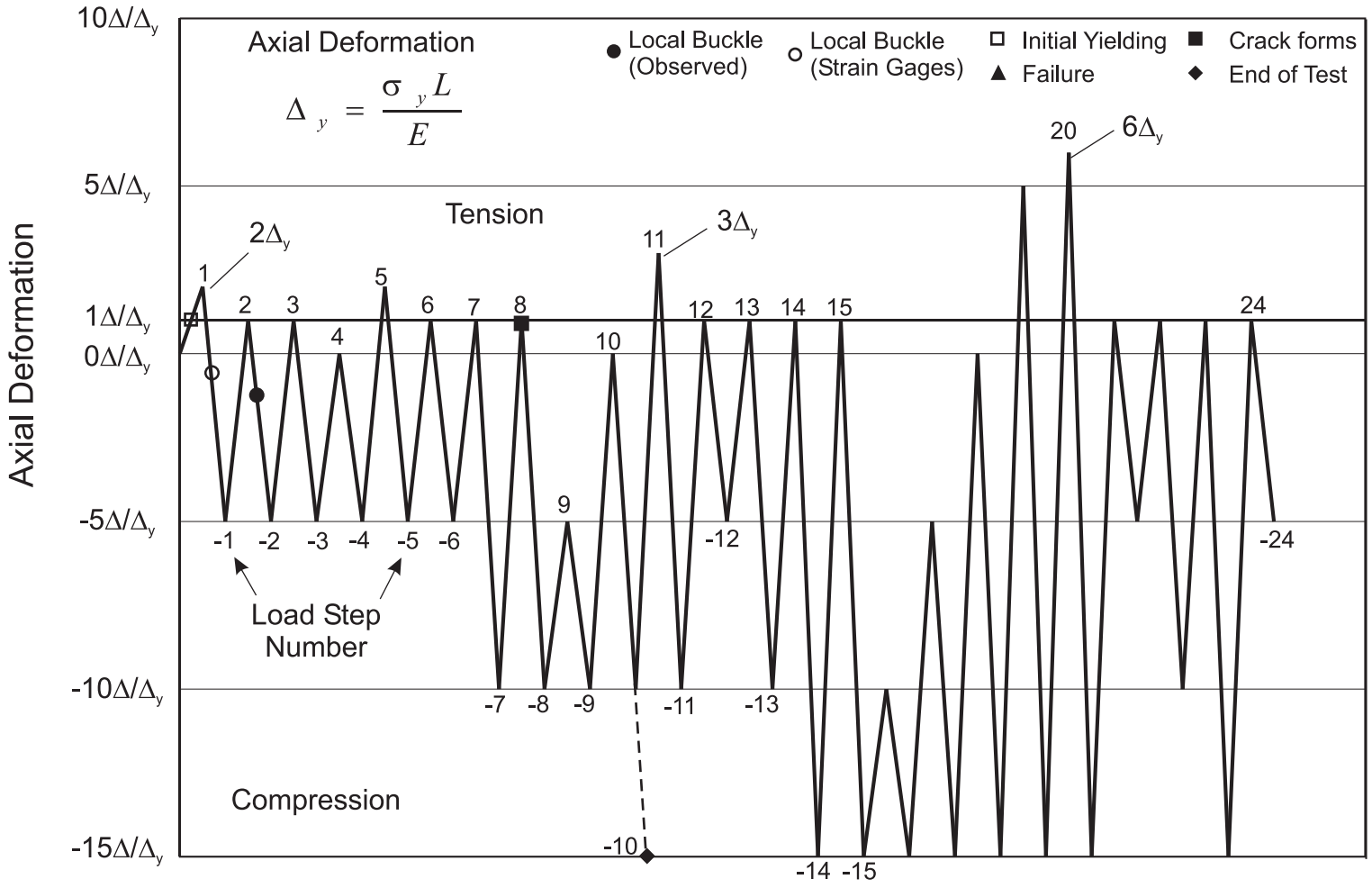

Figure 5.2 Displacement History with Events of Interest Noted, Specimen C40-100-0

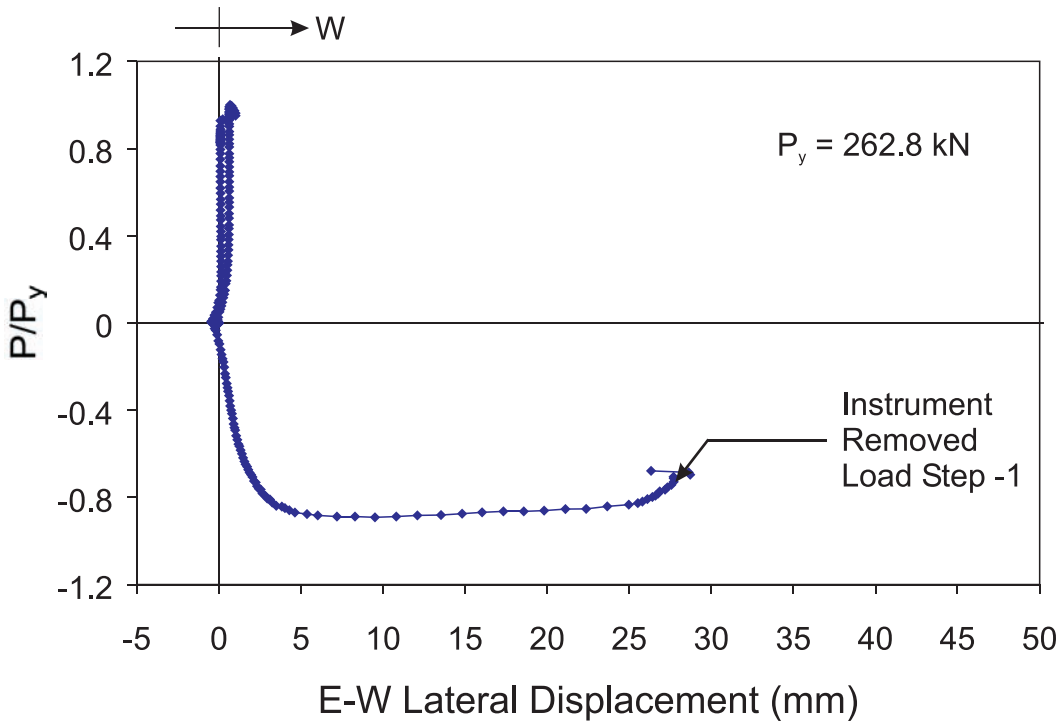

Figure 5.3 Measured Lateral Displacement in the East-West Direction, Specimen C40-100-0

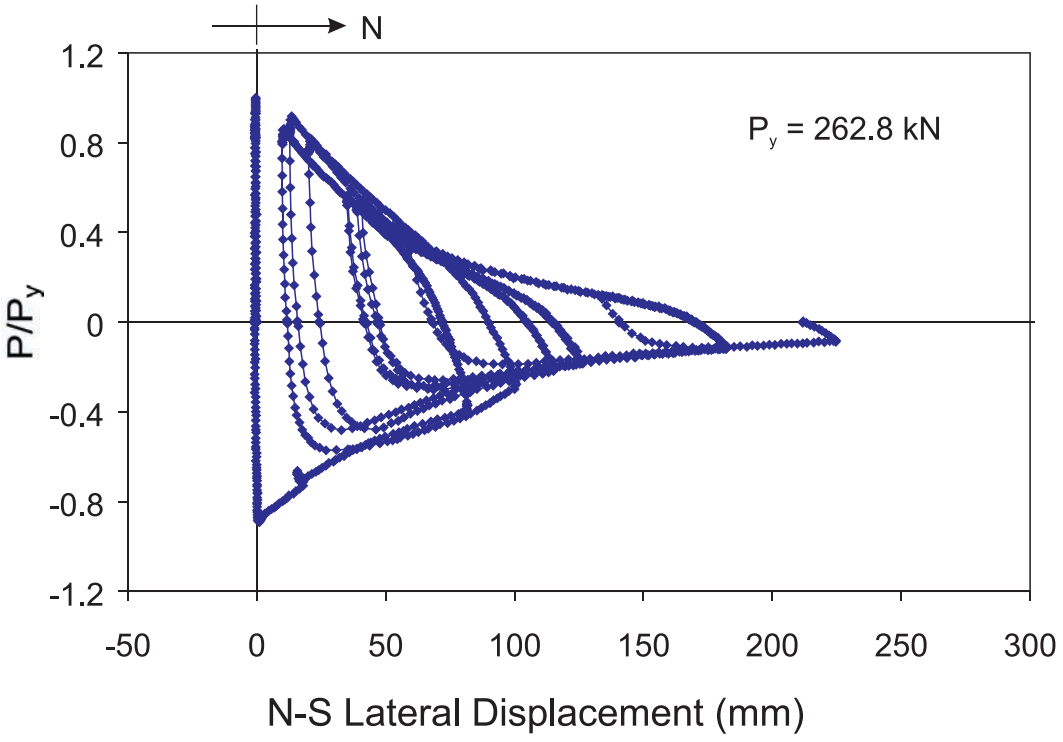

Figure 5.4 Measured Lateral Displacement in the North-South Direction, Specimen C40-100-0

Figure 5.5 Side View of Yielding at Mid-height (Load Step -1), Specimen C40-100-0

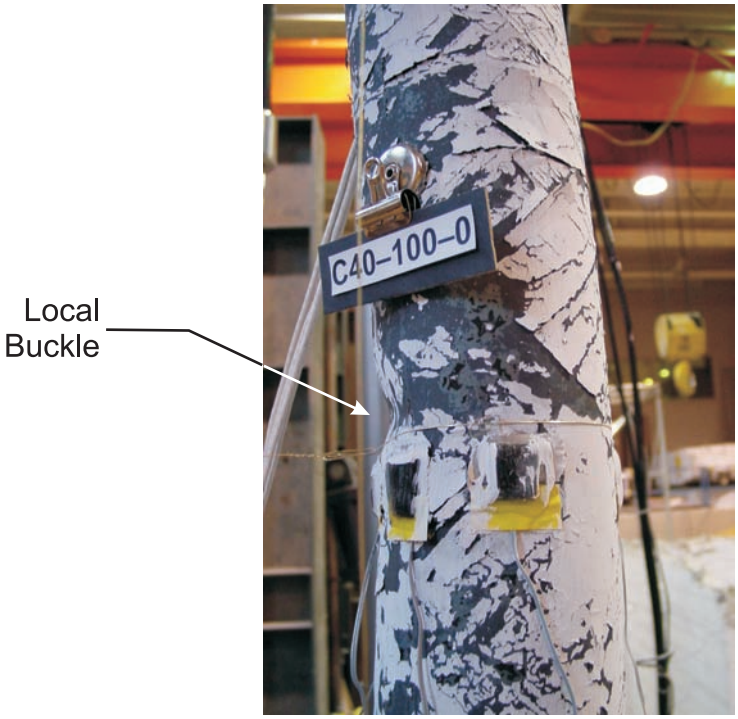

Figure 5.6 Side View of Local Buckle at Mid-height (Load Step -2), Specimen C40-100-0

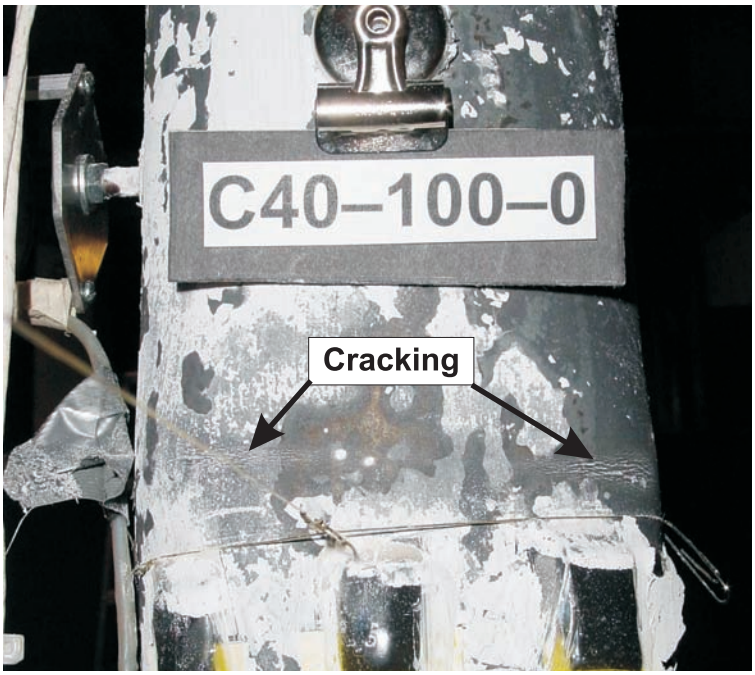

Figure 5.7 Initial Cracking at Edges of Local Buckle (Load Step +8), Specimen C40-100-0

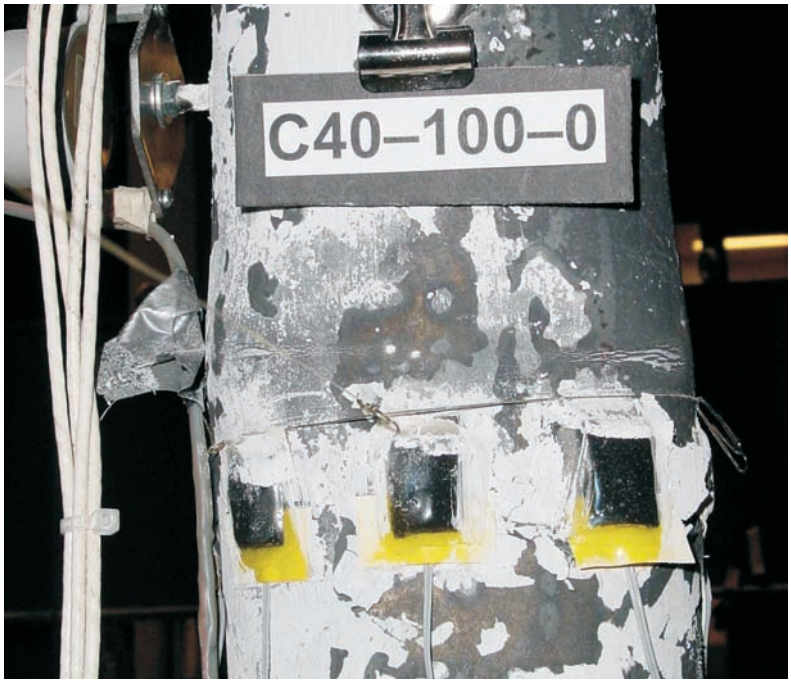

Figure 5.8 Cracking Across Local Buckle (Load Step +10), Specimen C40-100-0

Figure 5.9 Final State of Specimen C40-100-0

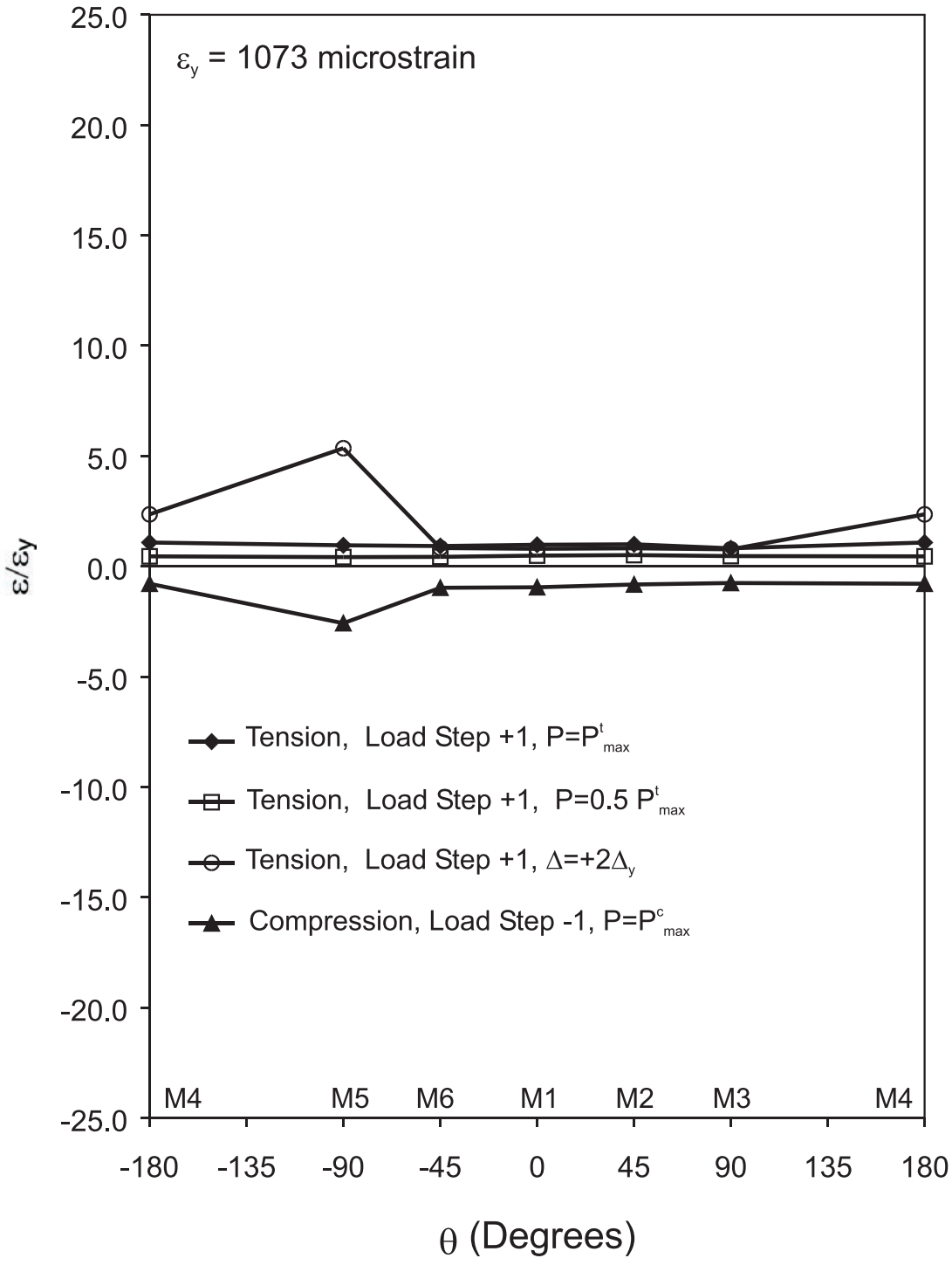

Figure 5.10 Strain Distribution of Cross Section at Mid-height, Specimen C40-100-0

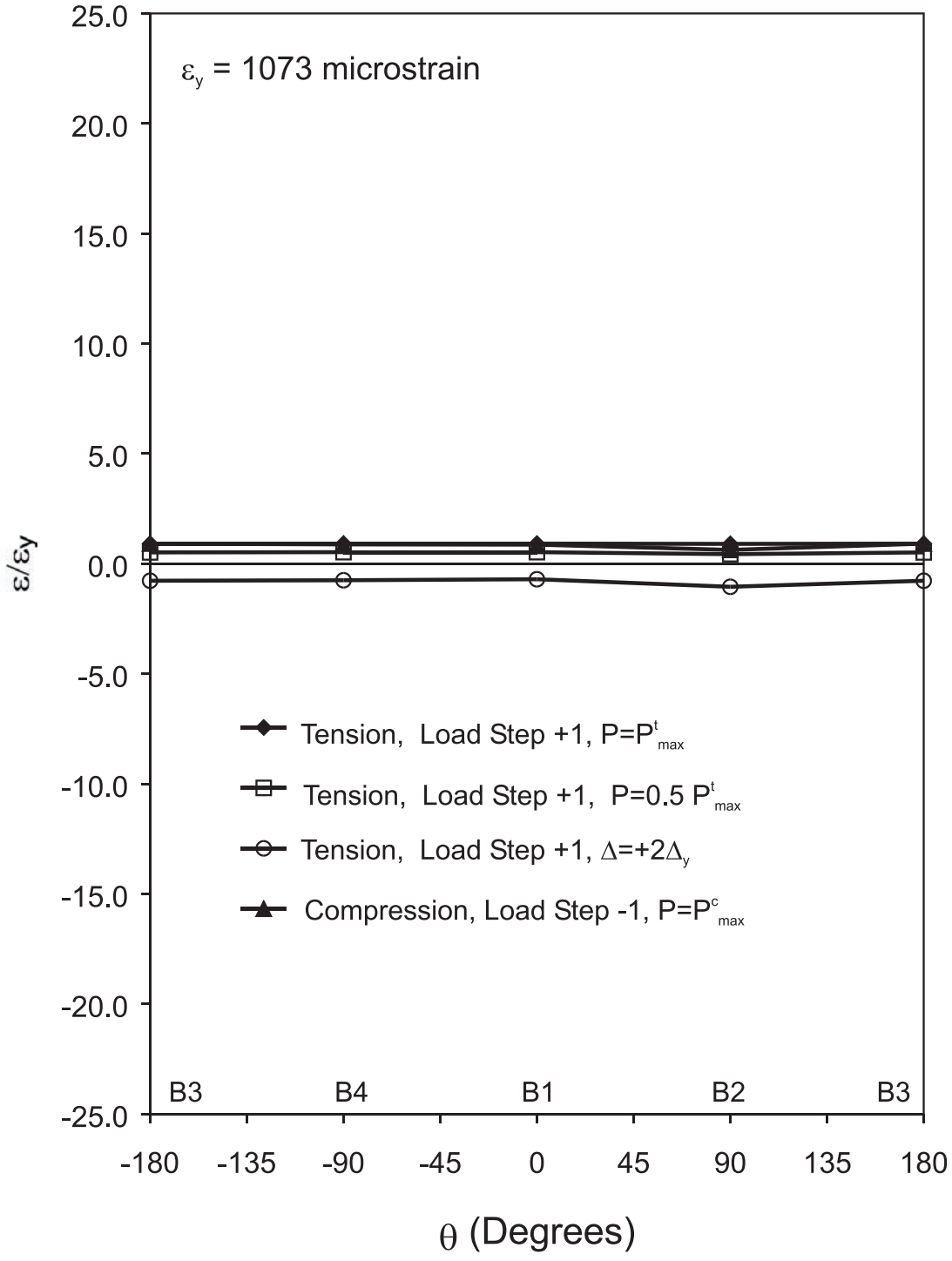

Figure 5.11 Strain Distribution of Cross Section at Lower Quarter-point, Specimen C40-100-0

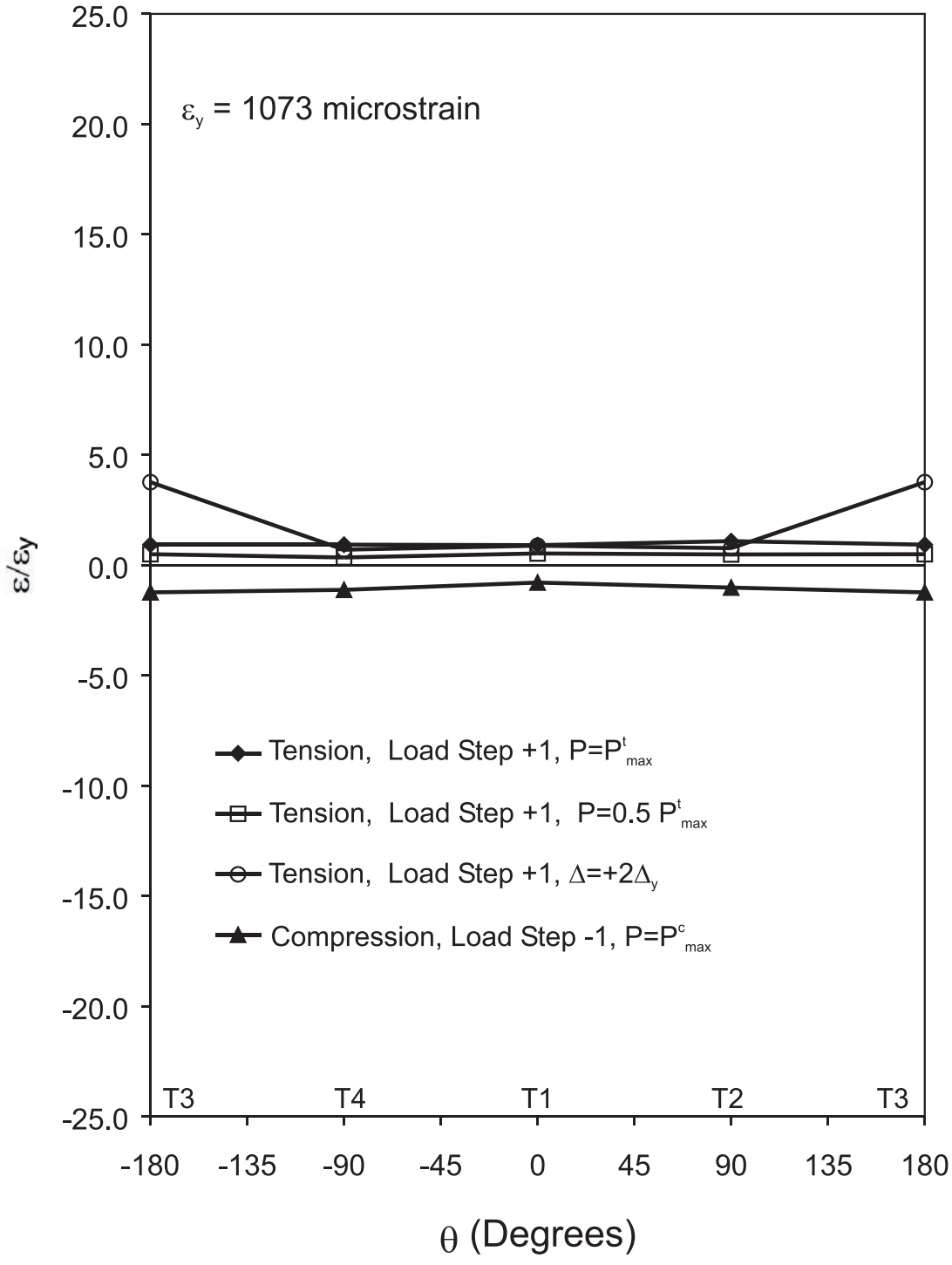

Figure 5.12 Strain Distribution of Cross Section at Upper Quarter-point, Specimen C40-100-0

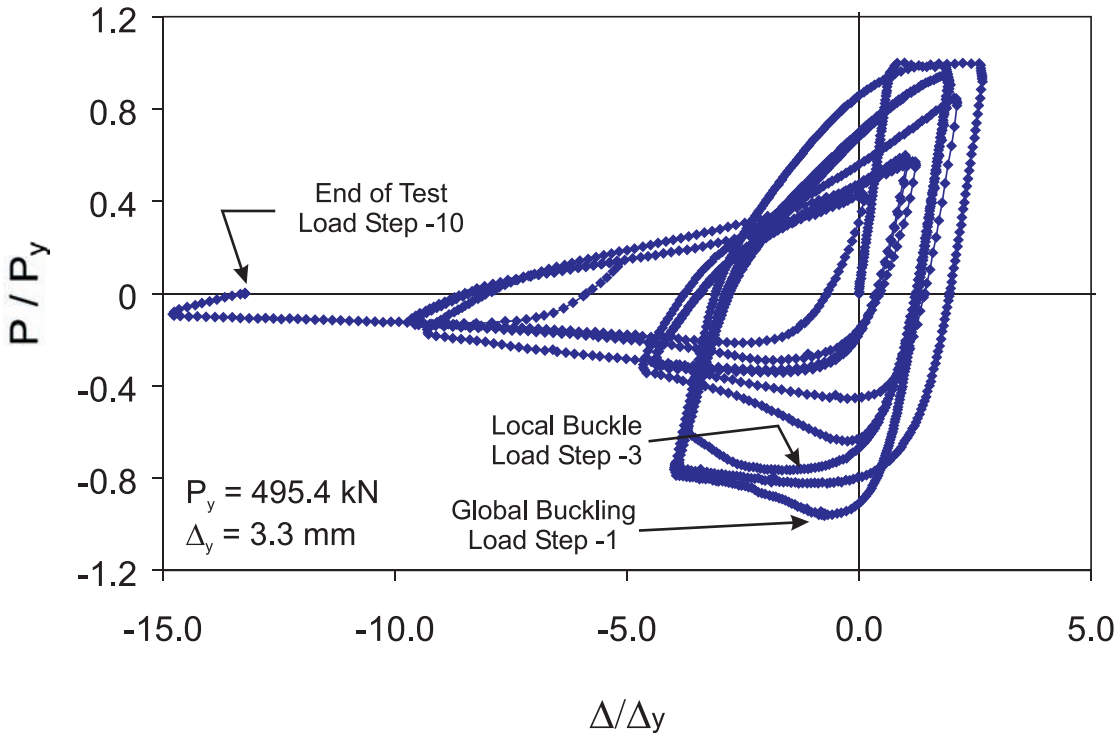

Figure 5.13 Normalized Axial Load - Axial Displacement, Specimen C27-100-0

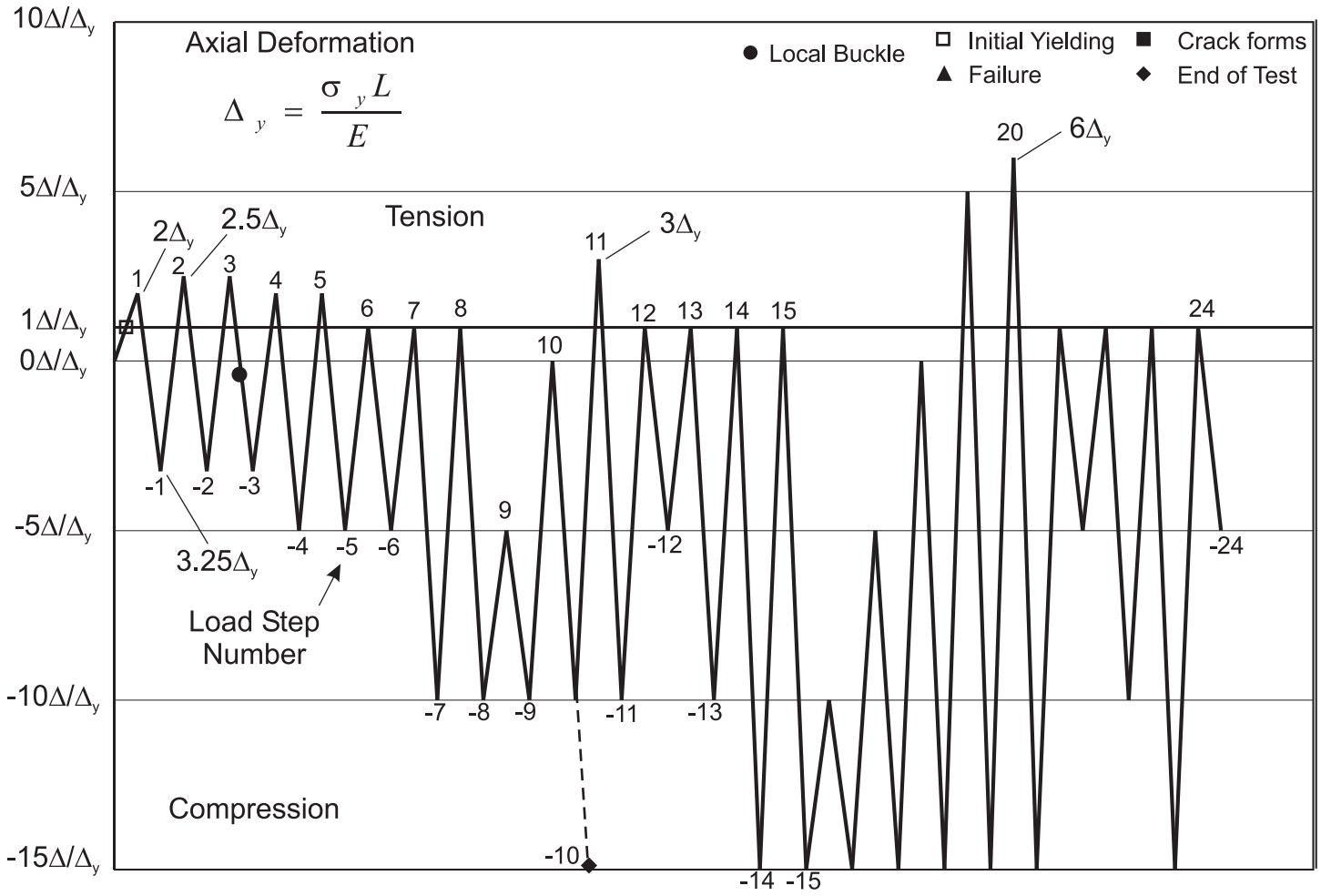

Figure 5.14 Displacement History with Events of Interest Noted, Specimen C27-100-0

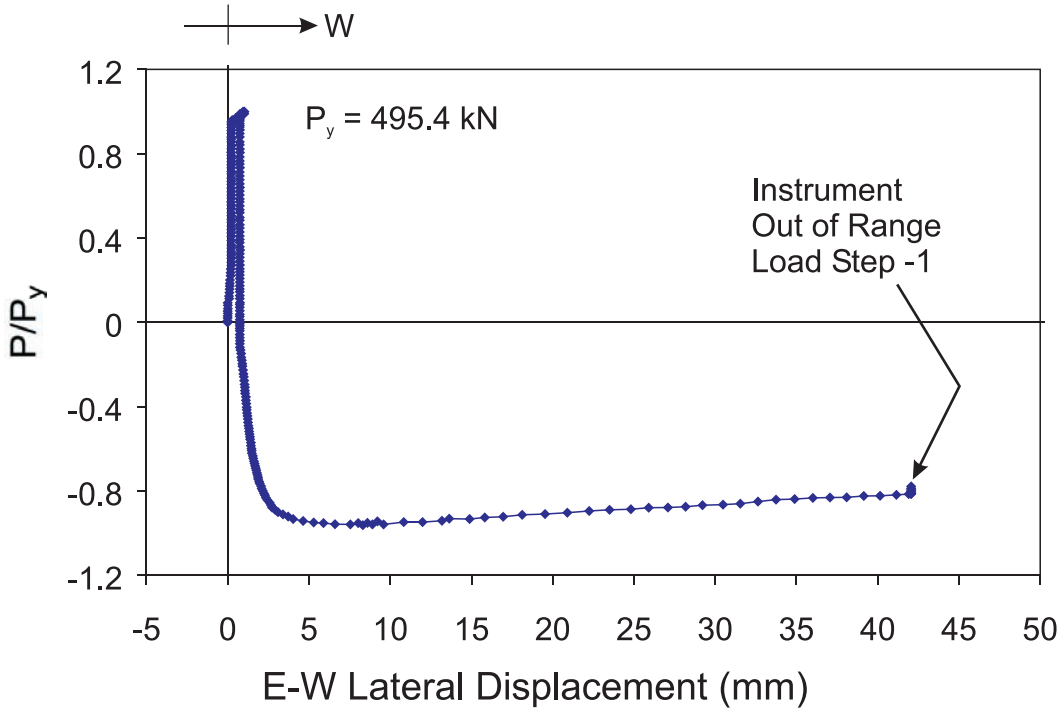

Figure 5.15 Measured Lateral displacement in the East-West Direction, Specimen C27-100-0

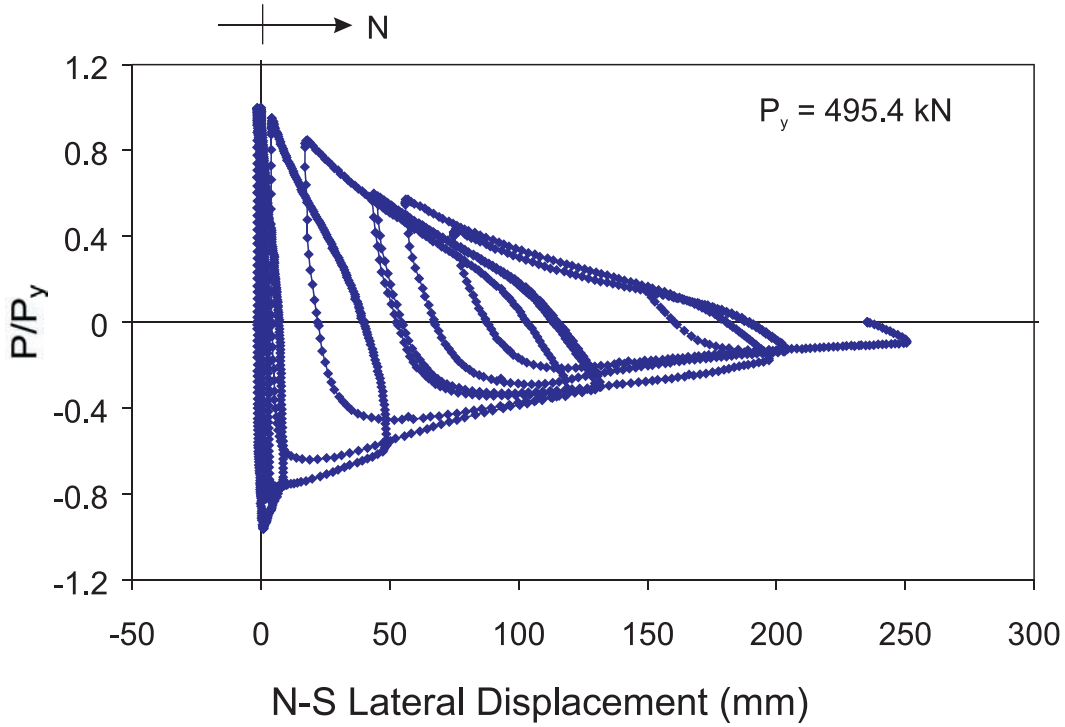

Figure 5.16 Measured Lateral Displacement in the North-South Direction, Specimen C27-100-0

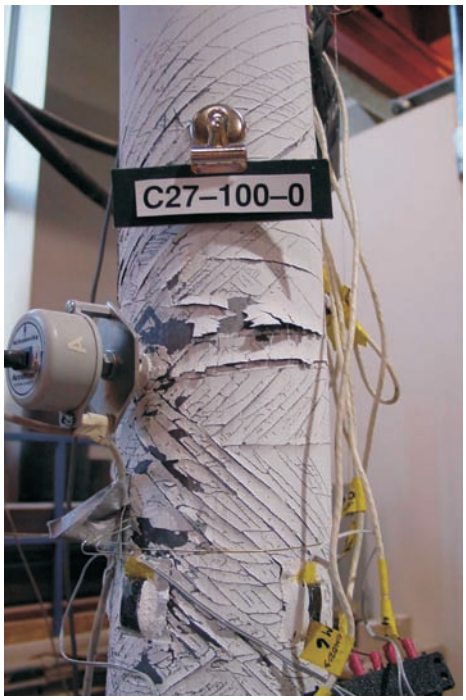

Figure 5.17 Side View of Yielding at Mid-height (Load Step -1), Specimen C27-100-0

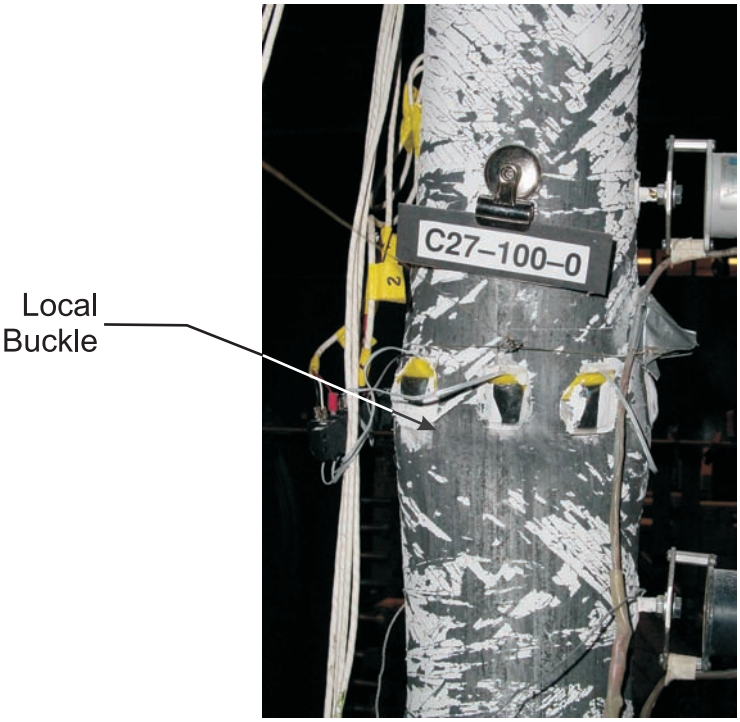

Figure 5.18 Front View of Local Buckle at Mid-height on Southern Face (Load Step -3), Specimen C27-100-0

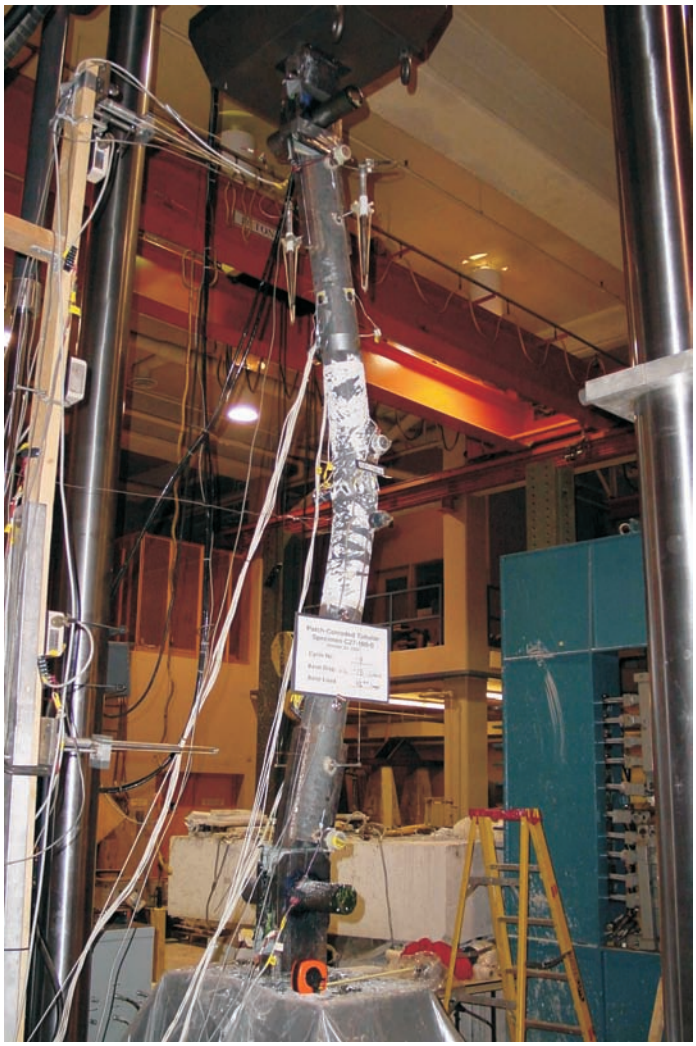

Figure 5.19 Final State of Specimen C27-100-0

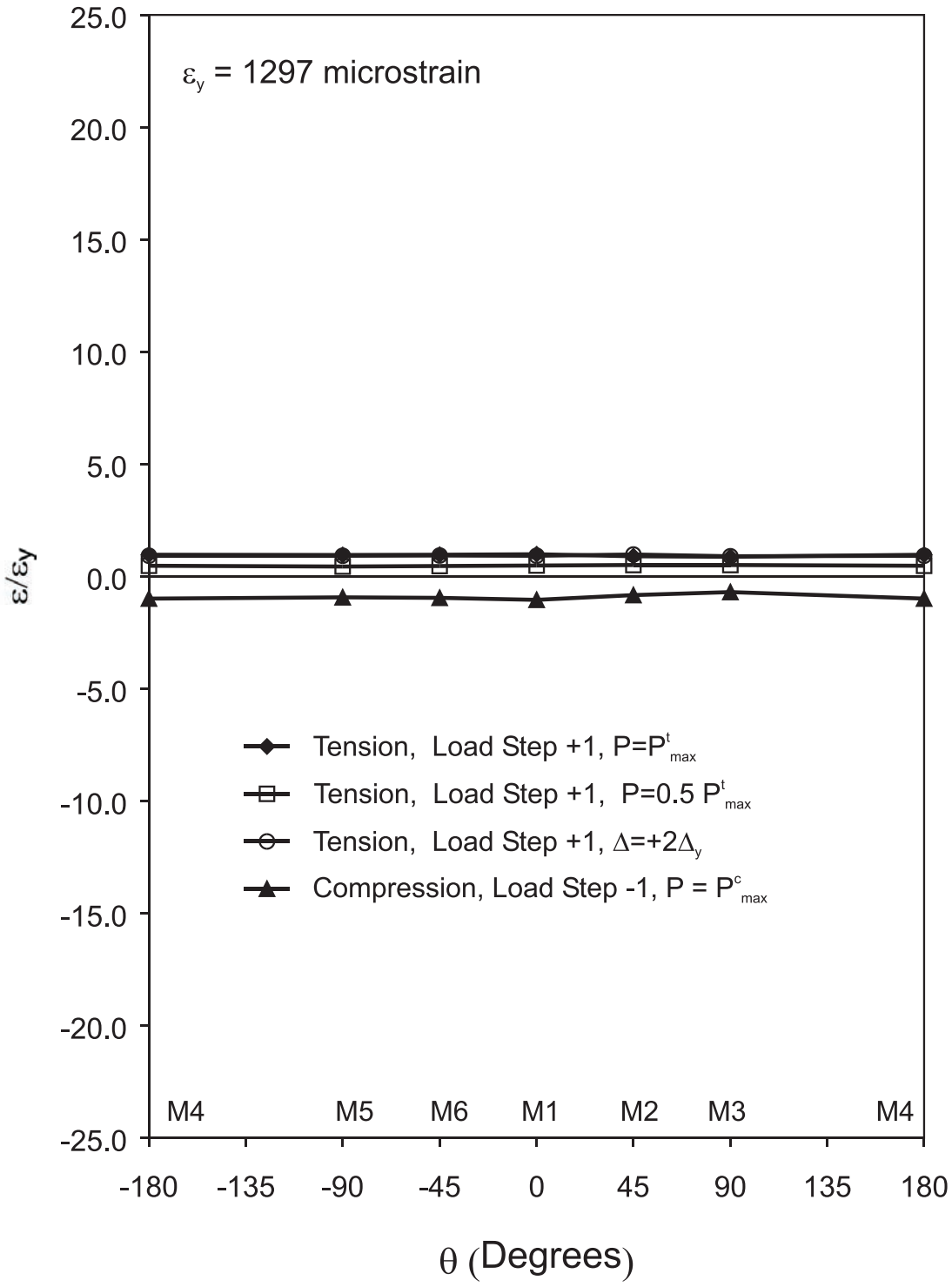

Figure 5.20 Strain Distribution of Cross Section at Mid-height, Specimen C27-100-0

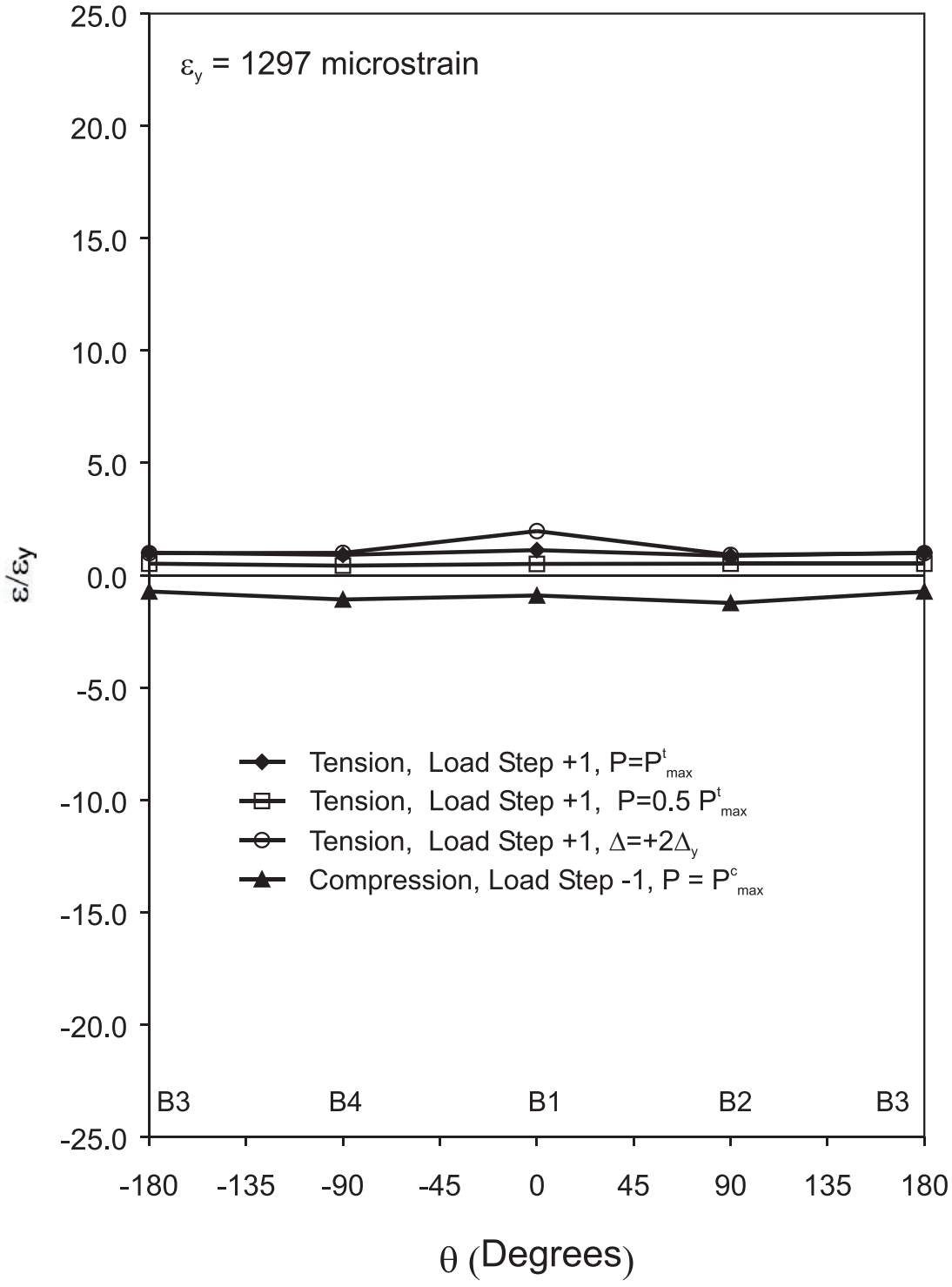

Figure 5.21 Strain Distribution of Cross Section at Lower Quarter-point, Specimen C27-100-0

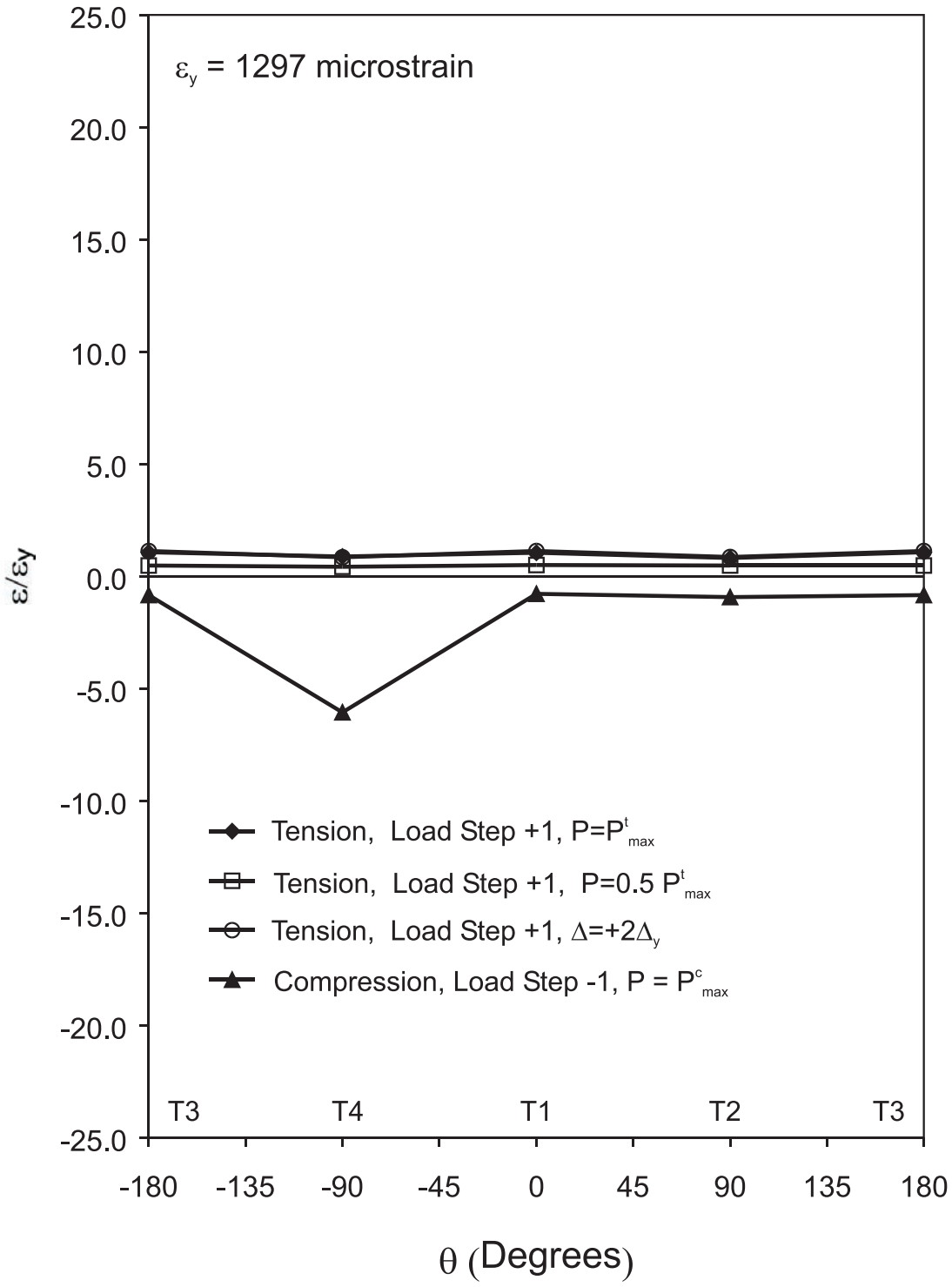

Figure 5.22 Strain Distribution of Cross Section at Upper Quarter-point, Specimen C27-100-0

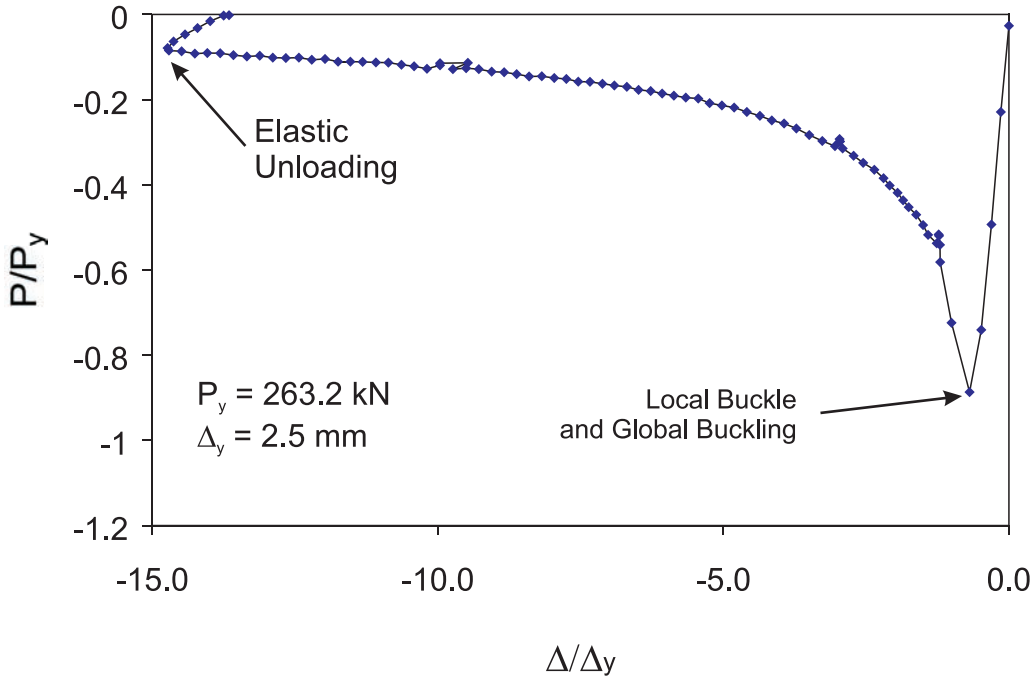

Figure 5.23 Normalized Axial Load - Axial Displacement, Specimen M40-33-95

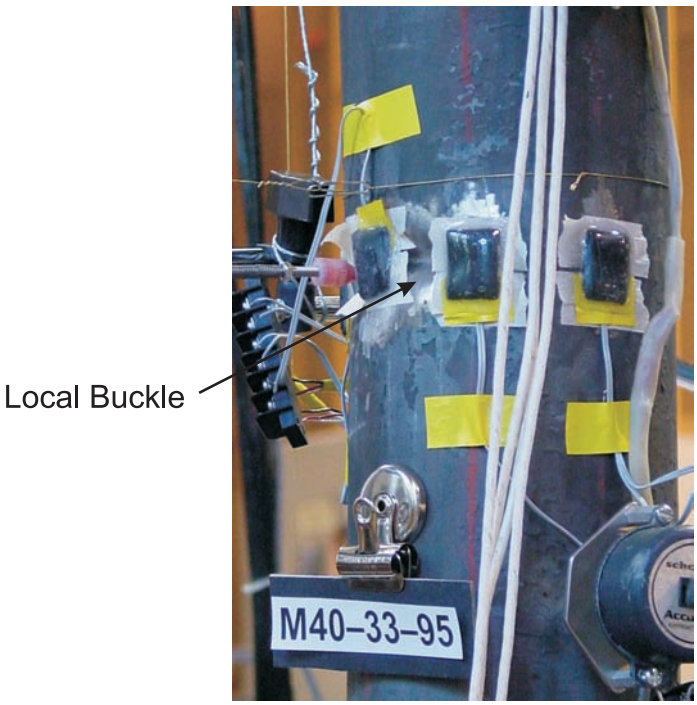

Figure 5.24 View of Local Buckle at Mid-height, Specimen M40-33-95

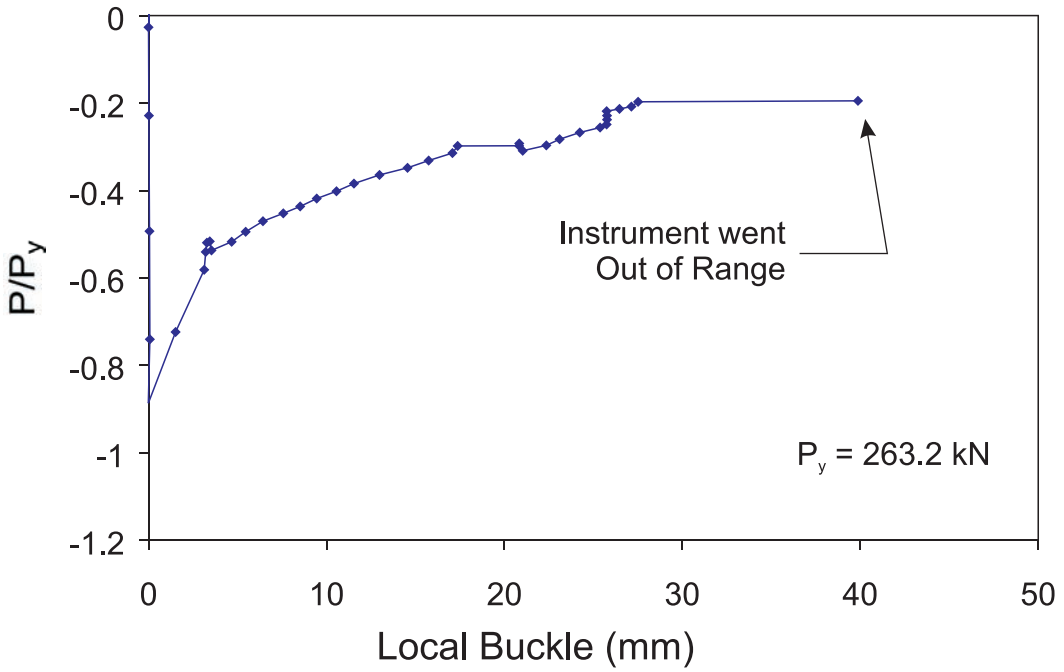

Figure 5.25 Measured Local Displacement of Buckle in Corrosion Patch, Specimen M40-33-95

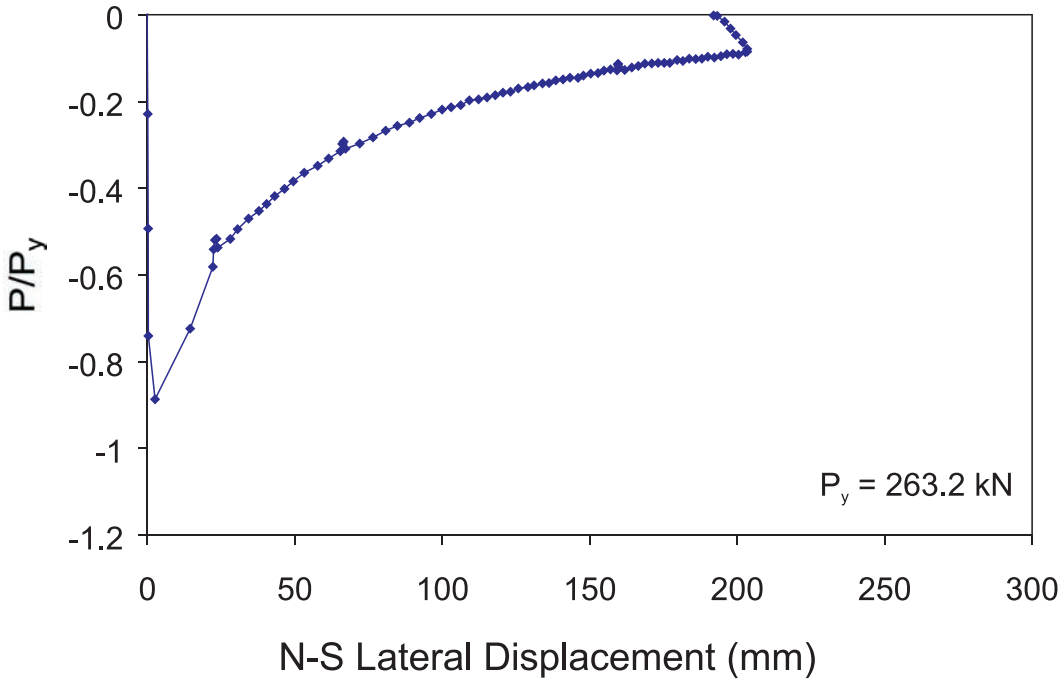

Figure 5.26 Measured Lateral Displacement in the North-South Direction, Specimen M40-33-95

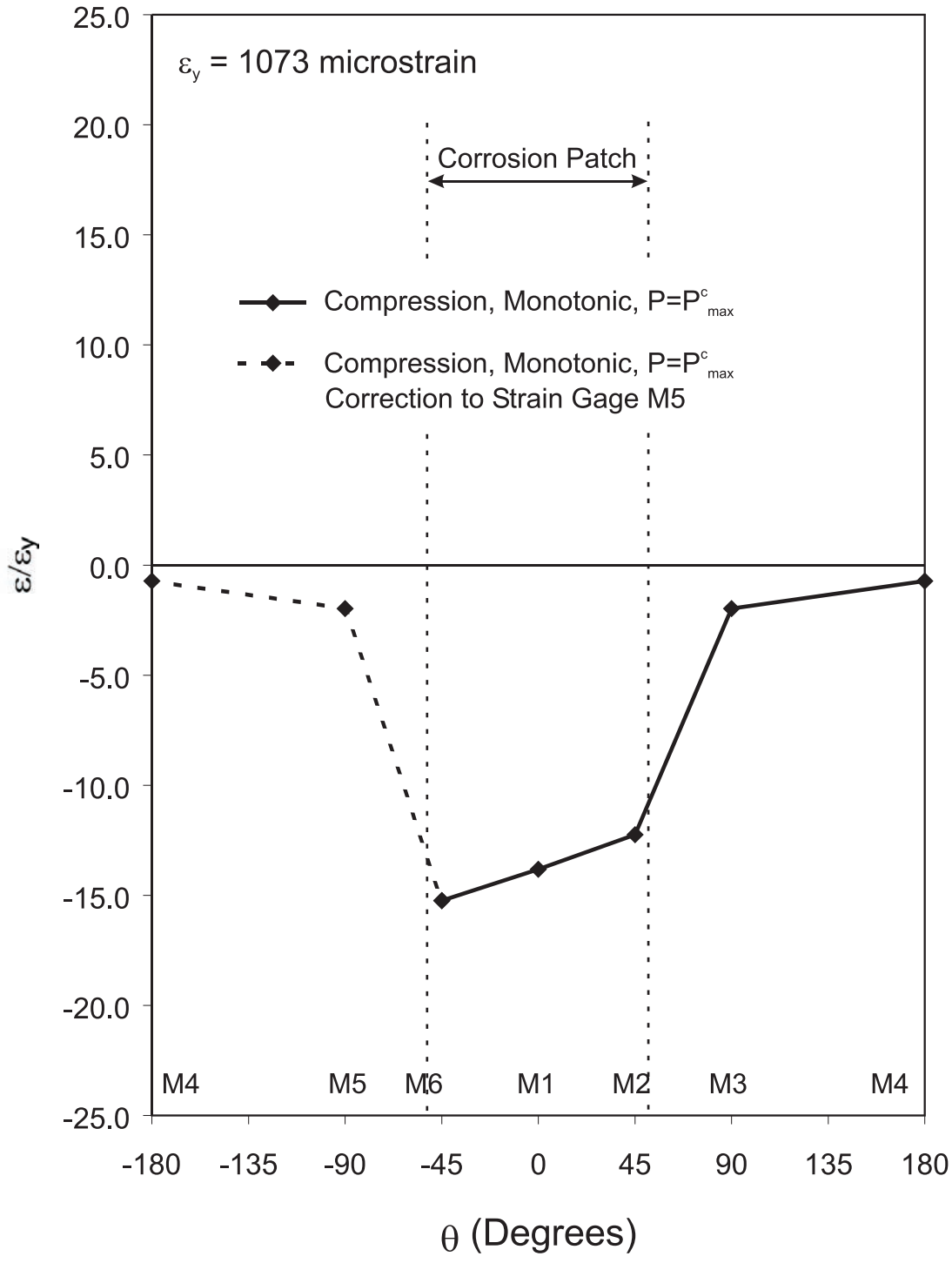

Figure 5.27 Strain Distribution of Cross Section at Mid-height, Specimen M40-33-95

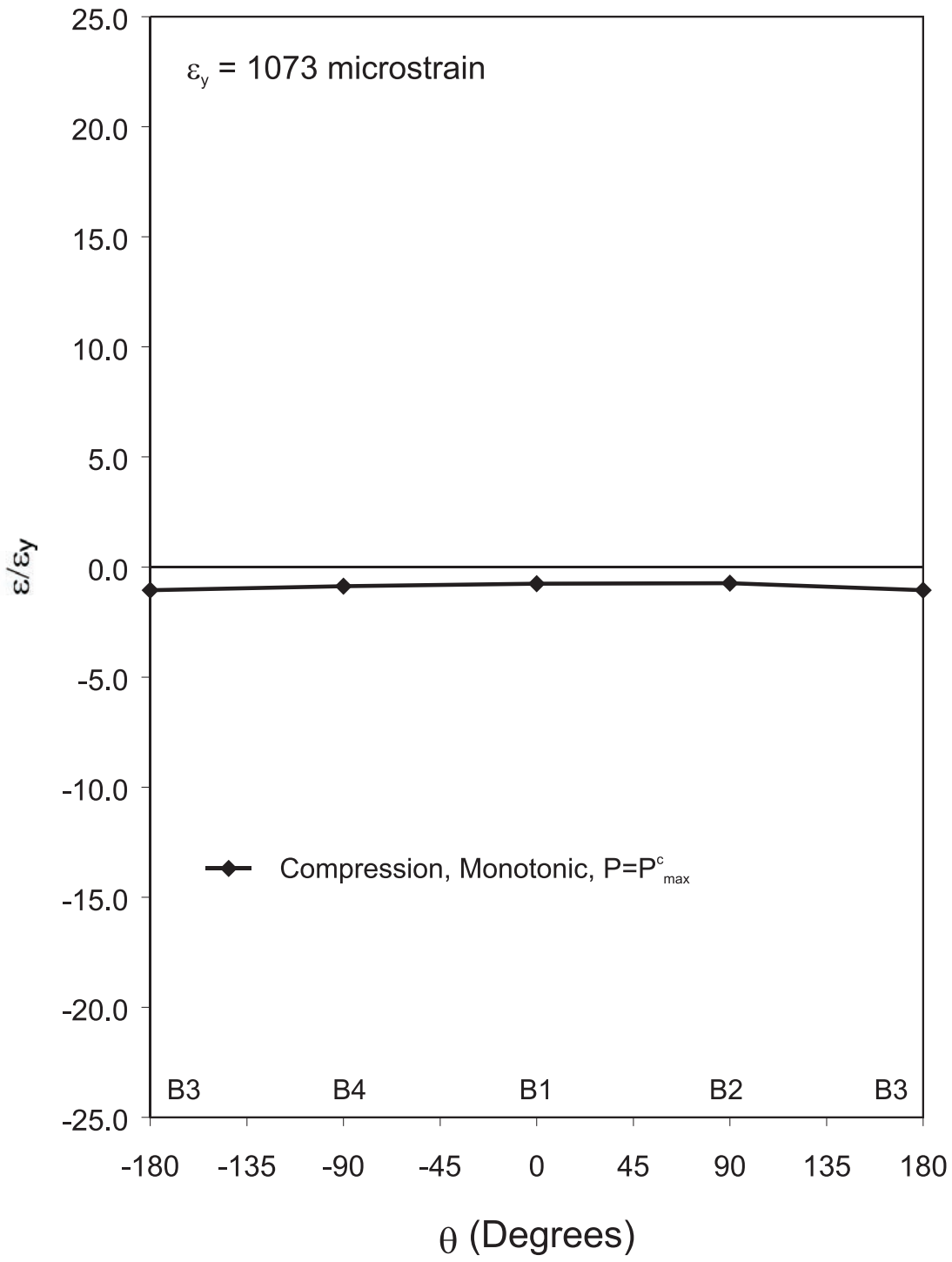

Figure 5.28 Strain Distribution of Cross Section at Lower Quarter-point, Specimen M40-33-95

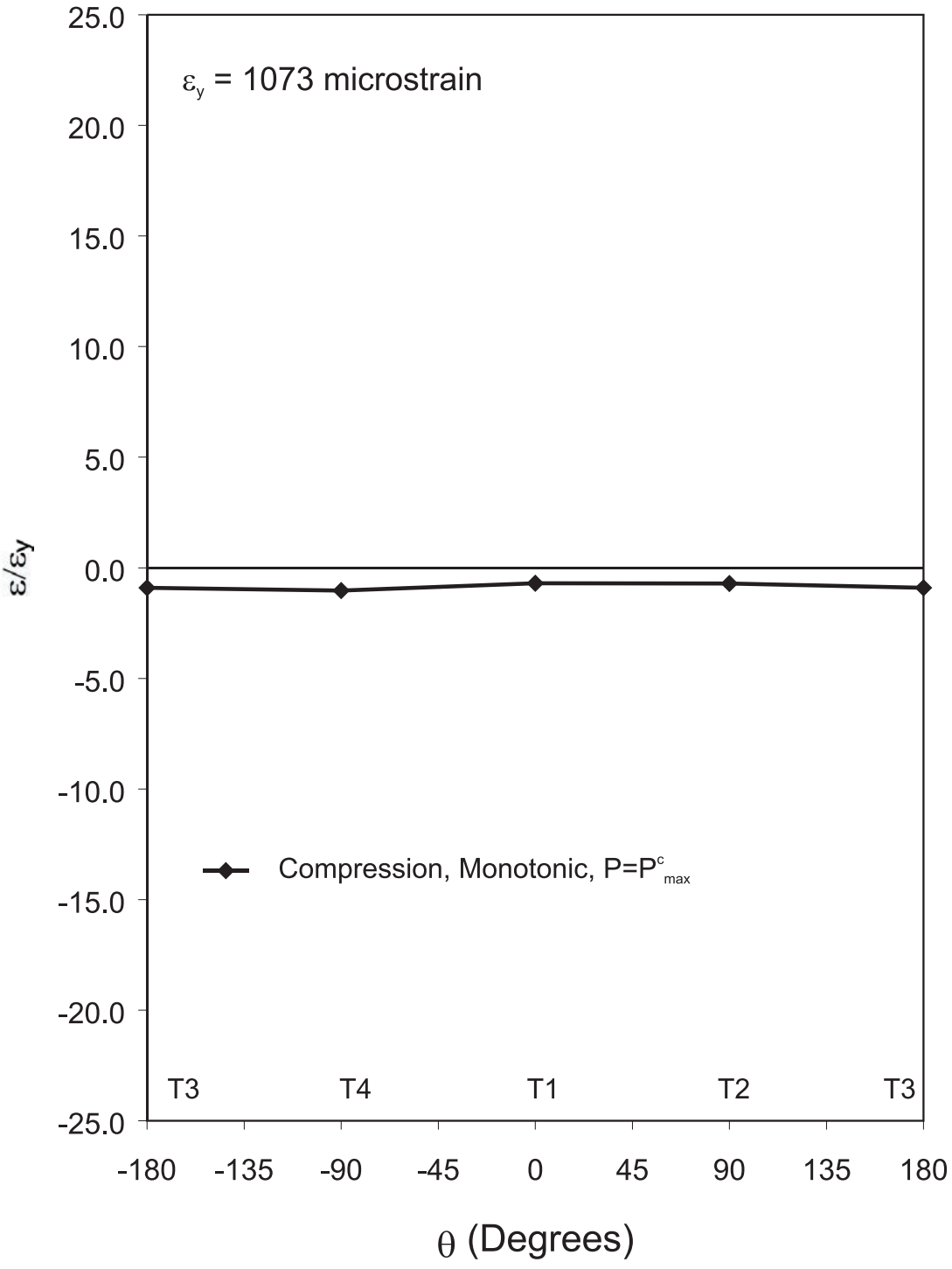

Figure 5.29 Strain Distribution of Cross Section at Upper Quarter-point, Specimen M40-33-95

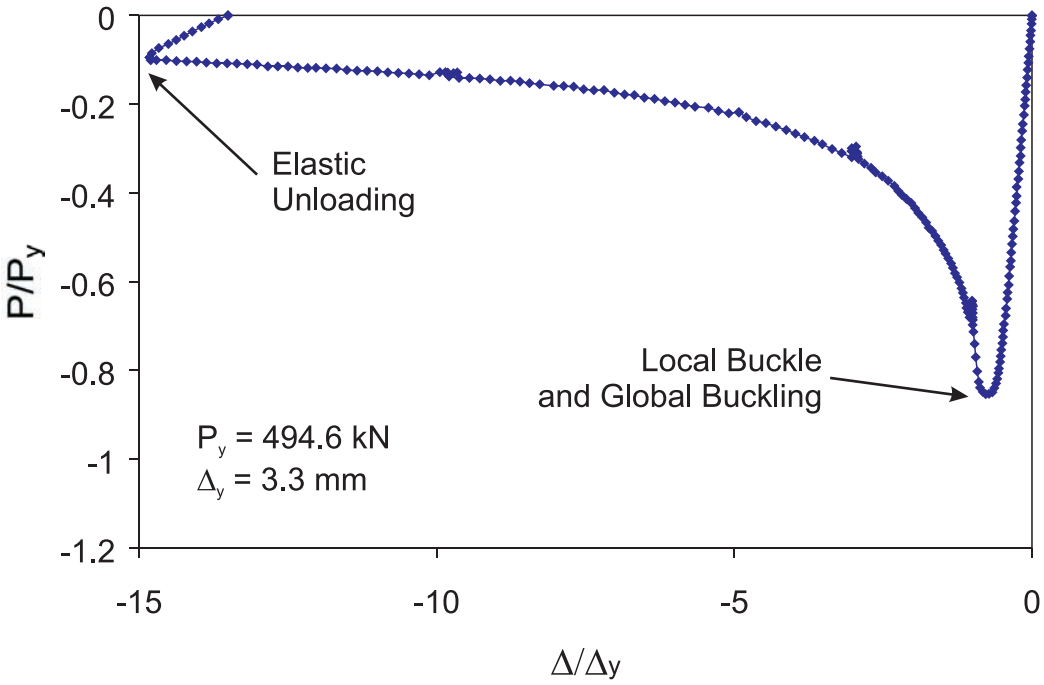

Figure 5.30 Normalized Axial Load vs Normalized Axial Displacement, Specimen M27-33-95

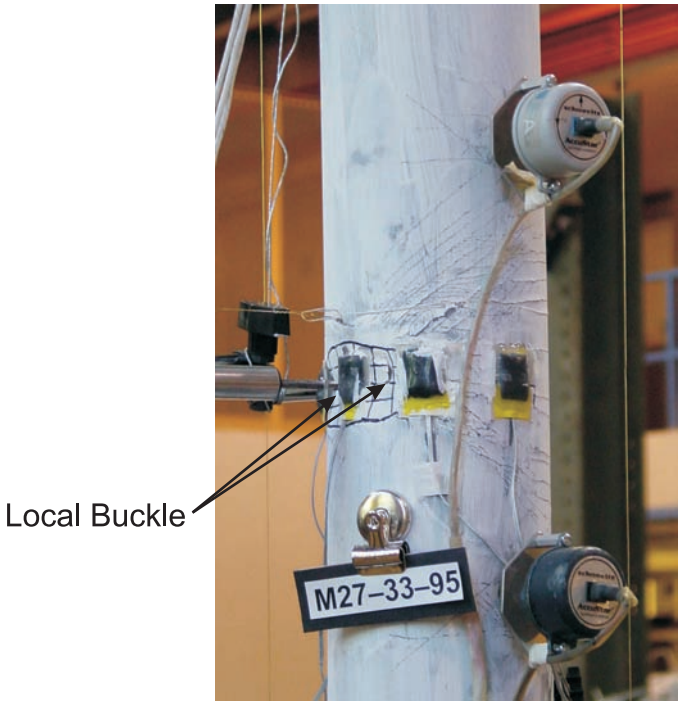

Figure 5.31 View of Local Buckle at Mid-height, Specimen M27-33-95

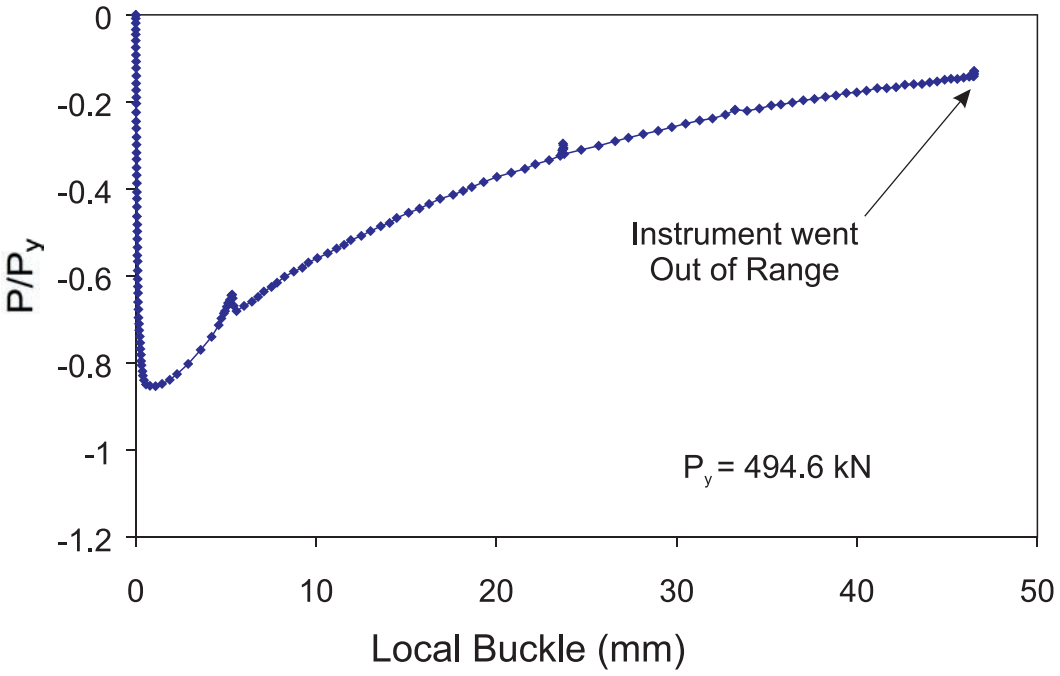

Figure 5.32 Measured Local Displacement of Buckle in Corrosion Patch, Specimen M27-33-95

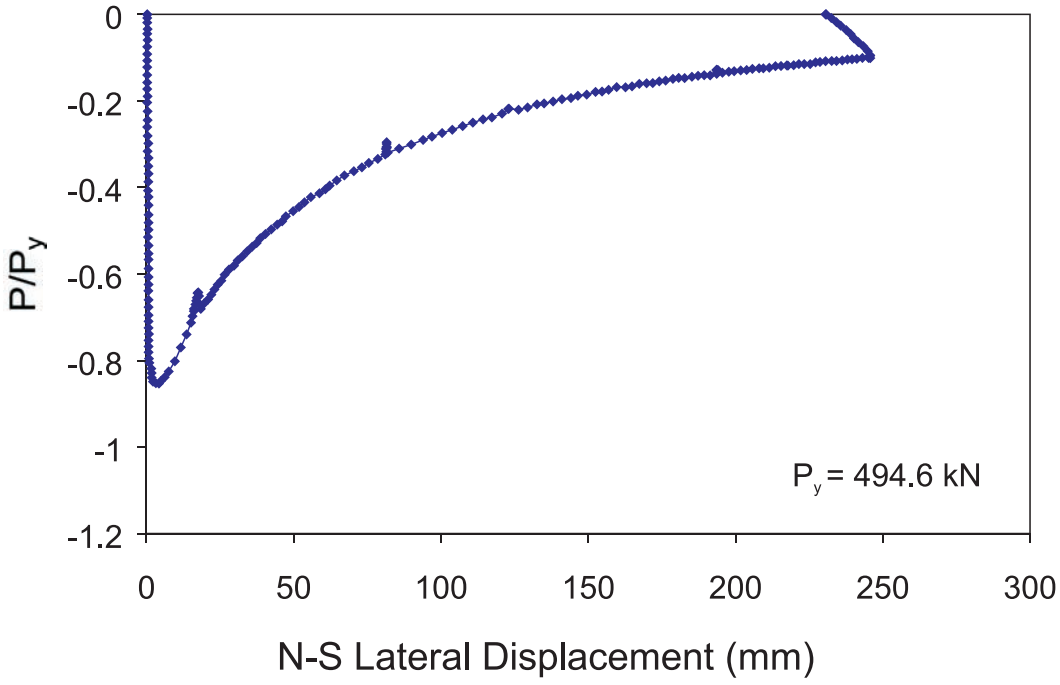

Figure 5.33 Measured Lateral Displacement in the North-South Direction, Specimen M27-33-95

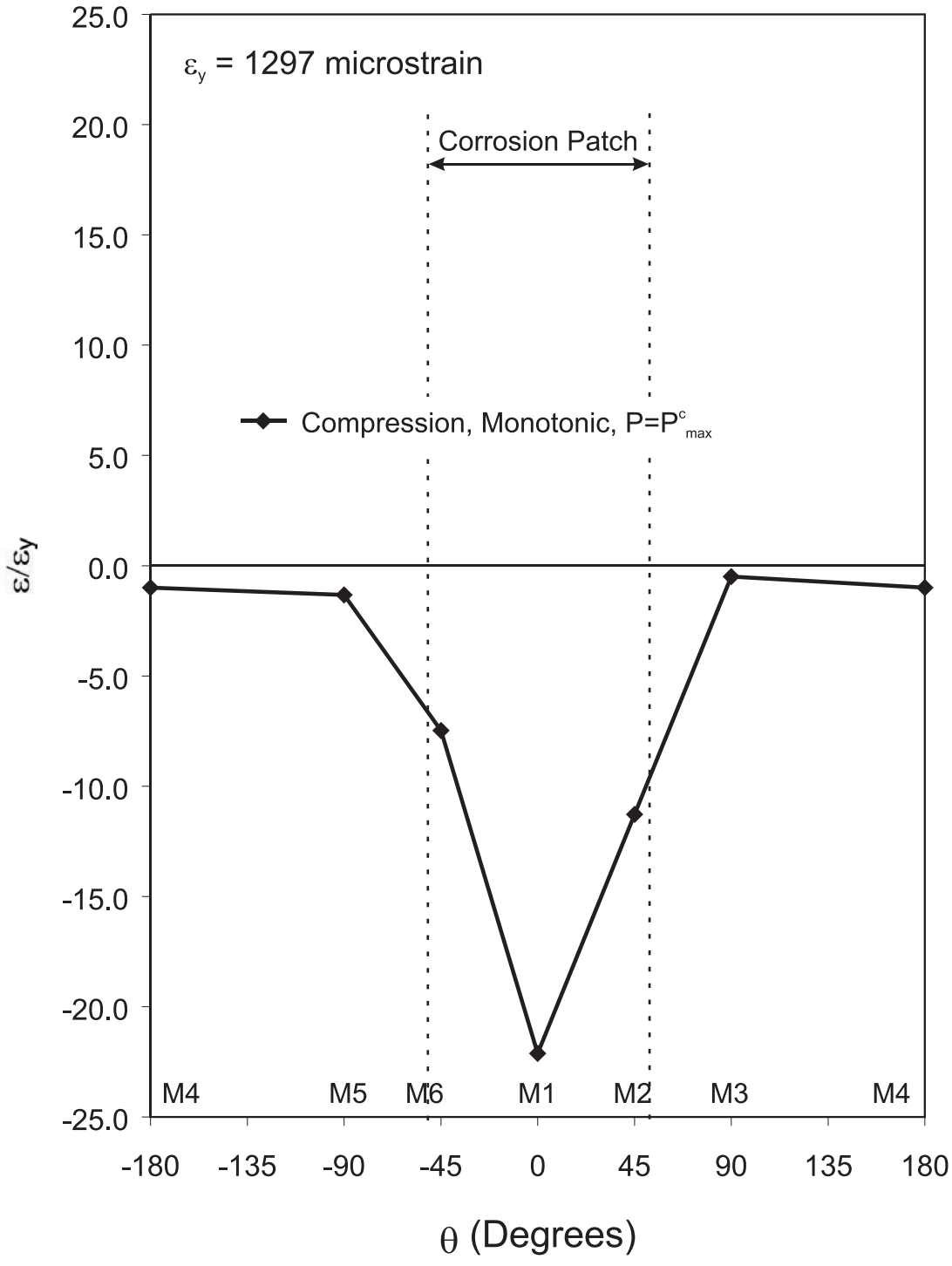

Figure 5.34 Strain Distribution of Cross Section at Mid-height, Specimen M27-33-95

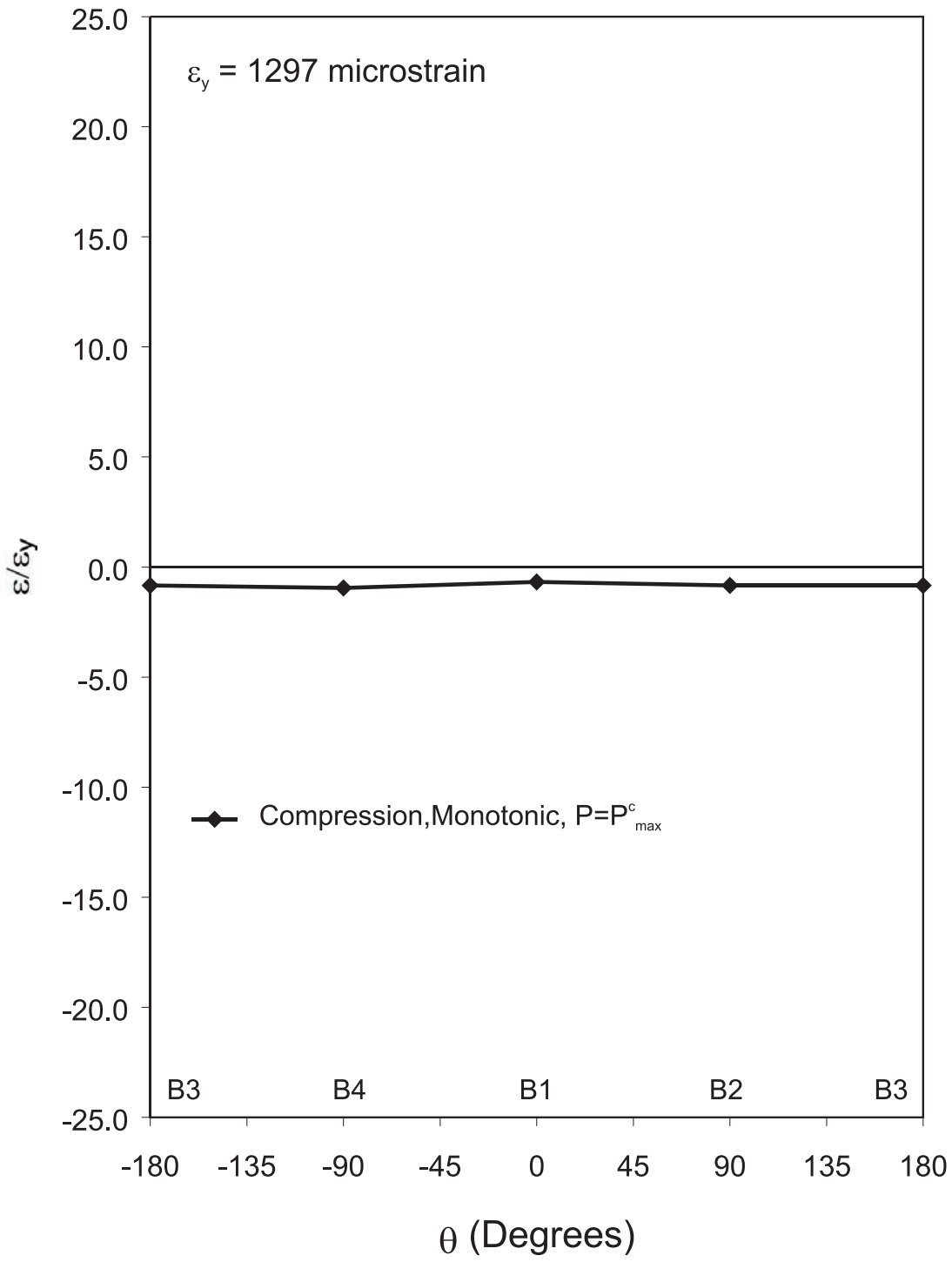

Figure 5.35 Strain Distribution of Cross Section at Lower Quarter-point, Specimen M27-33-95

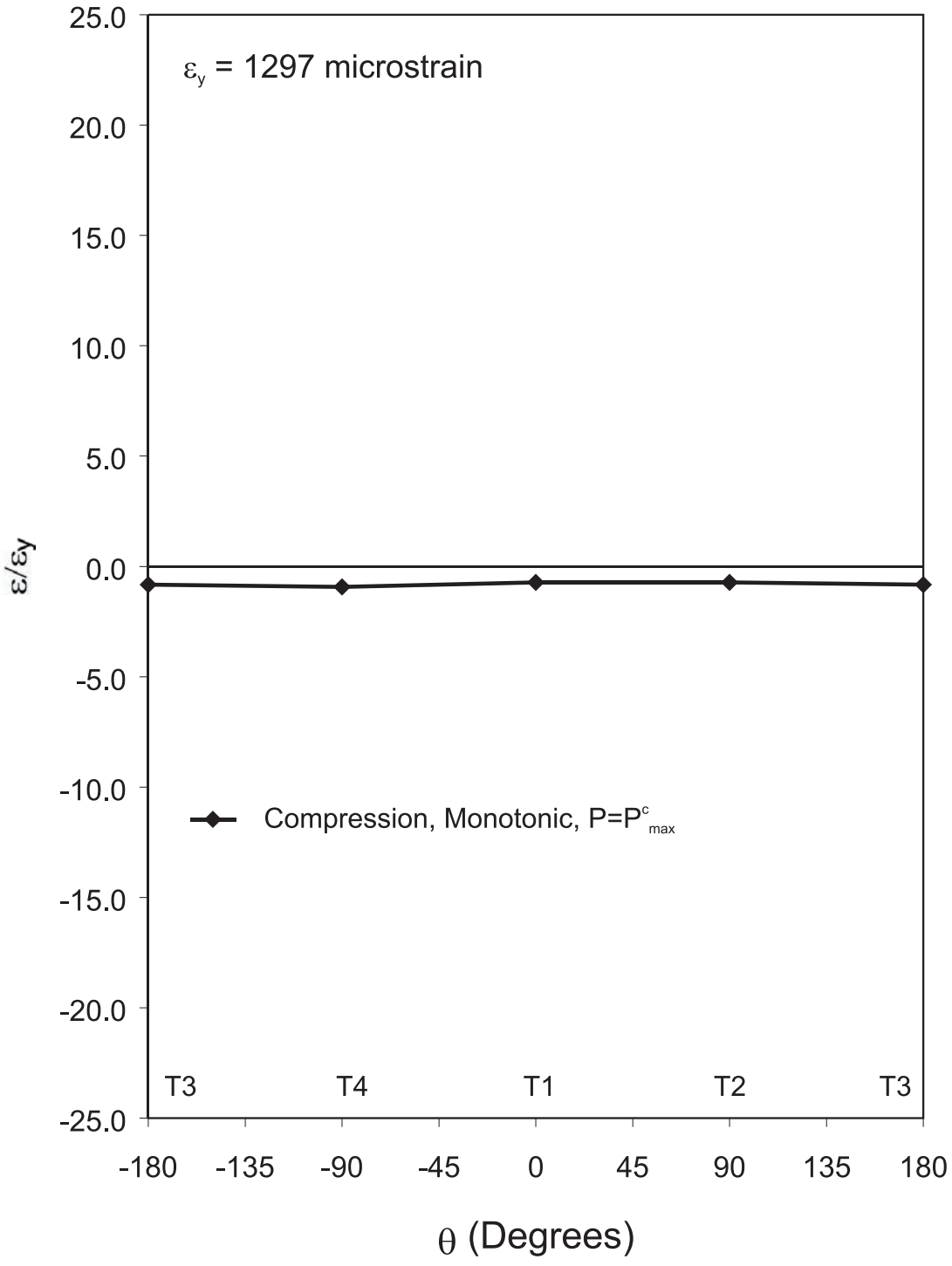

Figure 5.36 Strain Distribution of Cross Section at Upper Quarter-point, Specimen M27-33-95

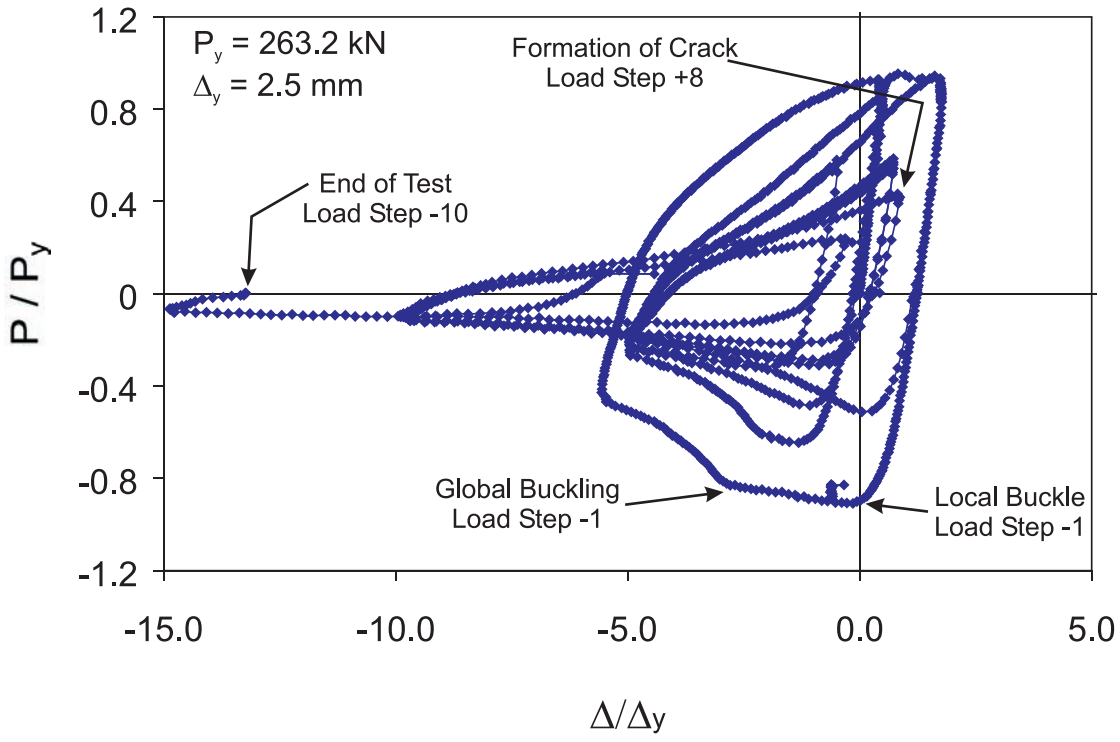

Figure 5.37 Normalized Axial Load - Axial Displacement, Specimen C40-67-95

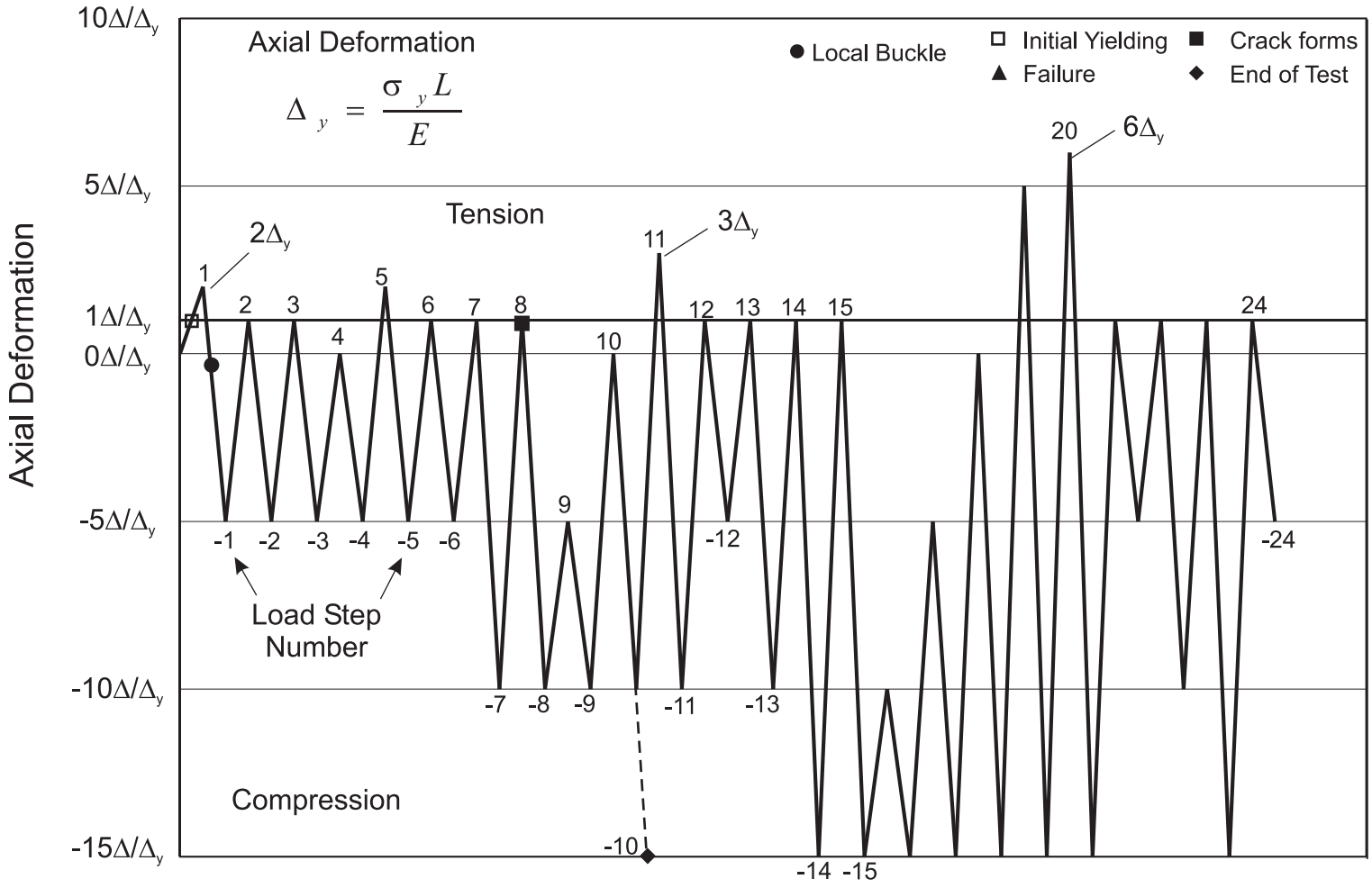

Figure 5.38 Displacement History with Events of Interest Noted
Specimen C40-67-95

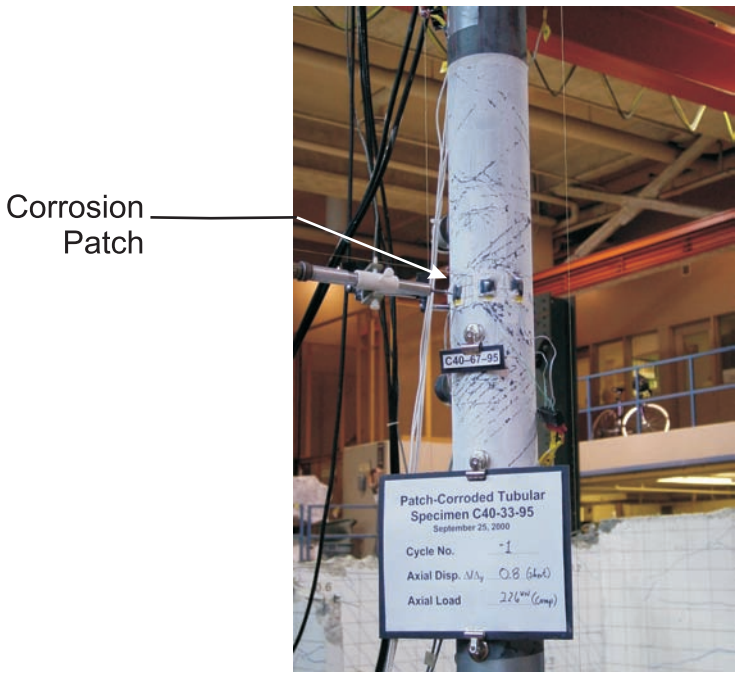

Figure 5.39 Side View of Yielding at Mid-height (Load Step -1), Specimen C40-67-95

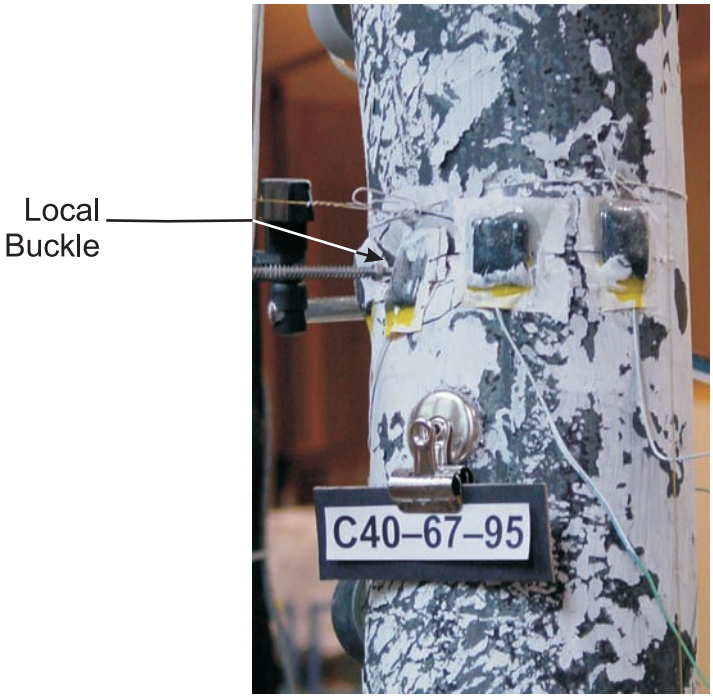

Figure 5.40 Side View of Local Buckle at Mid-height (Load Step -1), Specimen C40-67-95

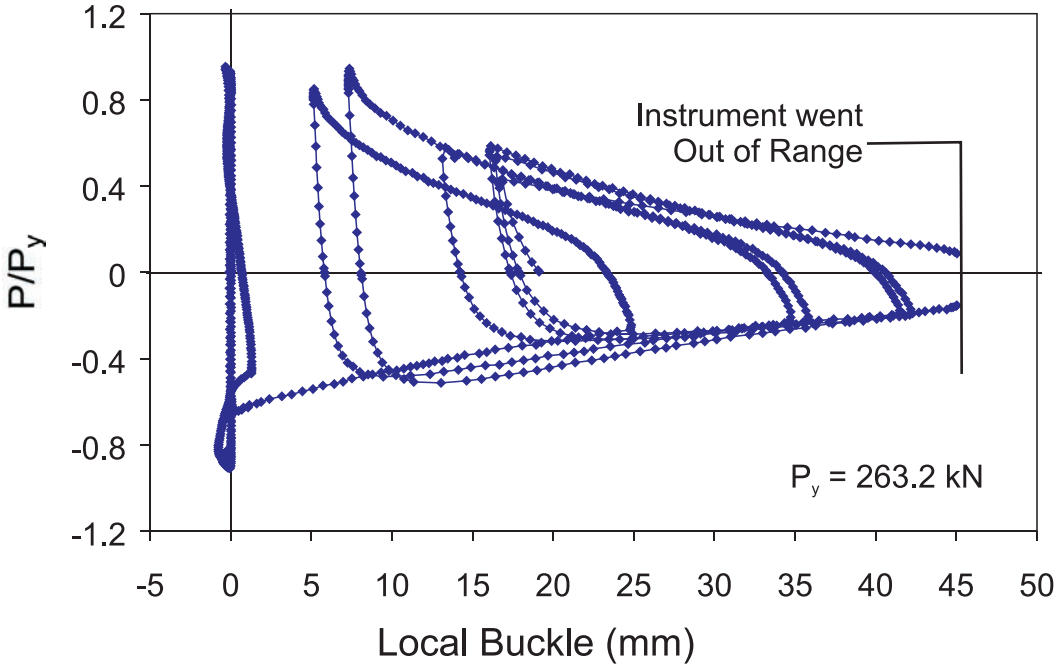

Figure 5.41 Measured Local Displacement of Buckle in Corrosion Patch, Specimen C40-67-95

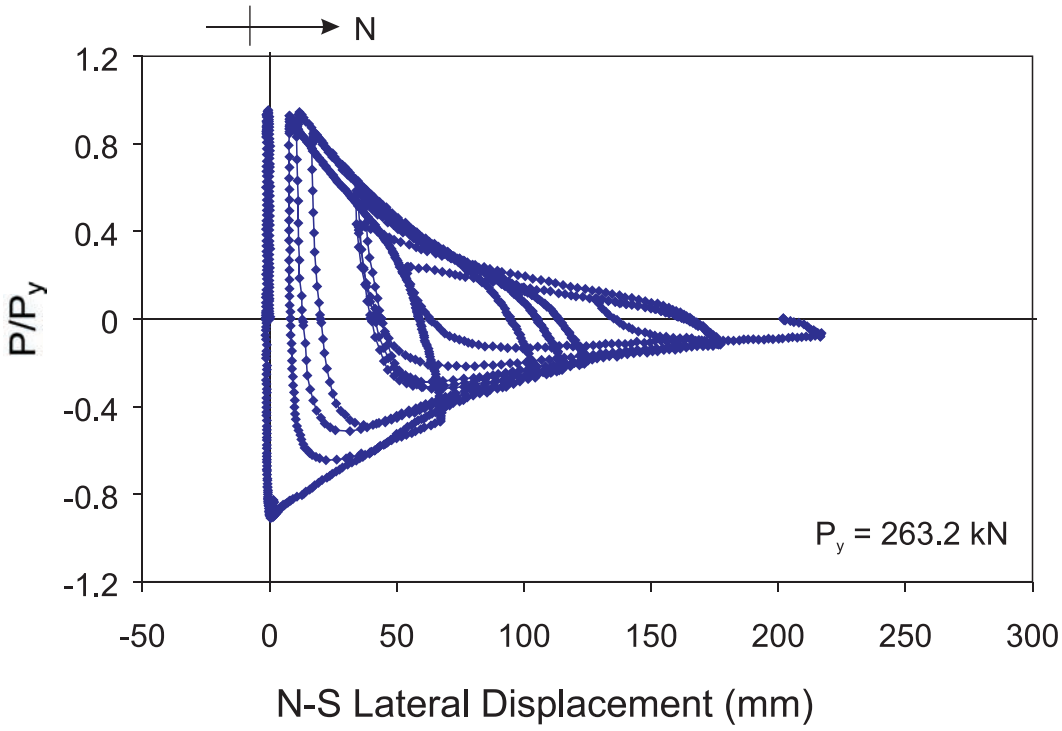

Figure 5.42 Lateral Displacement Measured in the North-South Direction, Specimen C40-67-95

Figure 5.43 Initial Cracking at Edges of Local Buckle
(Load Step +8), Specimen C40-67-95

Figure 5.44 Final State of Specimen C40-67-95

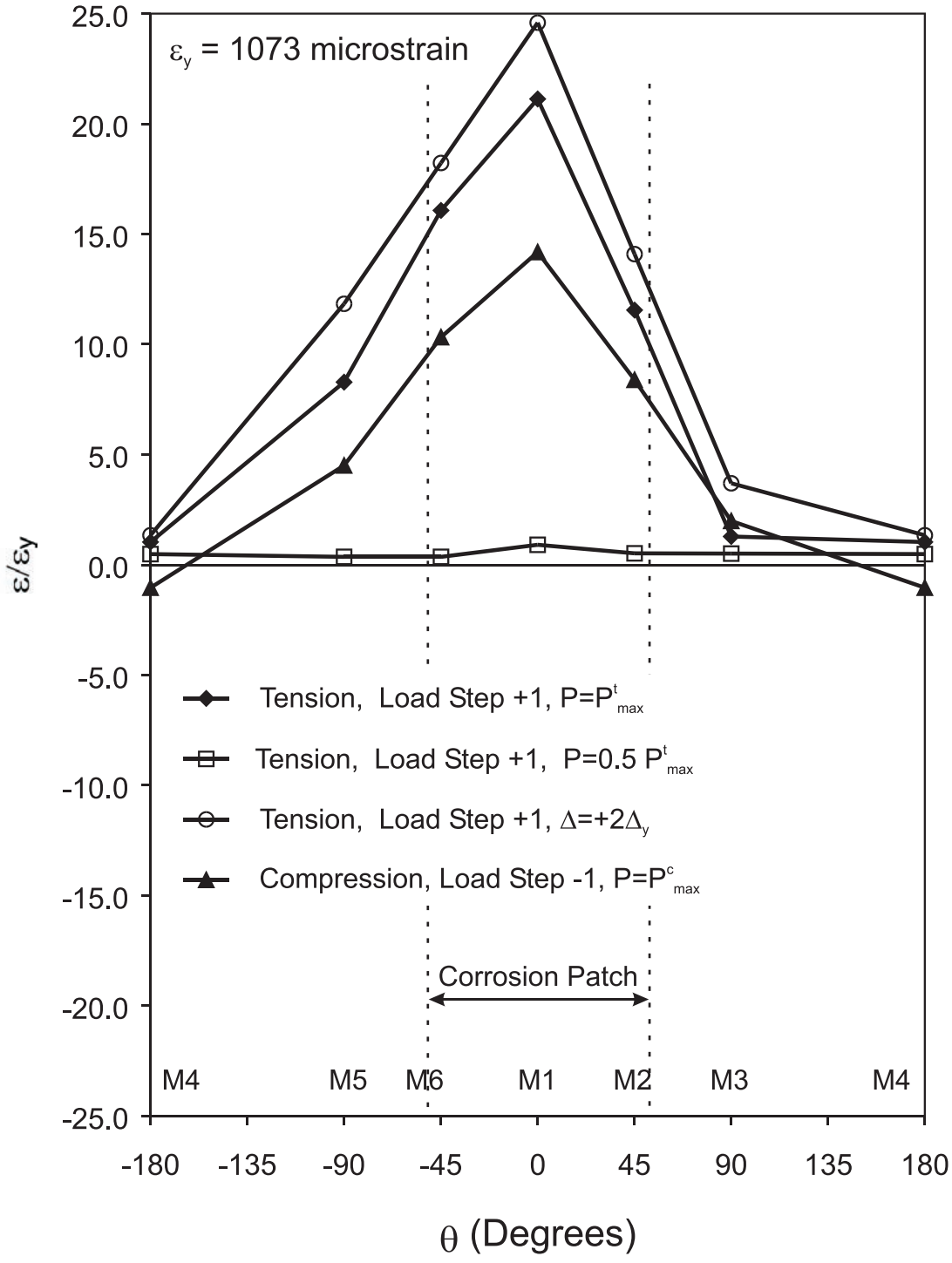

Figure 5.45 Strain Distribution of Cross Section at Mid-height, Specimen C40-67-95

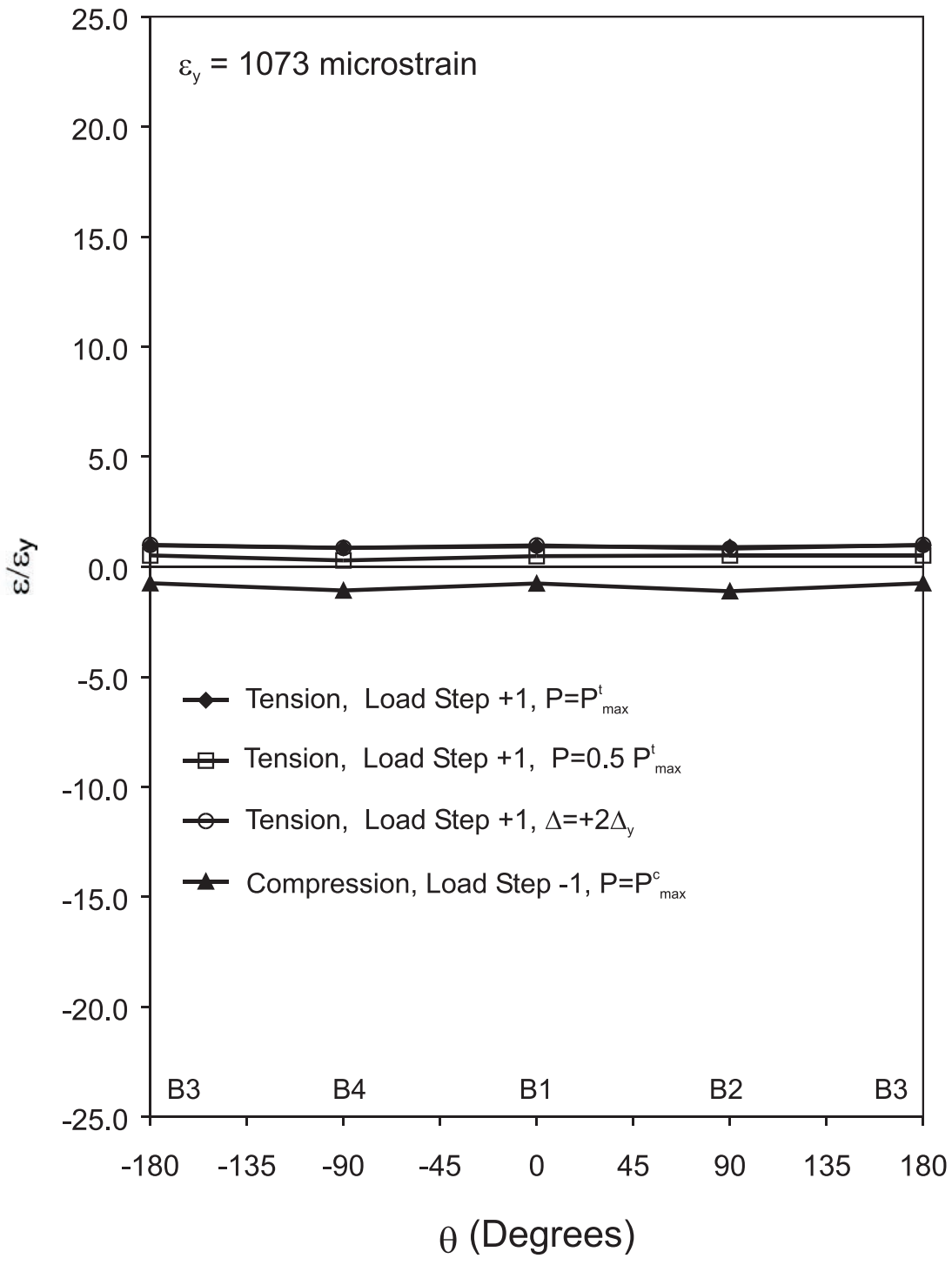

Figure 5.46 Strain Distribution of Cross Section at Lower Quarter-point, Specimen C40-67-95

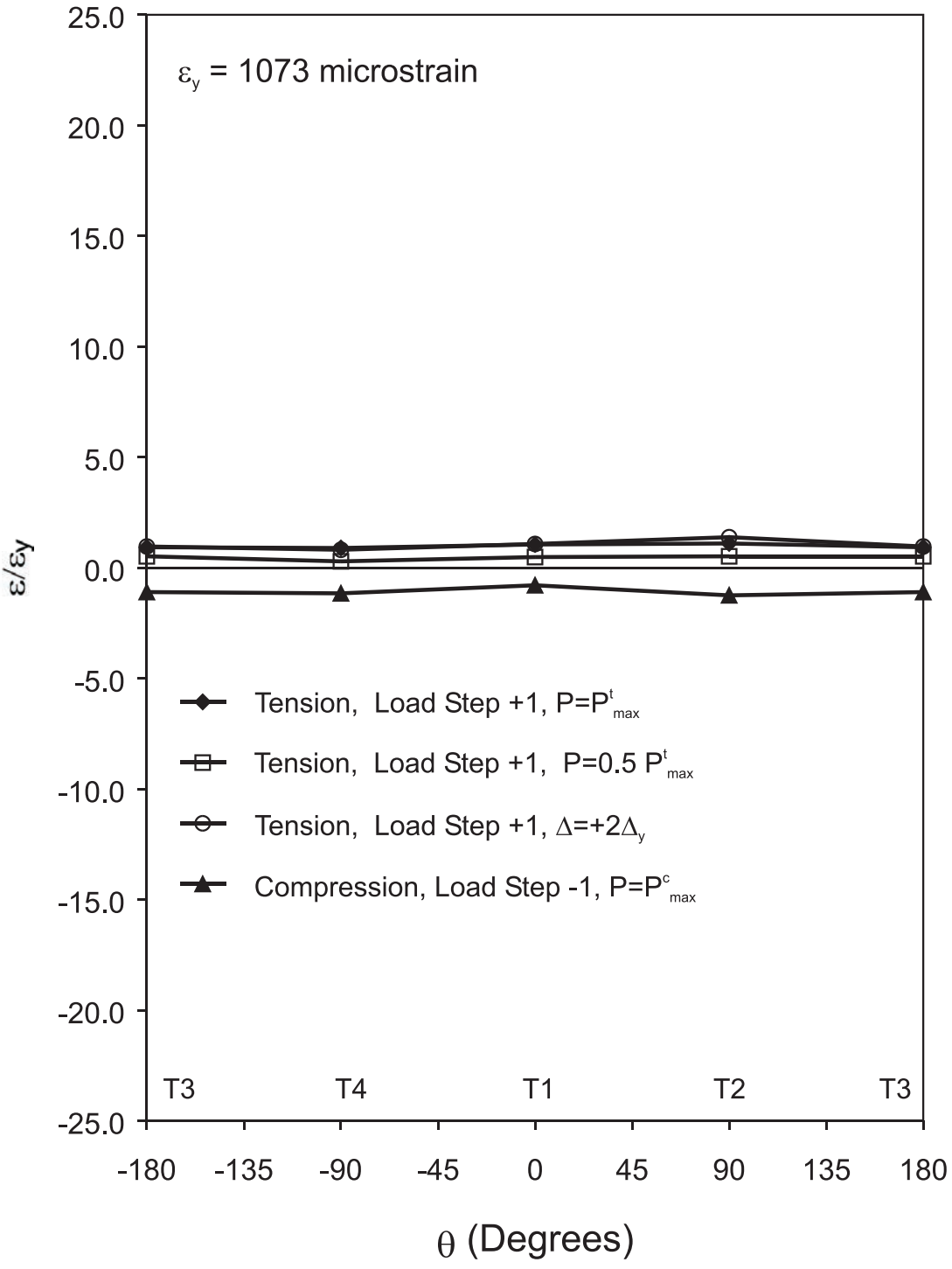

Figure 5.47 Strain Distribution of Cross Section at Upper Quarter-point, Specimen C40-67-95

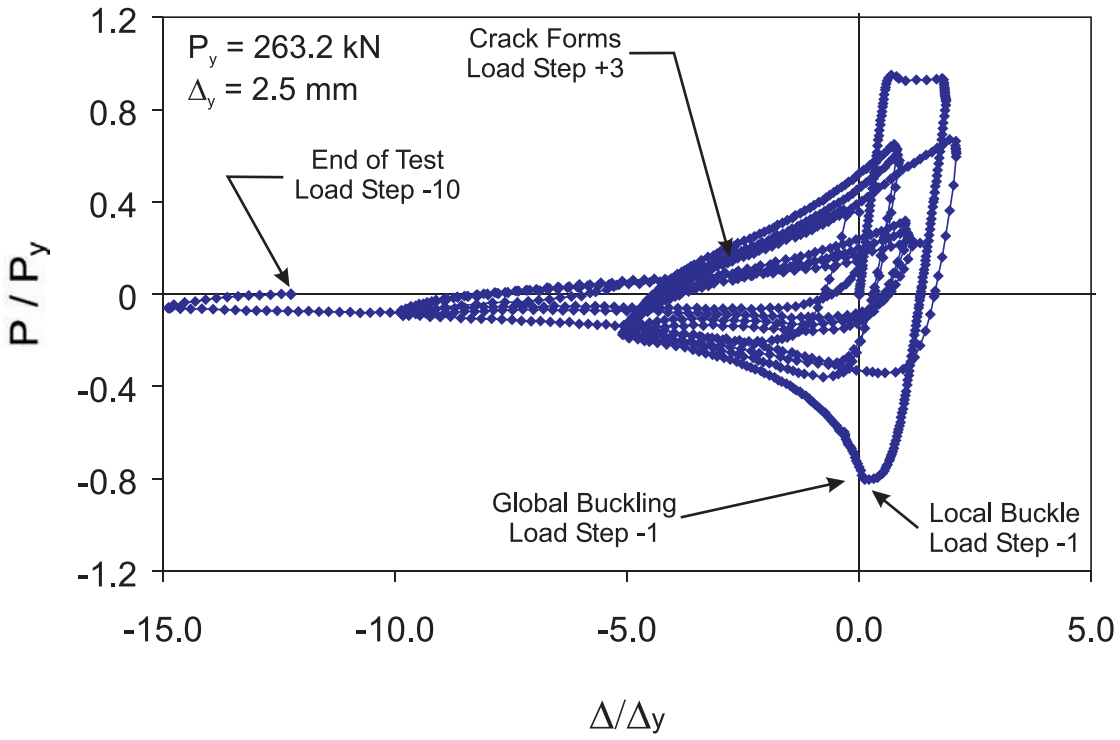

Figure 5.48 Normalized Axial Load - Axial Displacement, Specimen C40-33-95

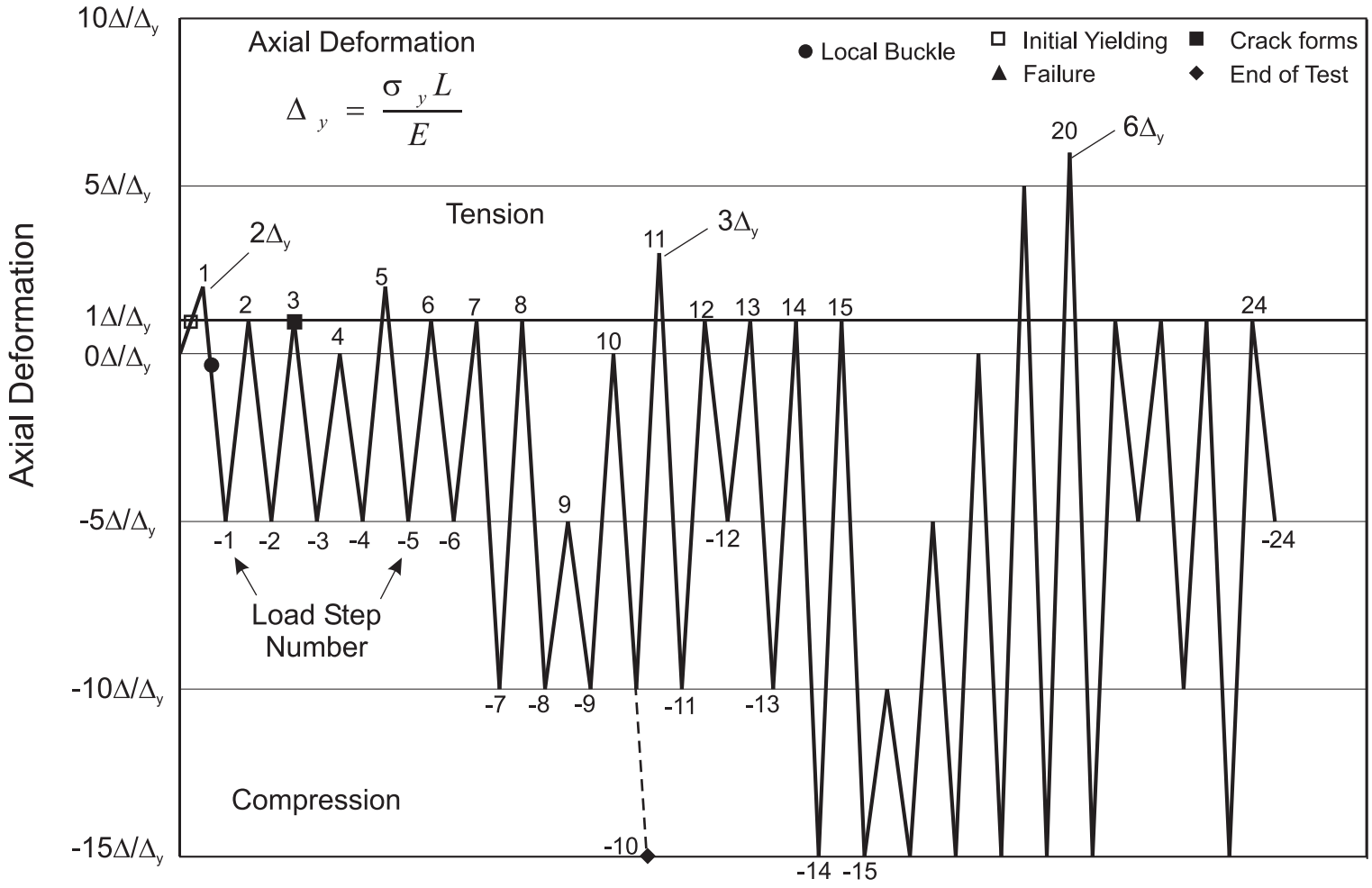

Figure 5.49 Displacement History with Events of Interest Noted, Specimen C40-33-95

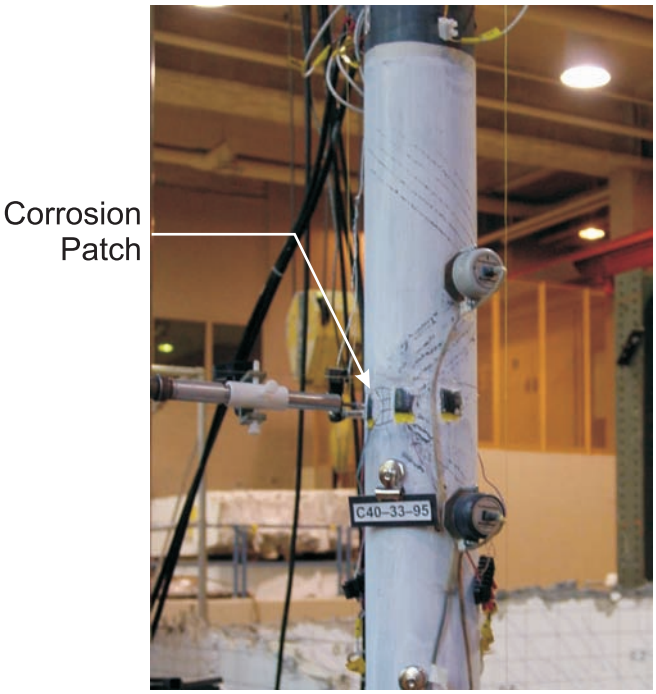

Figure 5.50 Side View of Yielding at Mid-height (Load Step -1), Specimen C40-33-95

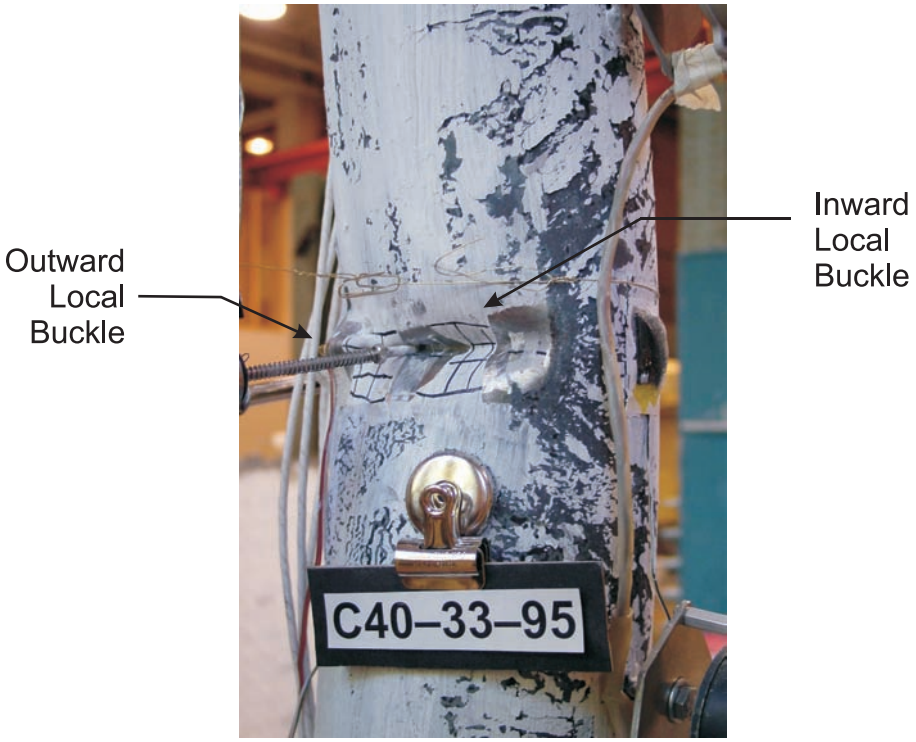

Figure 5.51 Side View of Local Buckle at Mid-height (Load Step -2), Specimen C40-33-95

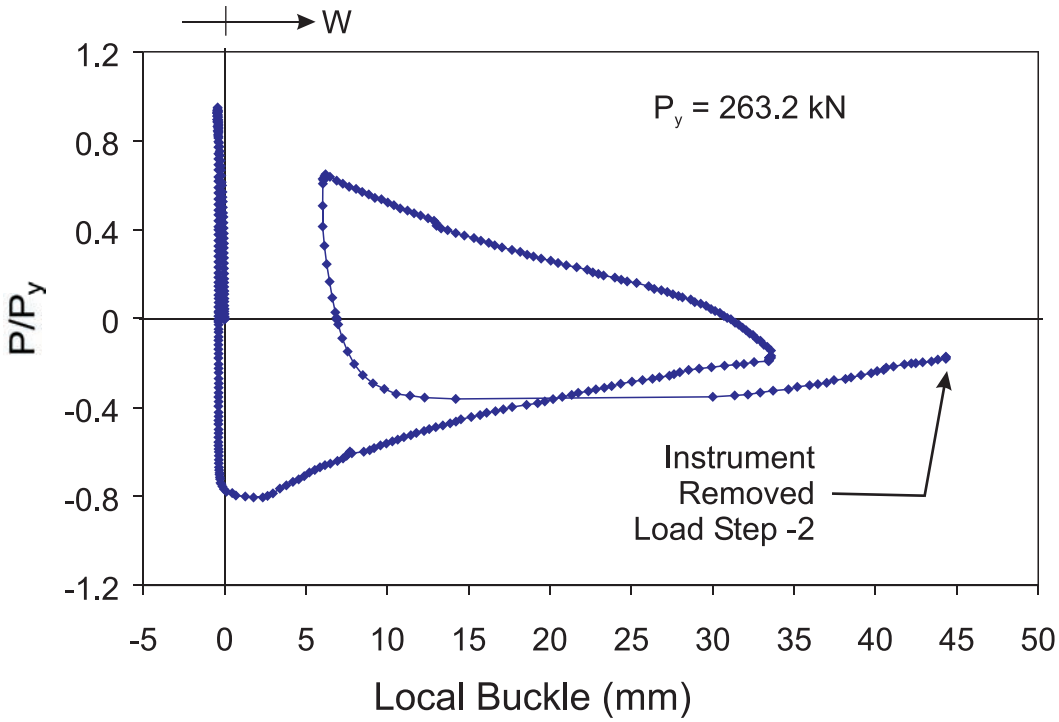

Figure 5.52 Measured Local Displacement of Buckle in Corrosion Patch, Specimen C40-33-95

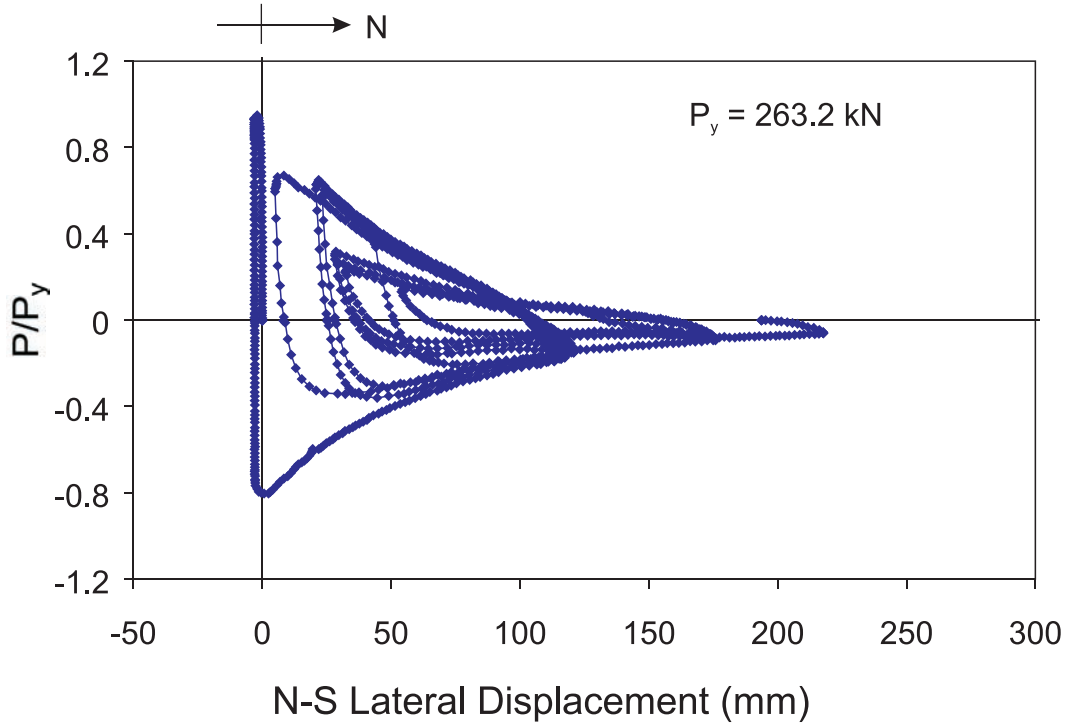

Figure 5.53 Measured Lateral Displacement in the North-South Direction, Specimen C40-33-95

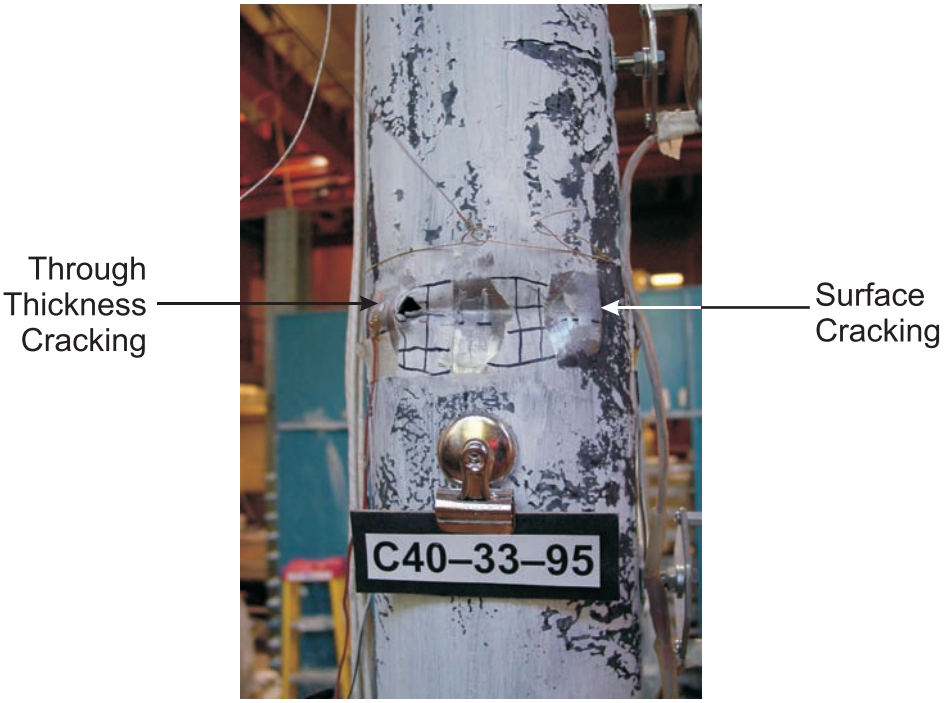

Figure 5.54 Initial Cracking at Edges of Local Buckle
(Load Step +3), Specimen C40-33-95

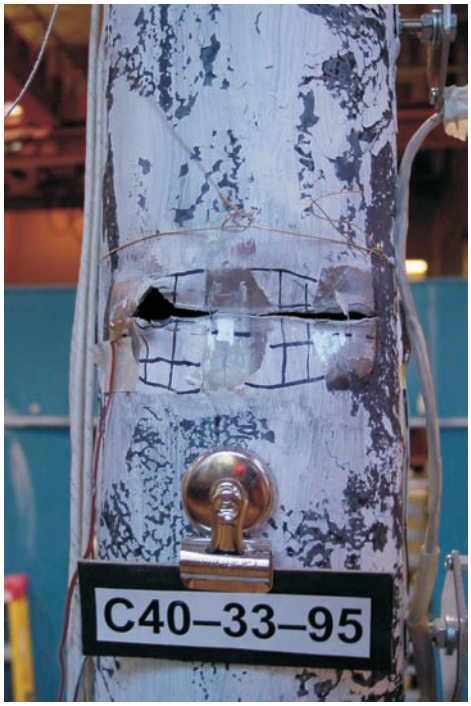

Figure 5.55 Through Thickness Cracking Across Local Buckle
(Load Step +4), Specimen C40-33-95

Figure 5.56 Final State of Specimen C40-33-95

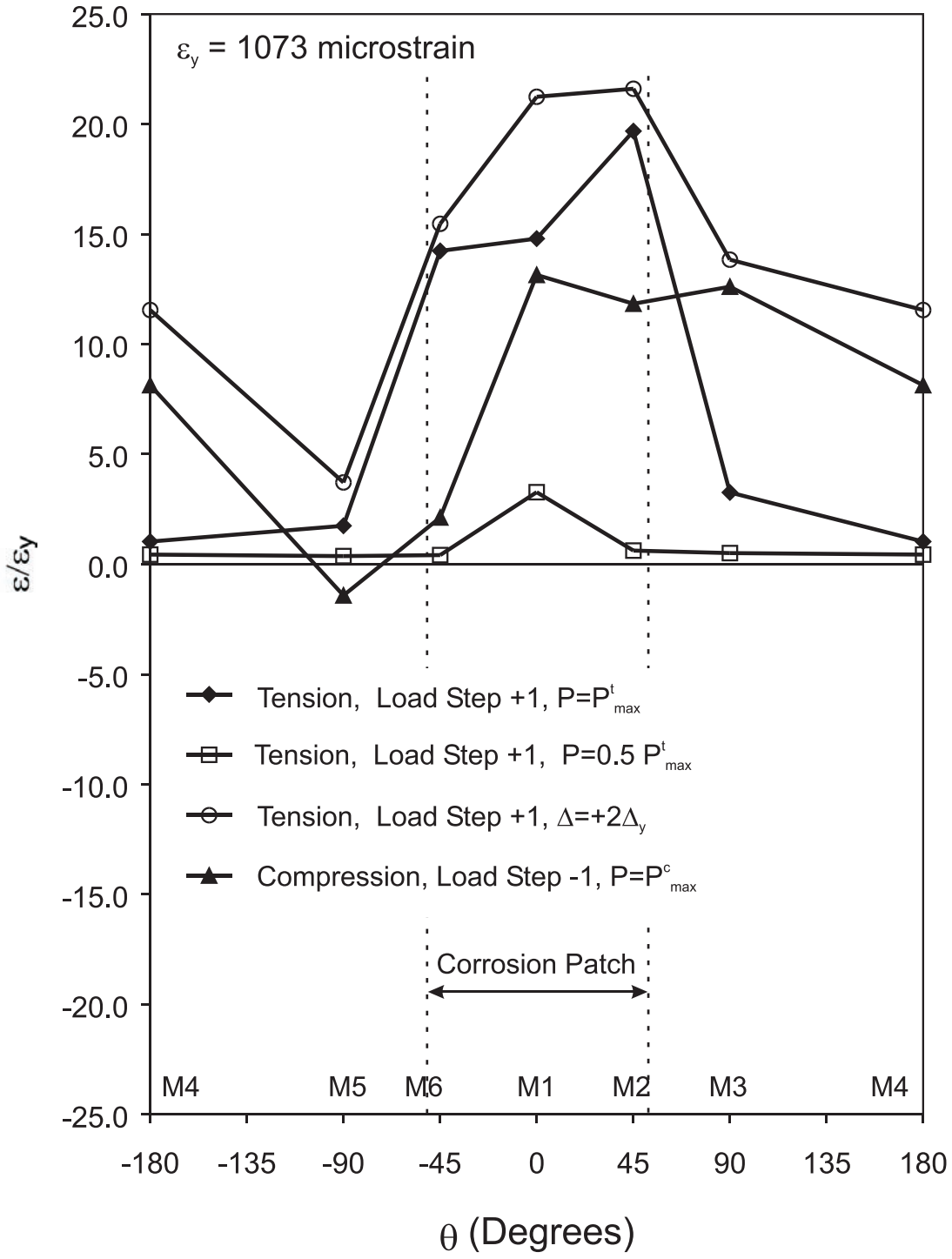

Figure 5.57 Strain Distribution of Cross Section at Mid-height, Specimen C40-33-95

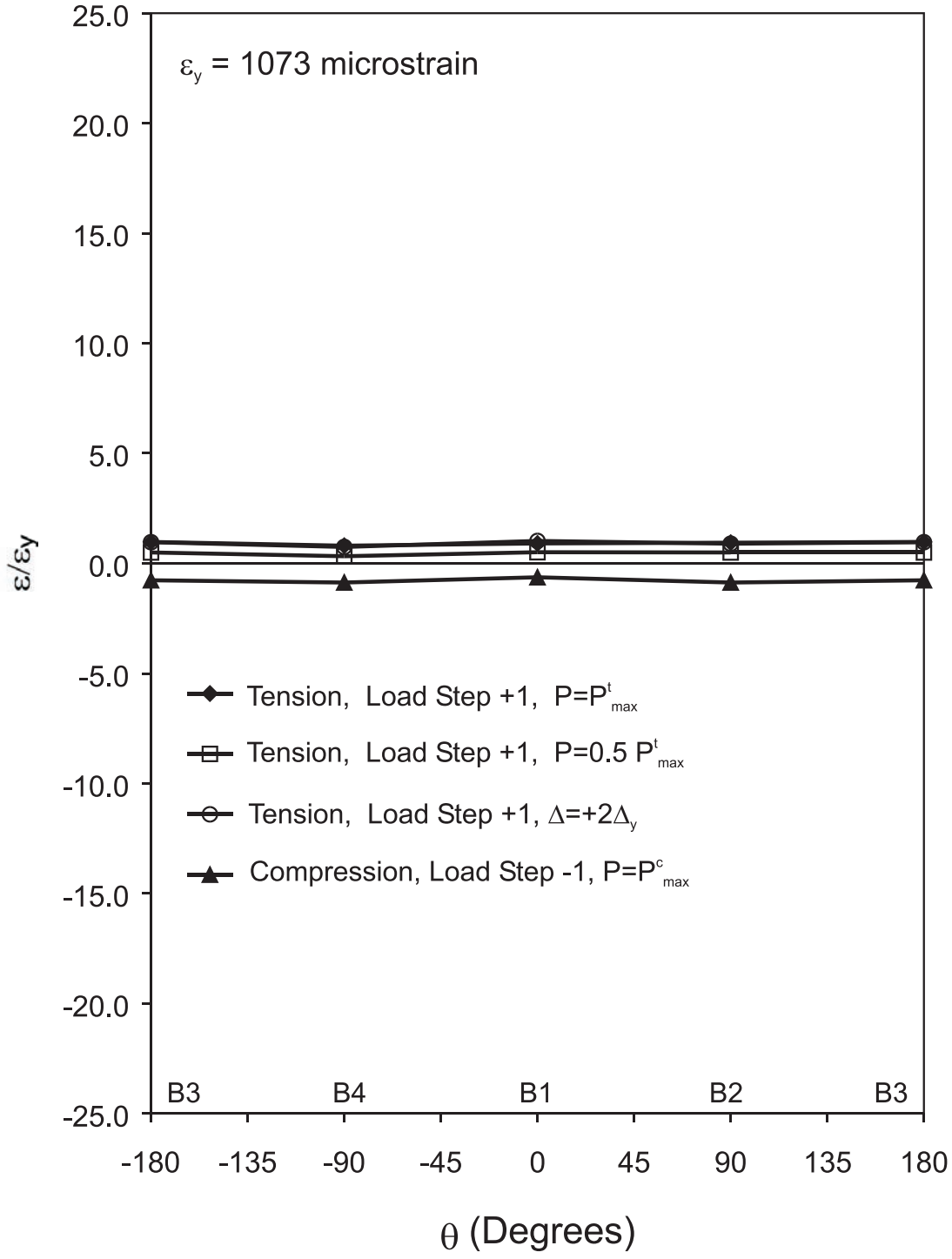

Figure 5.58 Strain Distribution of Cross Section at Lower Quarter-point, Specimen C40-33-95

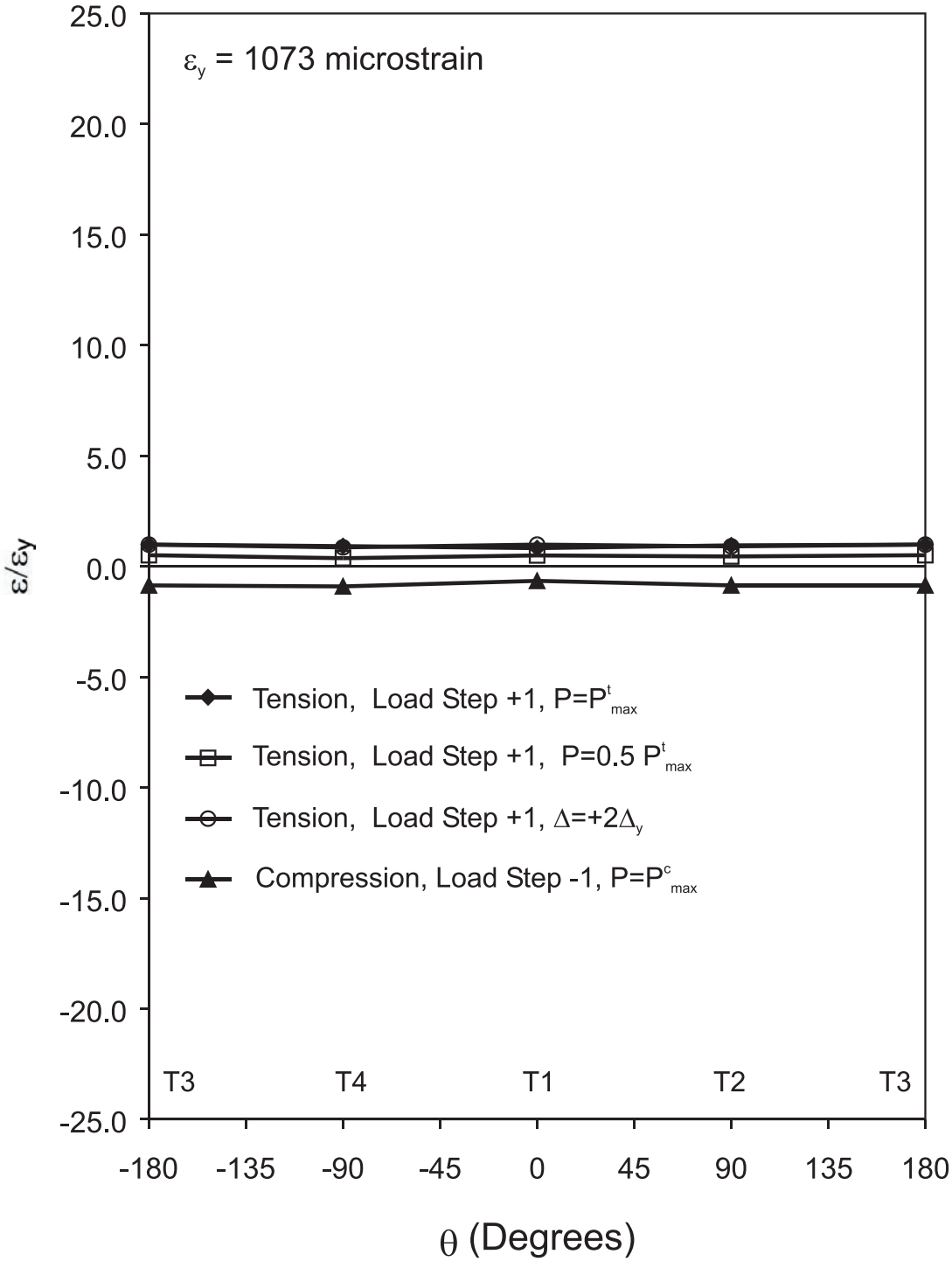

Figure 5.59 Strain Distribution of Cross Section at Upper Quarter-point, Specimen C40-33-95

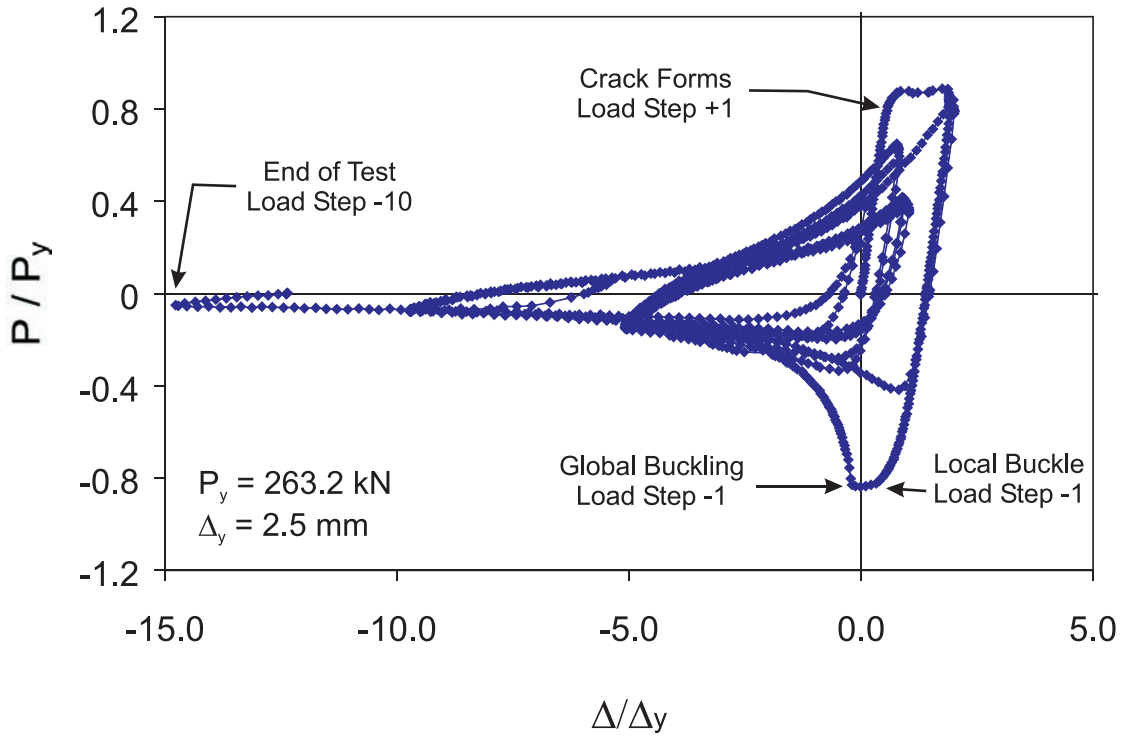

Figure 5.60 Normalized Axial Load - Axial Displacement, Specimen C40-00-95

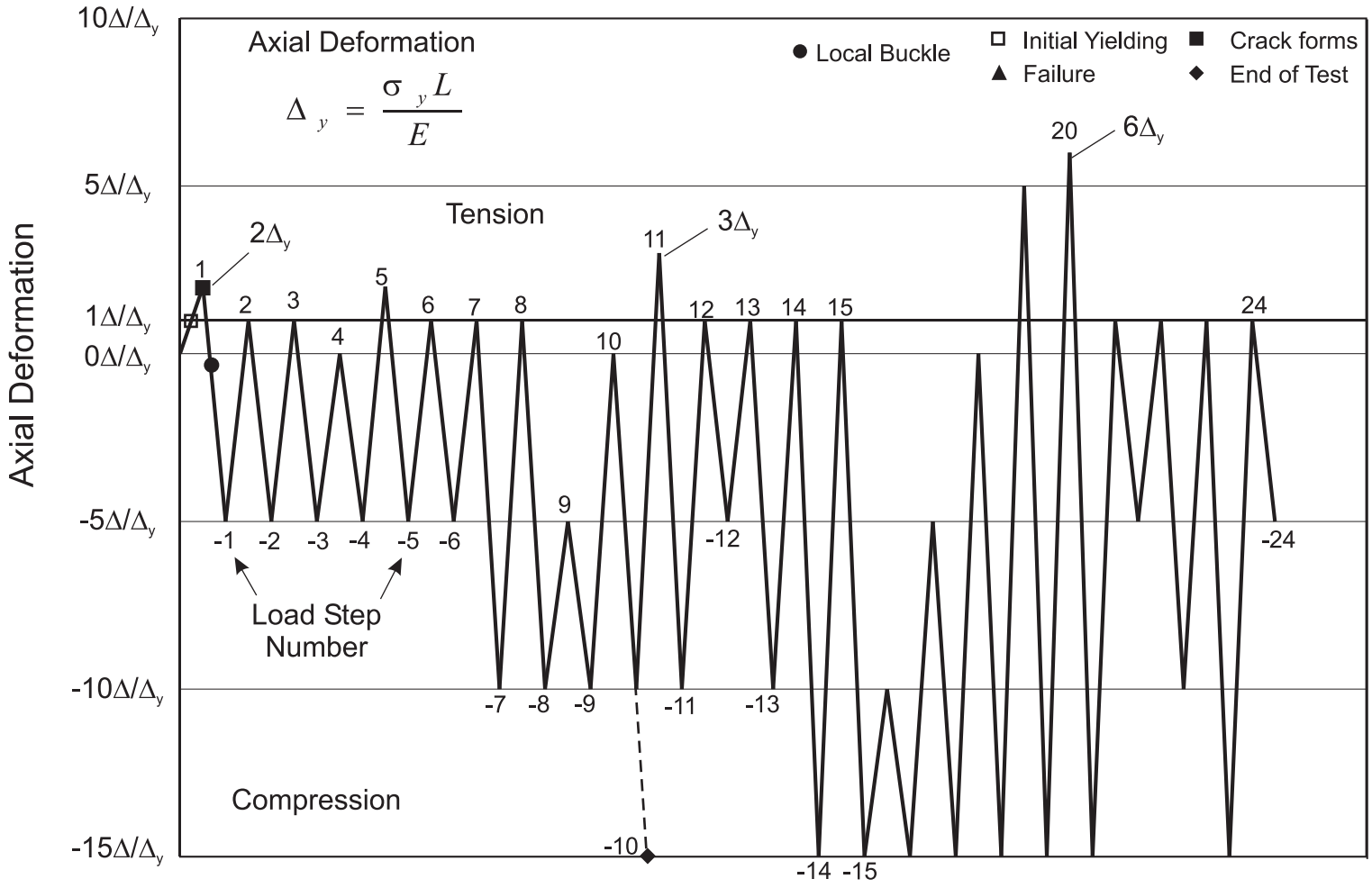

Figure 5.61 Displacement History with Events of Interest Noted, Specimen C40-00-95

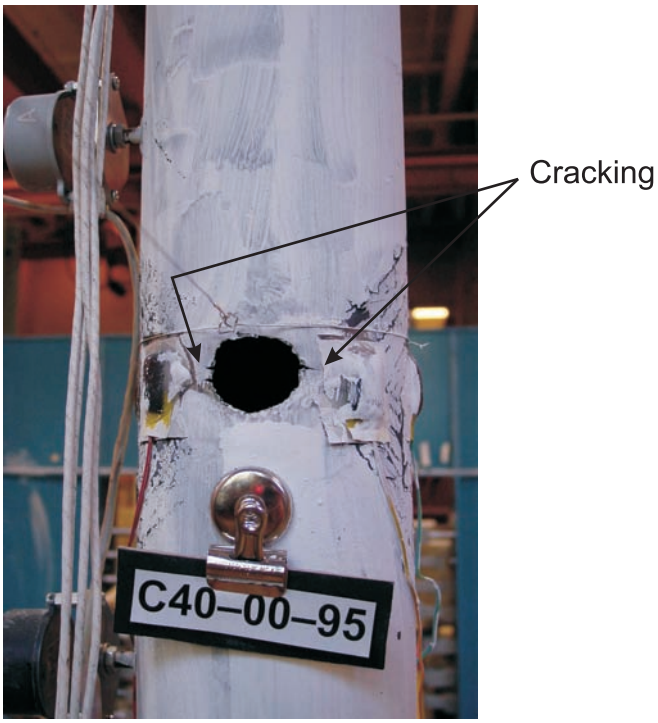

Figure 5.62 Front View of Cracking at Edges of Hole in Corrosion Patch (Load Step +1), Specimen C40-00-95

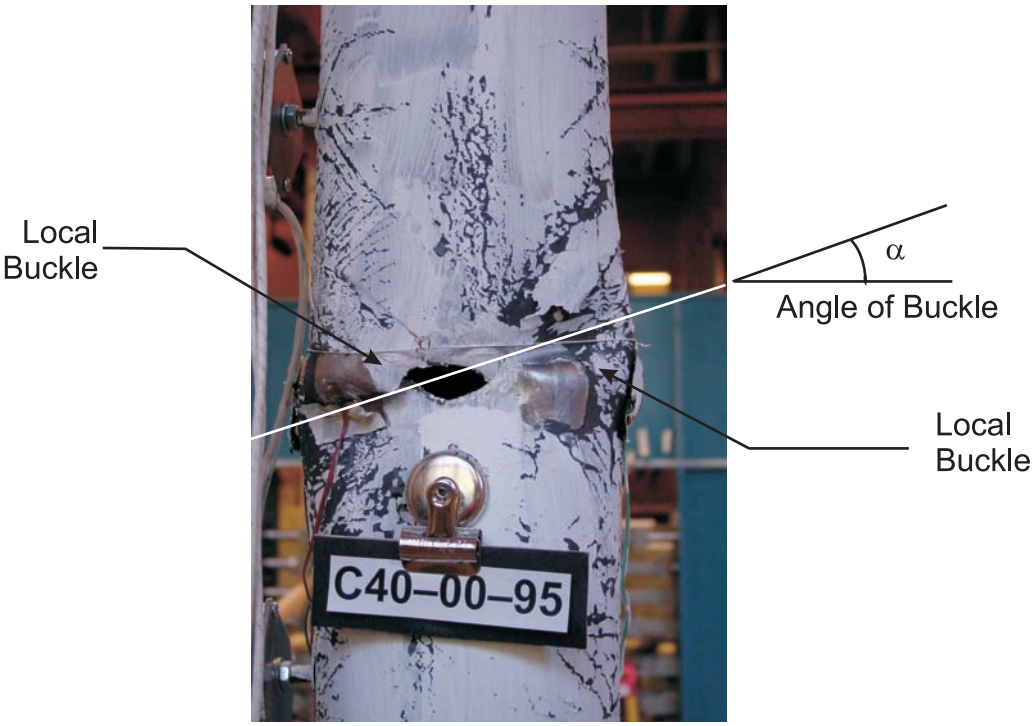

Figure 5.63 Front View of Local Buckle at Corrosion Patch (Load Step -1), Specimen C40-00-95

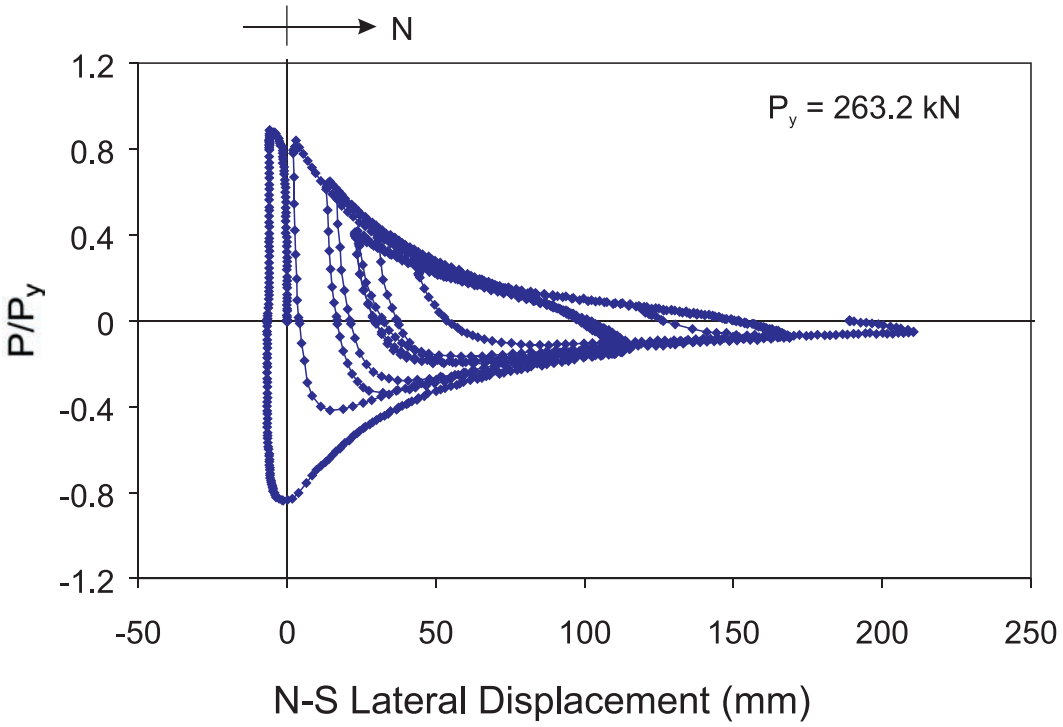

Figure 5.64 Measured Lateral Displacement in the North-South Direction, Specimen C40-00-95

Figure 5.65 Final State of Specimen C40-00-95

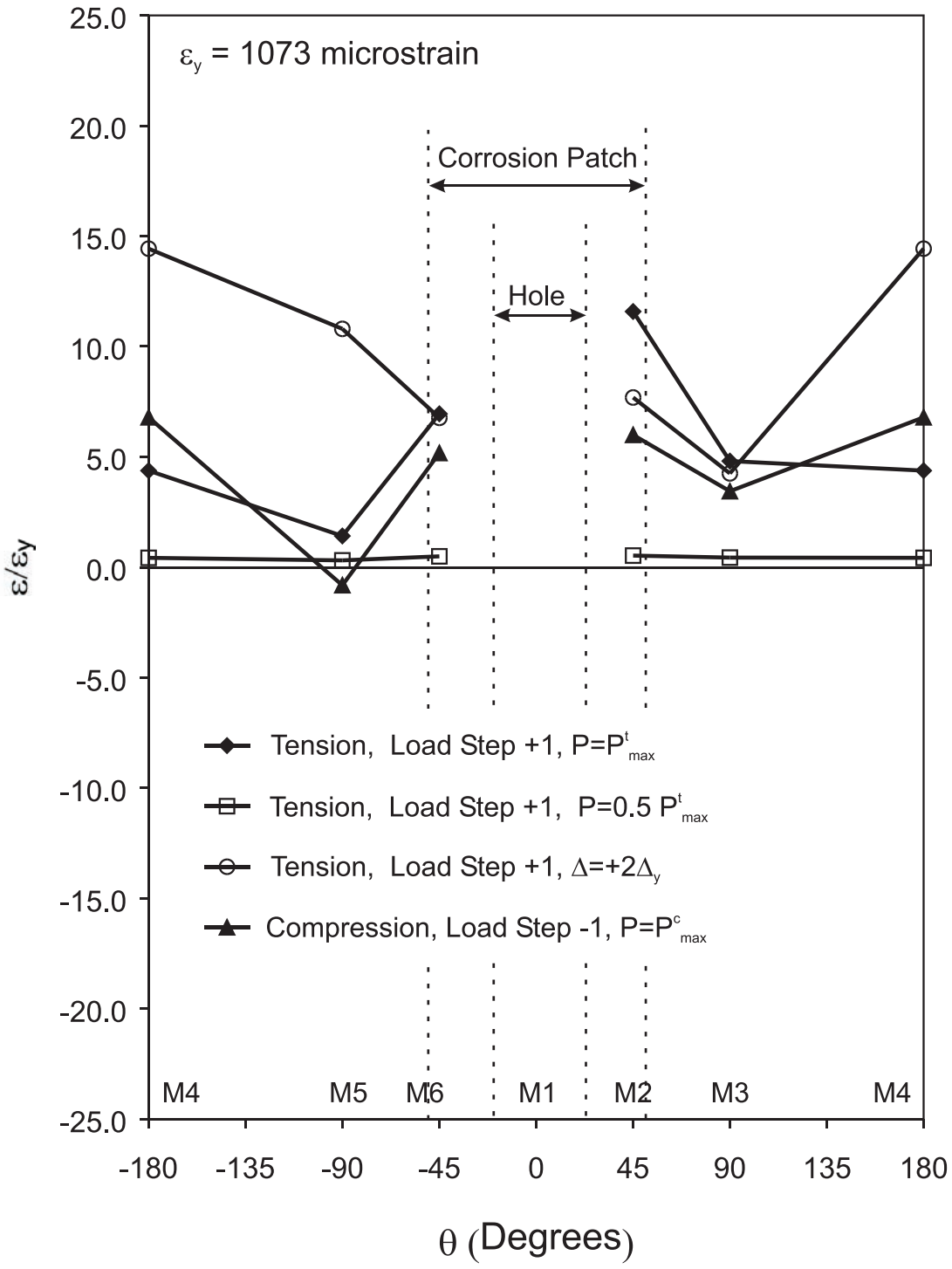

Figure 5.66 Strain Distribution of Cross Section at Mid-height, Specimen C40-00-95

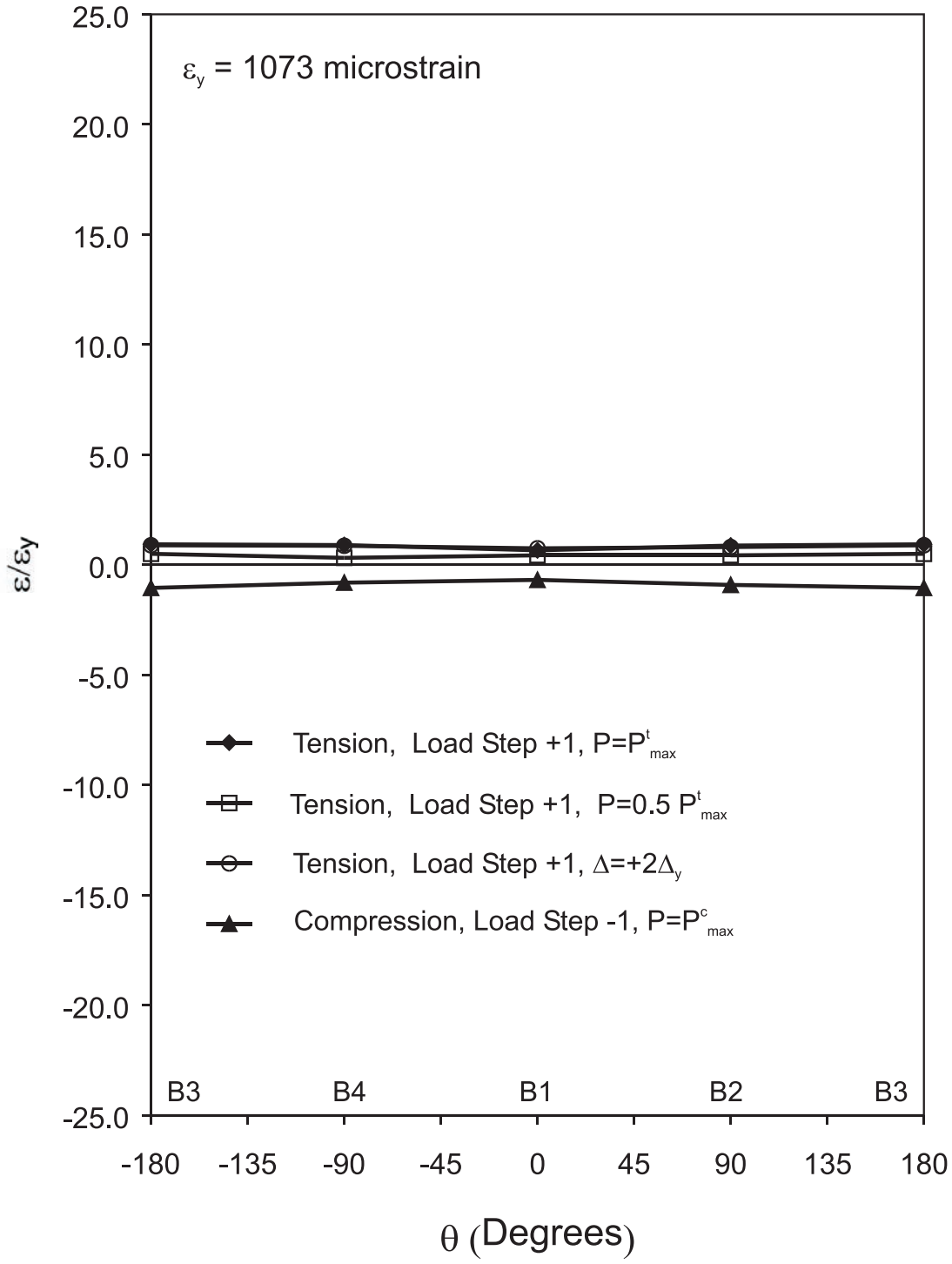

Figure 5.67 Strain Distribution of Cross Section at Lower Quarter-point, Specimen C40-00-95

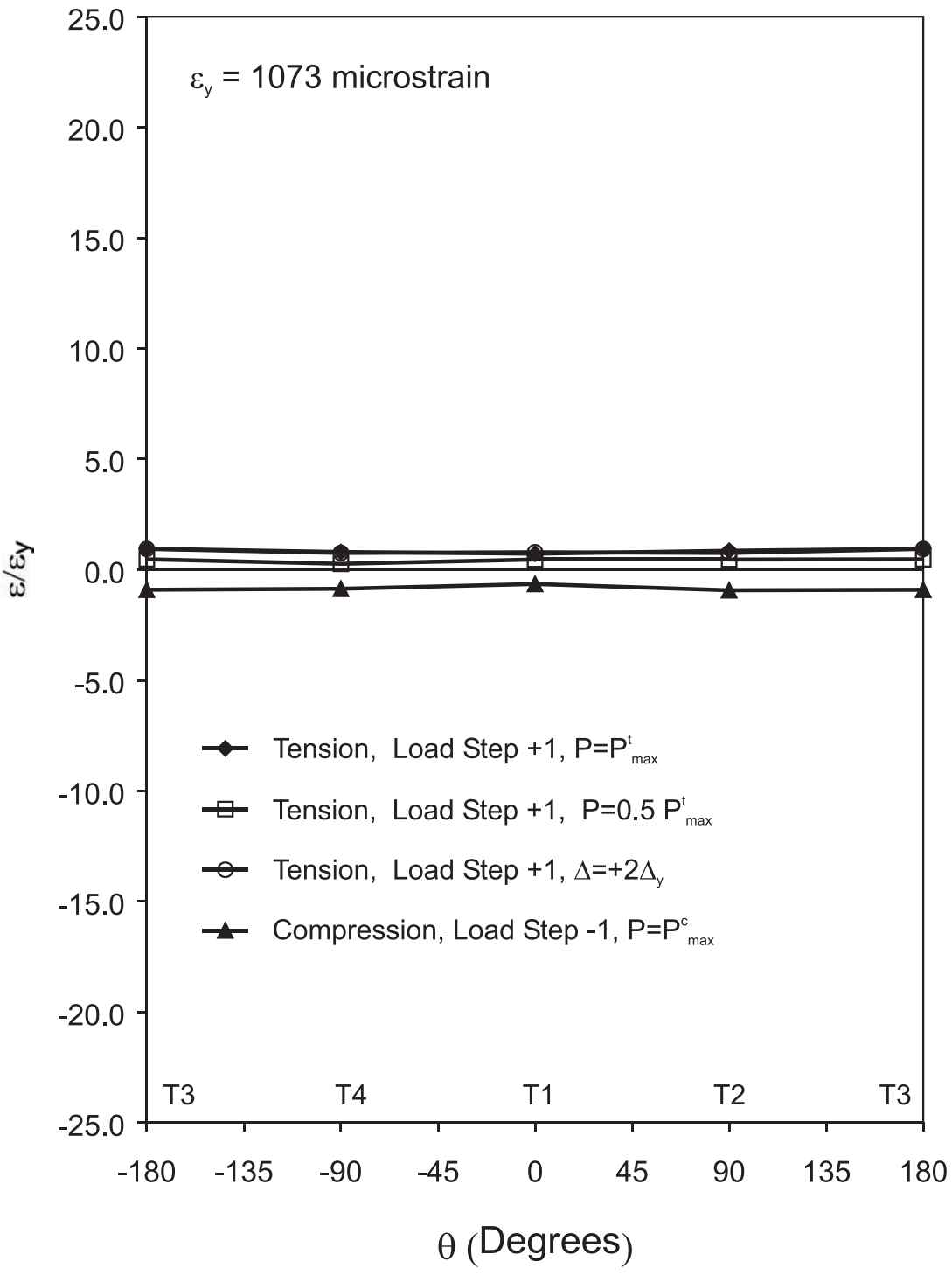

Figure 5.68 Strain Distribution of Cross Section at Upper Quarter-point, Specimen C40-00-95

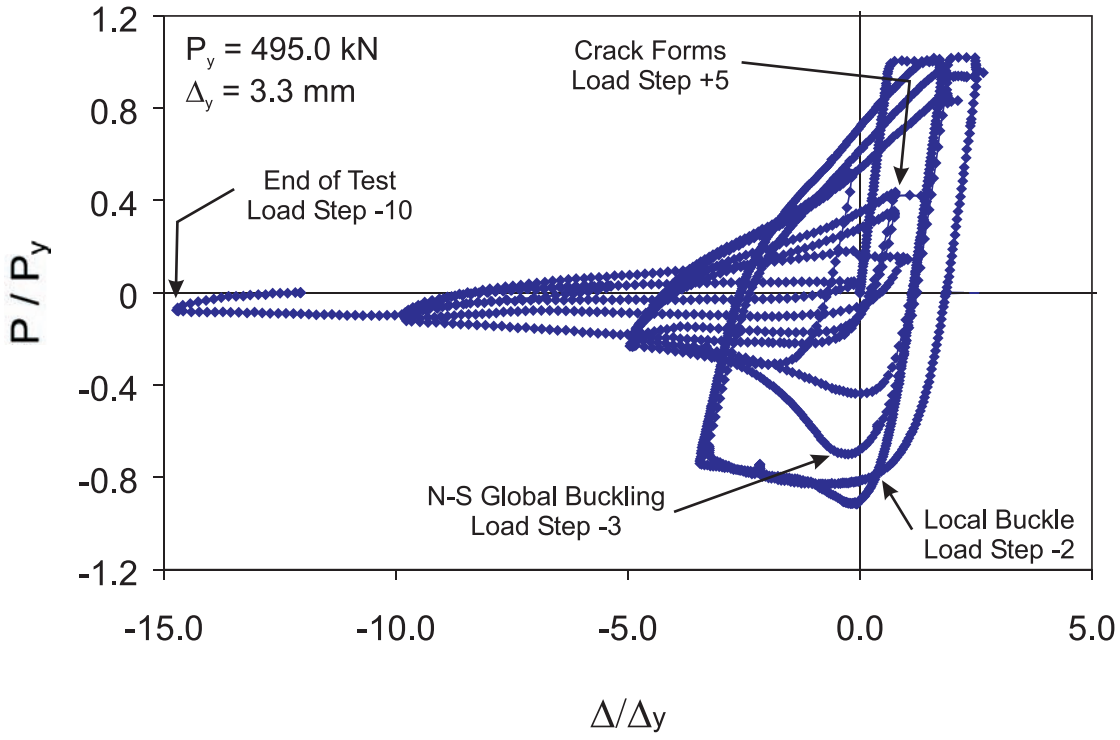

Figure 5.69 Normalized Axial Load - Axial Displacement, Specimen C27-33-58

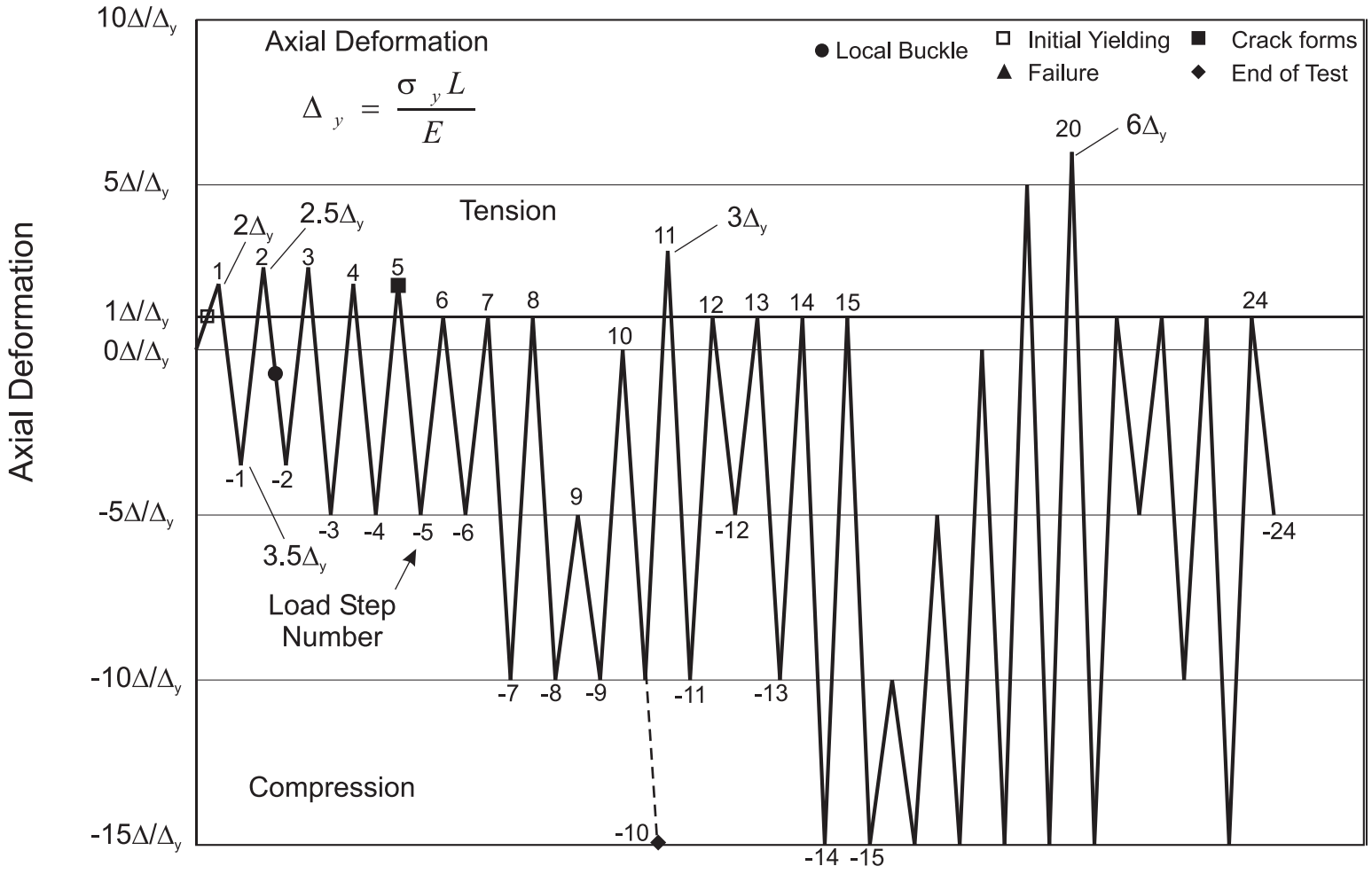

Figure 5.70 Displacement History with Events of Interest Noted, Specimen C27-33-58

Figure 5.71 Yielding at Mid-height (Load Step -1), Specimen C27-33-58

Figure 5.72 View of Buckle at the Right Side of the Corrosion Patch (Load Step -2), Specimen C27-33-58

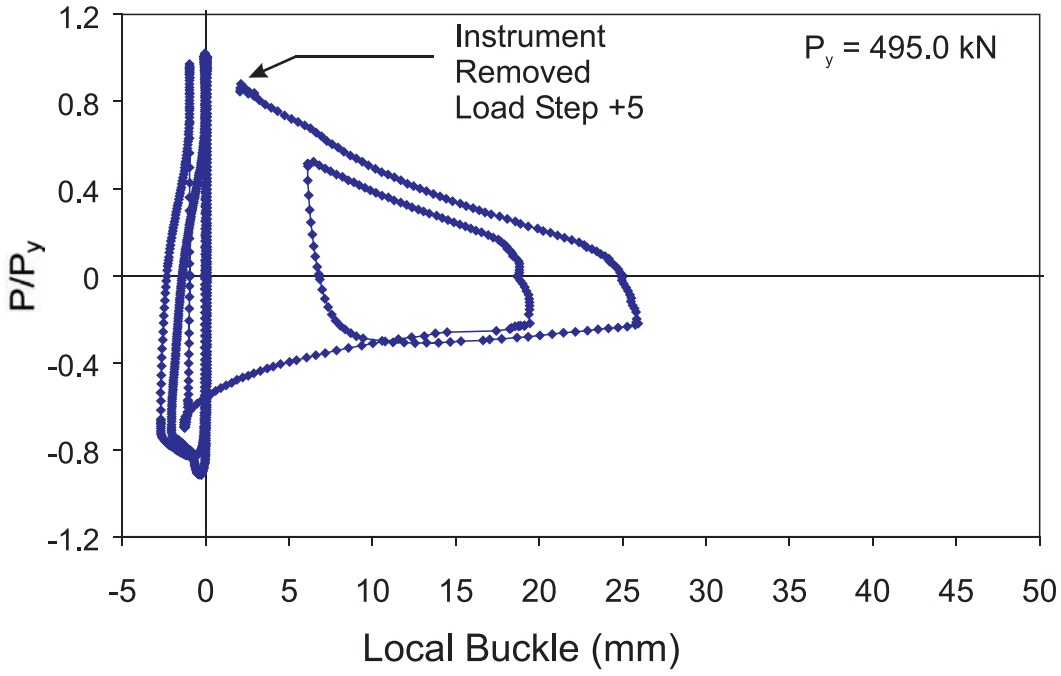

Figure 5.73 Measured Local Displacement of Buckle in Corrosion Patch, Specimen C27-33-58

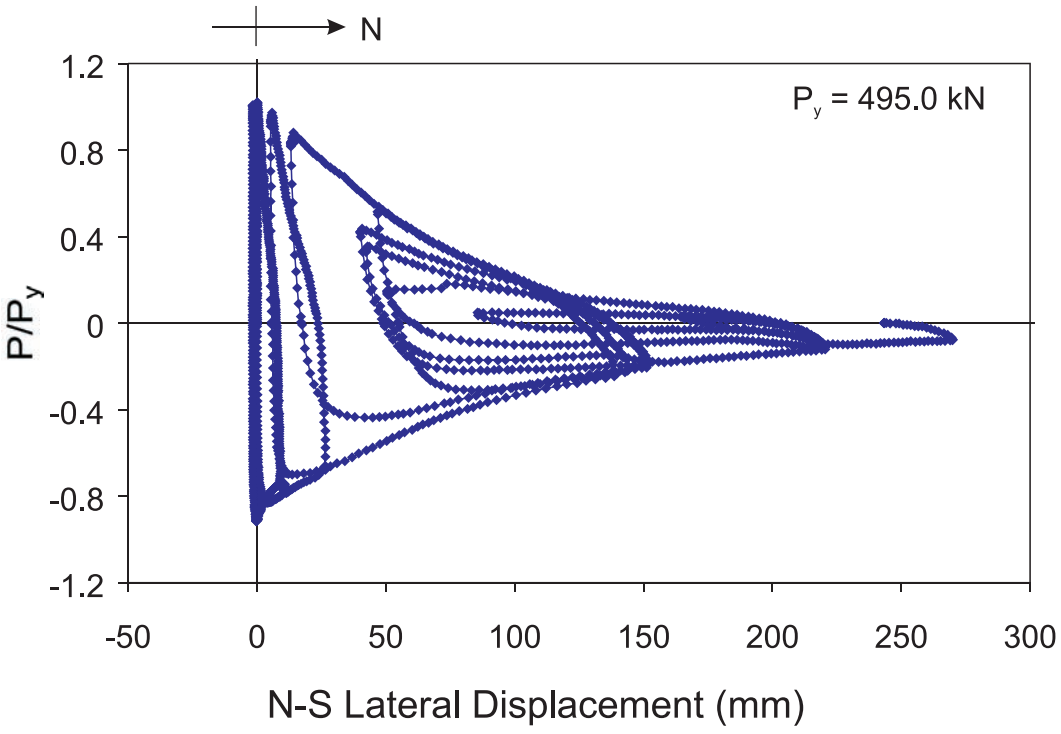

Figure 5.74 Measured Lateral Displacement in the North-South Direction, Specimen C27-33-58

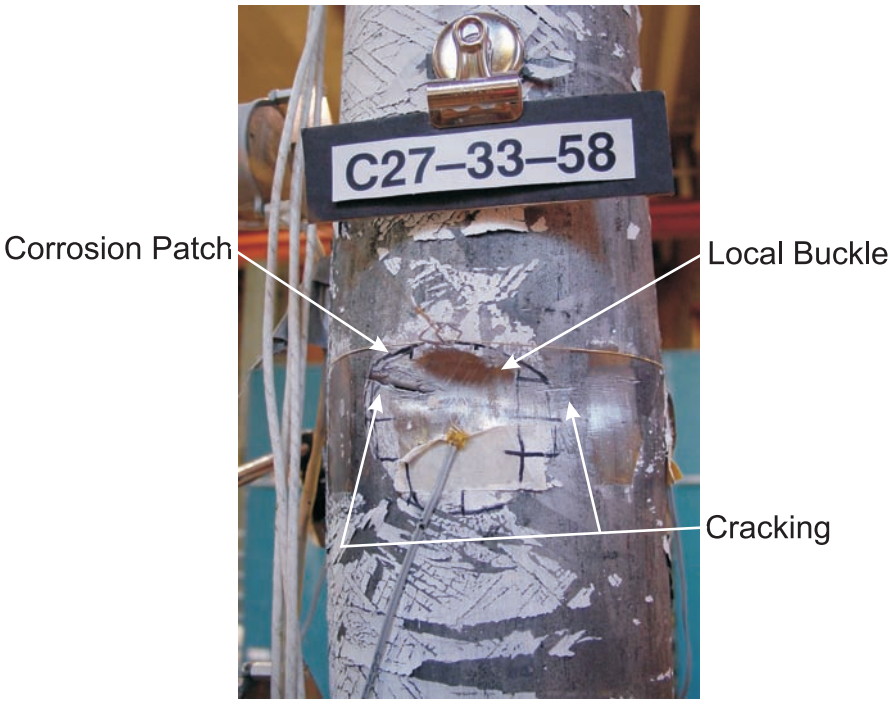

Figure 5.75 Initial Cracking at Edges of Local Buckle (Load Step +5), Specimen C27-33-58

Figure 5.76 Through Thickness Cracking Across Local Buckle (Load Step +7), Specimen C27-33-58

Figure 5.77 Final State of Specimen C27-33-58

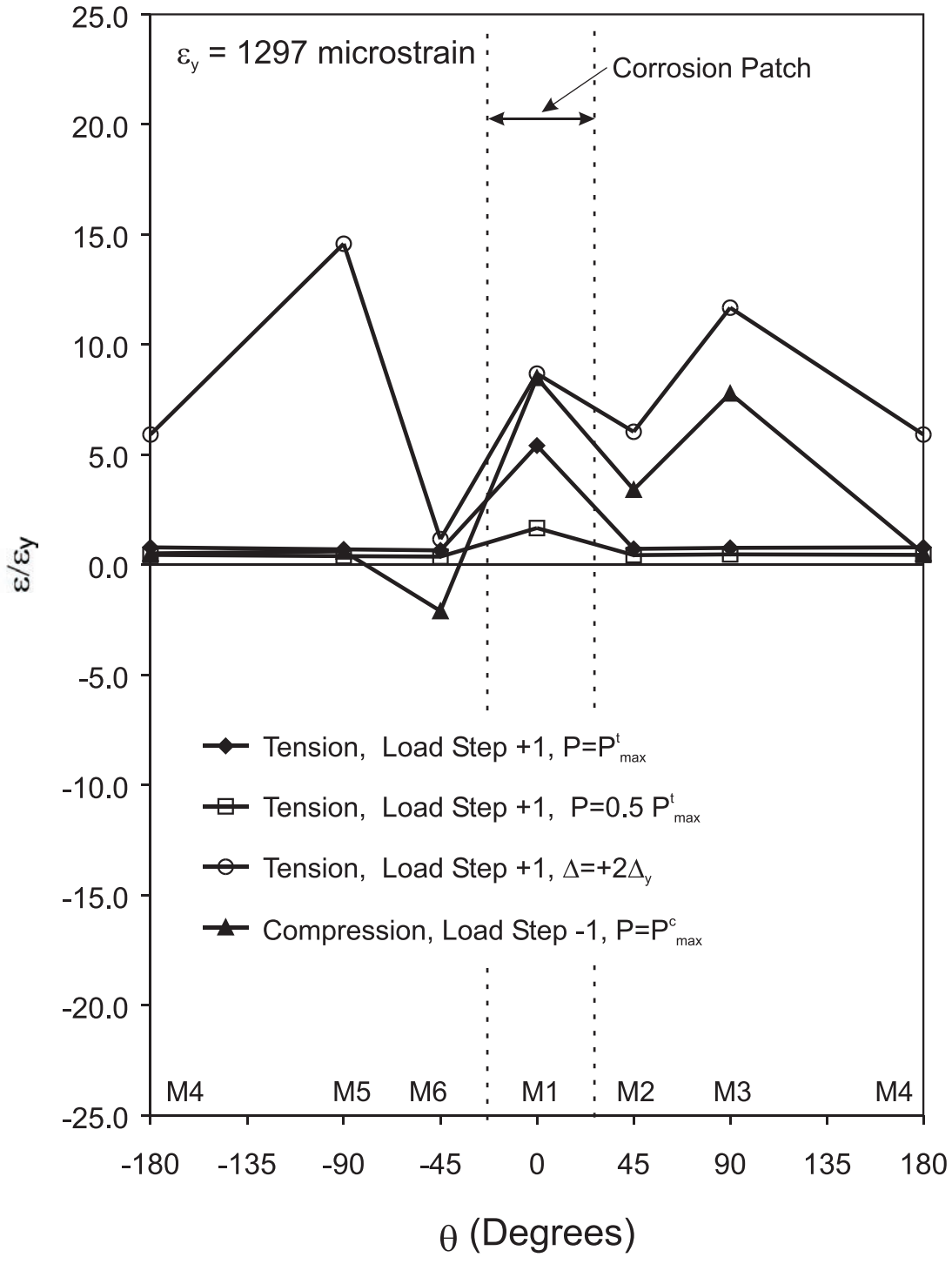

Figure 5.78 Strain Distribution of Cross Section at Mid-height, Specimen C27-33-58

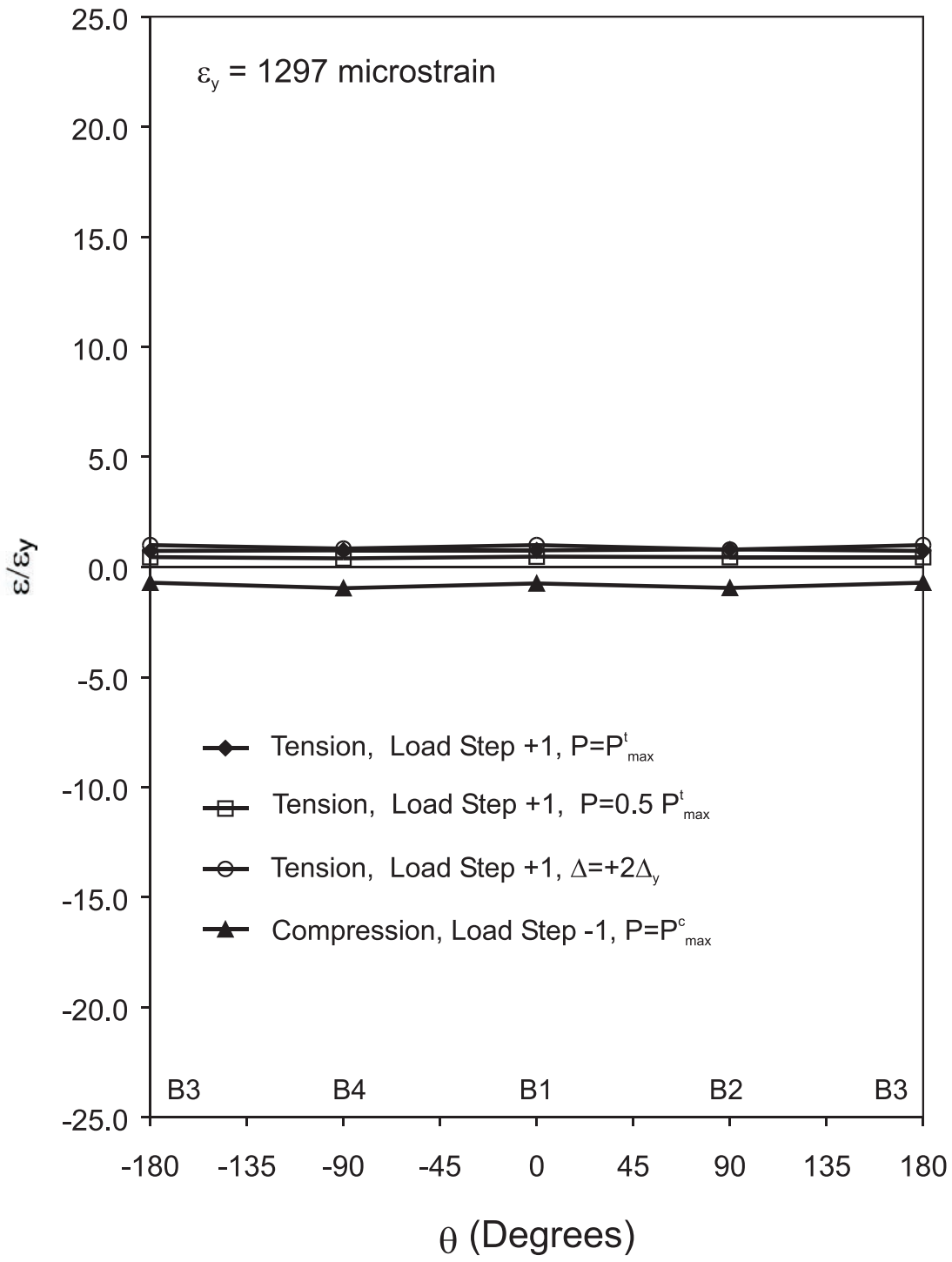

Figure 5.79 Strain Distribution of Cross Section at Lower Quarter-point, Specimen C27-33-58

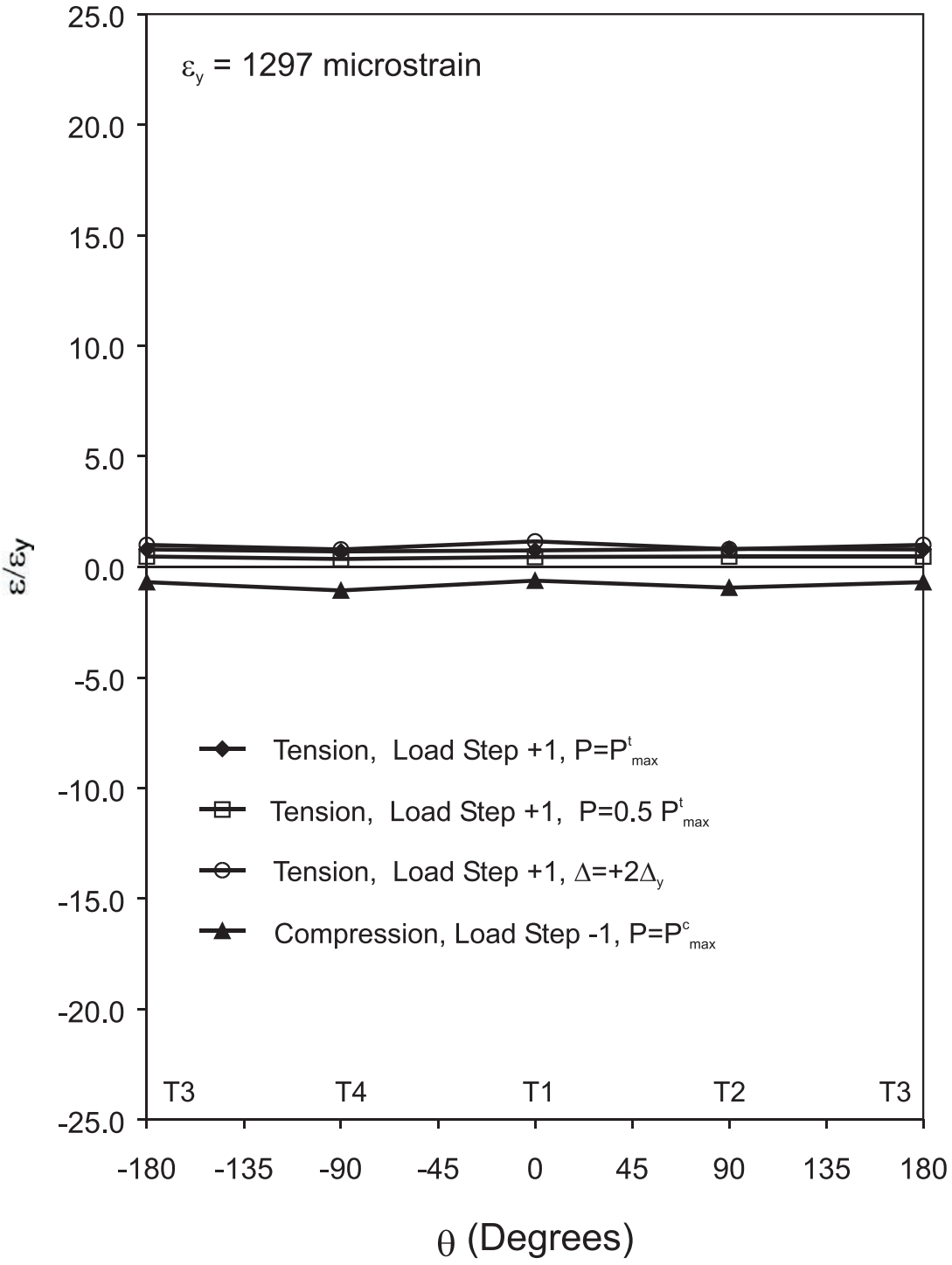

Figure 5.80 Strain Distribution of Cross Section at Upper Quarter-point, Specimen C27-33-58

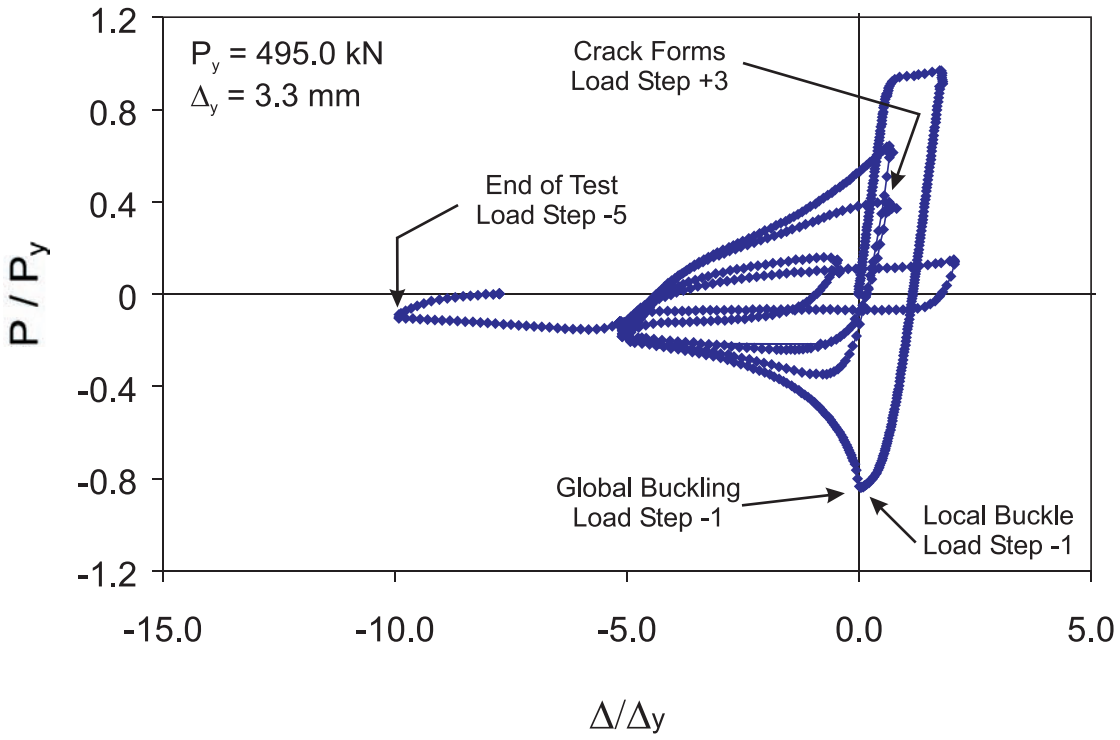

Figure 5.81 Normalized Axial Load - Axial Displacement, Specimen C27-33-95

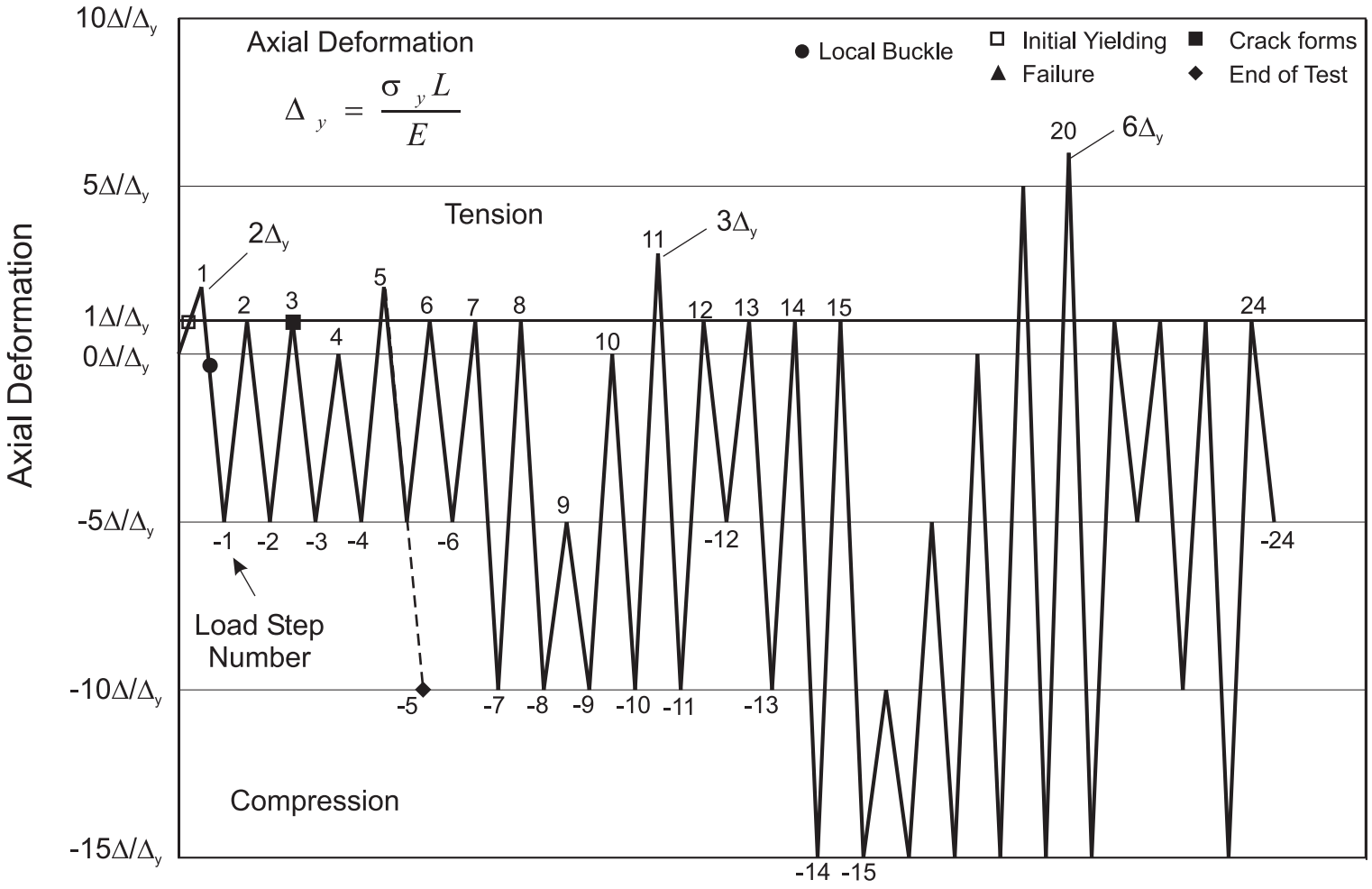

Figure 5.82 Displacement History with Events of Interest Noted, Specimen C27-33-95

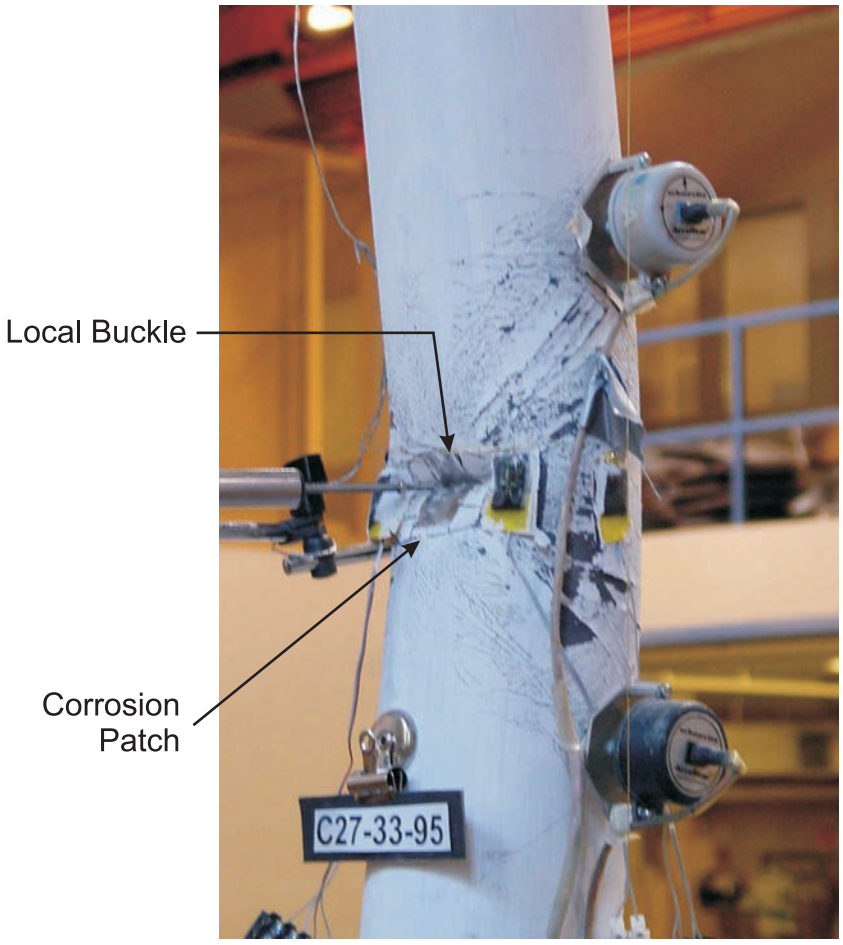

Figure 5.83 Front View of Local Buckle at Mid-height
(Load Step -2), Specimen C27-33-95

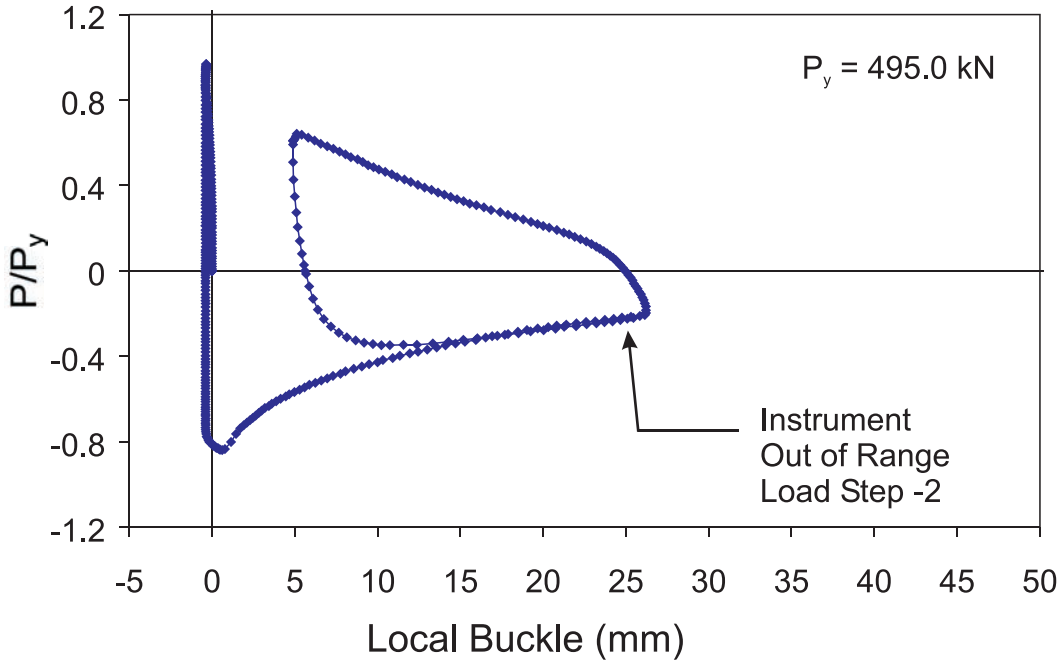

Figure 5.84 Measured Local Displacement of Buckle in Corrosion Patch, Specimen C27-33-95

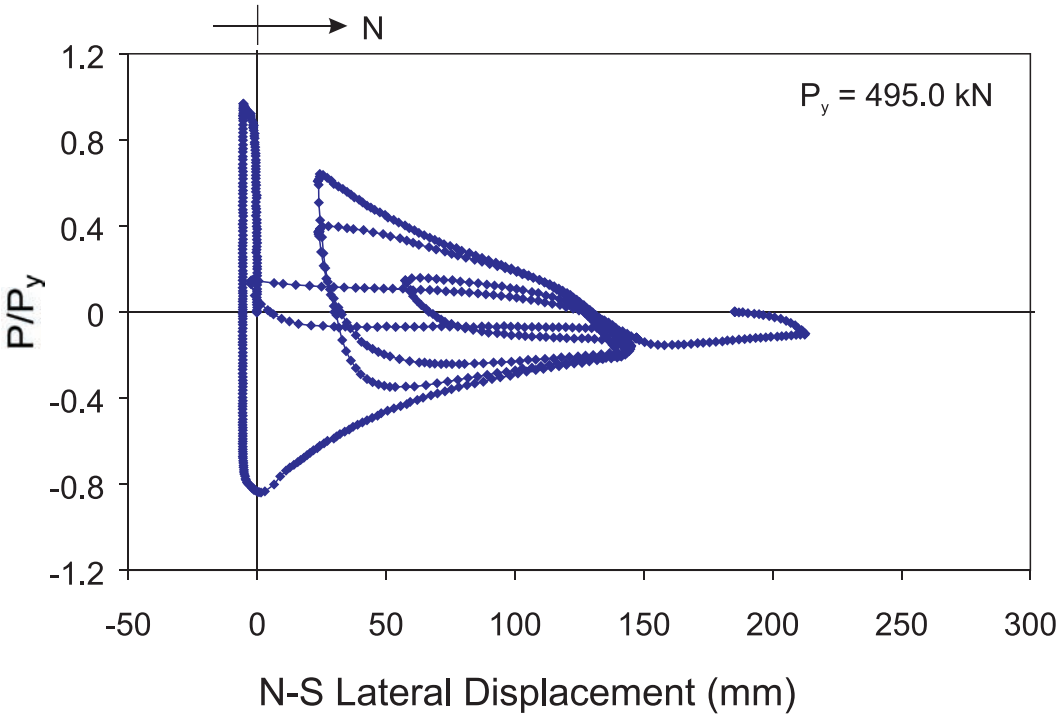

Figure 5.85 Measured Lateral Displacement in the North-South Direction, Specimen C27-33-95

Figure 5.86 Side View of Through-Thickness Cracking at Edges of Local Buckle (Load Step +3), Specimen C27-33-95

Figure 5.87 Through-Thickness Cracking Across Local Buckle (Load Step +4), Specimen C27-33-95

Figure 5.88 Final State of Specimen C27-33-95

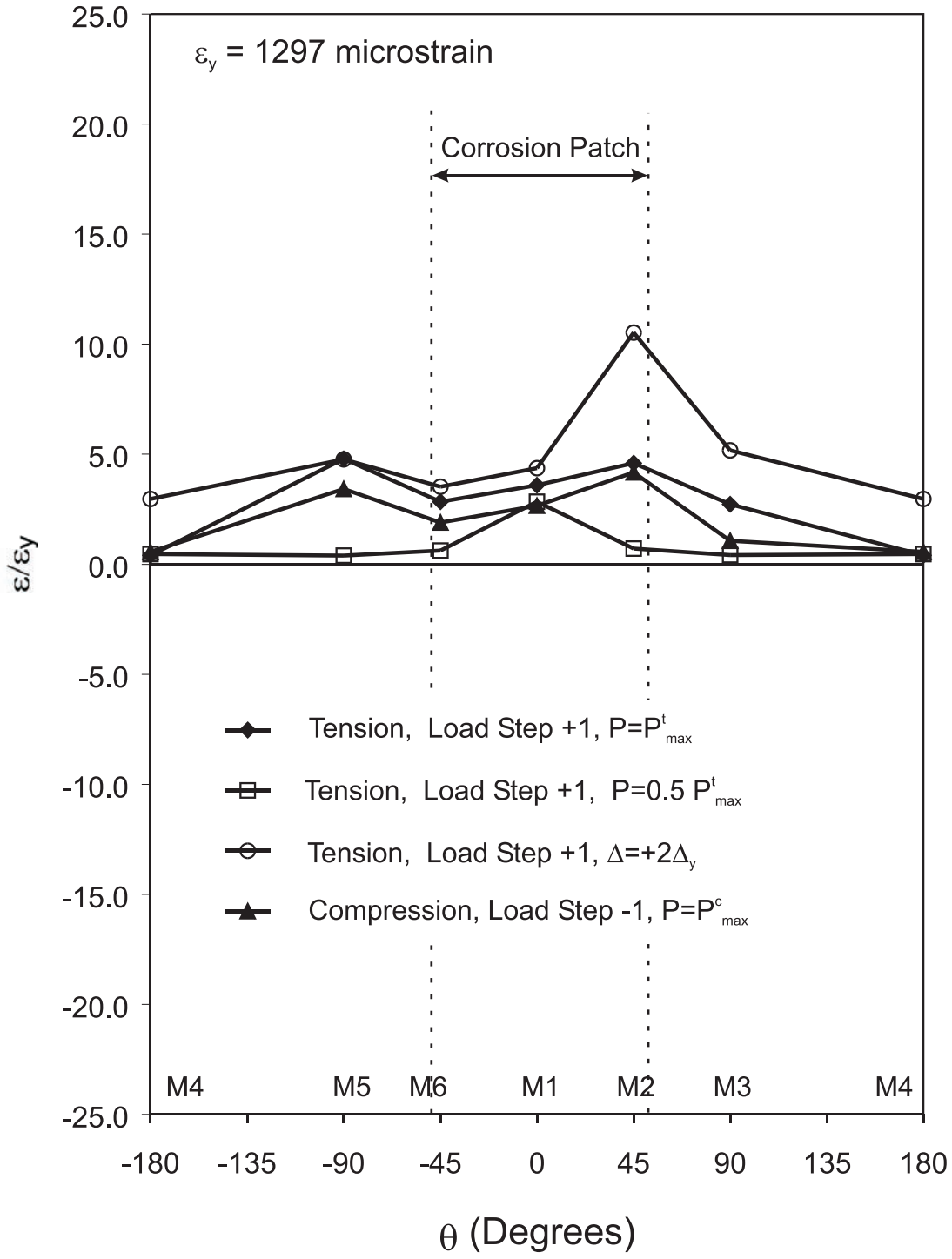

Figure 5.89 Strain Distribution of Cross Section at Mid-height, Specimen C27-33-95

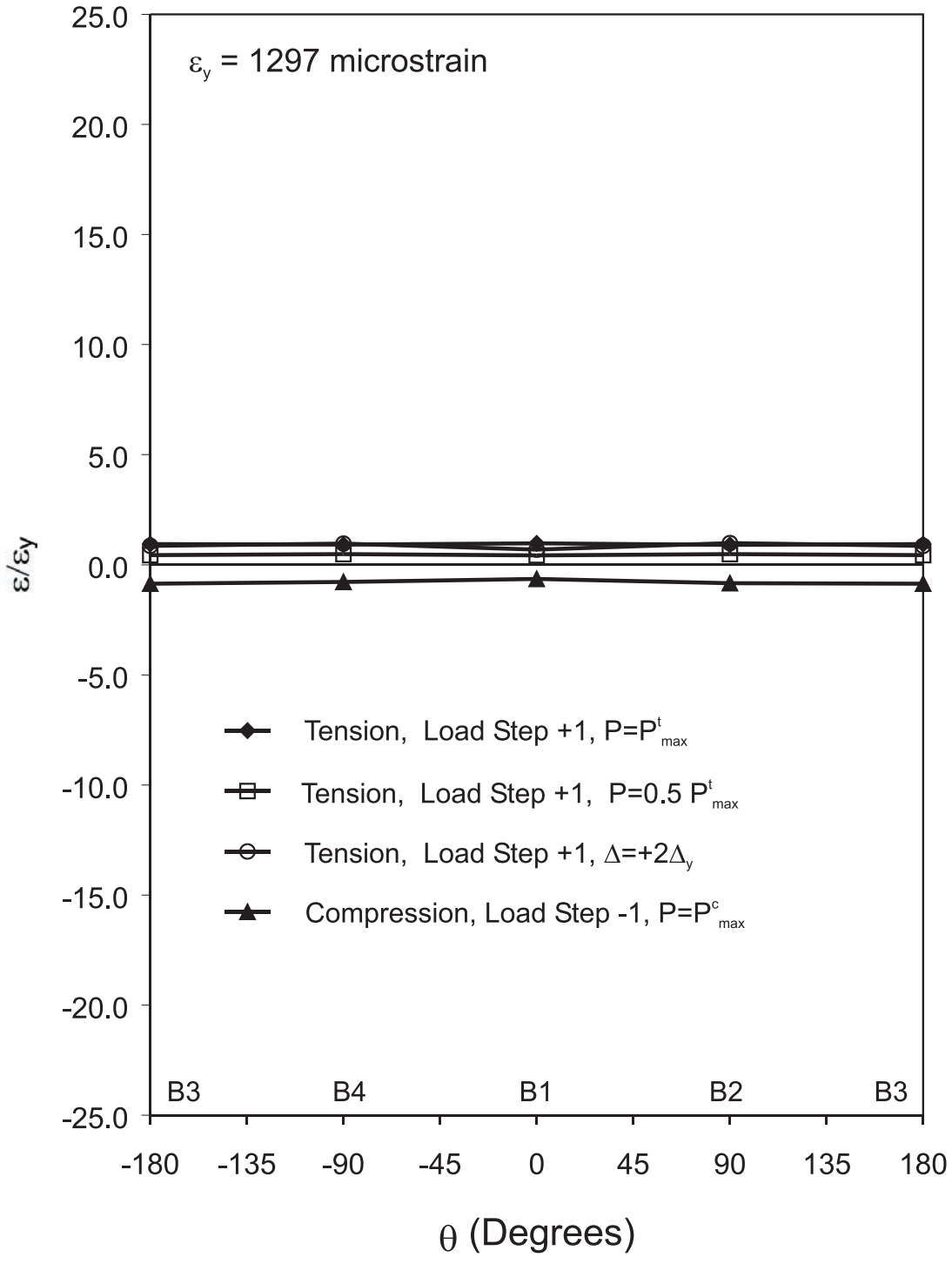

Figure 5.90 Strain Distribution of Cross Section at Lower Quarter-point, Specimen C27-33-95

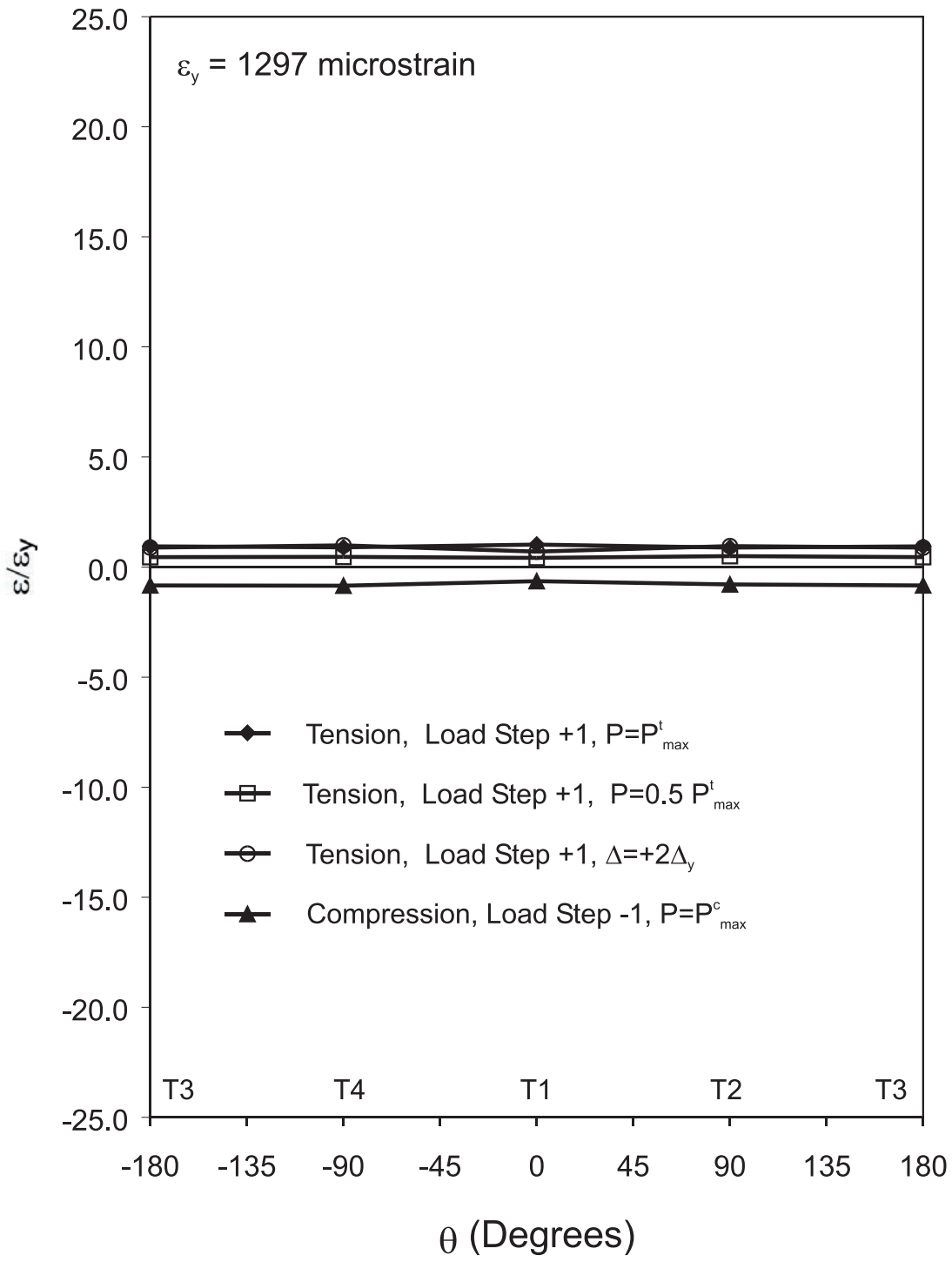

Figure 5.91 Strain Distribution of Cross Section at Upper Quarter-point, Specimen C27-33-95

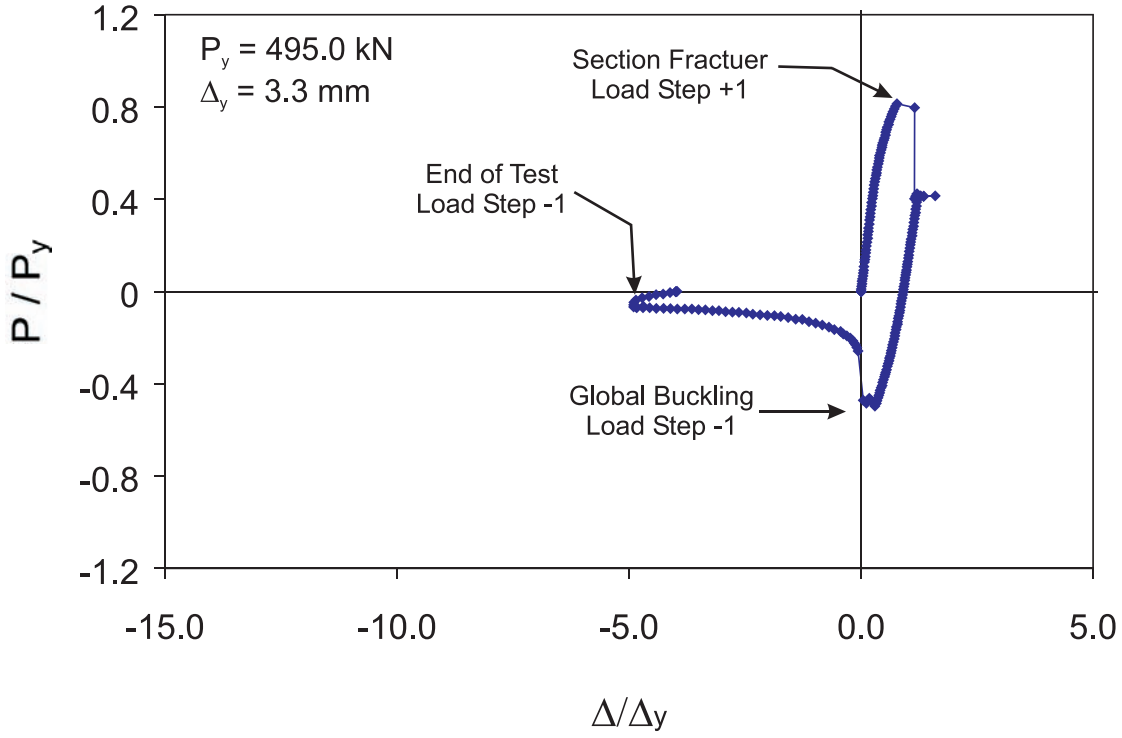

Figure 5.92 Normalized Axial Load - Axial Displacement for Specimen C27-33-311

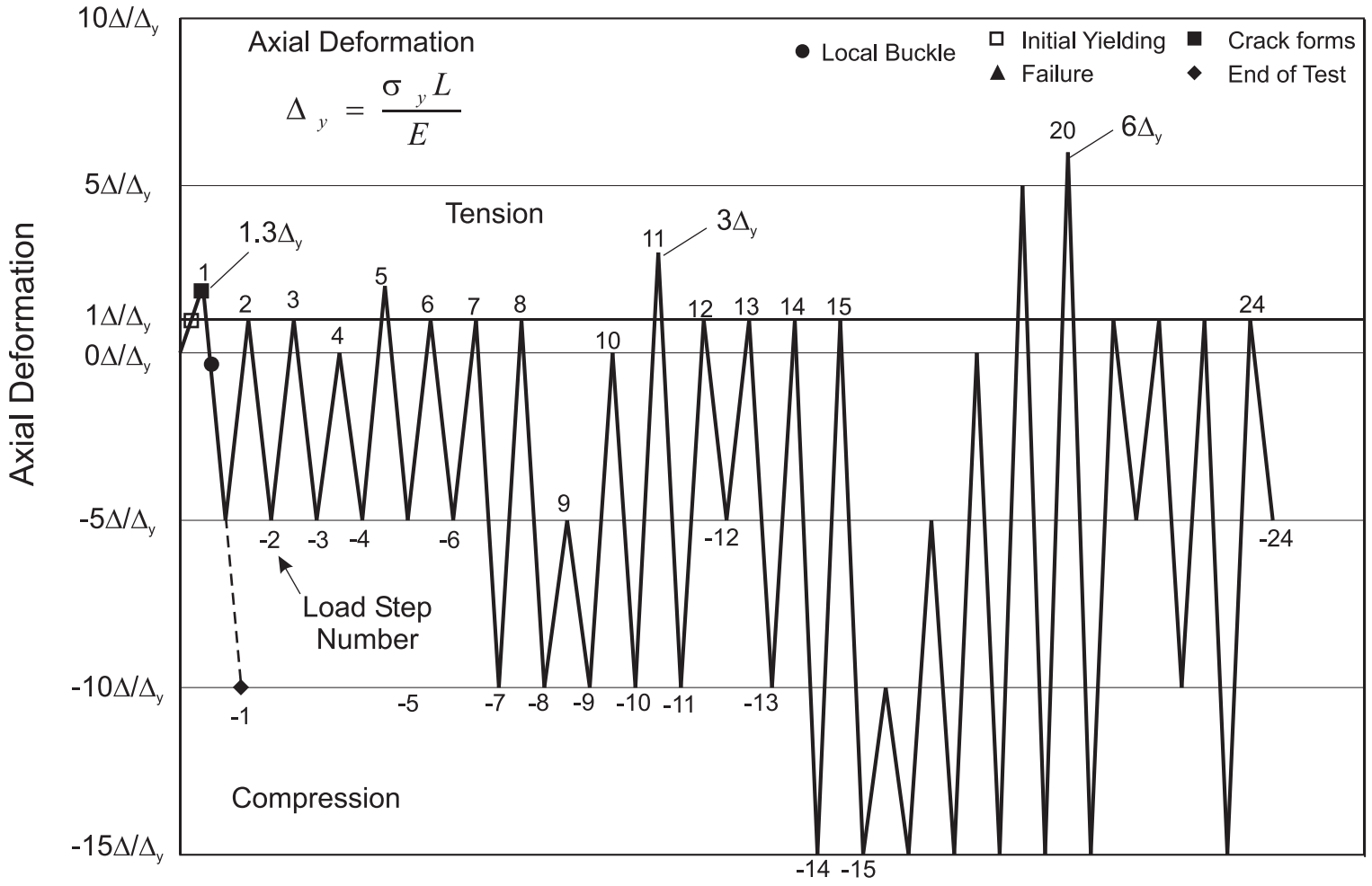

Figure 5.93 Displacement History with Events of Interest Noted, Specimen C27-33-311

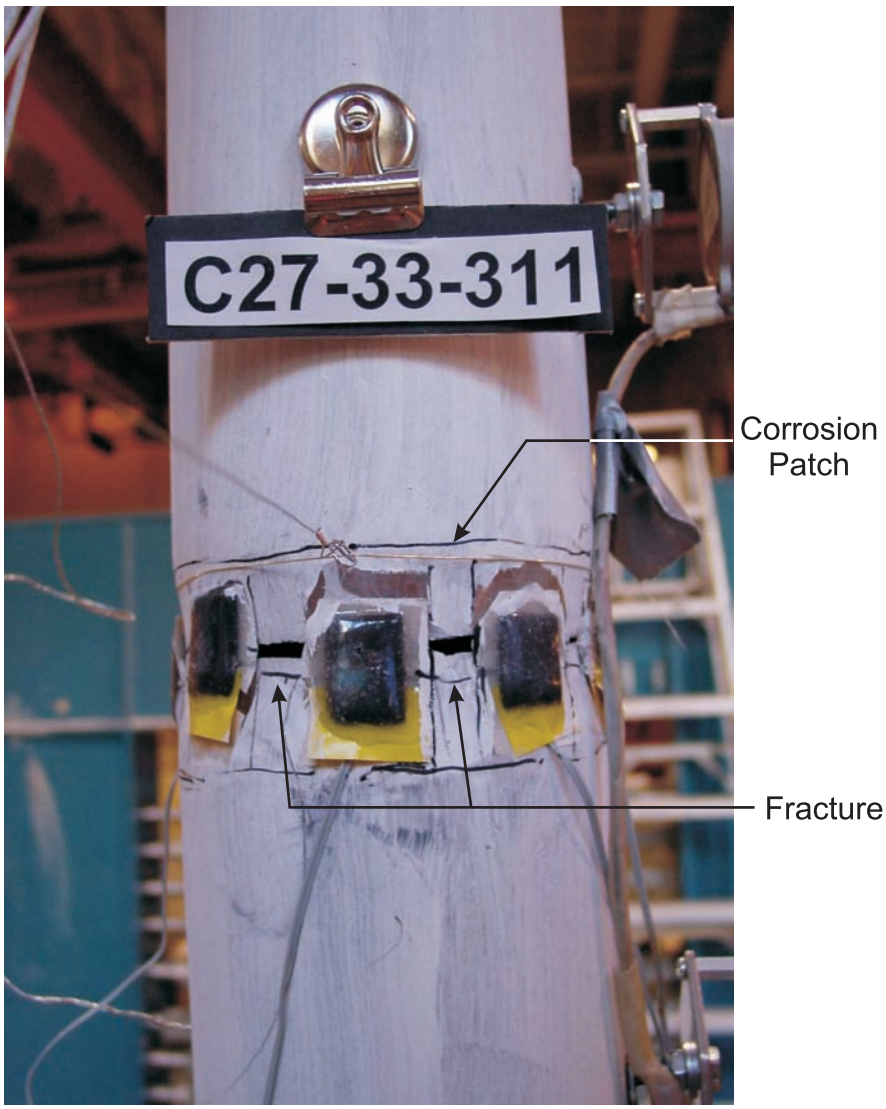

Figure 5.94 Fracture at Corrosion Patch (Load Step +1), Specimen C27-33-311

Figure 5.95 Final State of Specimen C27-33-311

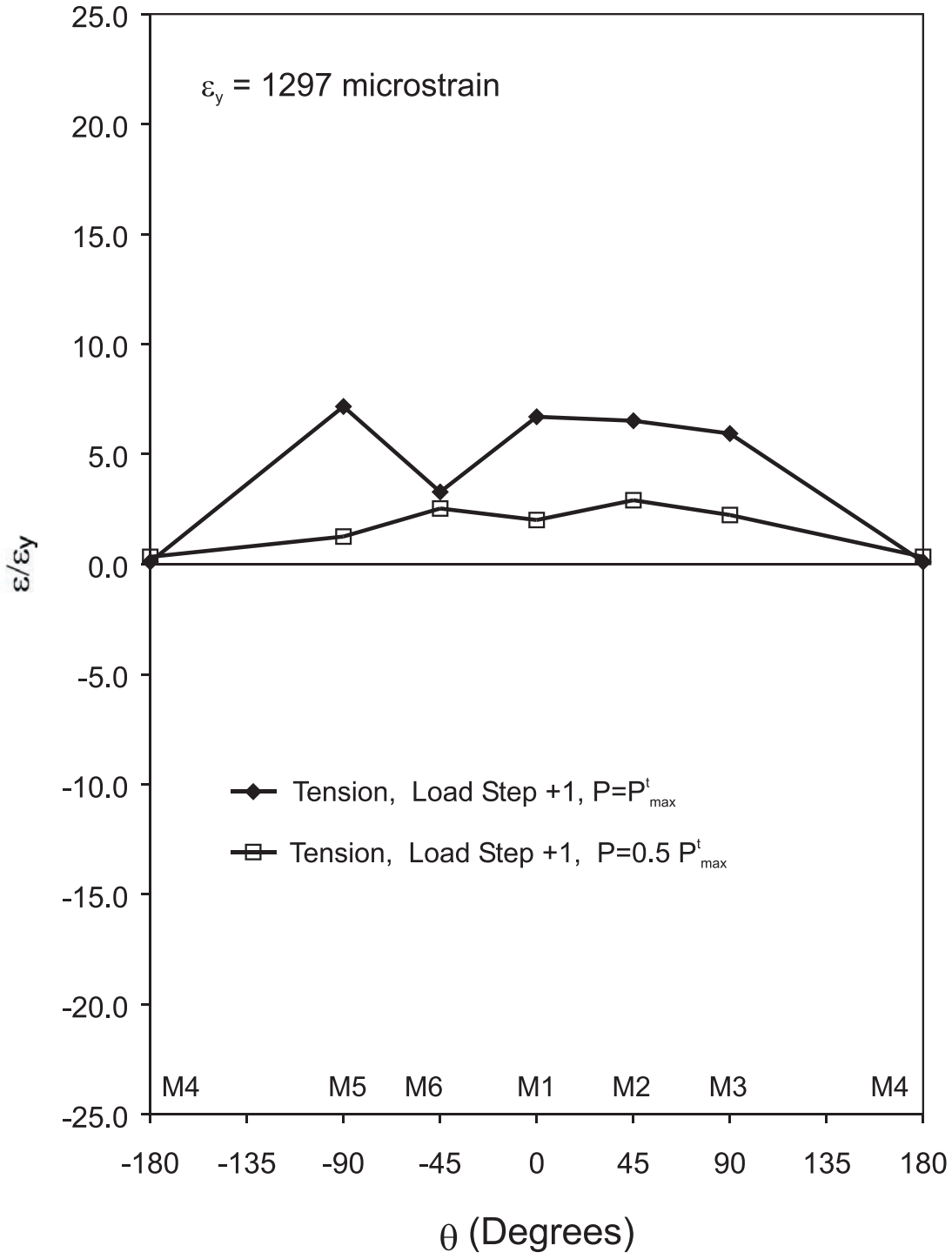

Figure 5.96 Strain Distribution of Cross Section at Mid-height, Specimen C27-33-311

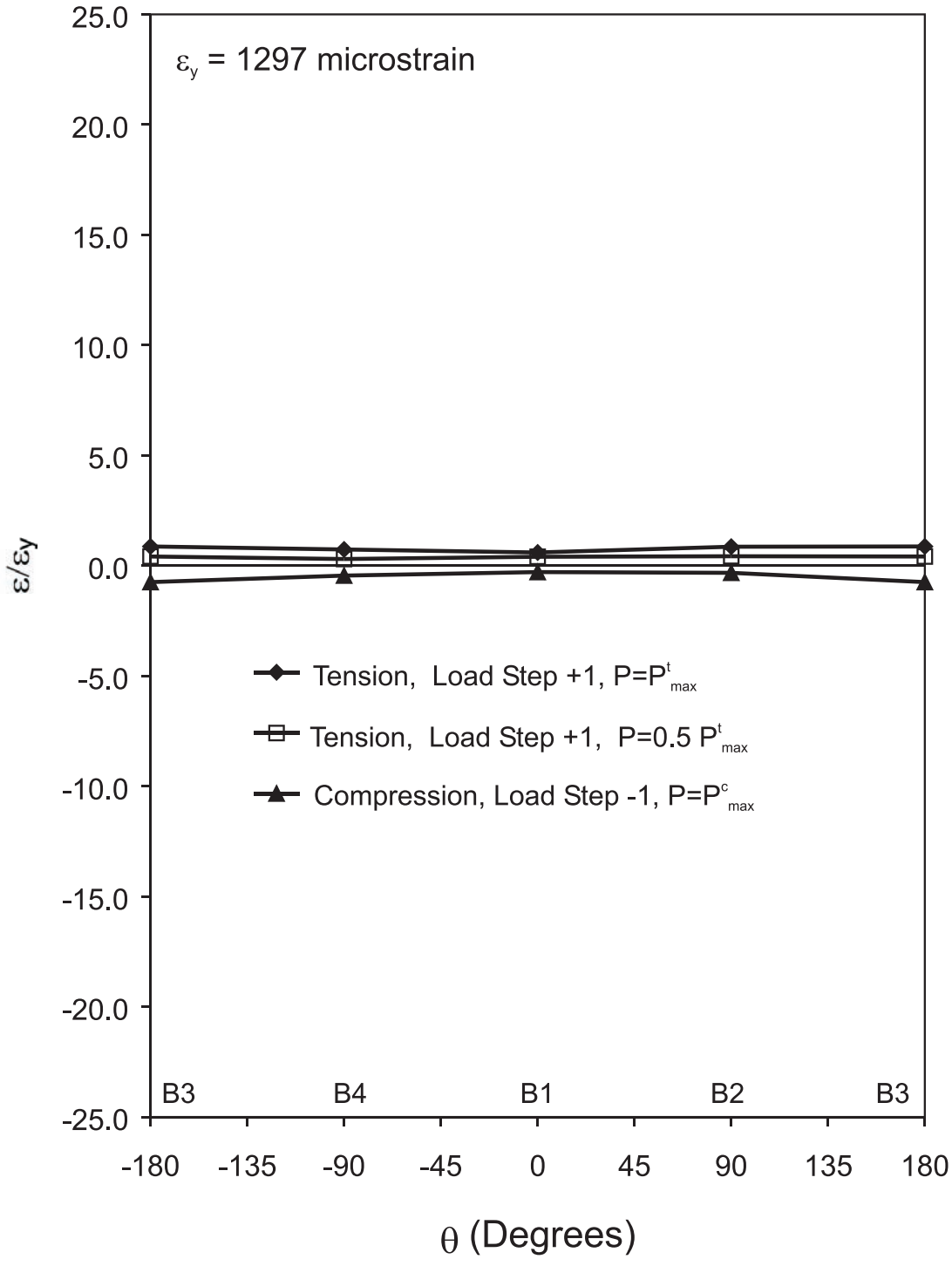

Figure 5.97 Strain Distribution of Cross Section at Lower Quarter-point, Specimen C27-33-311

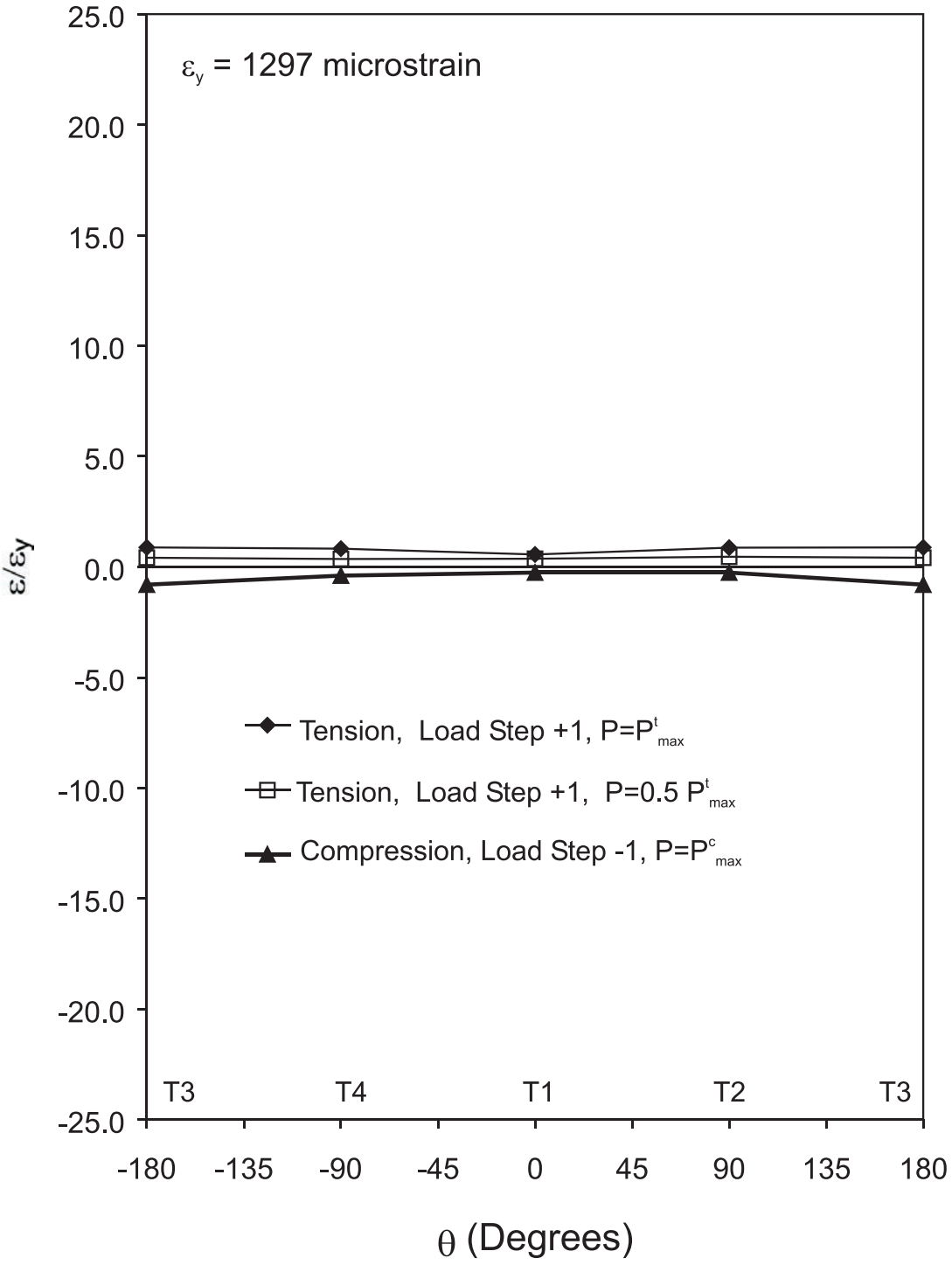

Figure 5.98 Strain Distribution of Cross Section at Upper Quarter-point, Specimen C27-33-311

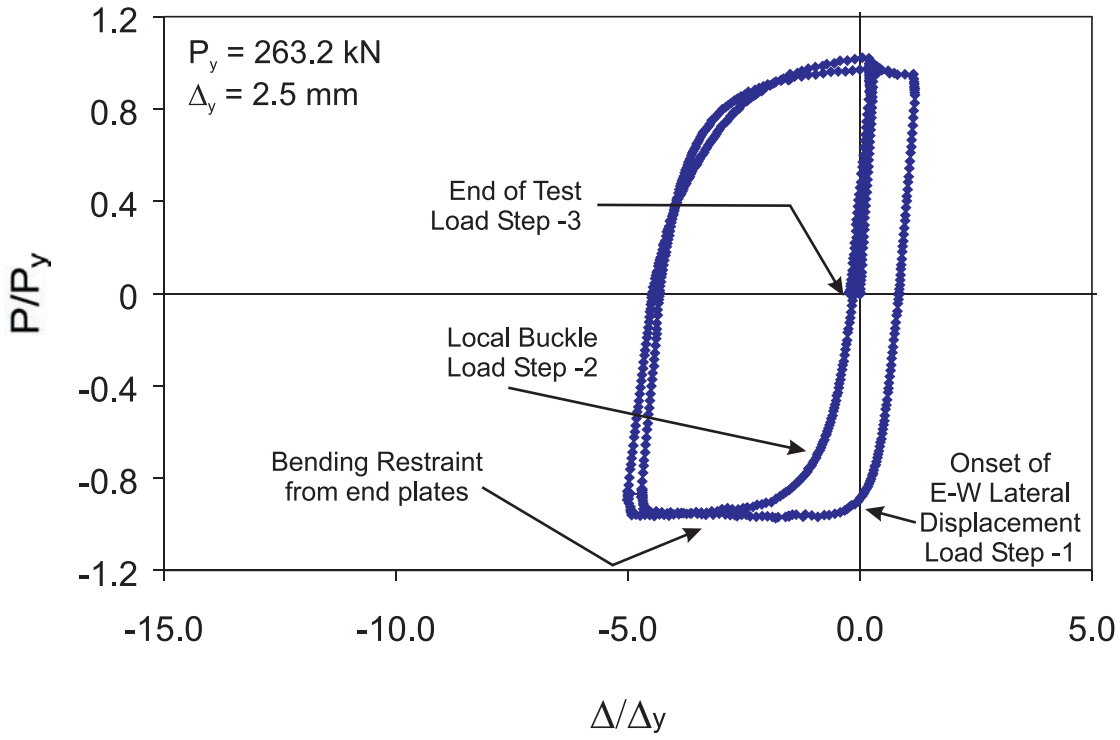

Figure 5.99 Normalized Axial Load - Axial Displacement, Specimen C40-00-95-RS

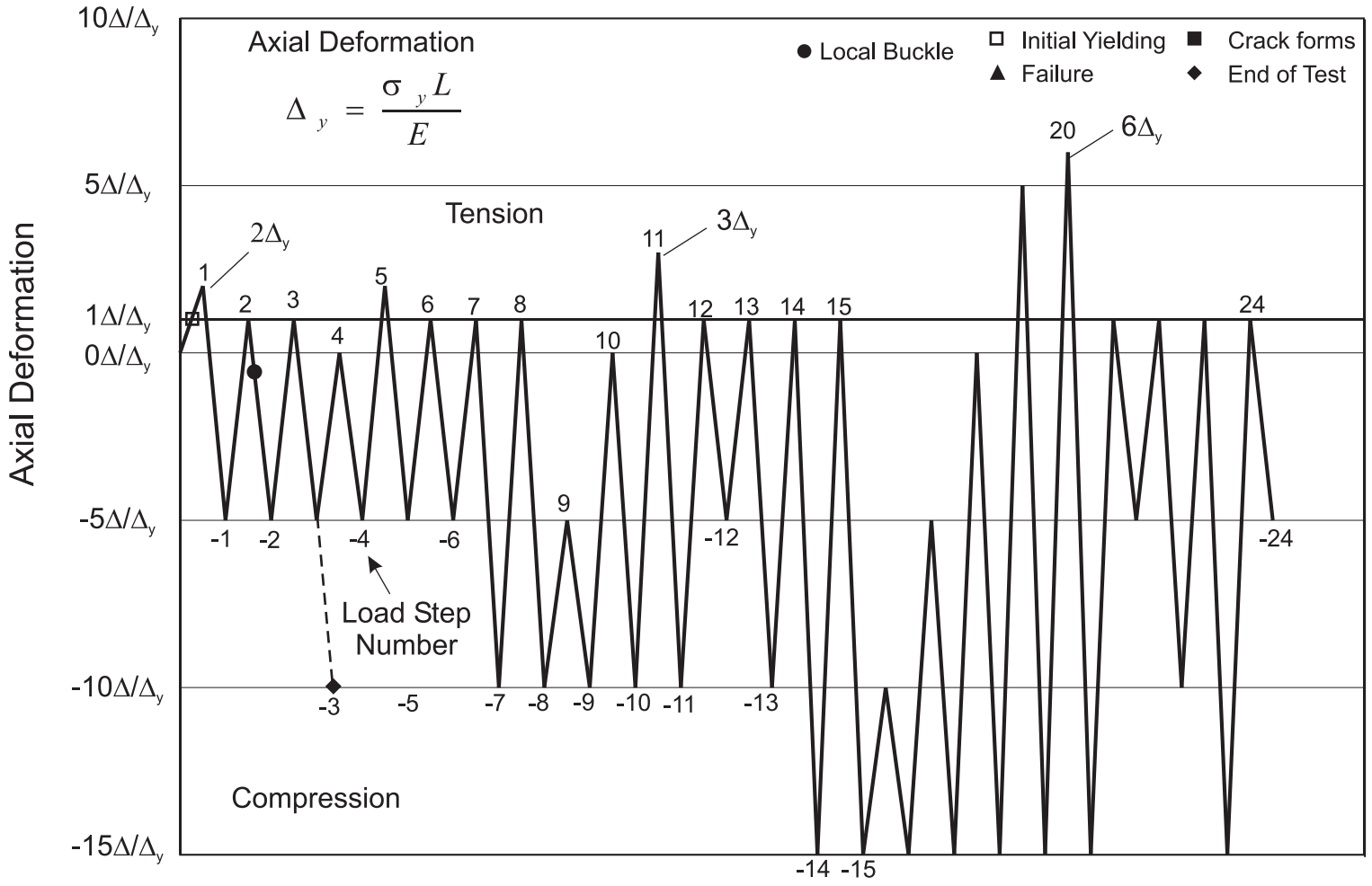

Figure 5.100 Displacement History with Events of Interest Noted, Specimen C40-00-95-RS

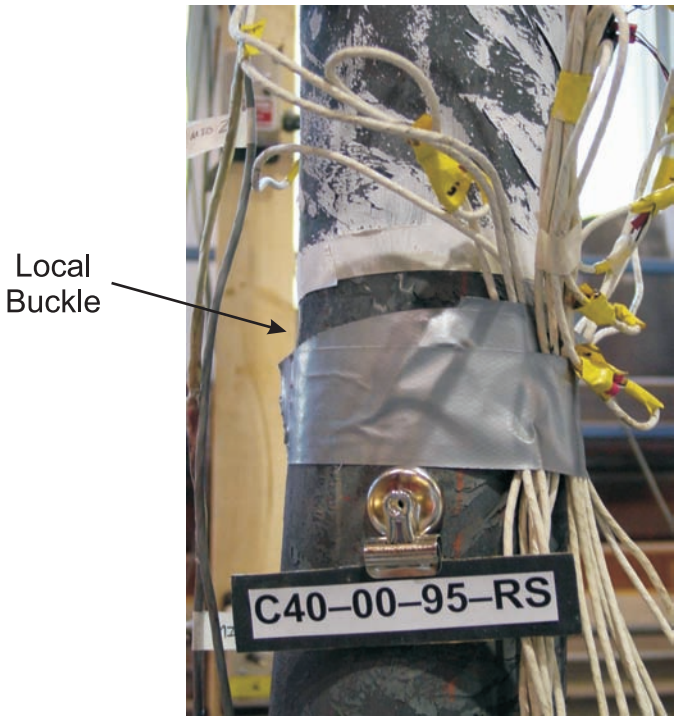

Figure 5.101 Side View of Local Buckle (Load Step -2), Specimen C40-00-95-RS

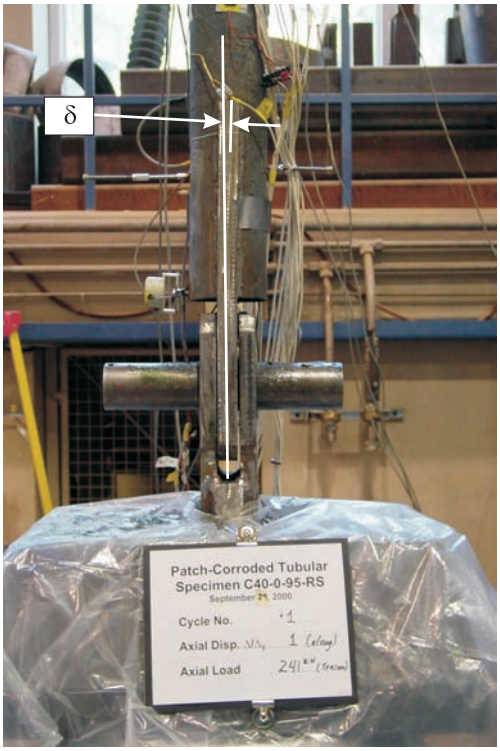

Figure 5.102 View of End Plate Bending (Load Step -2), Specimen C40-00-95-RS

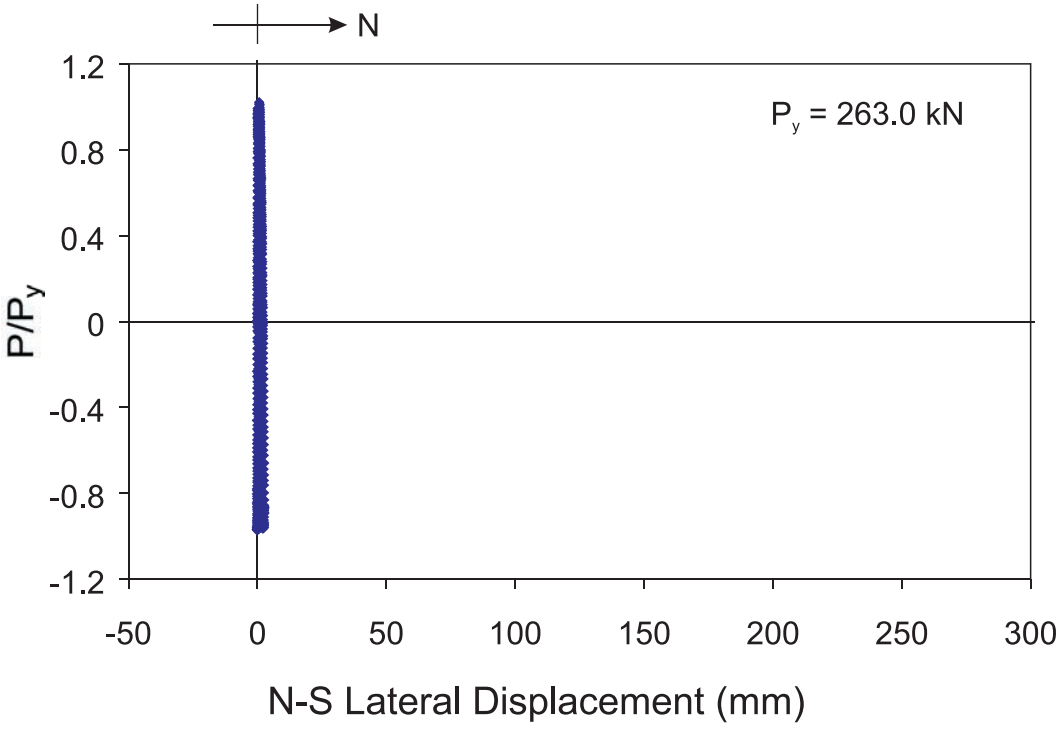

Figure 5.103 Measured Lateral Displacement in the North-South Direction, Specimen C40-00-95-RS

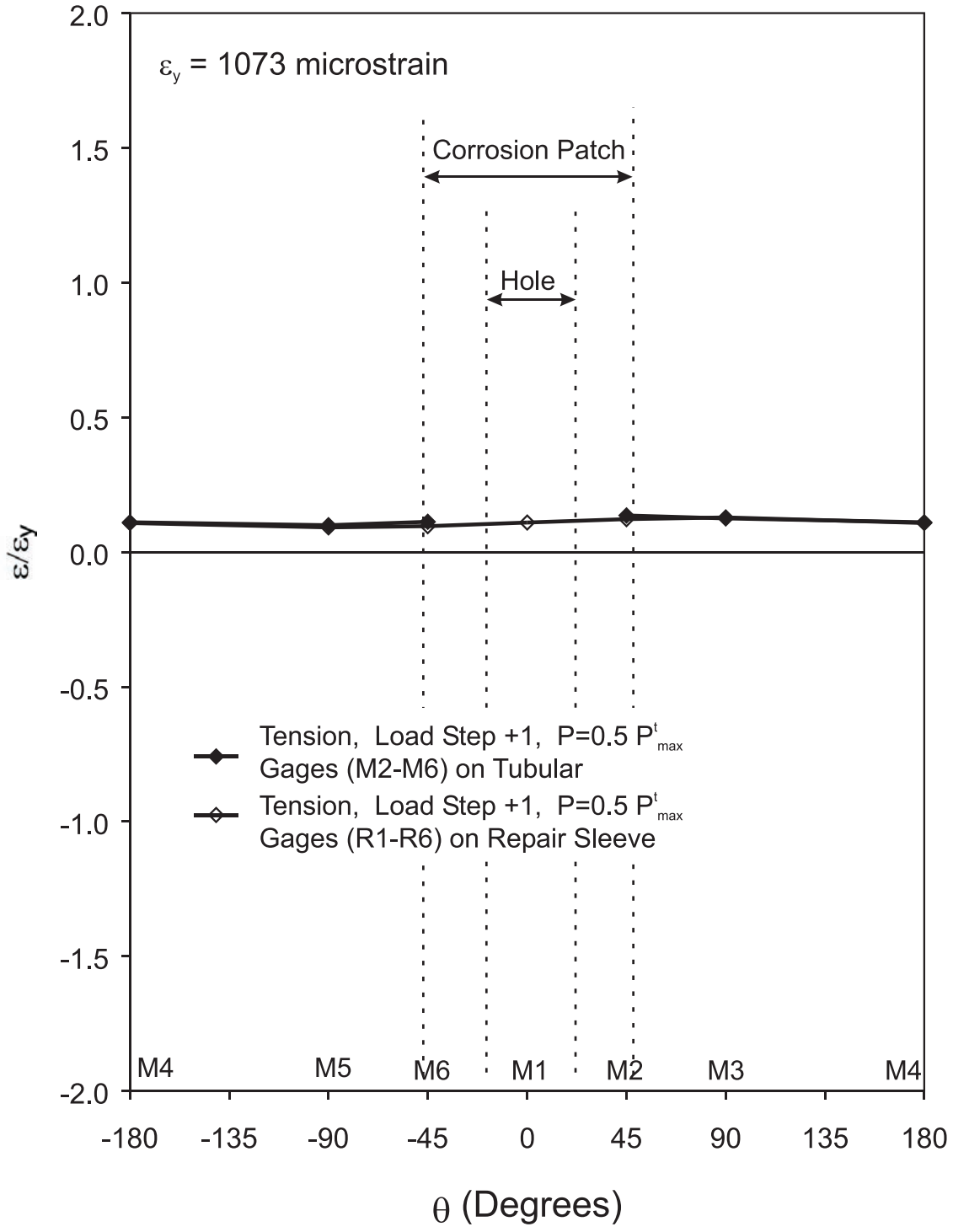

Figure 5.104 Strain Distribution of Cross Section at Mid-height on Tubular and Repair Sleeve at One Half Peak Tension Load (0.5 P^t_{max}), Specimen C40-00-95-RS

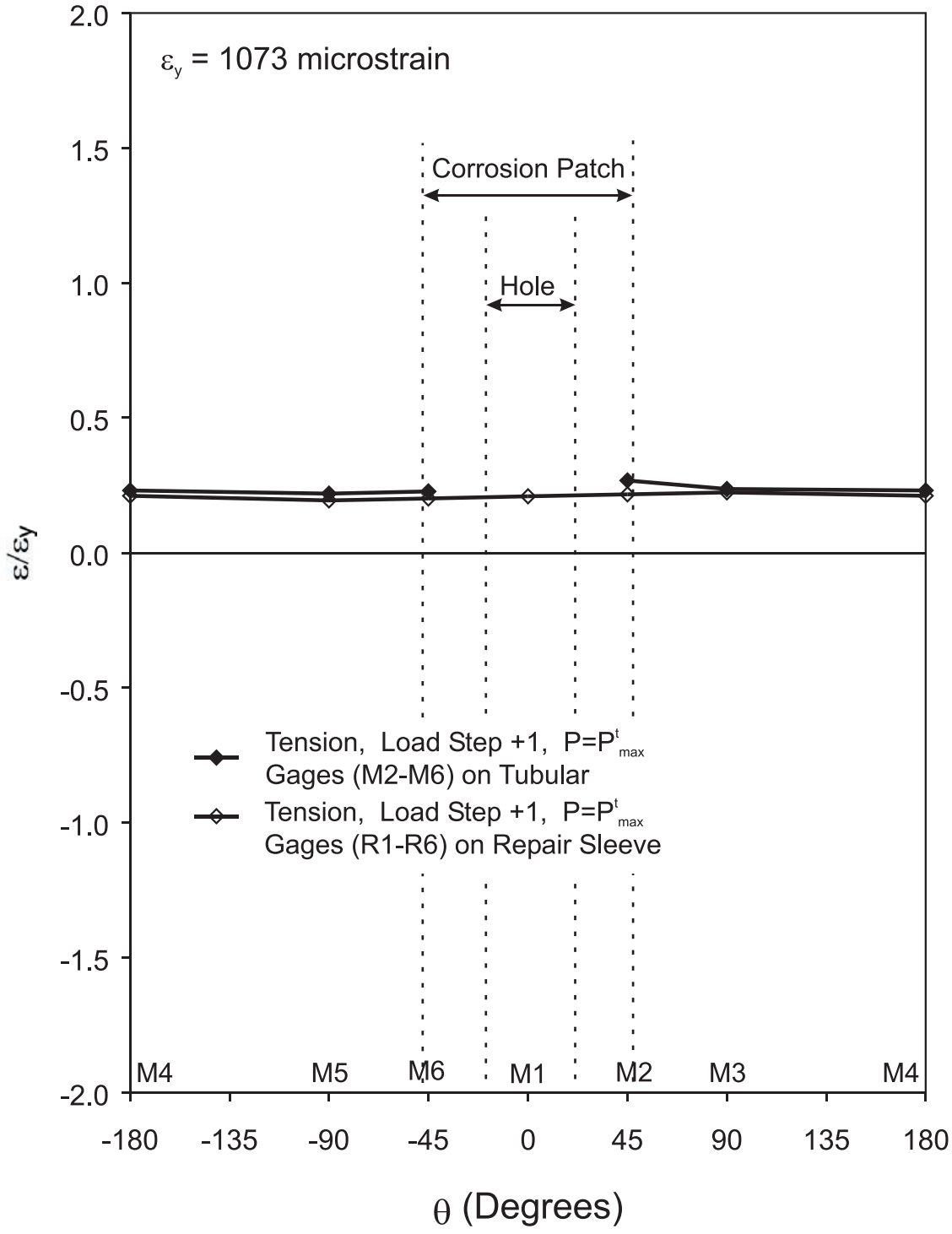

Figure 5.105 Strain Distribution of Cross Section at Mid-height on Tubular and Repair Sleeve at Peak Tension Load (P^t_{max}), Specimen C40-00-95-RS

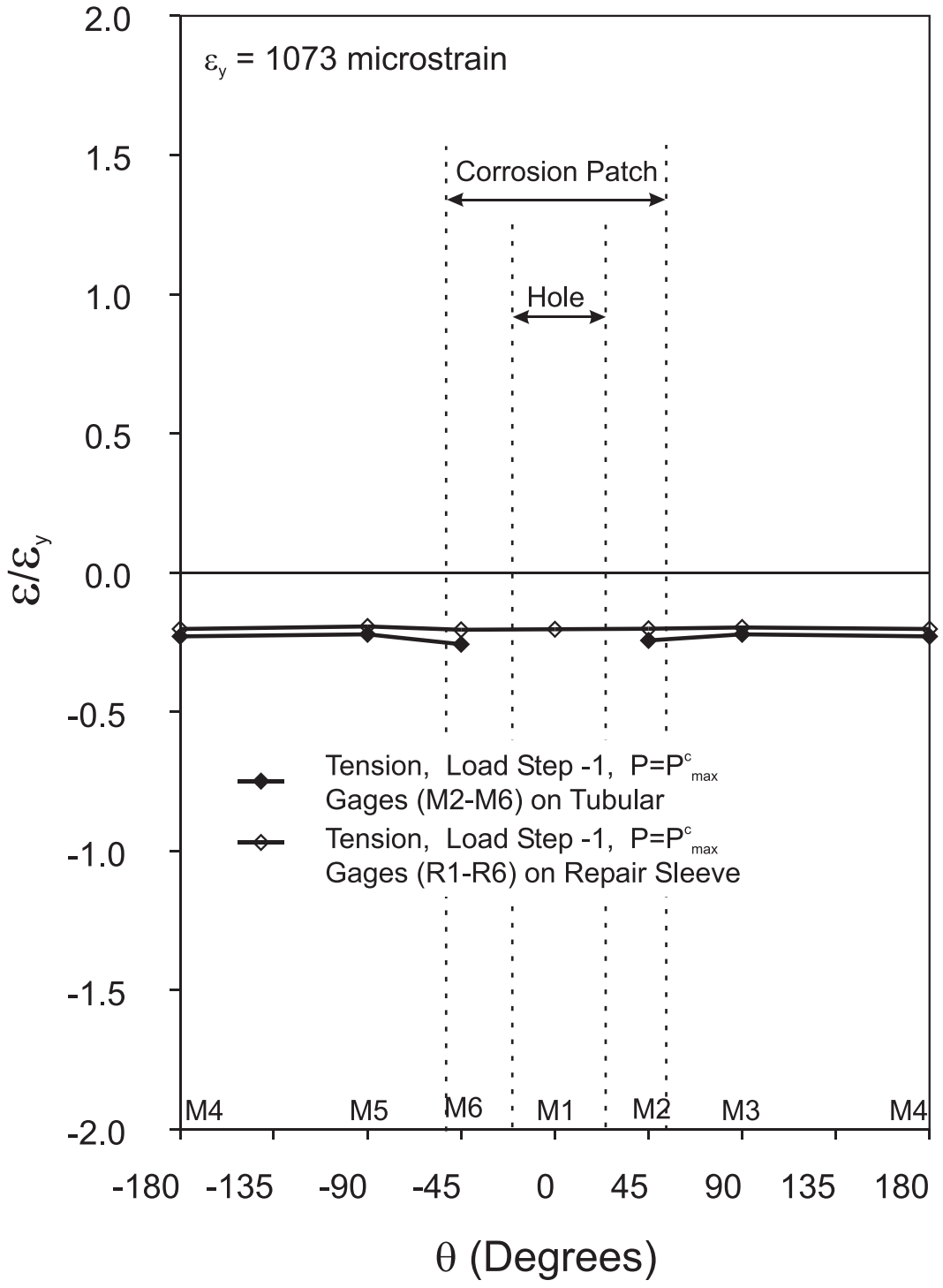

Figure 5.106 Strain Distribution of Cross Section at Mid-height on Tubular and Repair Sleeve at Peak Compression Load (P^c_{max}), Specimen C40-00-95-RS

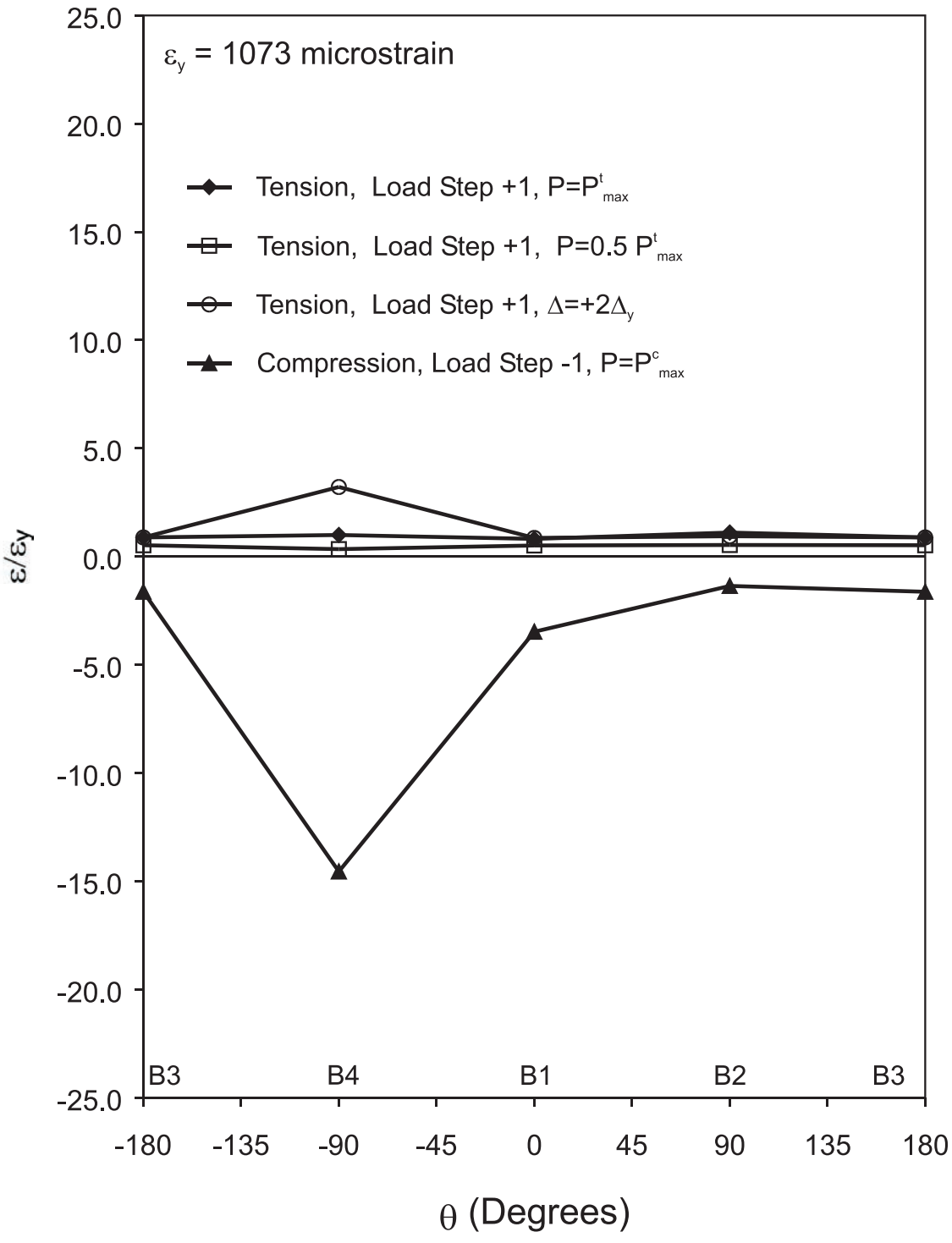

Figure 5.107 Strain Distribution of Cross Section at Lower Quarter-point, Specimen C40-00-95-RS

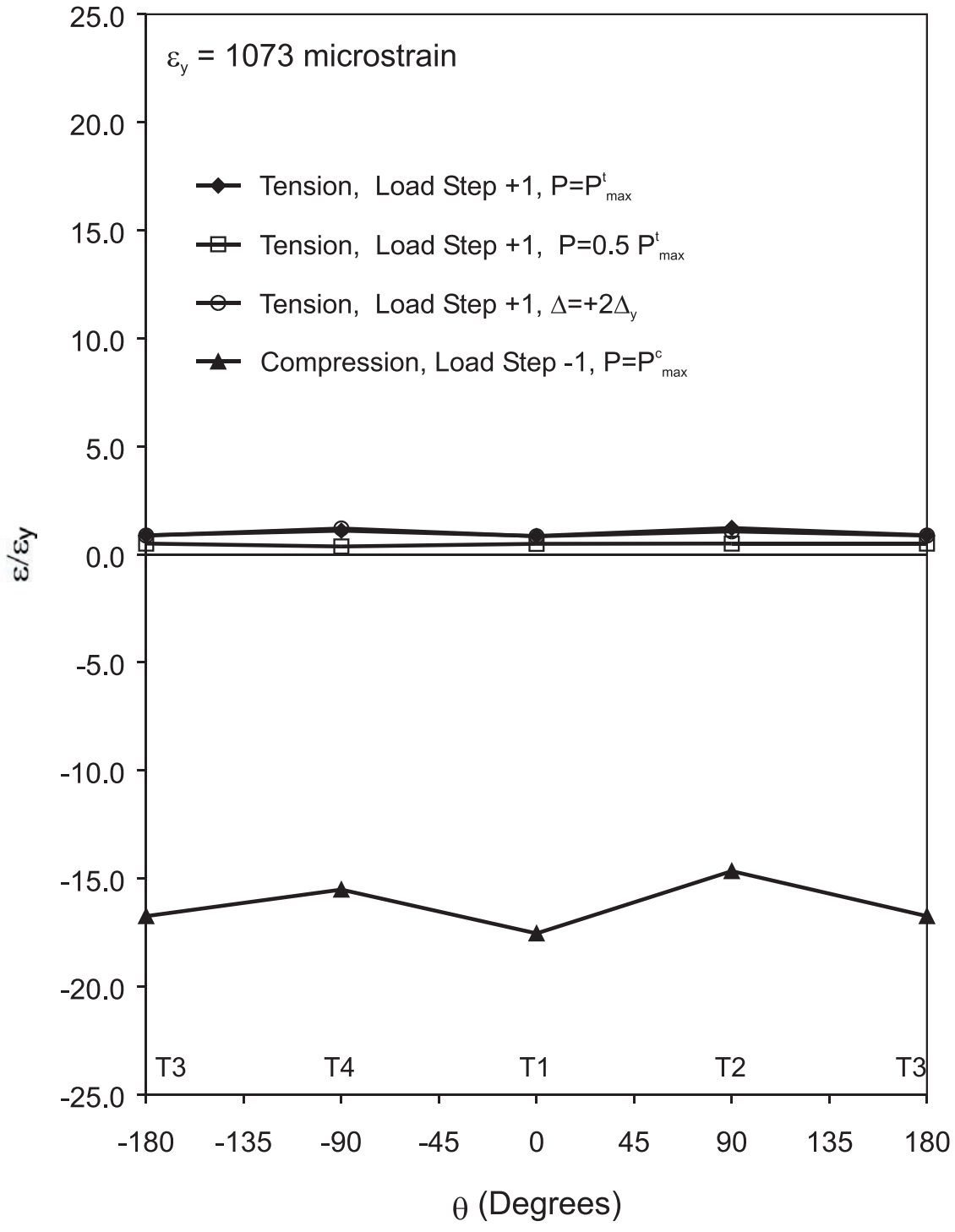

Figure 5.108 Strain Distribution of Cross Section at Upper Quarter-point, Specimen C40-00-95-RS

Figure 5.109 View of Top End of Sleeve Repair after Testing, Specimen C40-00-95-RS

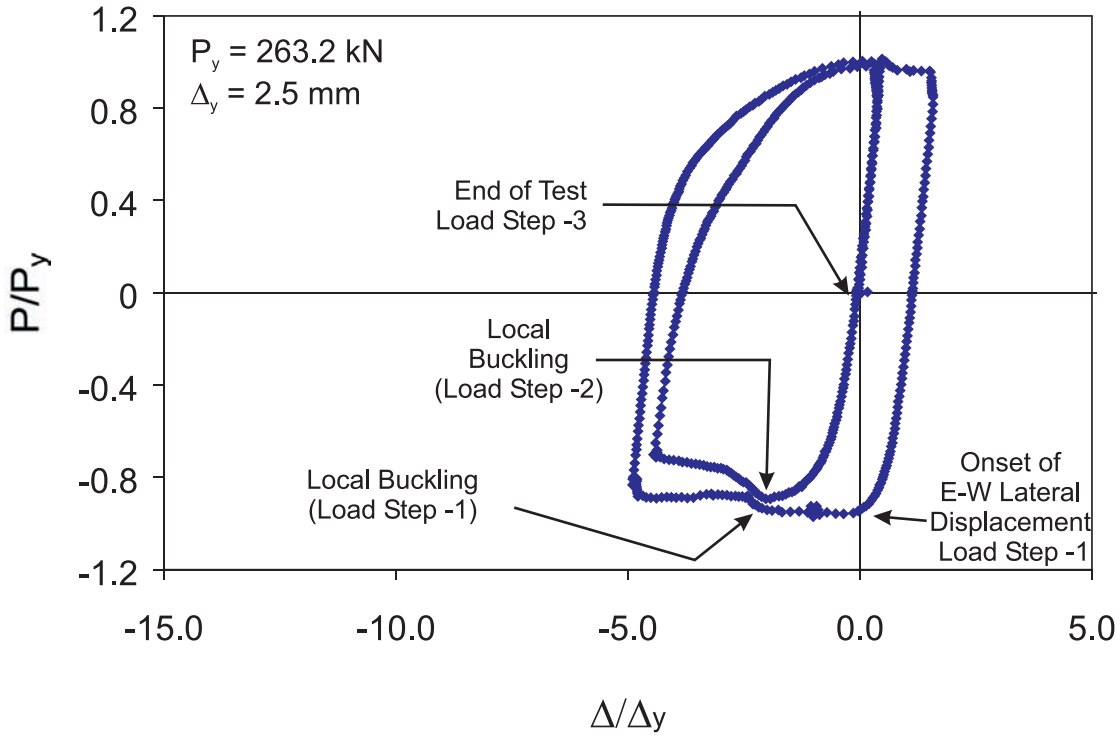

Figure 5.110 Normalized Axial Load - Axial Displacement, Specimen C40-00-95-RC

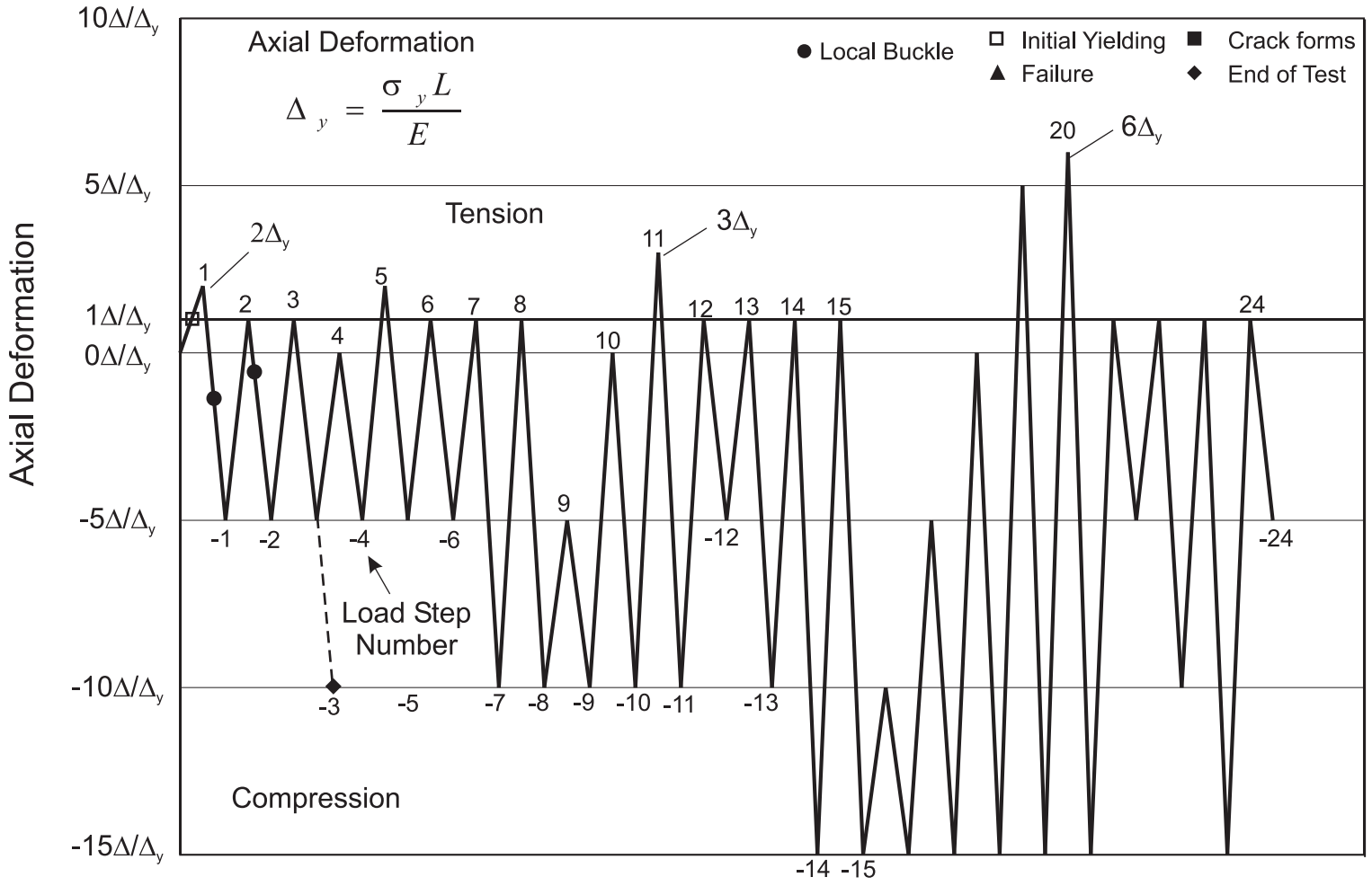

Figure 5.111 Displacement History with Events of Interest Noted, Specimen C40-00-95-RC

Figure 5.112 Side View of Local buckle (Load Step -1), Specimen C40-00-95-RC

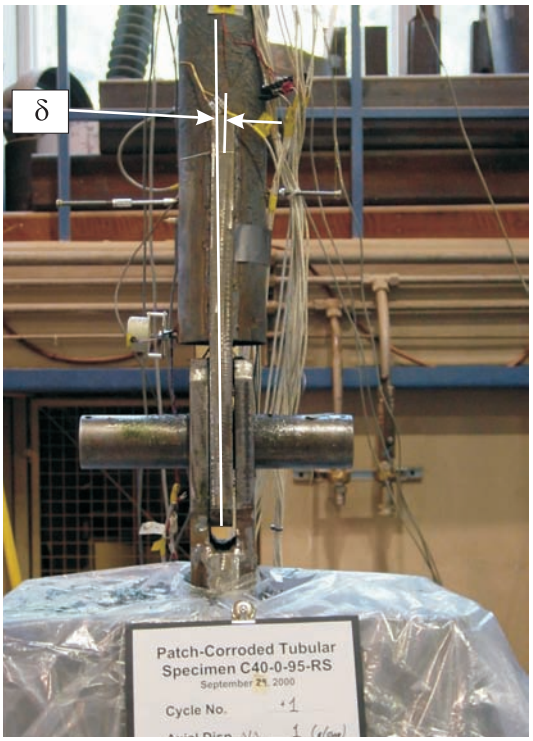

Figure 5.113 View of End Plate Bending (Load Step -2), Specimen C40-00-95-RC

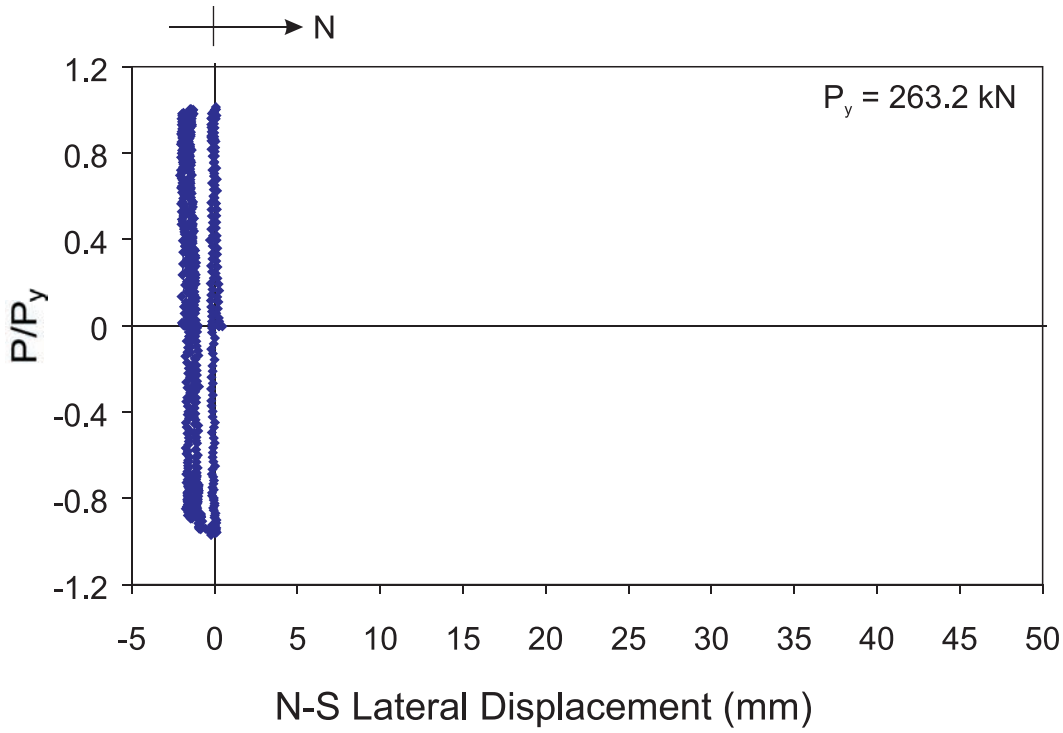

Figure 5.114 Measured Lateral Displacement in the North-South Direction, Specimen C40-00-95-RC

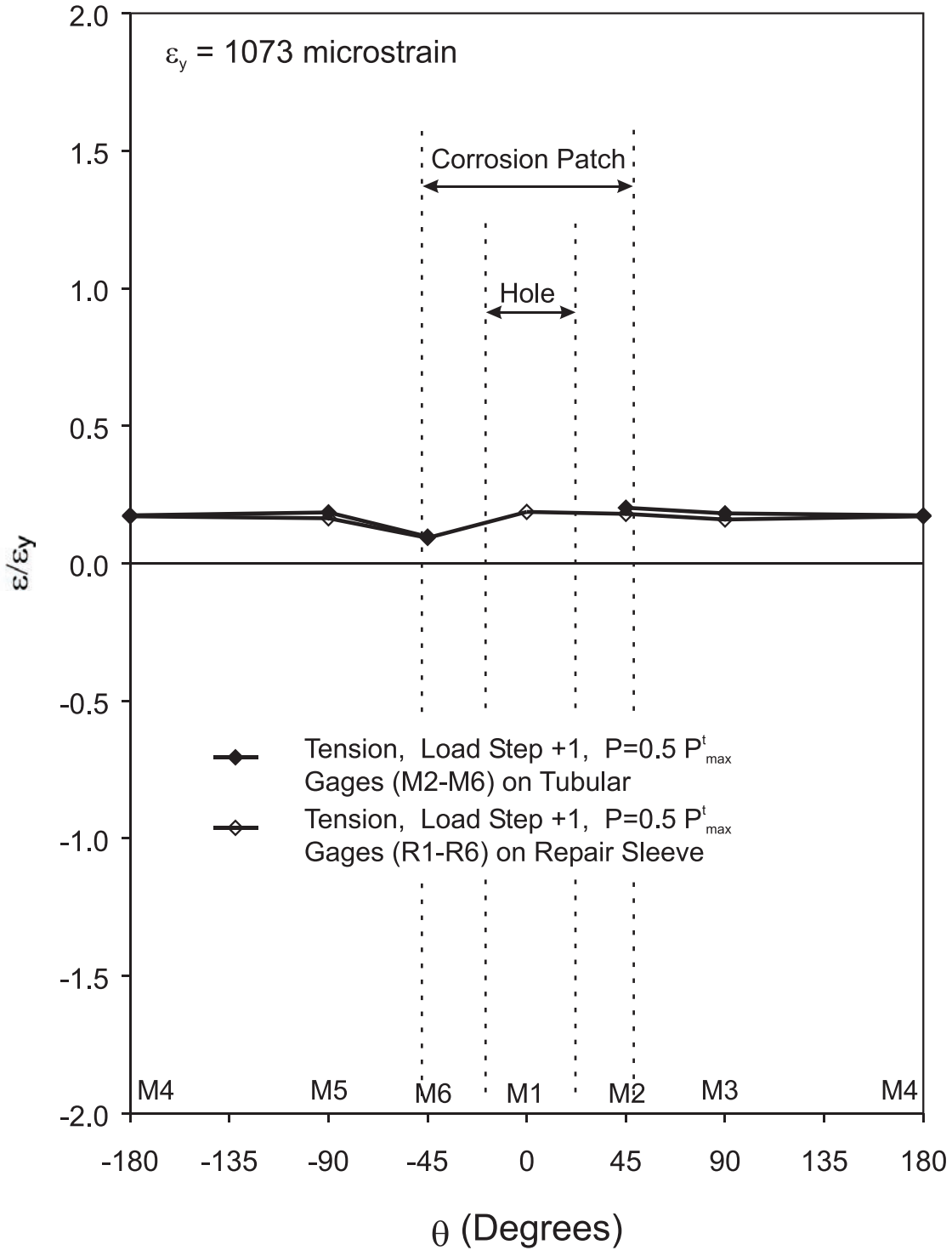

Figure 5.115 Strain Distribution of Cross Section at Mid-height on Tubular and Repair Sleeve at One Half Peak Tension Load (0.5 P^t_{max}), Specimen C40-00-95-RC

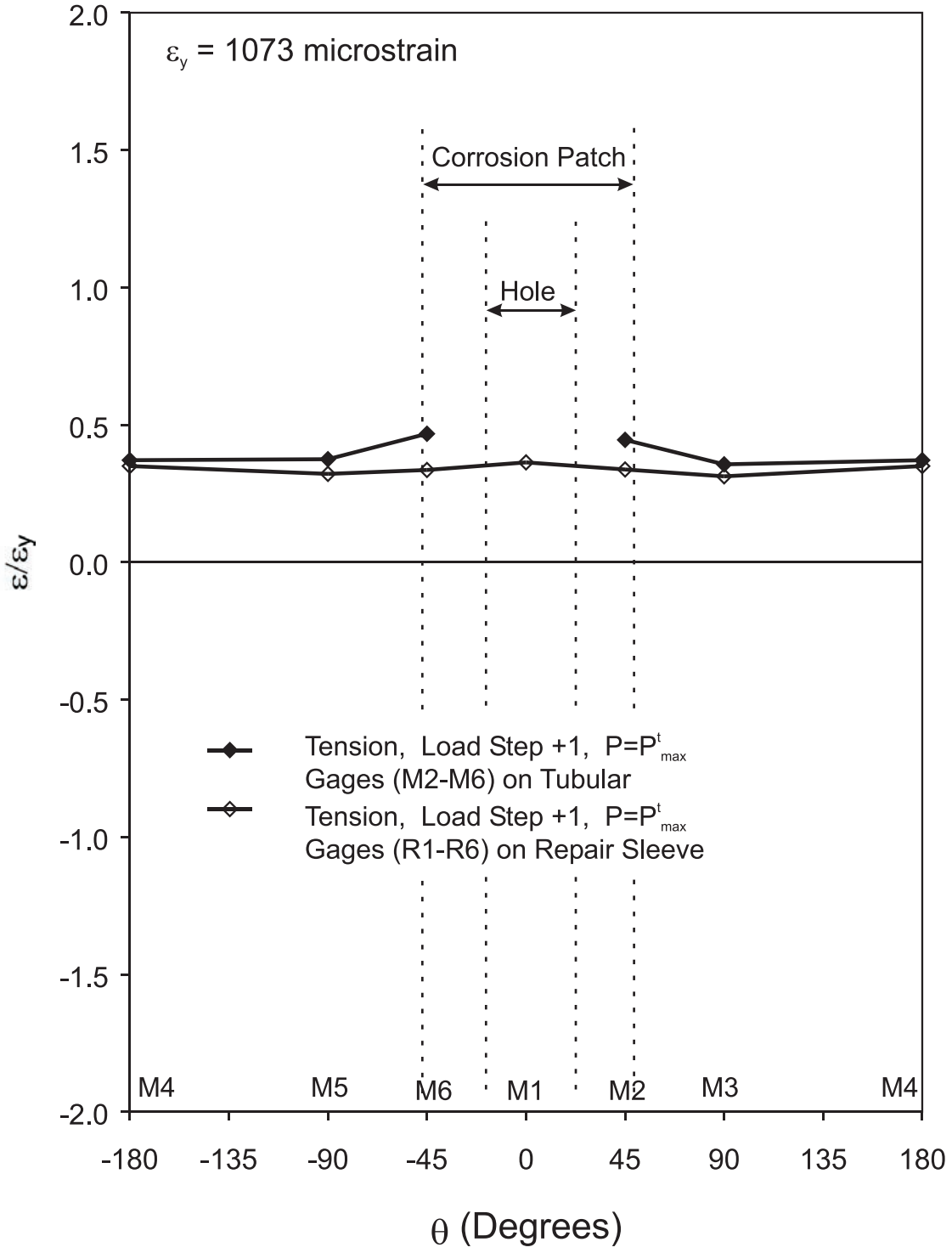

Figure 5.116 Strain Distribution of Cross Section at Mid-height on Tubular and Repair Sleeve at Peak Tension Load (P^t_{max}), Specimen C40-00-95-RC

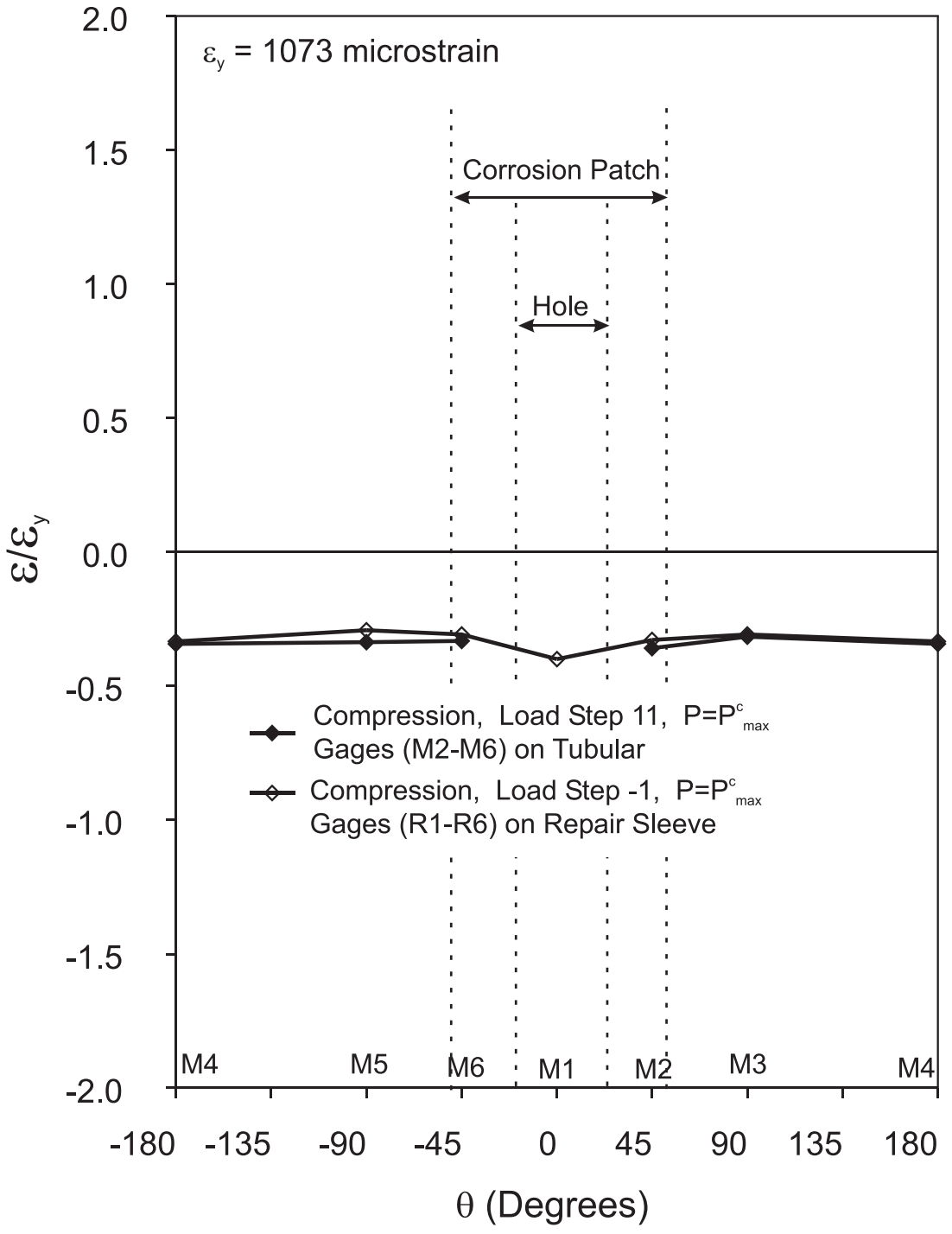

Figure 5.117 Strain Distribution of Cross Section at Mid-height on Tubular and Repair Sleeve at Peak Compression Load (P^c_{max}), Specimen C40-00-95-RC

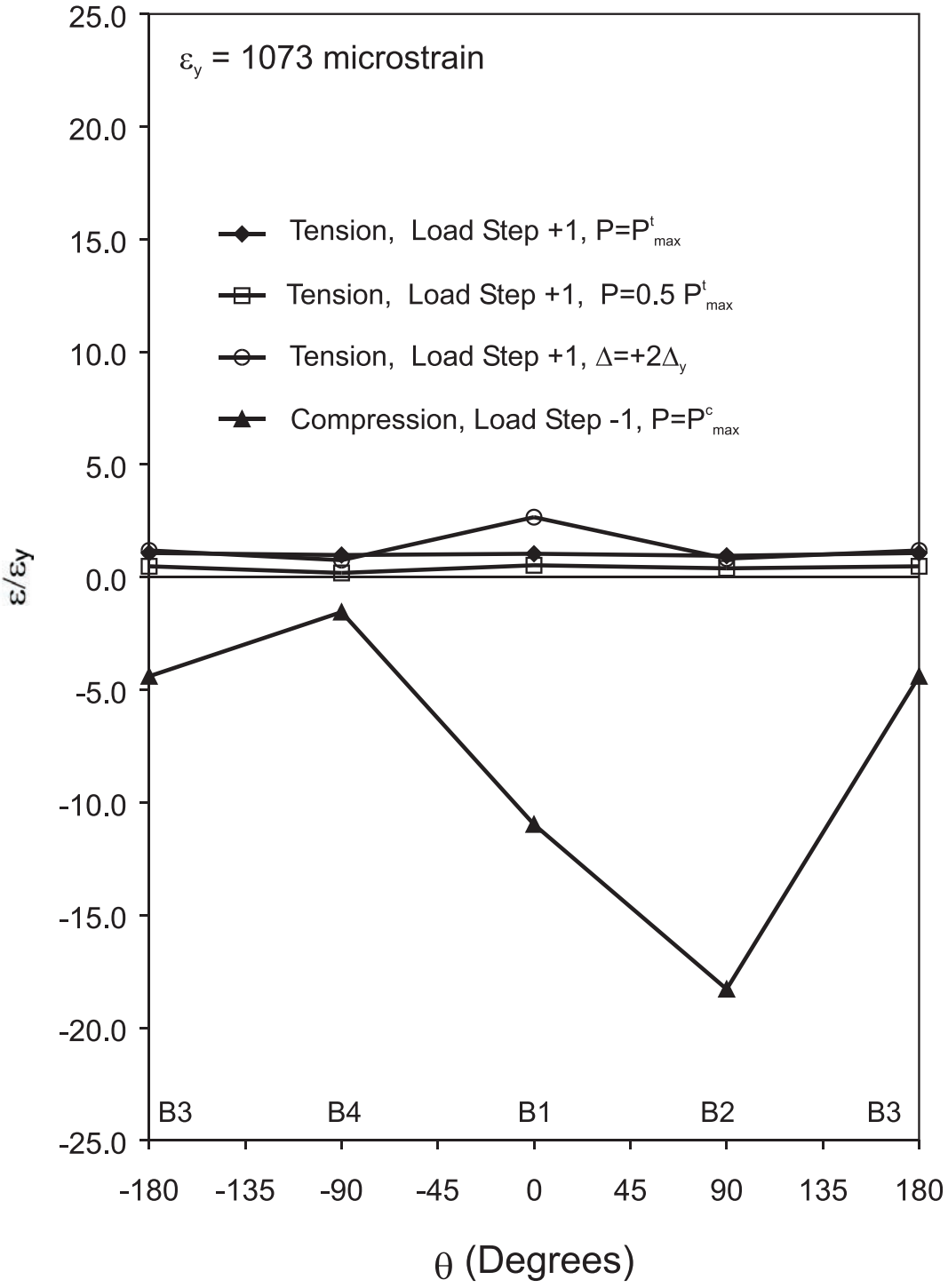

Figure 5.118 Strain Distribution of Cross Section at Lower Quarter-point, Specimen C40-00-95-RC

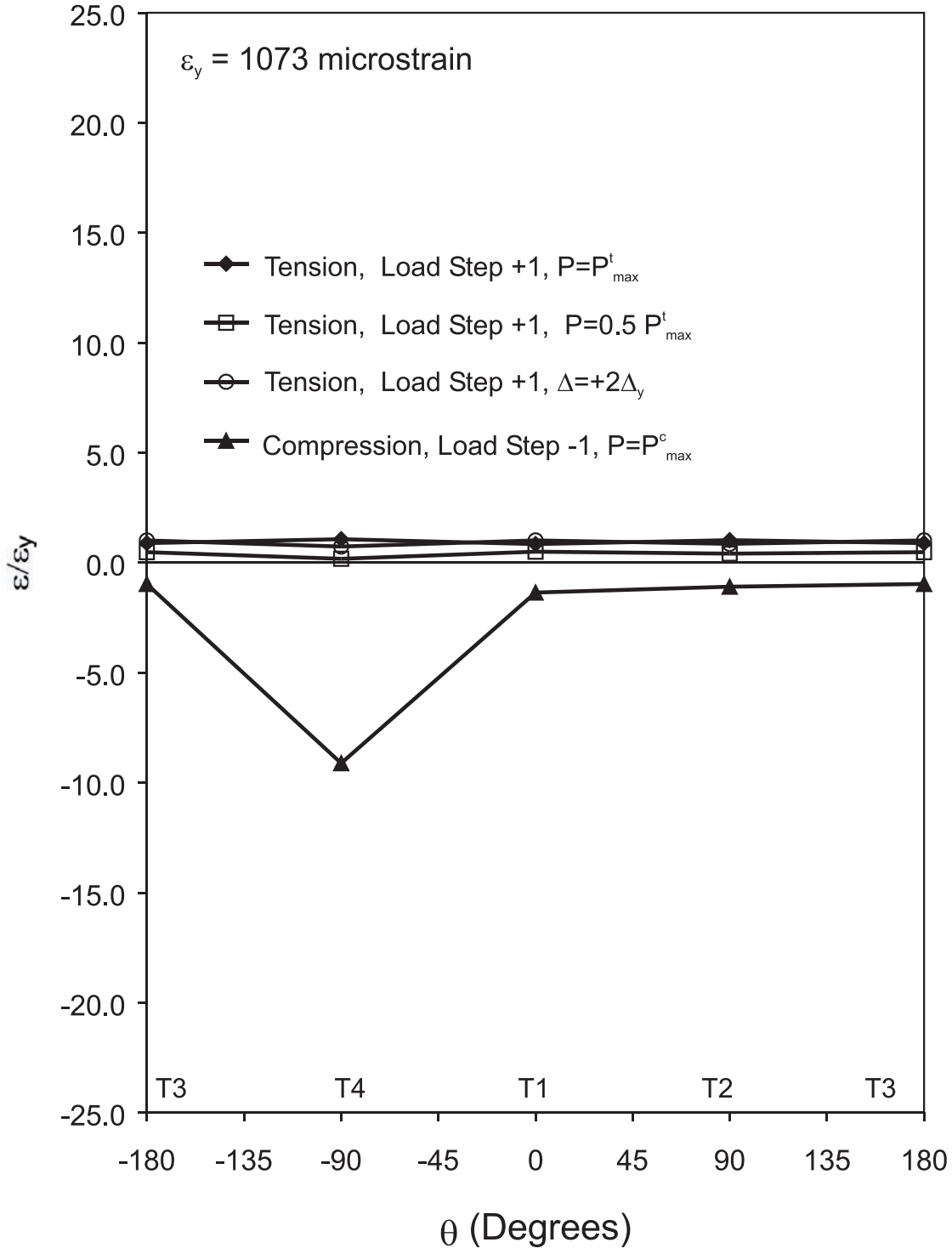

Figure 5.119 Strain Distribution of Cross Section at Upper Quarter-point, Specimen C40-00-95-RC

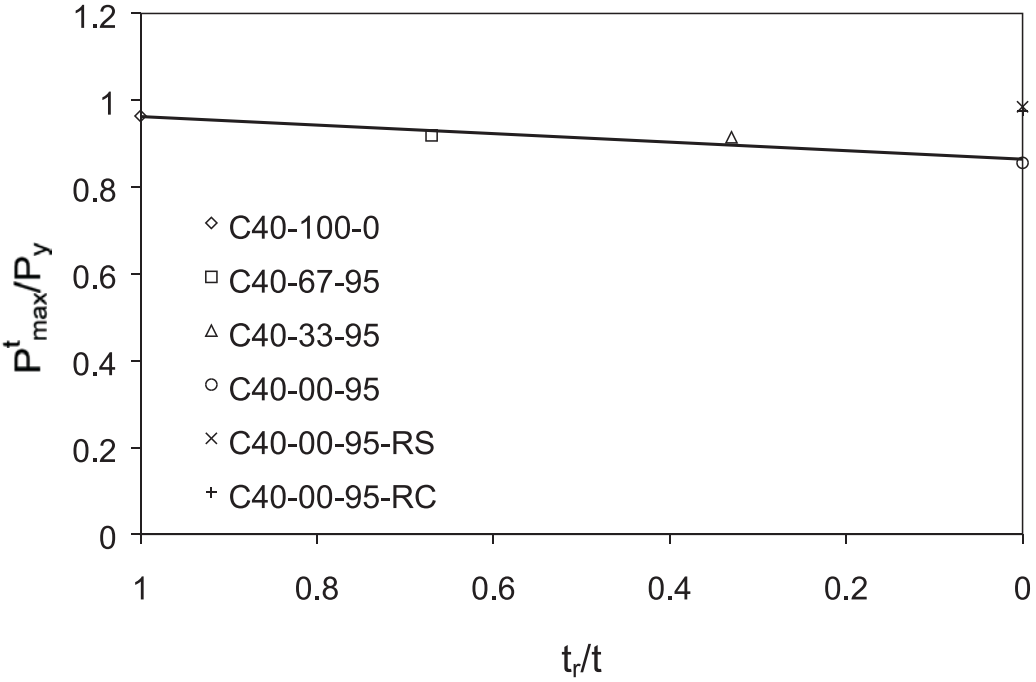

Figure 6.1 Effect of Reduced Thickness on Peak Tension Axial Load

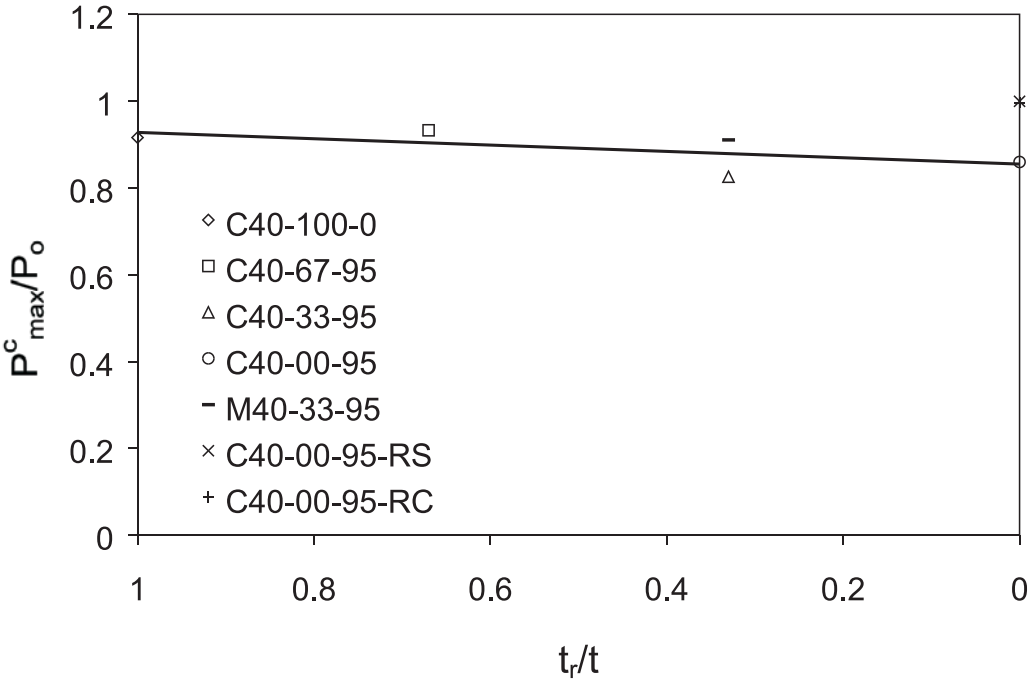

Figure 6.2 Effect of Reduced Thickness on Peak Compression Axial Load

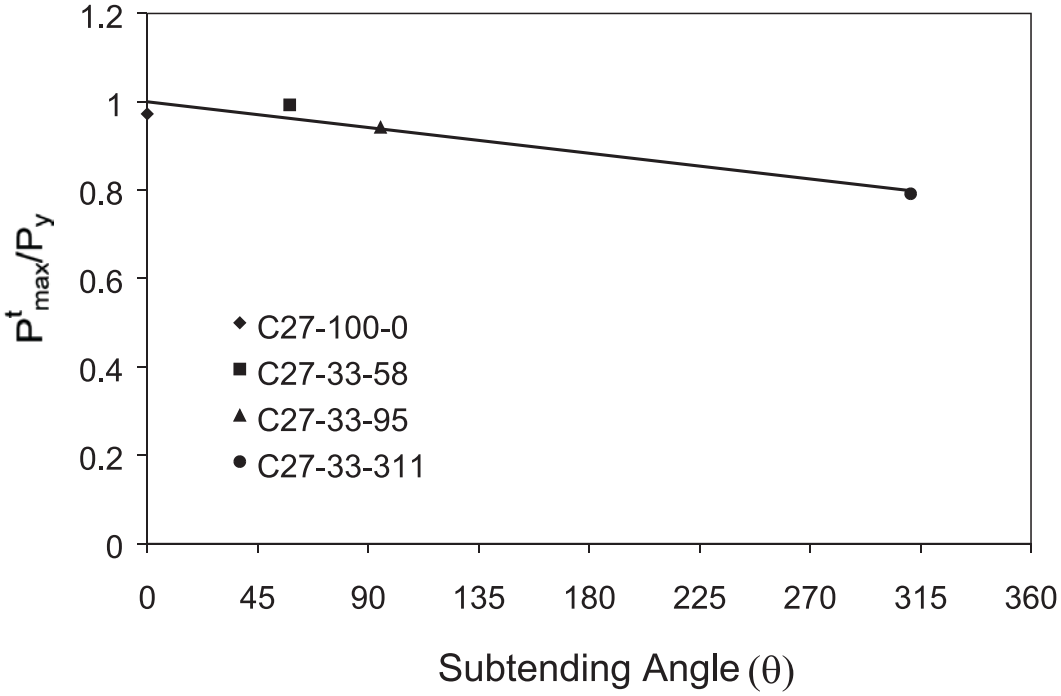

Figure 6.3 Effect of Subtending Angle on Peak Tension Axial Load

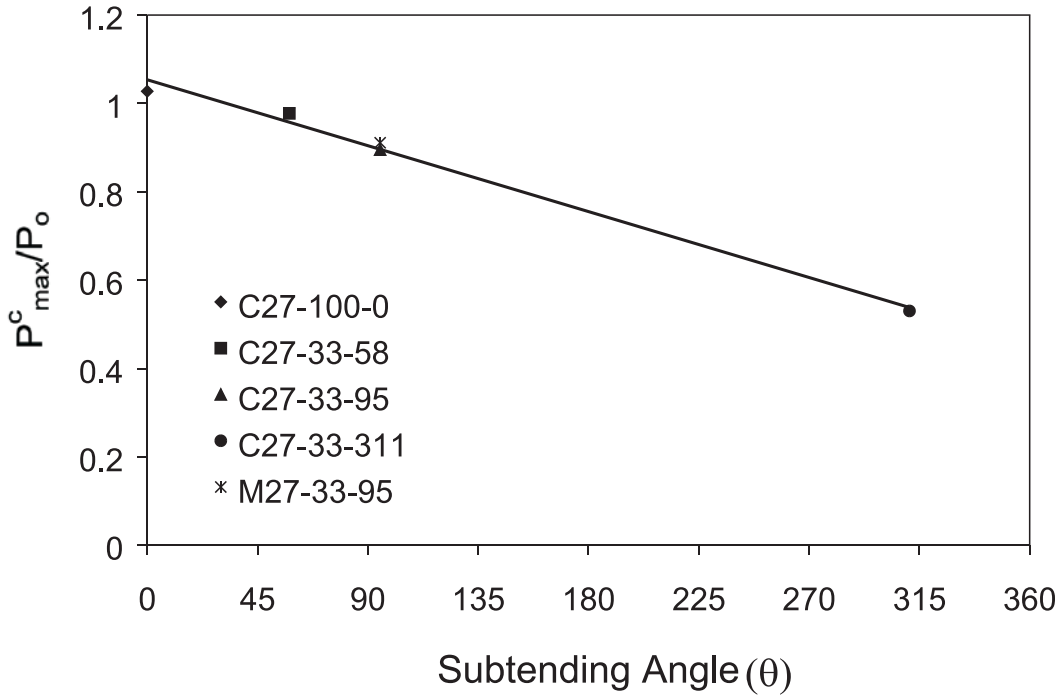

Figure 6.4 Effect of Subtending Angle on Peak Compression Axial Load

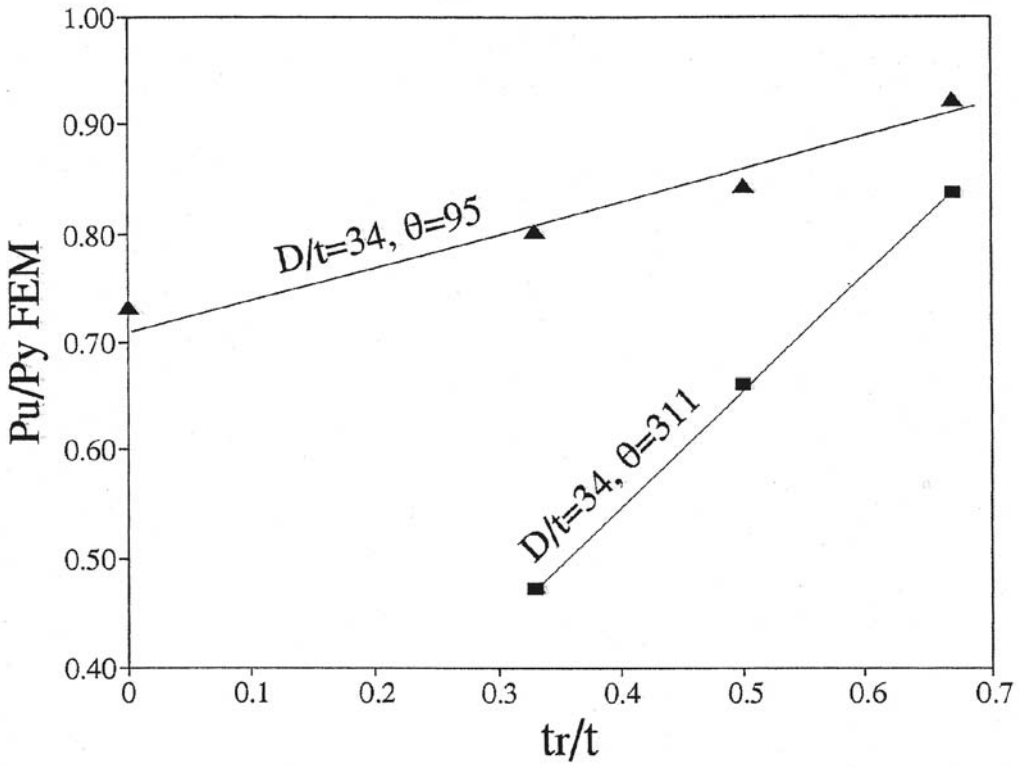

Figure 6.5 Combined Effect of Thickness Reduction and Subtending Angle (Hebor and Ricles 1994)

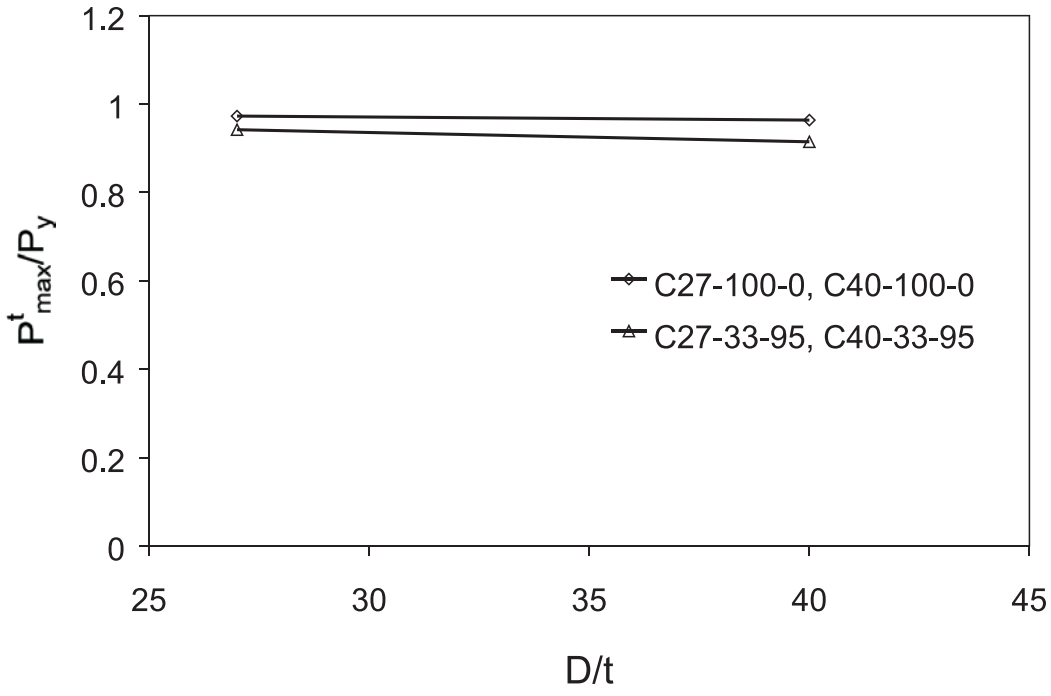

Figure 6.6 Effect of D/t on Peak Tension Axial Load

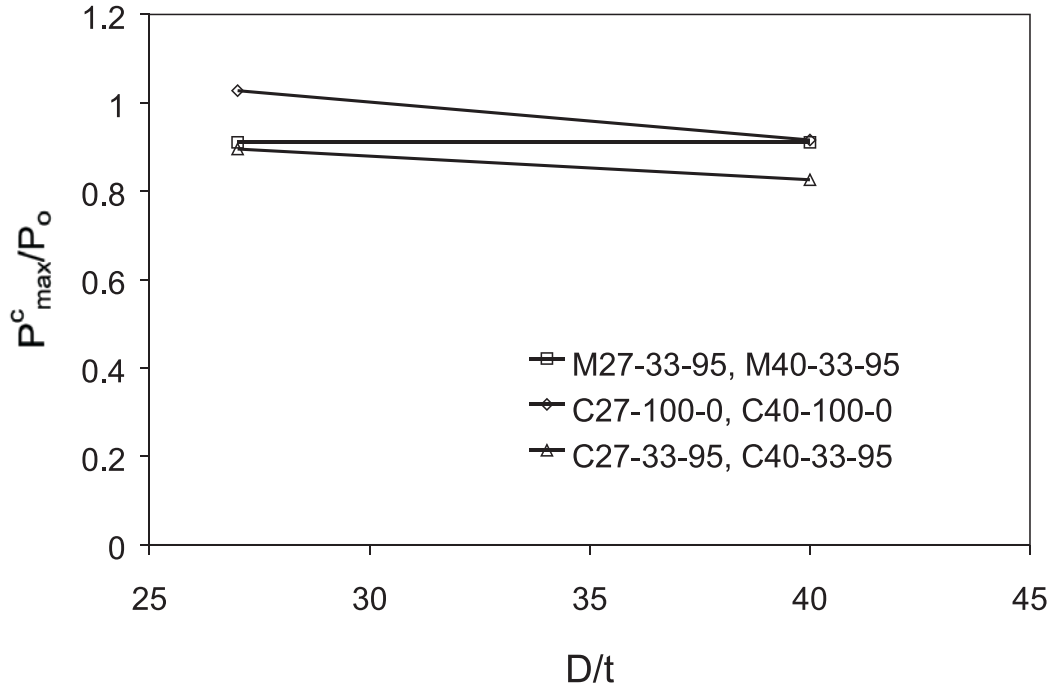

Figure 6.7 Effect of D/t on Peak Compression Axial Load

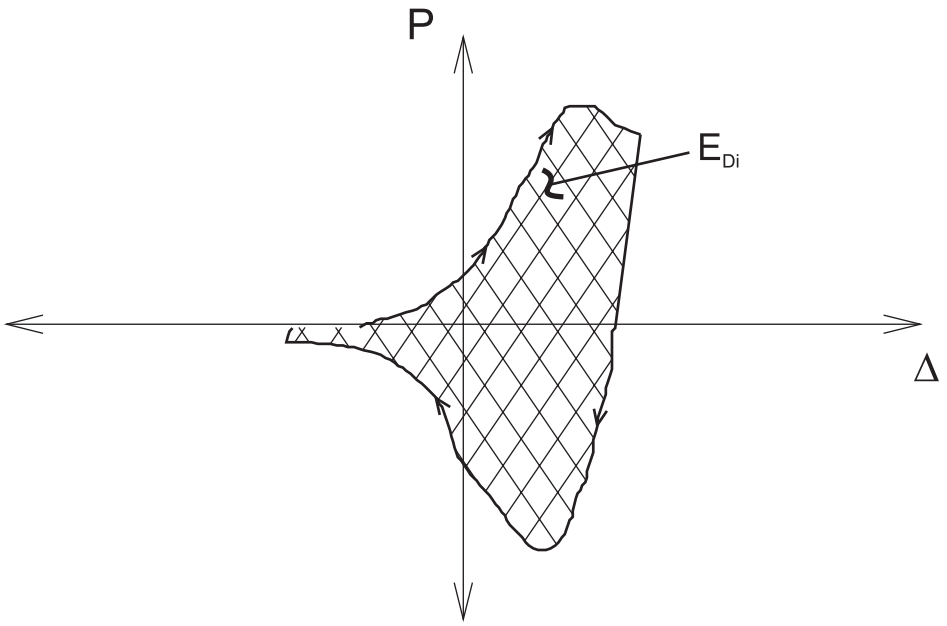

Figure 6.8 Energy Dissipation over a Load Cycle, E_{Di}

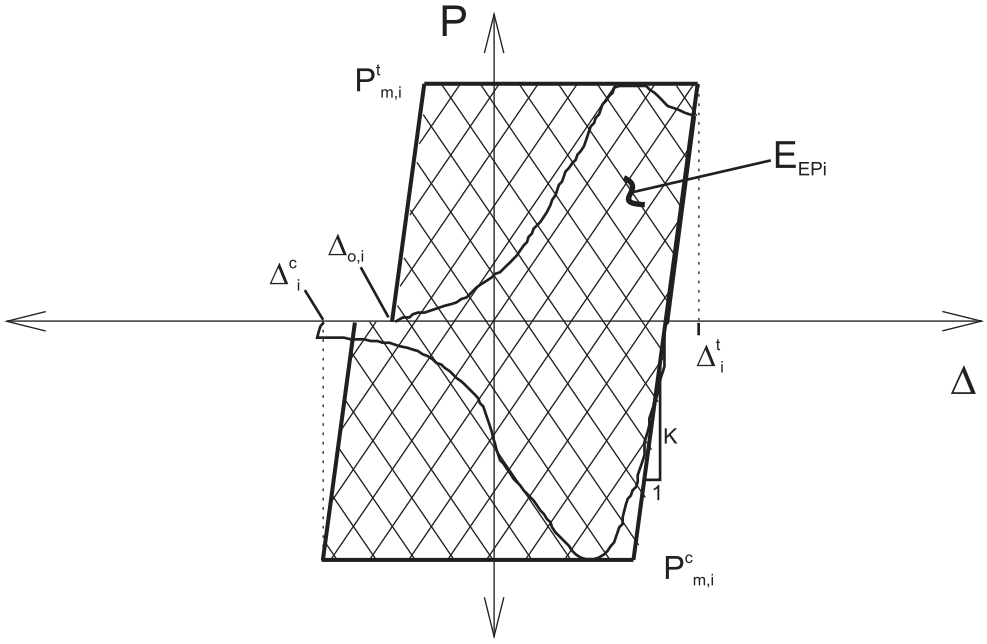

Figure 6.9 Definition of Energy Dissipation, E_{EPi}

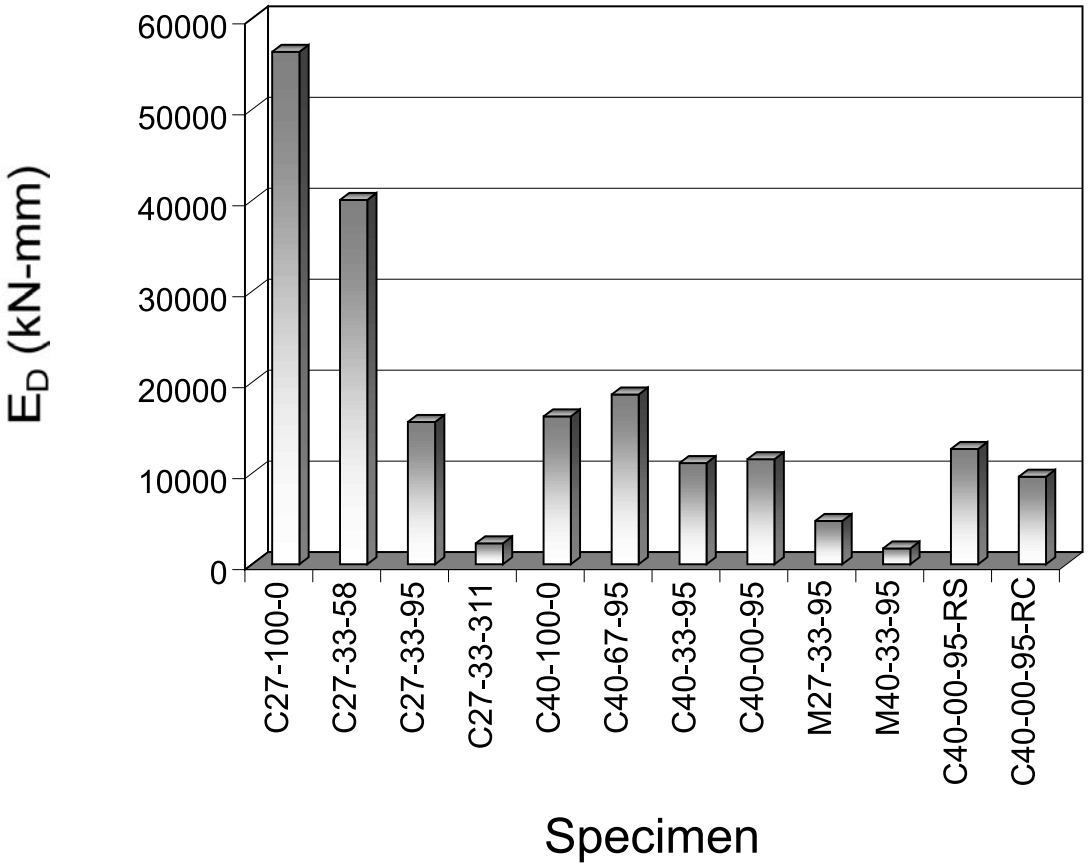

Figure 6.10 Total Energy Dissipated per Specimen

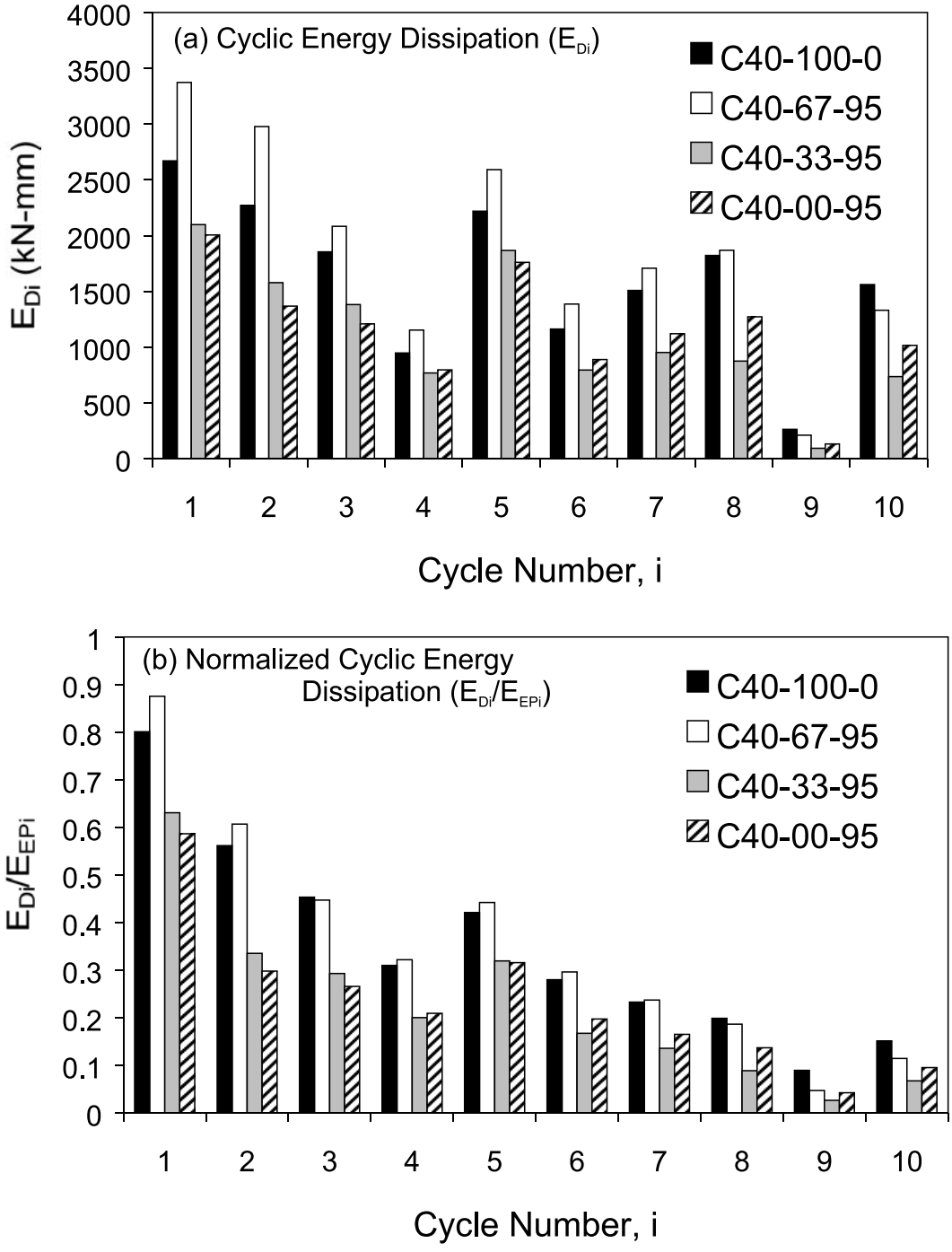

Figure 6.11 Effect of Reduced Thickness (t_r) on Deterioration of Energy Dissipation per Cycle

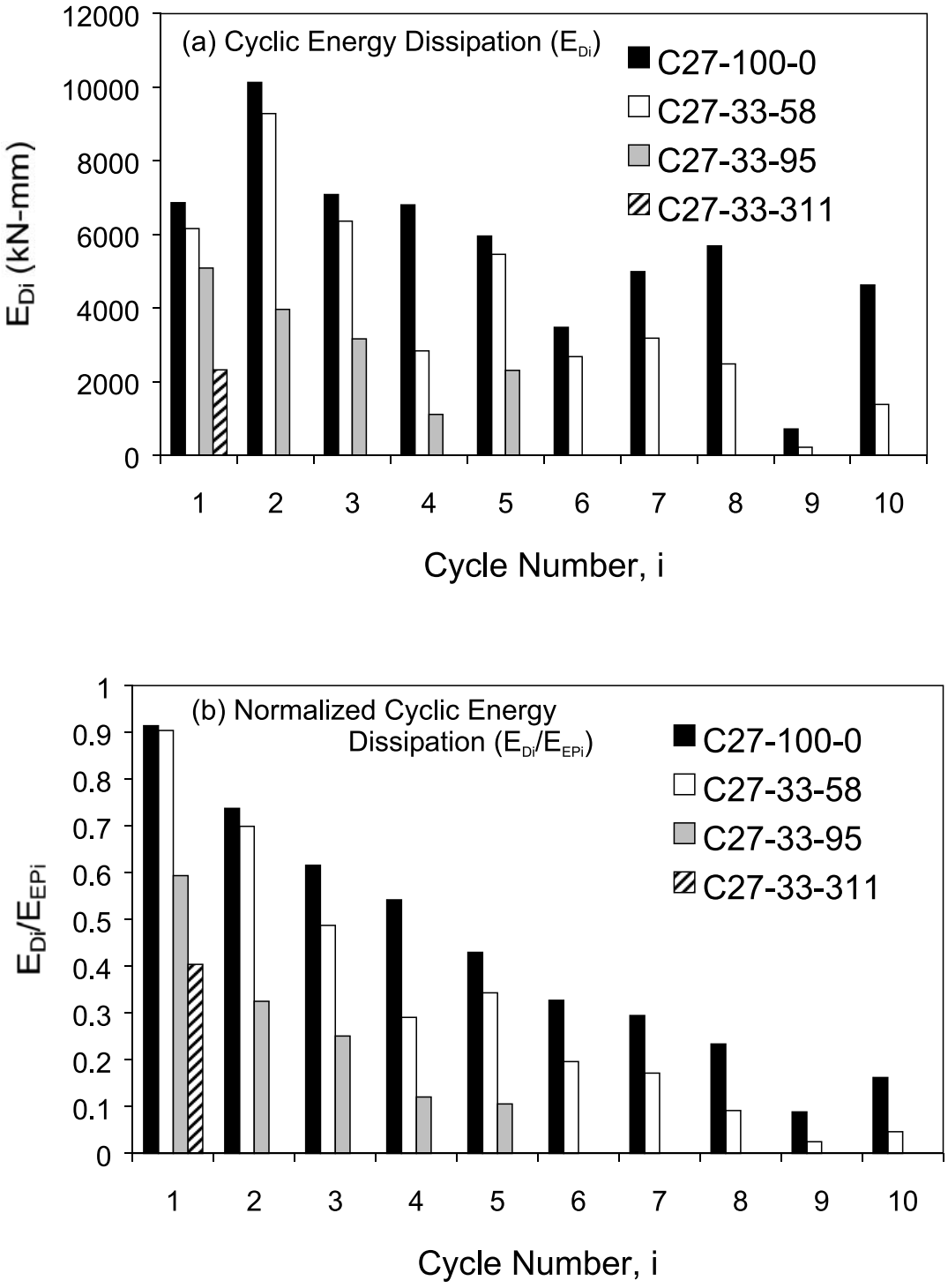

Figure 6.12 Effect of Subtending Angle (θ) on Deterioration of Energy Dissipation per Cycle

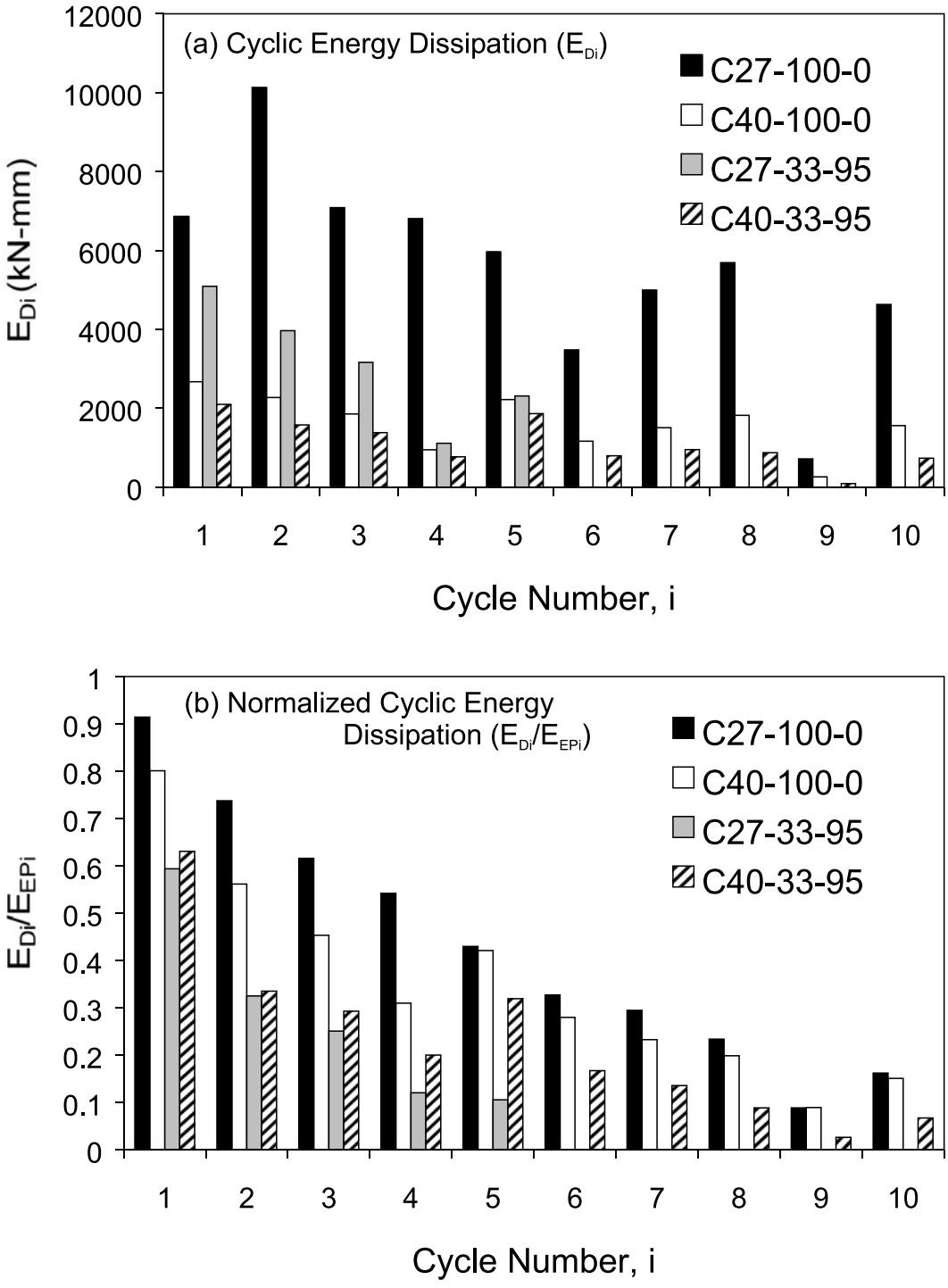

Figure 6.13 Effect of Diameter to Thickness Ratio (D/t) on Deterioration of Energy Dissipation per Cycle

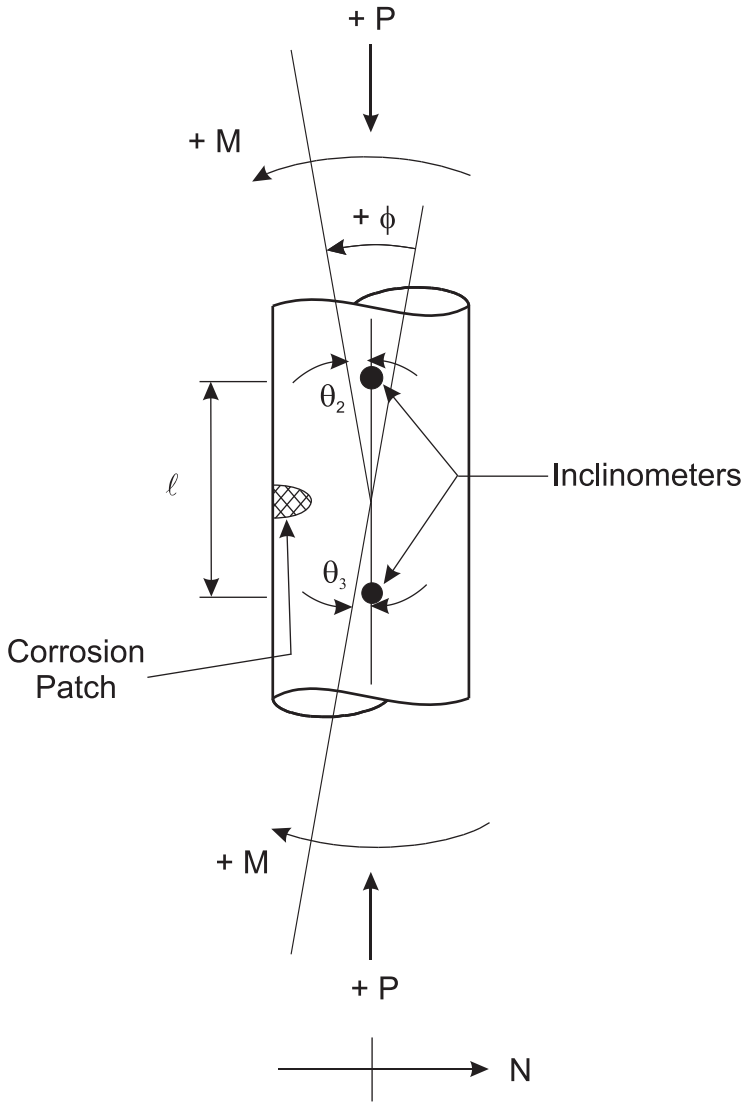

$$M = P(e + \delta_o + \delta)$$
$$\phi = (\theta_2 - \theta_3)\ell$$

M = Moment
ϕ = Curvature
e = Eccentricity
δ_o = Initial North-South Lateral Displacement at Mid-height
δ = North-South Lateral Displacement at Mid-height
θ = Rotation of Inclinometer (Counter Clockwise is Positive)

Figure 6.14 Definition of Positive Moment and Curvature

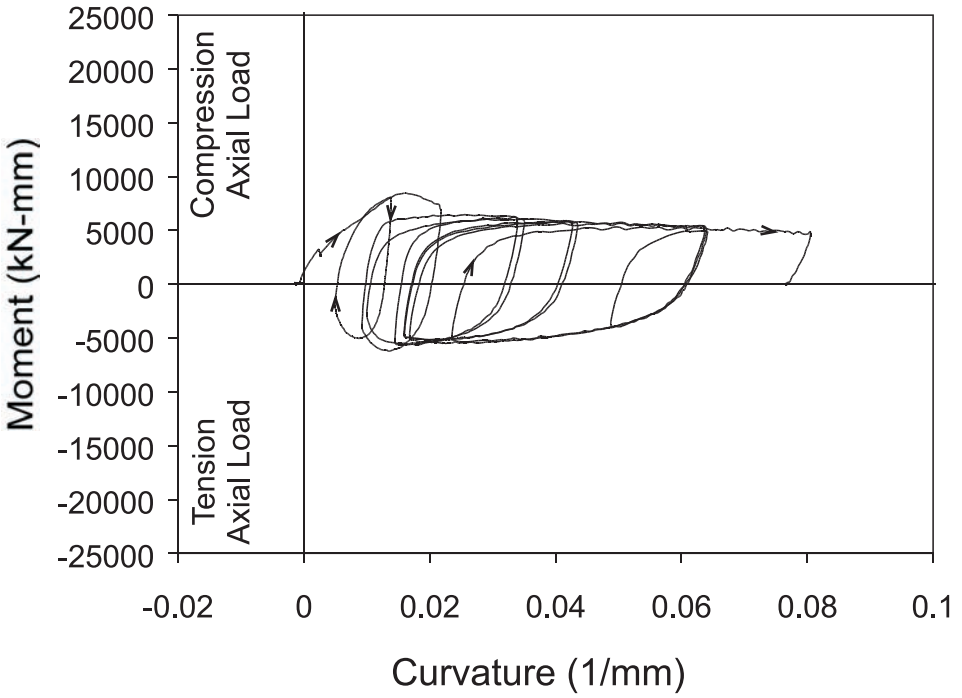

Figure 6.15 Moment - Curvature Response in Corroded Section, Specimen C40-100-0

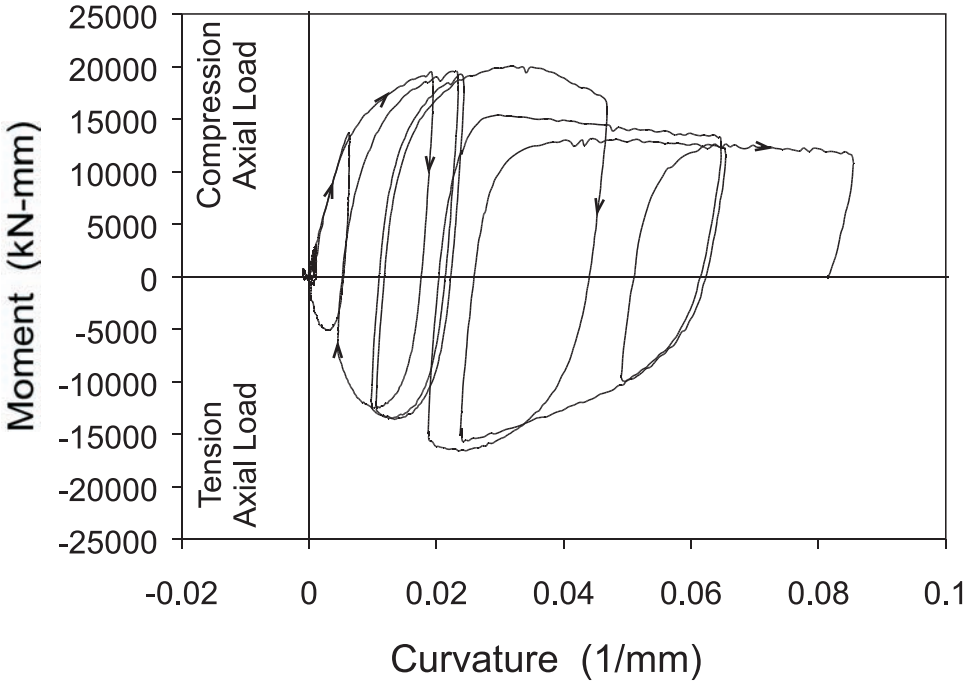

Figure 6.16 Moment - Curvature Response in Corroded Section, Specimen C27-100-0

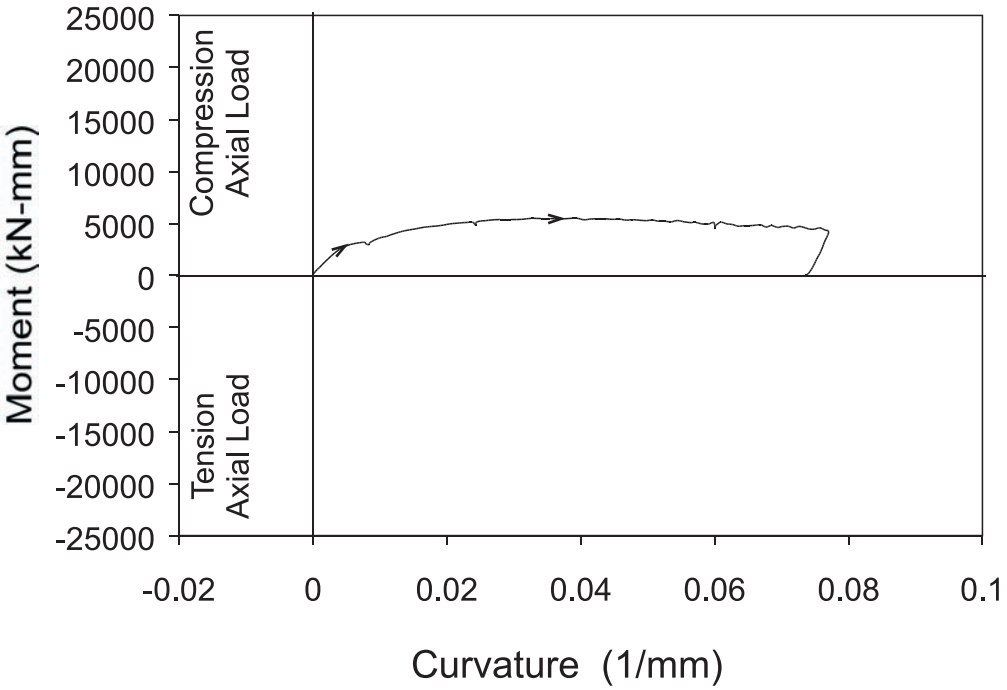

Figure 6.17 Moment - Curvature Response in Corroded Section, Specimen M40-33-95

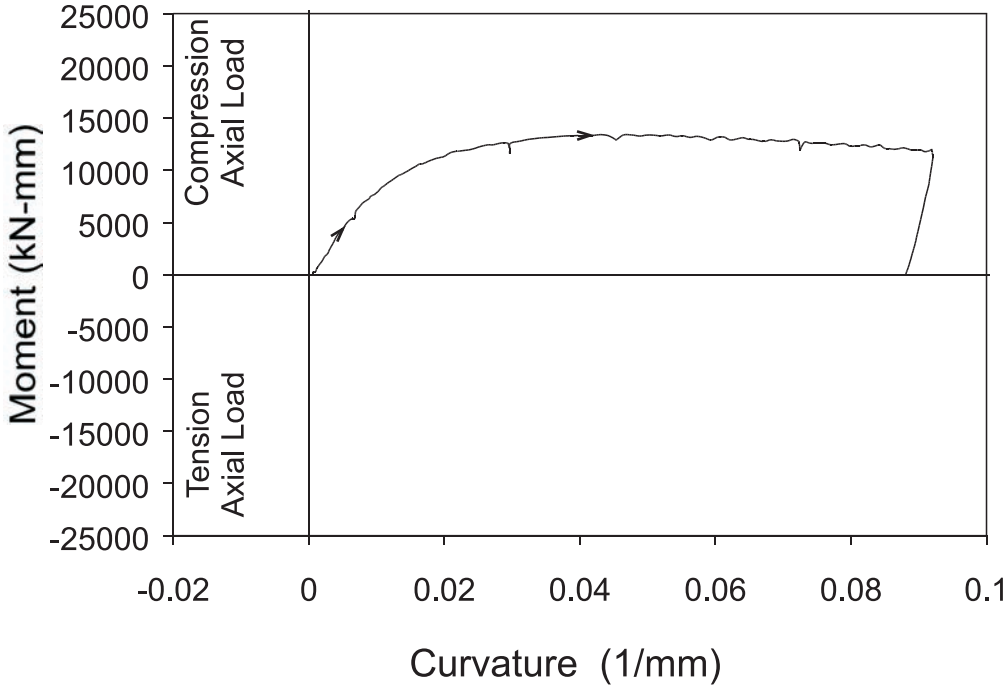

Figure 6.18 Moment - Curvature Response in Corroded Section, Specimen M27-33-95

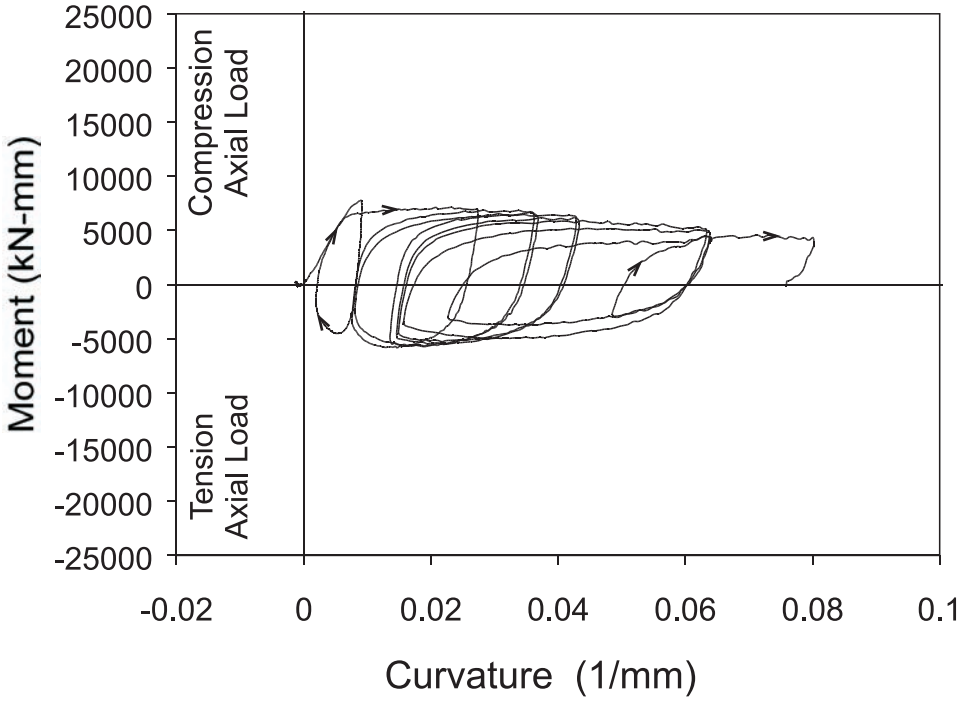

Figure 6.19 Moment - Curvature Response in Corroded Section, Specimen C40-67-95

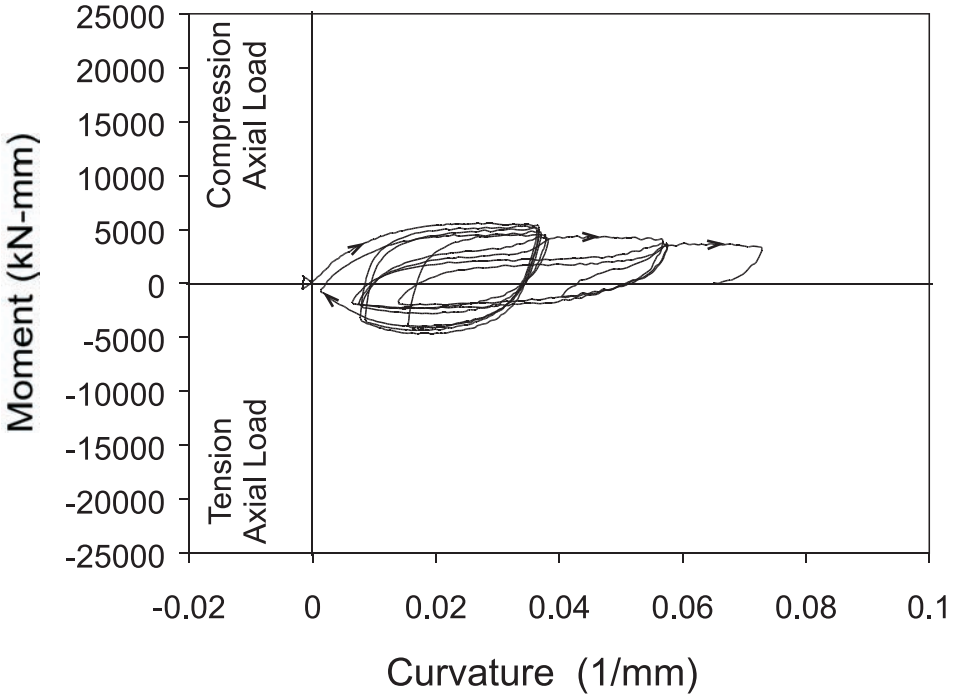

Figure 6.20 Moment - Curvature Response in Corroded Section, Specimen C40-33-95

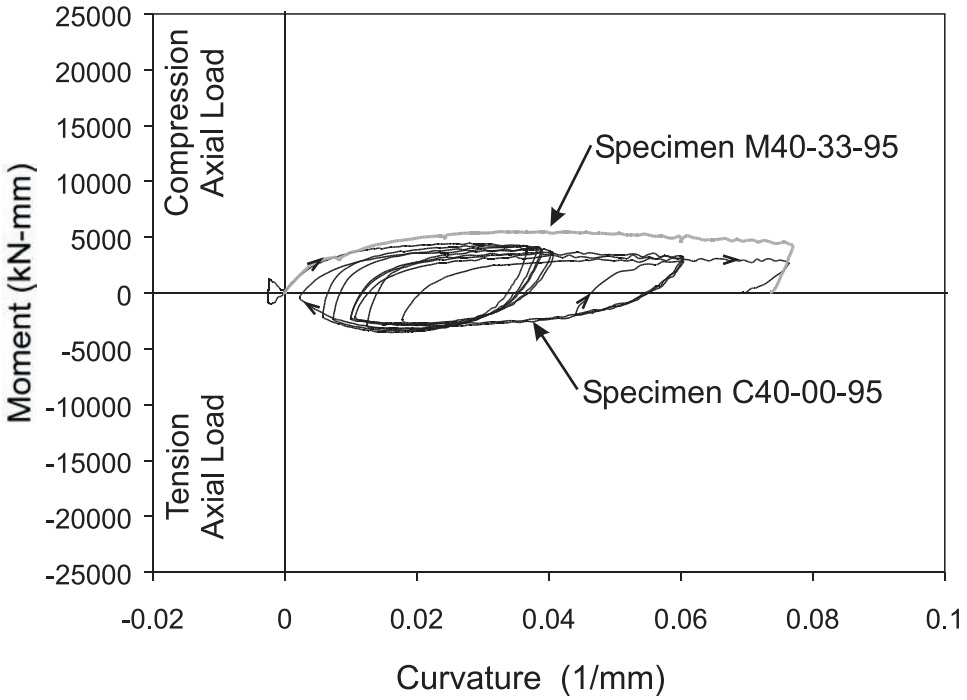

Figure 6.21 Moment - Curvature Response in Corroded Section, Specimen C40-00-95

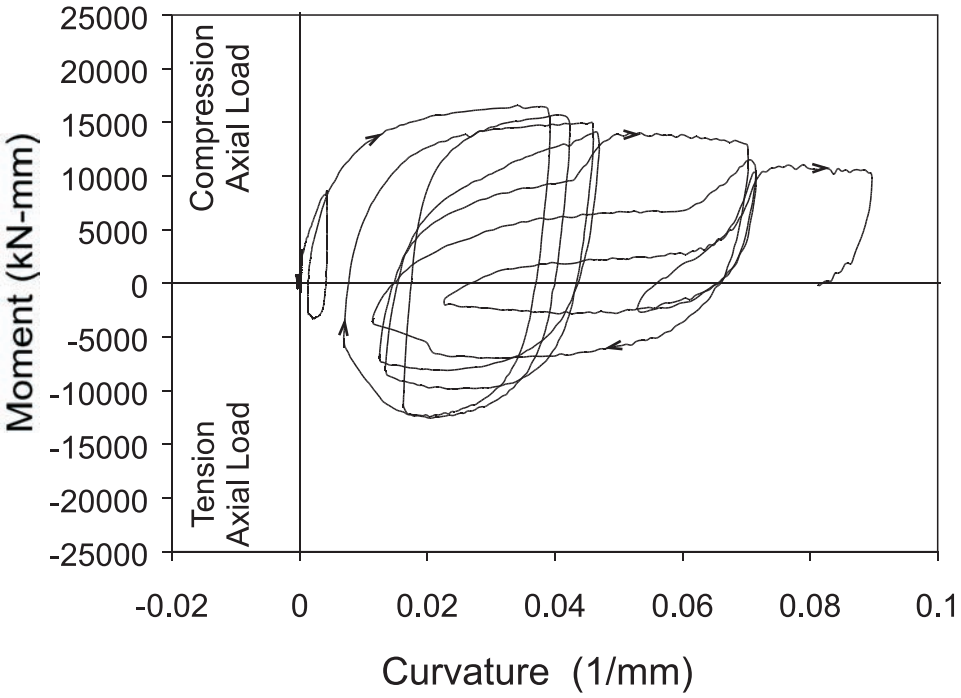

Figure 6.22 Moment - Curvature Response in Corroded Section, Specimen C27-33-58

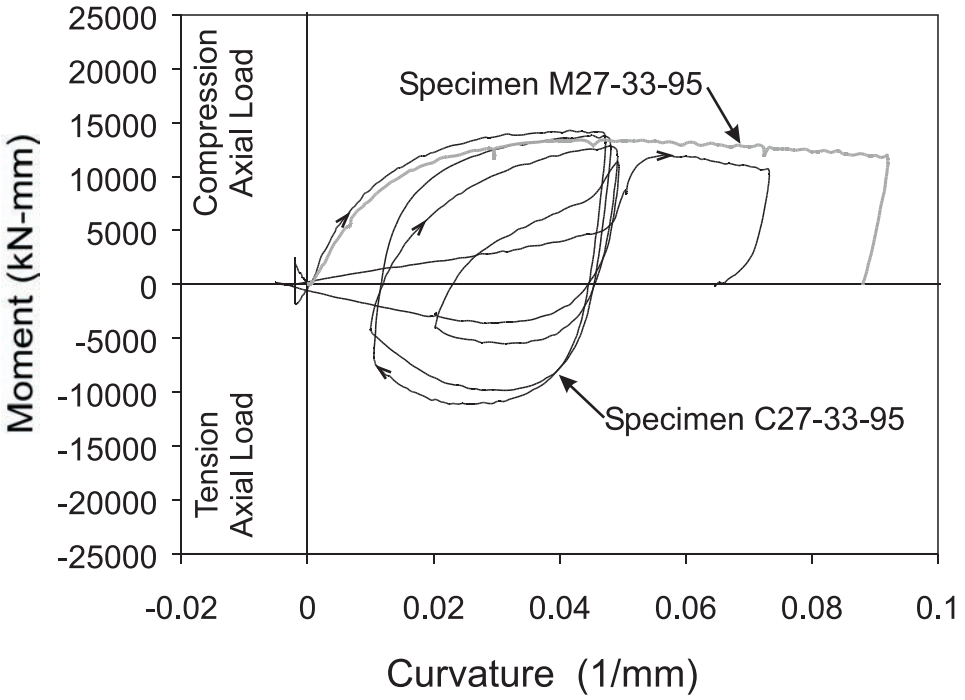

Figure 6.23 Moment - Curvature Response in Corroded Section, Specimen C27-33-95

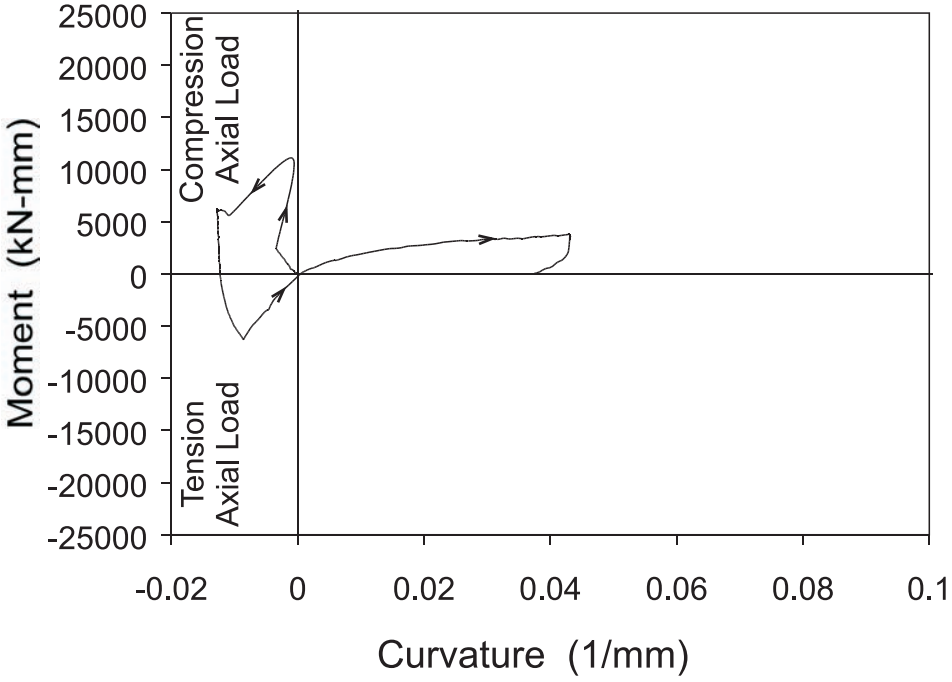

Figure 6.24 Moment - Curvature Response in Corroded Section, Specimen C27-33-311

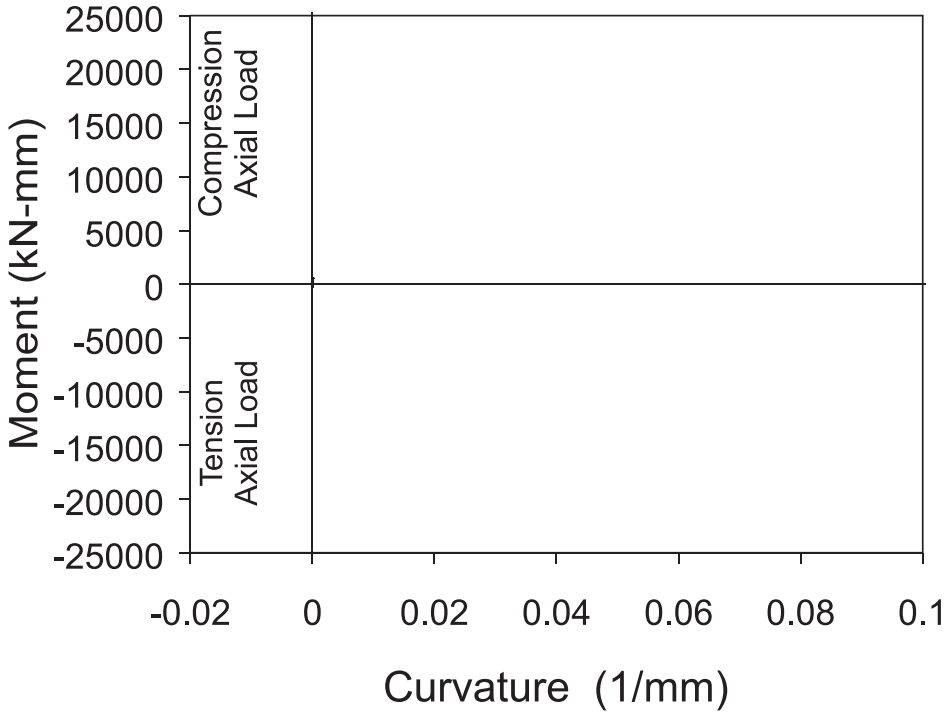

Figure 6.25 Moment - Curvature Response in Corroded Section, Specimen C40-00-95-RS

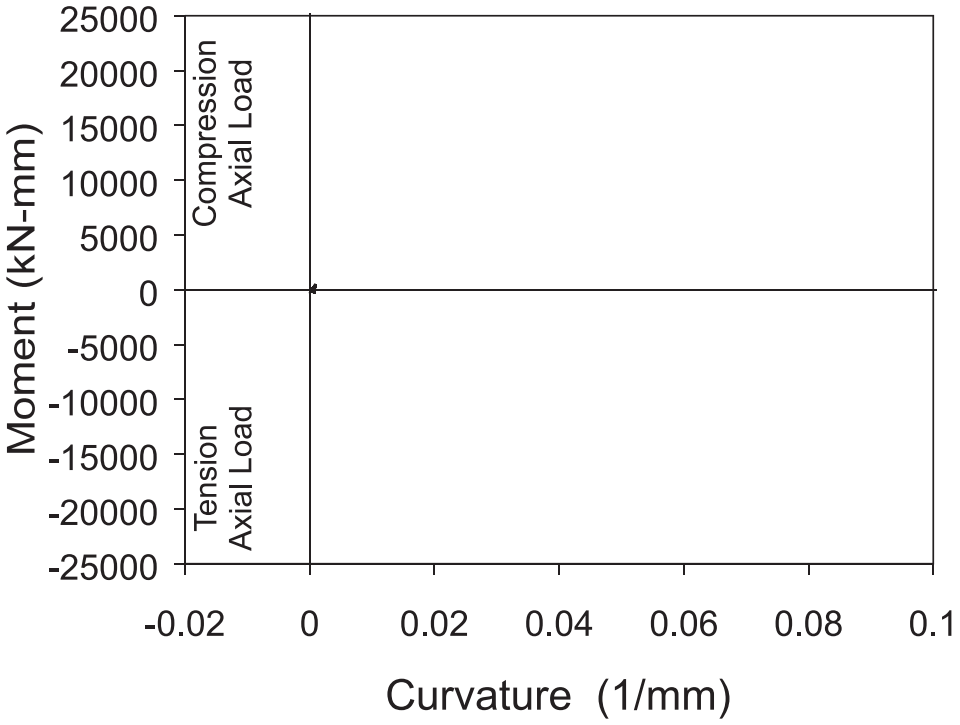

Figure 6.26 Moment - Curvature Response in Corroded Section, Specimen C40-00-95-RC

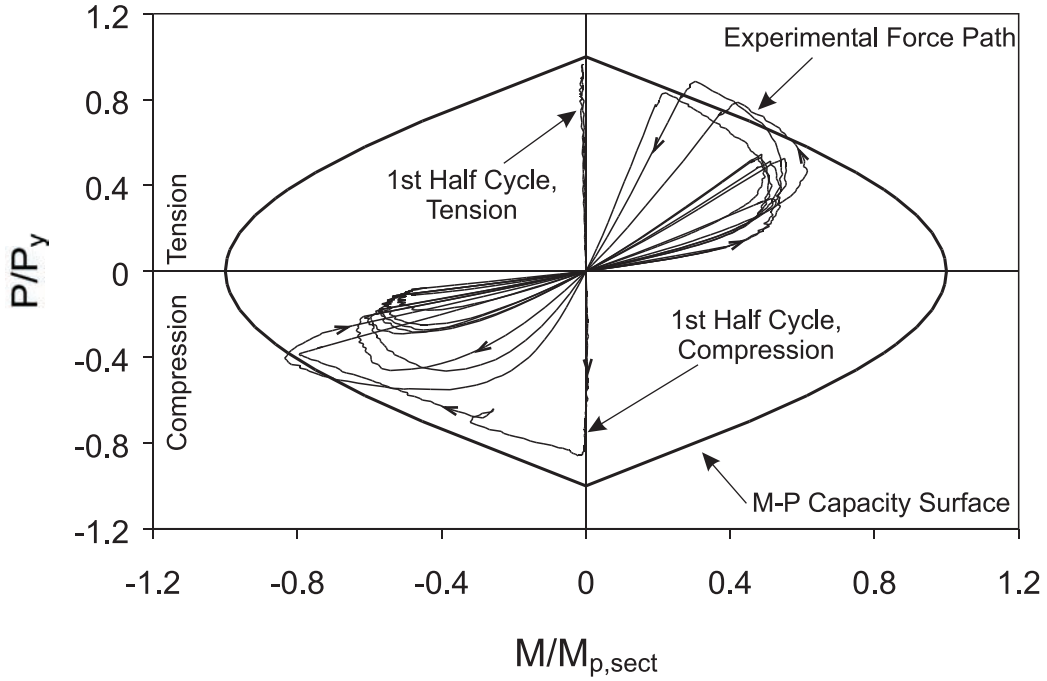

Figure 6.27 Axial Load - Moment Relationship,
Specimen C40-100-0

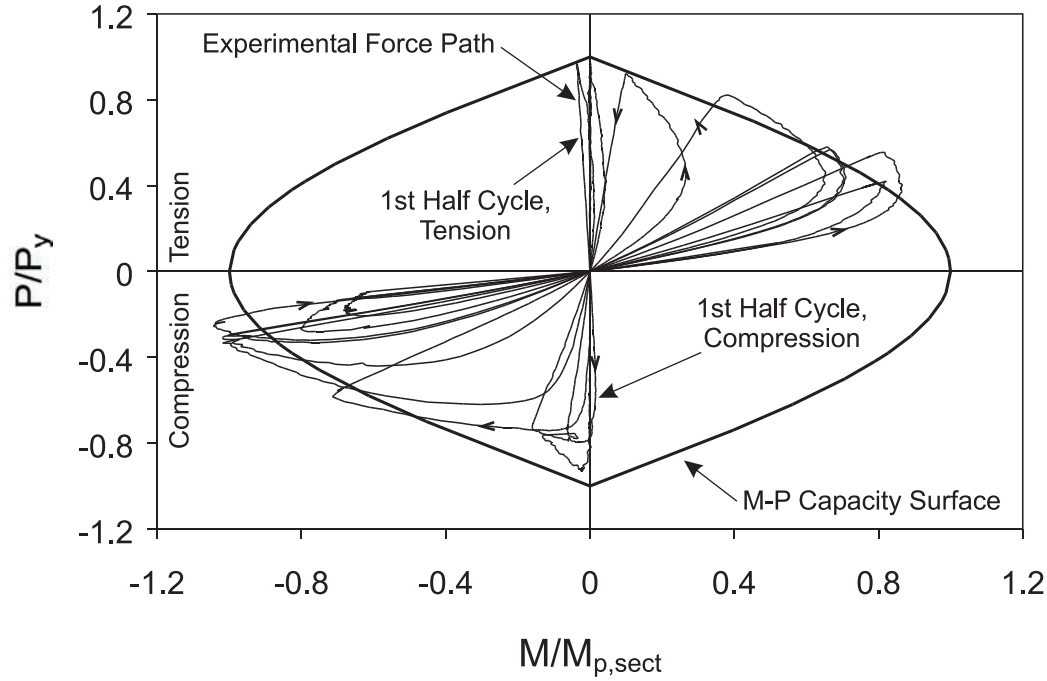

Figure 6.28 Axial Load - Moment Relationship,
Specimen C40-100-0

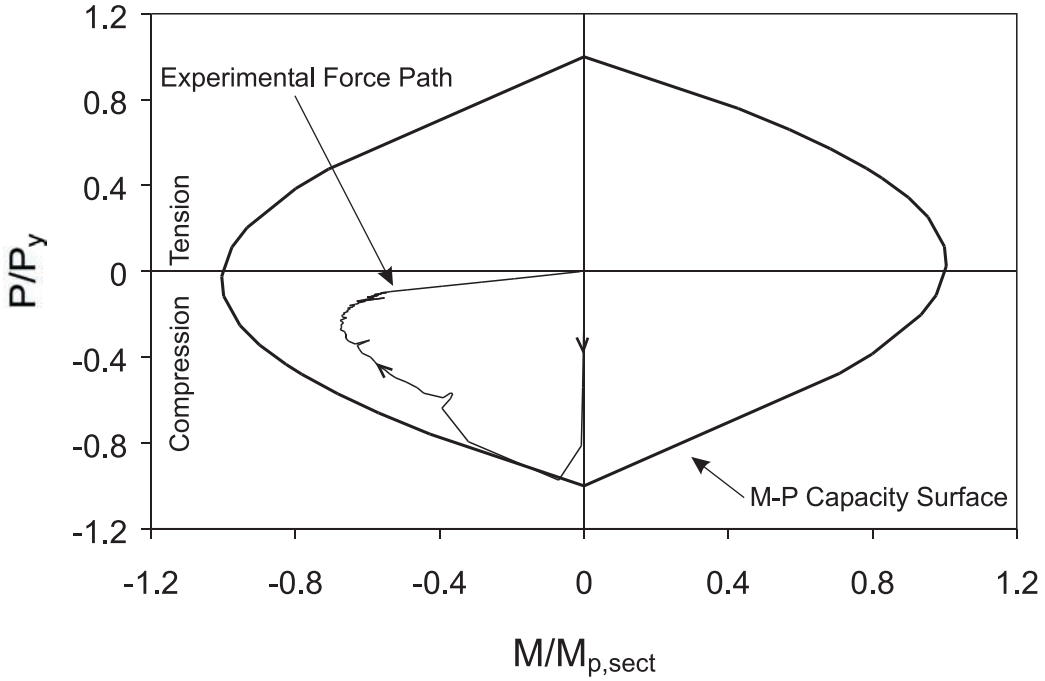

Figure 6.29 Axial Load - Moment Relationship,
Specimen M40-33-95

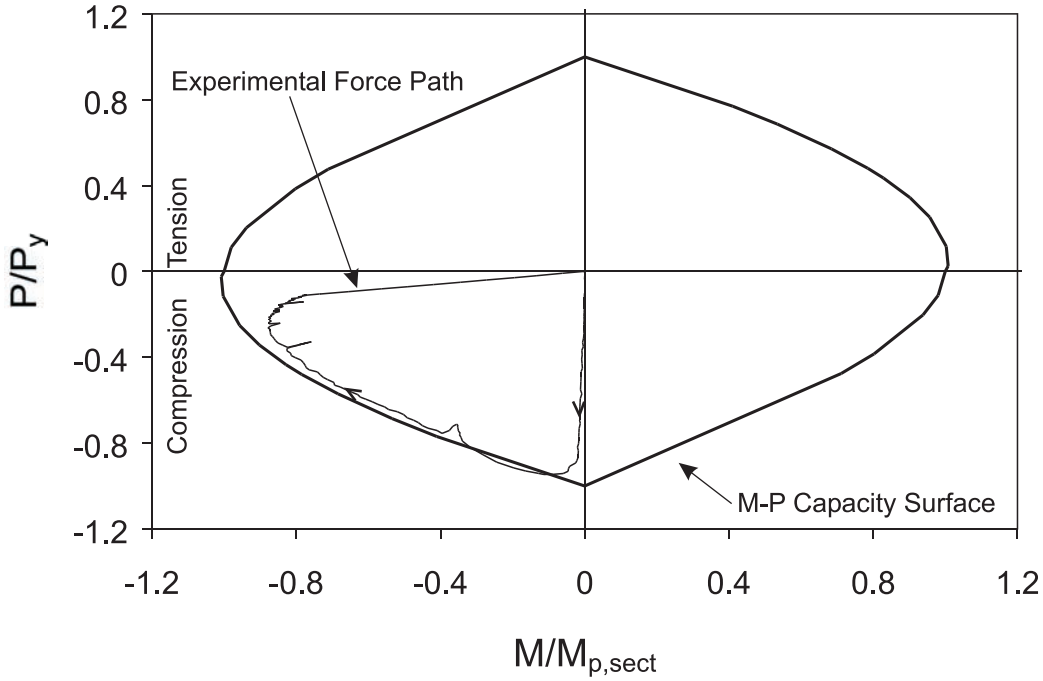

Figure 6.30 Axial Load - Moment Relationship,
Specimen M27-33-95

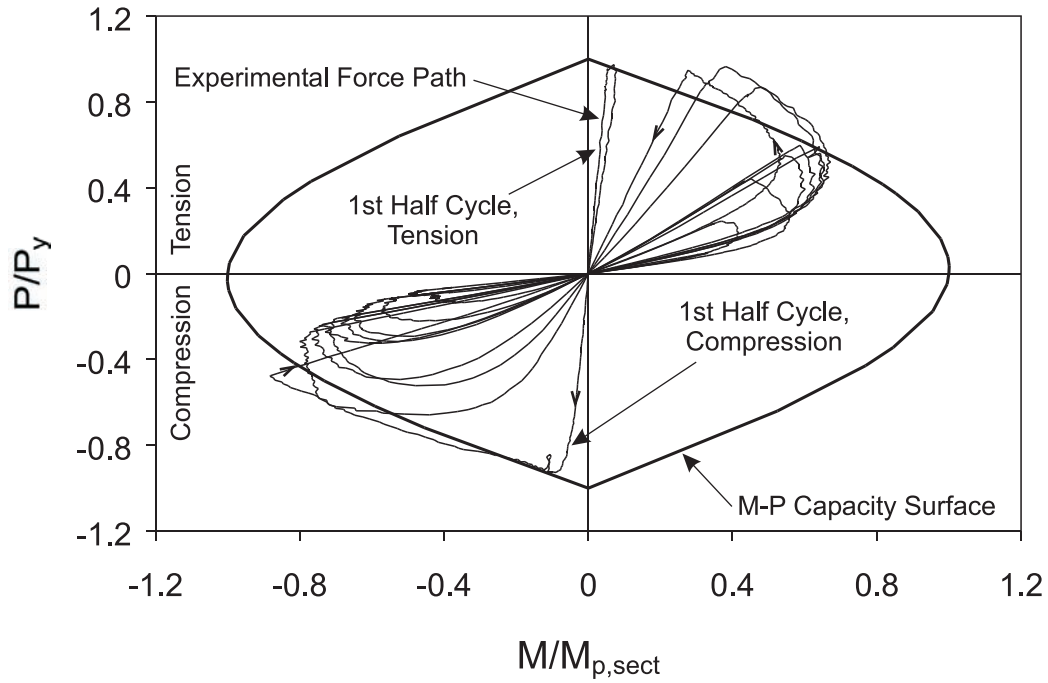

Figure 6.31 Axial Load - Moment Relationship,
Specimen C40-67-95

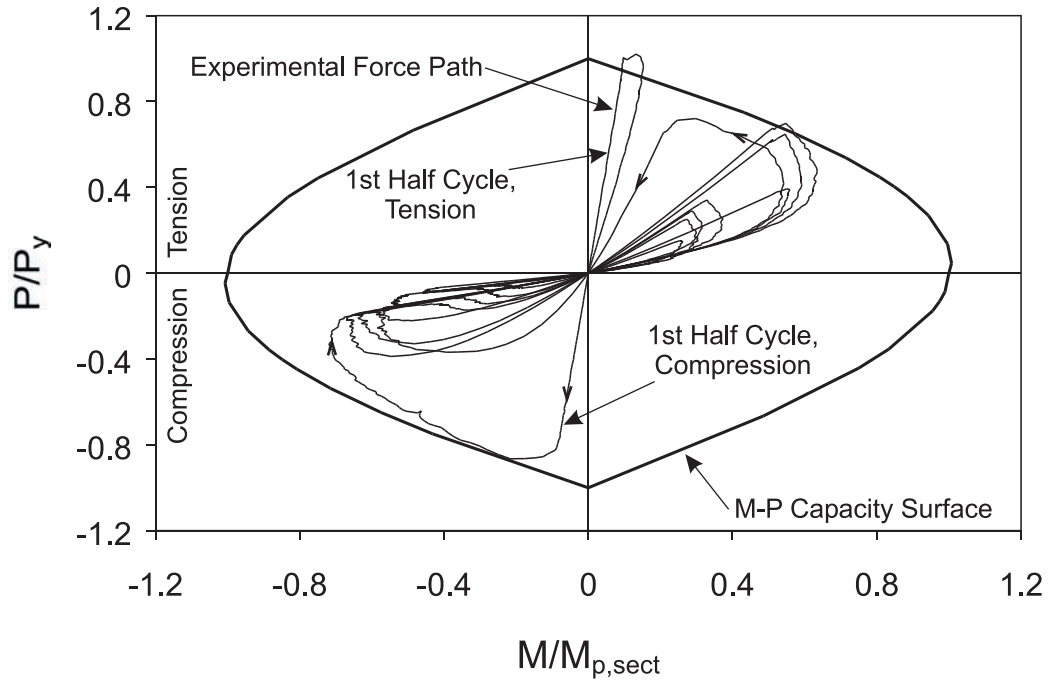

Figure 6.32 Axial Load - Moment Relationship,
Specimen C40-33-95

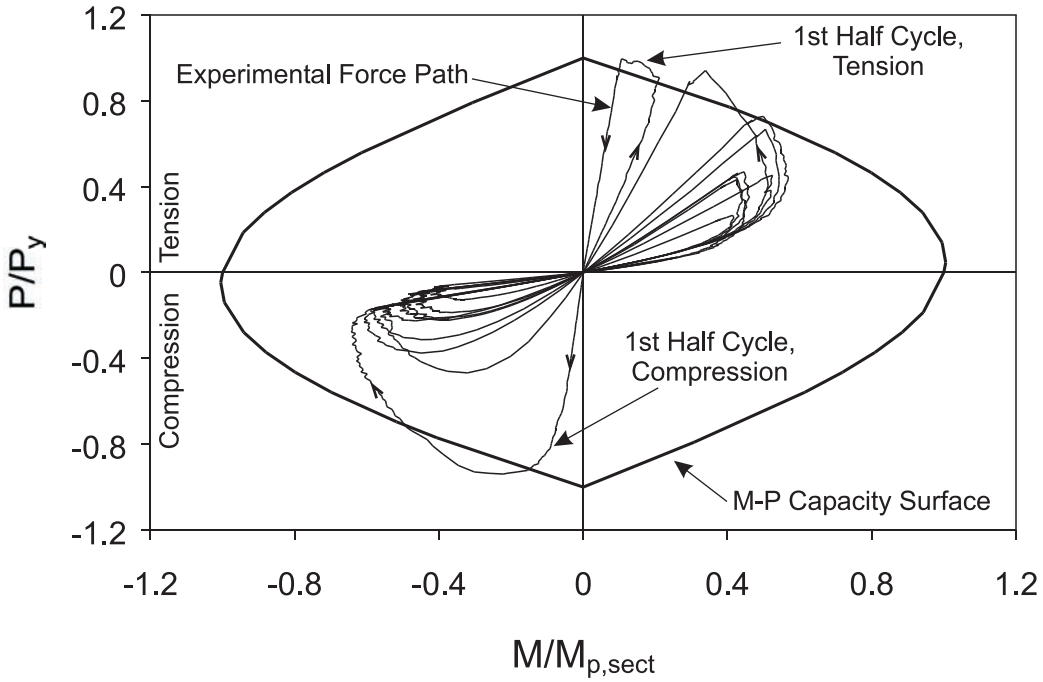

Figure 6.33 Axial Load - Moment Relationship,
Specimen C40-00-95

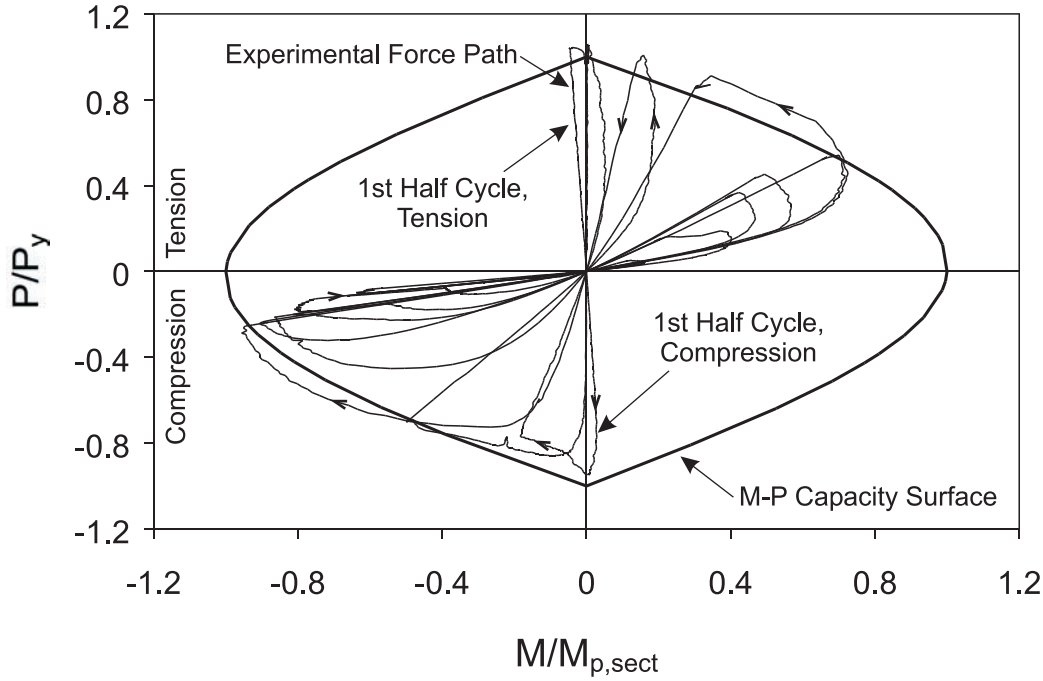

Figure 6.34 Axial Load - Moment Relationship,
Specimen C27-33-58

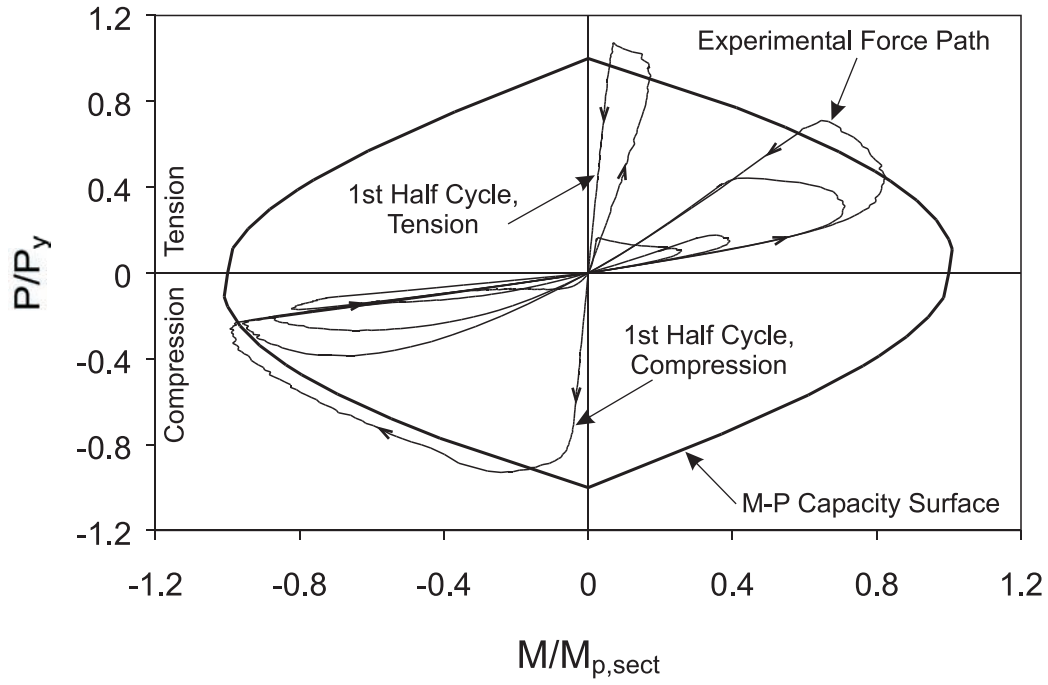

Figure 6.35 Axial Load - Moment Relationship,
Specimen C27-33-95

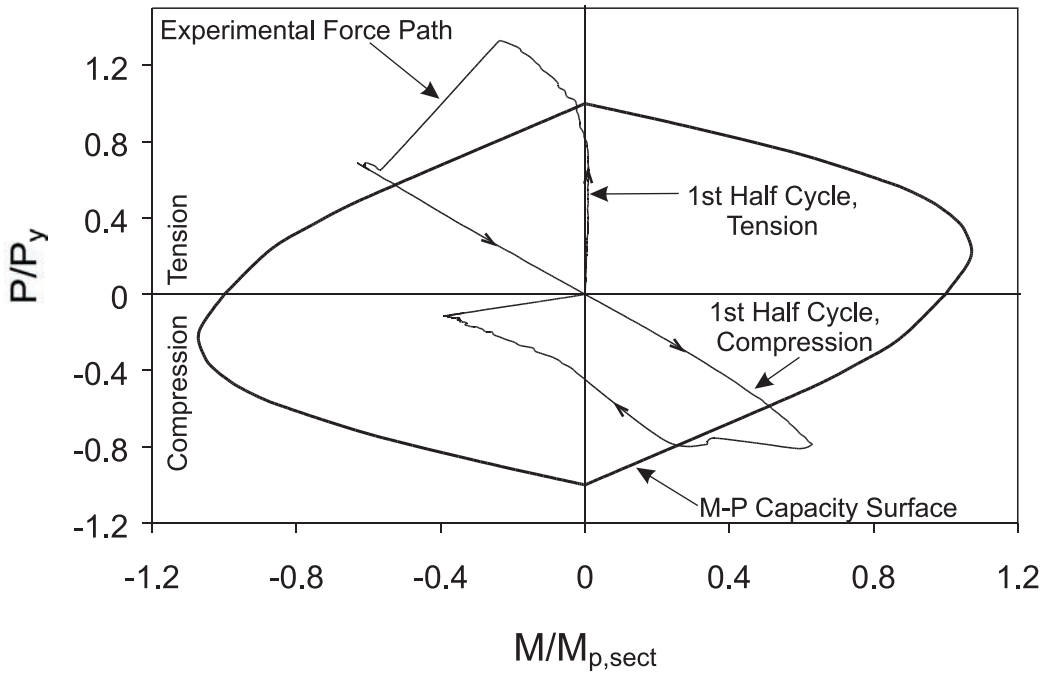

Figure 6.36 Axial Load - Moment Relationship,
Specimen C27-33-311

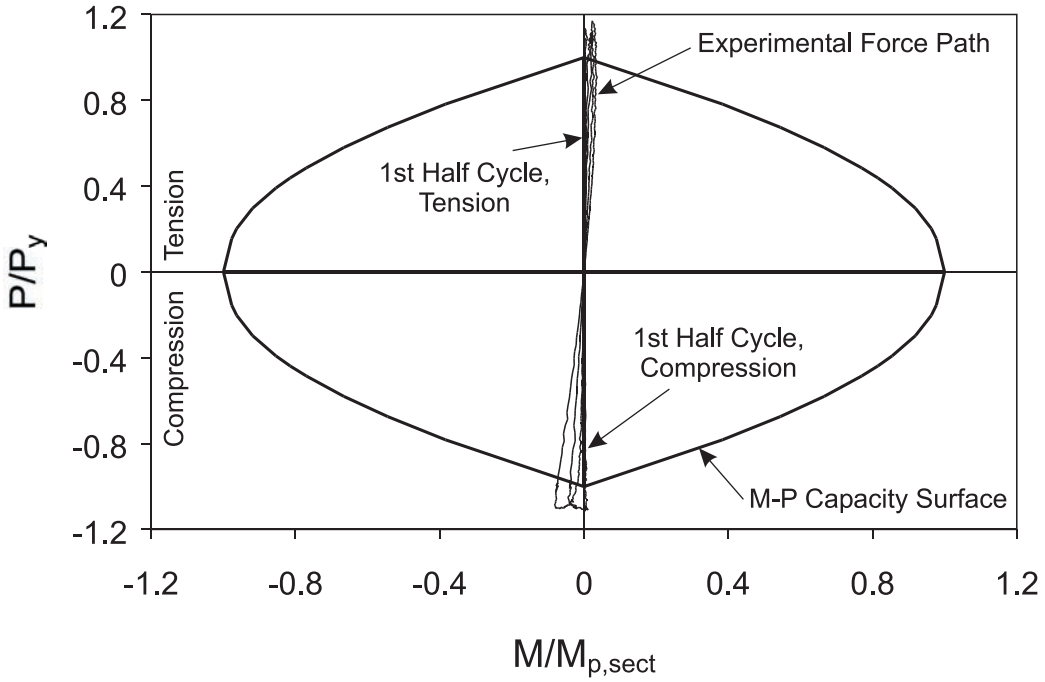

Figure 6.37 Axial Load - Moment Relationship,
Specimen C40-00-95-RS

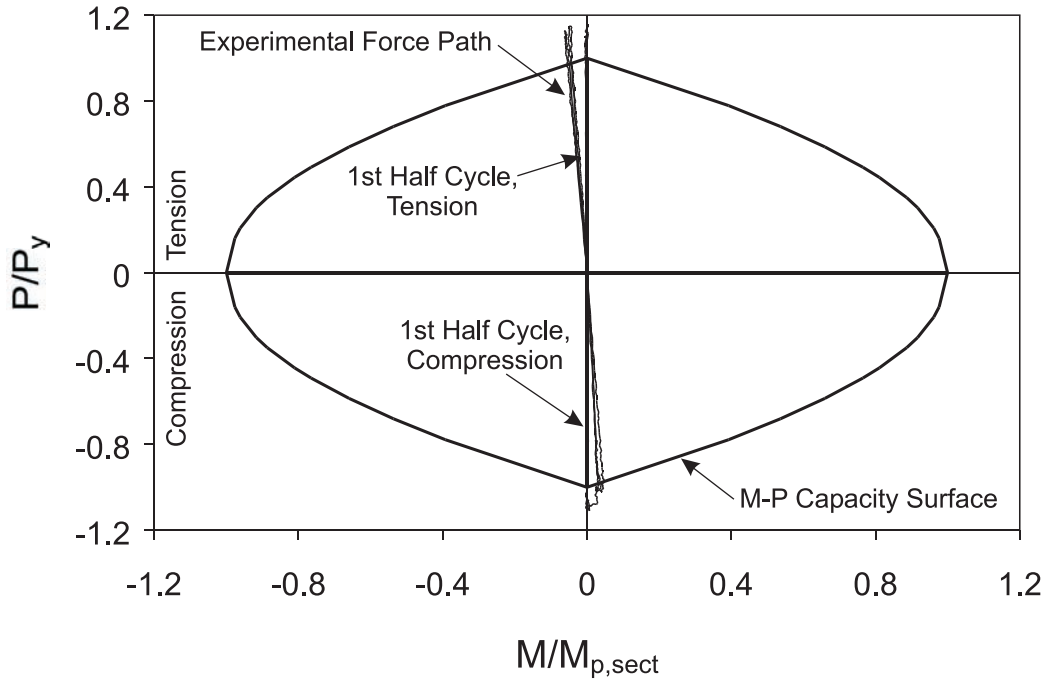

Figure 6.38 Axial Load - Moment Relationship,
Specimen C40-00-95-RC

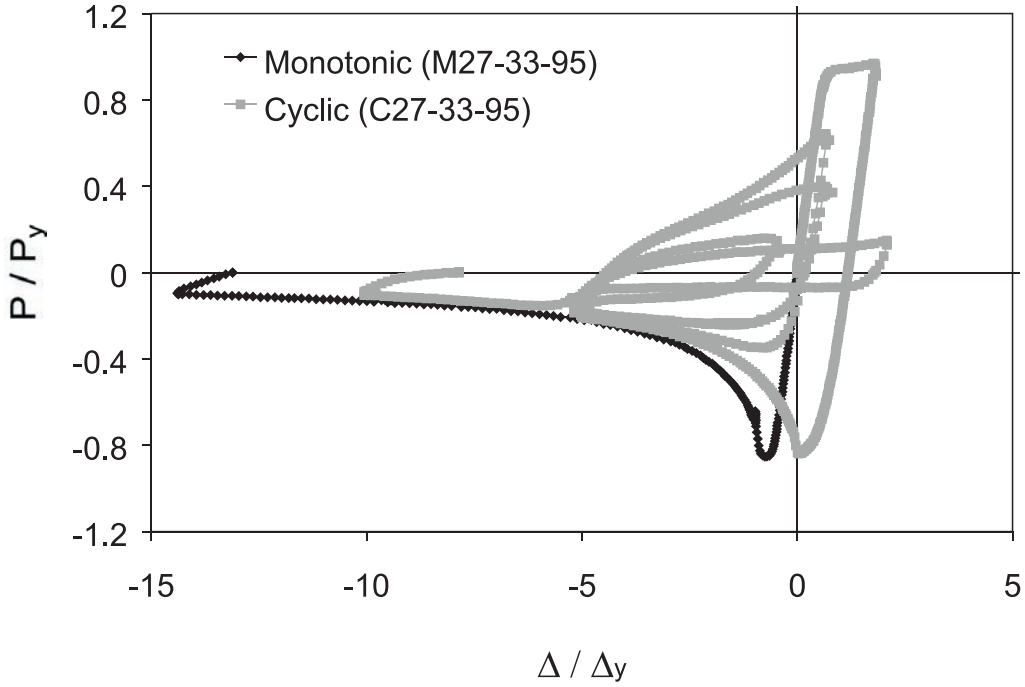

Figure 6.39 Comparison of Monotonic and Cyclic Response of Specimens C27-33-95 and M27-33-95

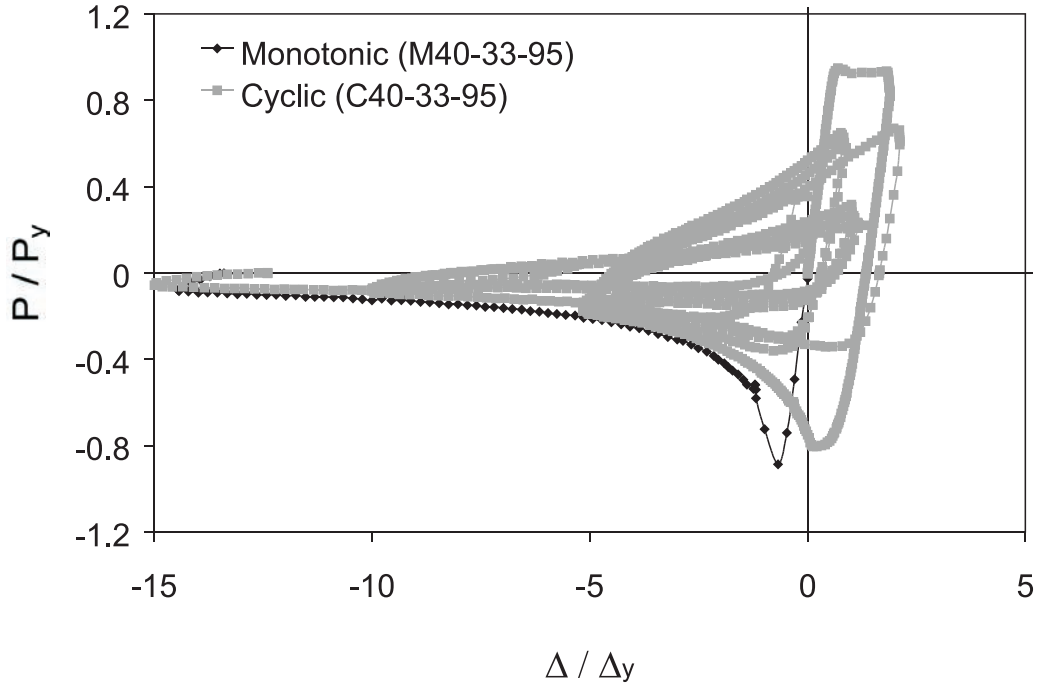

Figure 6.40 Comparison of Monotonic and Cyclic Response of Specimens C40-33-95 and M40-33-95

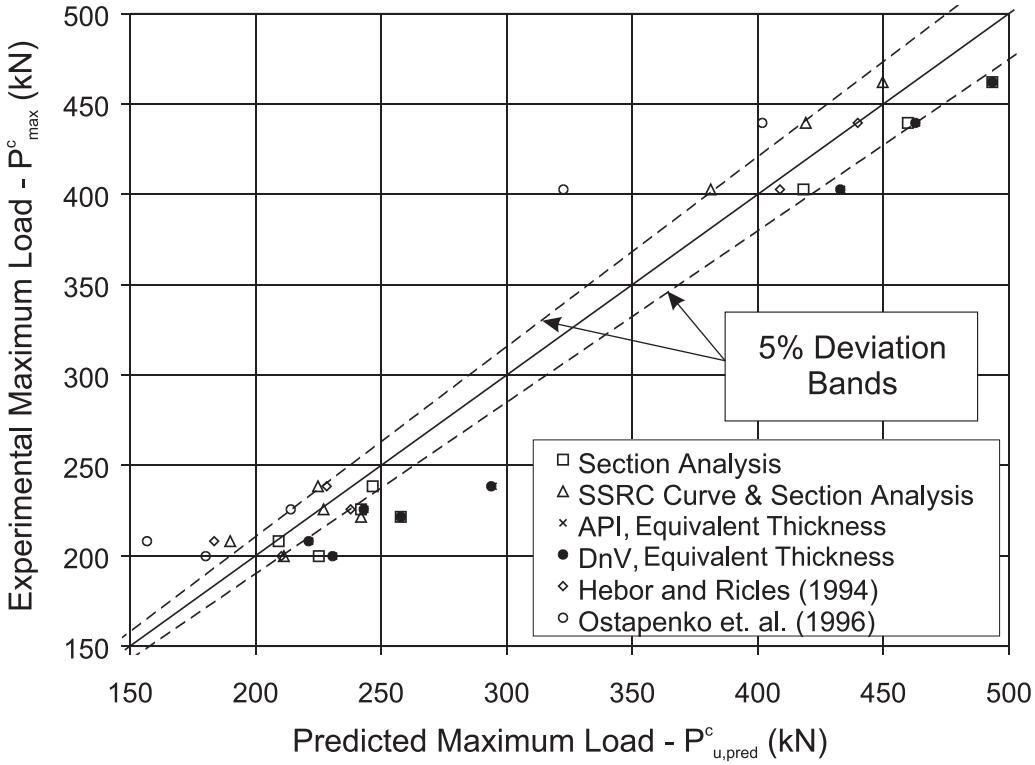

Figure 6.41 Scatter Diagram of Experimental and Predicted Axial Compression Load Capacity for all Specimens

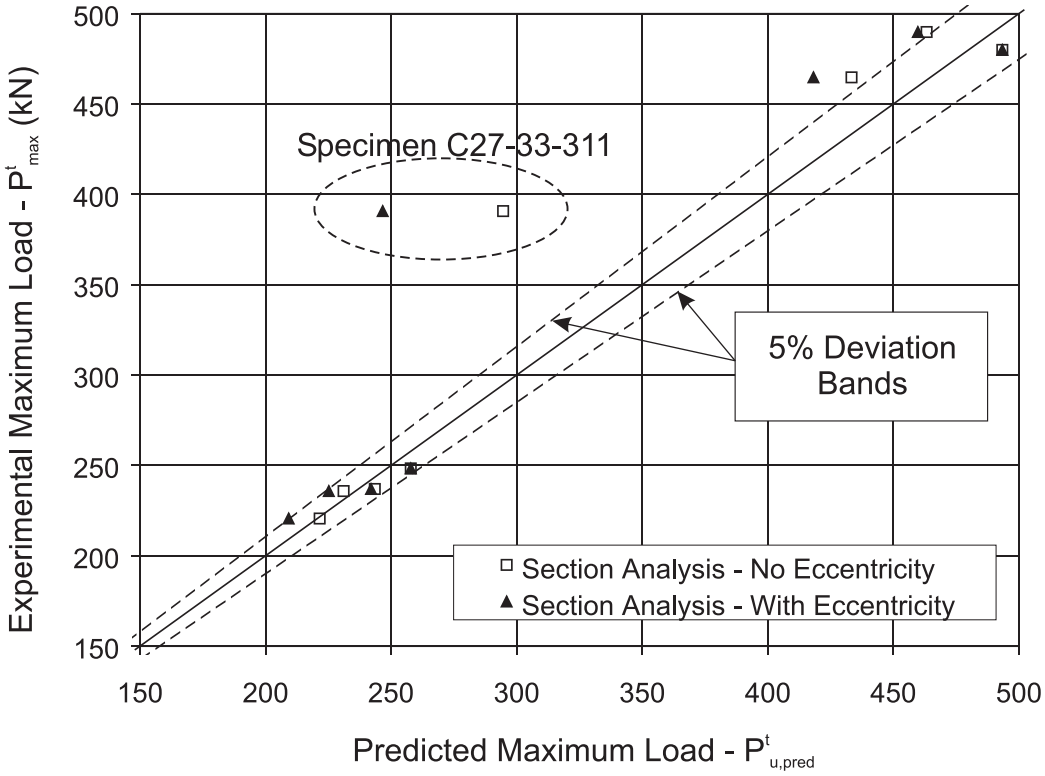

Figure 6.42 Scatter Diagram of Experimental And Predicted Axial Tension Load Capacity for all Specimens

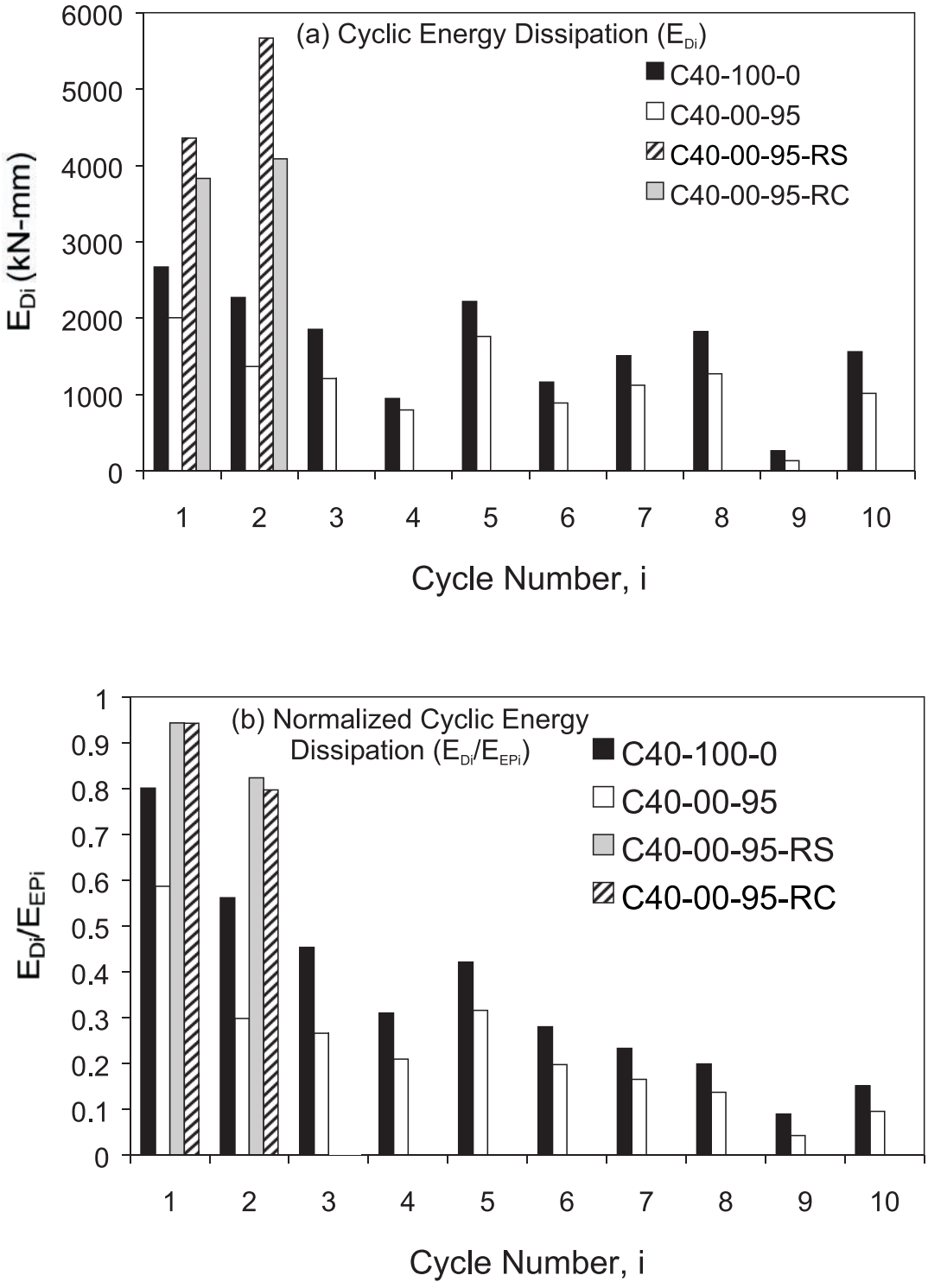

Figure 6.43 Effect of Repair on Energy Dissipation